A Parallel Hypothesis Method of Autonomous Underwater Vehicle Navigation
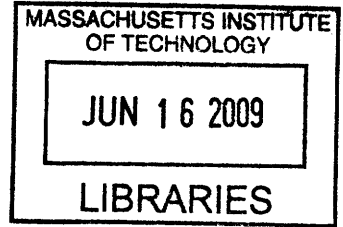
by

Cara Elizabeth Grupe LaPointe

B.S., United States Naval Academy (1997)
M.Phil., University of Oxford (1999)
M.S., Massachusetts Institute of Technology (2006)
Eng., Massachusetts Institute of Technology (2006)

Submitted to the Joint Program in Applied Ocean Science & Engineering

in partial fulfillment of the requirements for the degree of

Doctor of Philosophy

at the

MASSACHUSETTS INSTITUTE OF TECHNOLOGY

and the

WOODS HOLE OCEANOGRAPHIC INSTITUTION

June 2009

Signature of Author...
Joint Program in Applied Ocean Science & Engineering
March 11, 2009

Certified by...........   ....
Dana R. Yoerger
Senior Scientist, Woods Hole Oceanographic Institution
Thesis Supervisor

Accepted by.........   ....
James C. Preisig
Chairman, Joint Committee for Applied Ocean Science & Engineering
Woods Hole Oceanographic Institution

Accepted by....   ....
David E. Hardt
Chairman, Department Committee on Graduate Studies
Department of Mechanical Engineering, Massachusetts Institute of Technology

A Parallel Hypothesis Method of

Autonomous Underwater Vehicle Navigation

by

Cara Elizabeth Grupe LaPointe

Abstract

This research presents a *parallel hypothesis* method for autonomous underwater vehicle navigation that enables a vehicle to expand the operating envelope of existing long baseline acoustic navigation systems by incorporating information that is not normally used. The parallel hypothesis method allows the *in-situ* identification of acoustic multipath time-of-flight measurements between a vehicle and an external transponder and uses them in real-time to augment the navigation algorithm during periods when direct-path time-of-flight measurements are not available. A proof of concept was conducted using real-world data obtained by the Woods Hole Oceanographic Institution Deep Submergence Lab's Autonomous Benthic Explorer (ABE) and Sentry autonomous underwater vehicles during operations on the Juan de Fuca Ridge.

This algorithm uses a nested architecture to break the navigation solution down into basic building blocks for each type of available external information. The algorithm classifies external information as either line of position or gridded observations. For any line of position observation, the algorithm generates a multi-modal block of parallel position estimate hypotheses. The multimodal hypotheses are input into an arbiter which produces a single unimodal output. If *a priori* maps of gridded information are available, they are used within the arbiter structure to aid in the elimination of false hypotheses. For the proof of concept, this research uses ranges from a single external acoustic transponder in the hypothesis generation process and grids of low-resolution bathymetric data from a ship-based multibeam sonar in the arbitration process.

The major contributions of this research include the *in-situ* identification of acoustic multipath time-of-flight measurements, the multiscale utilization of *a priori* low-resolution bathymetric data in a high-resolution navigation algorithm, and the design of a navigation algorithm with a flexible architecture. This flexible architecture allows

the incorporation of multimodal beliefs without requiring a complex mechanism for real-time hypothesis generation and culling, and it allows the real-time incorporation of multiple types of external information as they become available *in situ* into the overall navigation solution.

Thesis Supervisor: Dana R. Yoerger
Title: Senior Scientist, Woods Hole Oceanographic Institution

Acknowledgments

First and foremost, I would like to thank the members of my thesis committee: Dr. Dana Yoerger, Professors John Leonard and Brian Bingham, and Captain Mark Welsh. My deepest gratitude goes to my advisor, Dana Yoerger. Over the past four years, Dana has become a true friend and mentor as well as advisor. I am indebted to him for introducing me to the unique and exciting world of underwater exploration and deep-sea engineering. His patient guidance and encouragement have made my research possible, and our frequent discussions about life, politics, dogs and the Red Sox have helped me keep perspective through it all. I was extremely fortunate to have on my committee John Leonard, whose energy, enthusiasm and advocacy on behalf of his students are unparalleled. His knowledge of robotics is profound and I have learned much from him. I want to thank in particular Brian Bingham who was instrumental to the completion of my research. He went above and beyond in many ways through his advice, his thoughtful comments about my research, and in providing me with time-saving research tools. Captain Mark Welsh was a late addition to my committee, but he was invaluable in bridging the gap between the vastly different worlds of the Navy and MIT to ensure the successful completion of my degree. I would also like to thank his predecessor, Captain Patrick Keenan, for his support along the way.

I thank the United States Navy for giving me this incredible opportunity, especially all of the people who have worked in the Navy Postgraduate Office during my time here. They have been supportive of me as I have continued down countless unbeaten intellectual and career paths. I look forward to embarking on the rest of my career in the US Navy with the unique perspective that this road less traveled has given me.

No research would be possible at either MIT or WHOI without the many people who make everything possible. I would like to thank Marsha Gomes, Julia Westwater, and everyone in the Academic Programs Office at WHOI for continually supporting me throughout this endeavor and for funding my final year in the Joint Program. Leslie Regan and her team in the Mechanical Engineering Graduate Office have helped me navigate the confused seas left in the wake of the Ocean and Mechanical Engineering Departments merger. They have somehow managed to keep everything straight as I have journeyed through MIT as a 13A, 13B, 13W, 2N, and 2W. Leslie is undoubtedly MIT's most valuable asset and its students' most ardent advocate. I also thank Pete Beaulieu and Mary Mullowney in the Navy PG Office at MIT and Melissa Keane, Karen Schwamb, and Ann Stone in the Deep Submergence Lab at WHOI for all of their help over the past years. Most importantly, I could never have finished this research without Judy Fenwick. Her encouragement and eternal willingness to be there in times of need have made possible the constant juggling act that is my life.

I have greatly enjoyed being part of the Deep Submergence Lab at WHOI which is a dynamic and creative intellectual family. On a daily basis the members of DSL take seemingly impossible technological challenges and turn them into reality. I would like

Contents

List of Figures

16

18

List of Tables

Chapter 1

Introduction

Autonomous underwater vehicles (AUVs) are increasingly prevalent in modern society. The military, industry and academia use AUVs for a wide range of applications. As mobile platforms for sensing equipment and cameras, AUVs are drastically improving human understanding of the vast ocean depths. The relative importance of AUVs among underwater vehicles has been increasing over the last two decades as their capabilities have improved. They cost less than, and do not involve the inherent risk to human life of, manned submersibles. AUVs are not constrained by tethers like remotely operated vehicles (ROVs). However, AUVs are not a substitute for manned or remotely operated vehicles because of current limitations. For instance, they are not able to send real-time video to the surface and few have any ability to collect samples. Therefore, for scientific missions involving deep sea floor exploration, AUVs often work in concert with other types of vehicles. AUVs are well suited to accomplish high-resolution mapping and survey operations that allow scientists to pinpoint areas of interest for further study by ROVs or manned submersibles. However, the quality of science data collected by the AUV and the ensuing cooperation with other platforms is limited by the navigational accuracy of the AUV. Therefore, effective localization and navigation is critical to AUV mission accomplishment.

Many existing unmanned underwater navigation methods are precise, accurate

and reliable when operated within the given parameters of that method. One such navigation scheme often used in deep-ocean scientific operations is acoustic long base-line navigation (LBL) [36] in which an AUV localizes itself and navigates by communicating with a deployed network of acoustic transponders. For a distance scale on the order of ten kilometers, an AUV using LBL can often localize itself with precision on the order of ten meters or less in good conditions. However, in a cluttered acoustic underwater environment or when the AUV tries to escape the operating box of that LBL network and operate on its fringes, the localization accuracy quickly degrades and incorrect fix computations usually occur. The parallel hypothesis (PH) navigation method was designed to push the edges of the existing operational envelope by incorporating additional information that is available *in situ* to the AUV but is not normally used within the navigation solution.

1.1   Context: AUV Navigation

Most underwater vehicle navigation involves some form of dead reckoning with varying techniques to bound the error growth using external information. Dead reckoning (DR) is the process of using knowledge of a vehicle's motion since its last known position to estimate the vehicle location at any given time [9]. Since inexpensive and accurate depth sensors are widely available [37], the three-dimensional localization problem can be easily geometrically transformed into a two-dimensional horizontal plane localization problem. In the horizontal plane, a vehicle's speed is integrated over time to provide distance traveled. In dead reckoning, this distance is applied along the vehicle's traveled course to provide estimated vehicle location.

Rudimentary methods of determining vehicle course and speed involve odometric models using basic magnetic compass headings and propeller revolutions. More advanced sensors for determining course and speed include doppler velocity logs (DVL) and inertial measurement units (IMU). However, even navigation systems based on

these types of sophisticated sensors, such as inertial navigation systems (INS), require periodic reinitialization with external information to bound their continually growing error. For surface and air vehicles, the Global Positioning System (GPS) is a prevalent method of reinitializing navigation solutions. However, the radio-frequency signals used in GPS cannot effectively penetrate seawater, so AUVs can only use GPS directly to constrain position error when they are at or very near the surface. For underwater navigation, there exists a spectrum of methods used to constrain the growth of positional estimation error. At one end of the spectrum there are probabilistic robotics filtering algorithms such as Gaussian or particle filters based on a time series of internal and external information with modeled error to provide the position update. At the other end of the spectrum are instantaneous localization methods such as acoustically-based ultra-short baseline (USBL) or long baseline (LBL) systems.

1.2   Motivation: The Research Problem

This research assumes that sophisticated scientific AUVs conducting long-duration, precision operations in the deep ocean often rely on LBL navigation systems for horizontal plane localization. This statement, however, includes several imprecise terms. Although not detailed definitions, the following list conveys the contextual connotations of the aforementioned terms:

Sophisticated Assumes a robust suite of onboard sensors including, at a minimum, a depth sensor, a doppler velocity log for course and speed over ground and altitude measurements, an acoustic transceiver for interrogating and replying to external acoustic transponders, and accurate heading and attitude sensors.

Long-duration Assumes an operating time period long enough that the error drift of any internal navigation solution would be greater than acceptable for the required level of precision.

Precision operations Assumes that the horizontal plane error is limited based on the mission, generally to a level on the order of 100 meters or less.

Deep ocean Assumes a depth where returning to the surface for periodic reinitializations of an internal navigation solution using GPS is not feasible.

In LBL navigation, an AUV obtains simultaneous direct path ranges from multiple external acoustic transponders. The AUV then trilaterates its position from these ranges and uses this position fix to reinitialize its internal navigation solution. This process requires that there be an unobstructed direct acoustic path between the AUV and a minimum of two, and preferably three or more, acoustic transponders at any given time.

Vehicles navigating using an LBL acoustic net are constrained by physical limitations of that net. The effectiveness of an LBL system begins to degrade at the fringes of the net or in other scenarios in which the direct path acoustic returns between the vehicle and transponders are not regularly received. When an AUV operates at low altitudes over complicated terrain there is a high risk of shadowing in which the line-of-sight path between the AUV and a given transponder is blocked. An increased density, or seeding, of transponders is required to provide adequate LBL coverage. However, it is a time-consuming and therefore expensive process to deploy and survey the positions of large numbers of acoustic transponders. The cost of the deployment, location survey, and recovery of seabed acoustic transponders depends on the depth of the water, type of underwater terrain, and the day rates of the deploying research vessels.

Scientific AUVs frequently conduct precise underwater mapping missions in deep water over complicated terrains; therefore, augmenting the navigation solution with other types of information would be valuable. This would allow an AUV to navigate precisely in a sparser field of acoustic transponders than would be required for a traditional LBL acoustic net in a given operating area. The PH navigation method is designed specifically to address this problem.

This research was inspired by the author's experience as a navigator of surface ships. As stated in Bowditch's seminal *The American Practical Navigator*, "In practice, a navigator synthesizes different methodologies into a single integrated system. He should never feel comfortable utilizing only one method when others are also available. Each method has advantages and disadvantages. The navigator must choose methods appropriate to each situation, and never rely completely on only one system [9]." Throughout recorded history, humans have navigated the world's waterways and oceans by incorporating all information available to them. For a modern navigator, this includes, among other types of information,

- ship heading and speed,

- set and drift by water currents,

- visual lines of bearings,

- ranges to objects of known position,

- GPS,

- celestial navigation, and

- soundings.

The PH navigation method was created to mimic the flexible data synthesis methods used by a human navigator and allow an AUV to expand the traditional operating envelope of an LBL system by incorporating more types of information as they become situationally available.

1.3 Methodology

The PH navigation method uses a novel filter architecture that breaks the navigation solution down into basic building blocks for each type of external information

available. These building blocks are then assembled in a format that allows a vehicle to navigate in an efficient way, leveraging all available sensors and navigational sources. External information is classified as one of two types of information: line of position or gridded. A line of position (LOP) is any measured range or bearing to an external feature of known location. Gridded information is any physical quantity for which there is an *a priori* map available of the measurements of that quantity for the operating area.

For any LOP observation, the AUV generates a block of possible position hypotheses from that measurement. The PH algorithm then arbitrates between these hypotheses, choosing the correct one to incorporate into the overall navigation solution. Any available gridded information is used within the arbiter as negative information. In other words, comparisons between the observed gridded information and the charted values at each hypothesis location from the available *a priori* maps of that physical quantity identify impossible hypotheses for elimination. This research uses one example of each type of information to provide a proof of concept of the overall PH navigation method, including ranges from a single external acoustic transponder as LOP observations and low-resolution bathymetric data from an EM300 ship-based multibeam sonar as gridded information.

1.4   Relation to Existing State of the Art

This research exists at the nexus of numerous different fields of research in underwater vehicle navigation. It incorporates elements from the following related research topics:

- Instantaneous Localization Techniques

- Probabilistic Localization Techniques

- Terrain Relative Navigation

- Acoustic Multipath Identification

30

- Single Transponder Navigation

- Data Association Techniques

1.5 Terminology

Two of the central terms within this research, *navigation* and *negative information*, have multiple usages in the related literature.

Navigation In robotics, the term *navigation* often pertains to the two-stage process that includes both localization and path planning. Similarly, on surface ships, the term navigation can encompass both localization and voyage planning. However, sometimes on surface ships the term is used to refer only to the localization step [9]. The oceanographic engineering community often follows the latter convention. Within the scope of this research, this second convention is followed and the term *navigation* is used interchangeably with the term *localization*.

Negative Information In statistics, the term *negative information* refers to information that paradoxically introduces more uncertainty about the relevant variable [95]. In robotics, negative information usually pertains to the absence of a feature either due to a false negative sensor reading or due to the physical absence of any feature within the effective range of the sensor. See, for example, [33, 34, 35, 85]. A third usage of the term stemming mainly from computer literature implies that one entity is not equivalent to another entity [48]. Within the scope of this research, negative information refers to the third usage convention in which one entity is not equivalent to another entity.

1.6   Contributions of Research

This research introduces a novel approach to AUV navigation that possesses a unique combination of characteristics which allow an AUV to escape the traditional operating limits of an acoustic LBL navigation system. These characteristics include the ability:

- to flexibly incorporate multiple types of *in-situ* external information into the localization algorithm,

- to represent multimodal beliefs without needing a complex structure for real-time generation and culling of hypotheses,

- to incorporate low-resolution *a priori* bathymetric data into a high-resolution localization algorithm,

- to identify acoustic multipath returns *in situ* and to incorporate these into a real-time navigation solution.

1.7   Thesis Roadmap

Chapter 1 presents a brief introduction to and motivation for the research problem, highlights the contributions of the research, and provides this overview of document structure.

Chapter 2 contextualizes this research within the applicable existing bodies of literature by identifying closely related works within each field of study.

Chapter 3 introduces the existing operational paradigm, the resulting capabilities gap, and the proposed solution in the form of the PH navigation method. Each step in the process is explicitly discussed including prediction, observation and hypothesis generation, arbitration, and update.

Chapter 4 presents the observation and hypothesis generation step in-depth using ranges to a single external acoustic transponder. The chapter first addresses modeling

of the underwater acoustic environment and then explains the design of the PH single transponder parallel hypothesis generator.

Chapter 5 presents in depth the grid arbiter portion of the arbitration step that incorporates *a priori* low-resolution bathymetric data from an EM300 multibeam echo sounder. Again, the first half of the chapter explains the intricacies of modeling the relevant aspects of the underwater environment, while the second half of the chapter explains the design of the EM300 grid arbiter.

Chapter 6 discusses the collection of over 155 hours of real-world data from scientific missions at the Juan de Fuca Ridge by two AUVs, the Autonomous Benthic Explorer (ABE) and Sentry, for use in the proof of concept.

Chapter 7 presents the results of the PH algorithm using the real-world data from ABE and Sentry, as a proof of concept.

Chapter 8 highlights the conclusions of the research and its novel contributions, as well as presents several areas of future work that would further advance this research.

Chapter 2

Research Context

This research exists at the nexus of numerous fields of research in underwater vehicle navigation, incorporating elements from

- Instantaneous Localization Techniques

- Probabilistic Localization Techniques

- Terrain Relative Navigation

- Acoustic Multipath Identification

- Single Transponder Navigation

- Data Association Techniques

Each of these fields is a broad area of research in its own right with extensive bodies of literature. Therefore, this thesis only addresses the concepts and literature that are most closely related to this research.

2.1 Instantaneous Localization Techniques

Effective navigation systems generally include two key elements. The first key element is vehicle location, or pose, estimates computed through a dead-reckoning (DR)

process [56]. Onboard sensors, such as inertial measurement units (IMU) or doppler velocity logs (DVL), generally provide the information to compute these pose estimates at a high update rate. The measured accelerations or velocities are combined with knowledge of vehicle attitude and integrated accordingly to provide pose estimates. These pose estimates are subject to errors that grow over time, often as a direct function of distance traveled. When DVL bottom-lock measurements are available, the resulting DR solution performs extremely well, often achieving accuracy within 0.1 % of distance traveled [46]. The second key element in effective navigation systems is periodic location updates using external information in order to bound the error growth in the internal position estimates. One way of obtaining these periodic updates is through instantaneous localization techniques. Instantaneous techniques use external information available in a single navigation cycle to calculate vehicle location and reinitialize the onboard estimates, as opposed to other temporal-based filtering techniques discussed in Section 2.2 which use information measured over multiple navigation cycles.

The most prevalent type of instantaneous localization in vehicle navigation is triangulation or trilateration of the vehicle's position using multiple bearings and/or ranges measured between the vehicle and external navigational aids at known locations. In air and land vehicles, the modern standard for this method is the Global Positioning System (GPS). GPS receivers locate multiple satellites in the GPS network that they can observe without obstruction, and the receiver position is triangulated after transforming the times-of-flight of the radio-frequency (RF) signals into ranges. The actual implementation of GPS is more complex, but the basic underlying concept is this triangulation calculation using instantaneously-available information [23]. However, RF cannot penetrate seawater adequately to make a satellite-based GPS system work underwater. For shallow water missions, vehicles can periodically surface to reinitialize their navigation solution using GPS. However, when periodic surfacing is not feasible, underwater vehicles must use an alternate method of updating

their positions. Standard practice in underwater navigation is to use acoustic instead of RF signals. Various underwater acoustic positioning methods exist for different types of missions with different operating ranges, because the distance and direction of acoustic signal propagation are highly dependent on the physical properties of the seawater.

The seminal text on underwater acoustic positioning methods was written by P.H. Milne in 1983 [63]. In that text, he describes the basic differences between the major types of acoustic positioning systems, including short baseline (SBL), ultra-short baseline (USBL), and long baseline (LBL) acoustic systems. The following descriptions are summarized from his discussions thereof. In an SBL configuration, an acoustic array of at least three transponders is mounted on the hull of a ship with maximum geometric separation and then it is precisely surveyed. When an undersea vehicle transmits an acoustic signal to the SBL array, the differences in signal arrival times between the hull-mounted transponders are used to determine the location of the vehicle. Since the localization calculation is performed on the ship, the SBL setup is appropriate for surface tracking of underwater vehicles or for navigation of tethered vehicles. Due to the installation and calibration precision required, an SBL system is a permanent fixture onboard a surface ship without any flyaway capability. To achieve a flyaway capability for use on any vessel of opportunity, the USBL system was invented. In a USBL system, the multiple sensors are mounted together on a single transducer which can be deployed over the side of any platform. The physical proximity of the sensors in a USBL system renders the algorithmic approach of SBL useless. Therefore, USBL systems rely on a phase difference approach where vehicle position is determined by comparing the differences in the phases of an acoustic signal carrier frequency as received by multiple sensors. USBL systems are commonly deployed from a surface ship to track an underwater vehicle. Commercial systems can resolve angles on the order of 0.1 degrees, which corresponds to approximately 0.2 % of slant range. Moreover, commercial systems may include integrated acoustic

modem capabilities, enabling the transmittal of the resulting geodetic fixes to the vehicle.

Today, a widely used method of acoustic localization for untethered undersea vehicles is LBL navigation. Hyperbolic LBL systems calculate vehicle position by measuring the differences in travel times between signals from the various transponders, similar to the SBL method described above [14]. The more prevalent type of LBL systems are based on spherical positioning. In spherical positioning, multiple transponders are deployed in an array on the seabed, and a weighted anchor and buoyant float system fix each transponder in place. A surface vessel with GPS then precisely surveys the fixed location of each transponder. To navigate using the transponder array, an undersea vehicle periodically interrogates all the deployed transponders on a master frequency. After a designated delay, each of the transponders replies either on a unique frequency or with a unique code. The vehicle then converts the two-way acoustic time-of-flight measurements into ranges to each transponder. The vehicle trilaterates its three-dimensional position from these ranges either deterministically or with a nonlinear least-squares routine for overdetermined systems.

The position updates obtained from an LBL network can be used independently to reinitialize the navigation solution without any consideration for prior position estimate. However, this creates discontinuities in the navigation solution. An alternative approach is to use complementary filtering to create a solution that is a hybrid of instantaneous and filtered localization methods. As discussed in Smith's text on mathematical modeling and digital simulation, complementary filters are useful for integrating information obtained at different frequencies [50, 78]. The particular complementary filter that has become a standard navigation approach in AUVs equipped with DVLs combines the LBL fixes with the DVL Doppler information, as presented by Whitcomb et al. [89, 90]. The LBL fixes, which are obtained at a much lower update rate than the DVL measurements, are passed through a low-pass filter. The Doppler information, after appropriate transformations to obtain position estimates,

is passed through a high-pass filter. The outputs from both of the filters are then combined to determine the vehicle pose estimates.

2.2 Probabilistic Localization Techniques

Whereas LBL navigation addresses the problem of instantaneous vehicle localization within a field of external navigational aids with known locations, probabilistic robotic techniques allow other localization scenarios. For example, probabilistic techniques allow a vehicle to localize its position within a field of navigational aids of unknown location. Simultaneous localization and mapping (SLAM) is a broad field encompassing multiple specific approaches to this problem. The basic idea of all of the SLAM techniques is that a vehicle can operate in a field of navigational aids of unknown location, take measurements of those navigational aid locations with onboard sensors, and use those measurements to build a map of the field, while also localizing itself within that map. SLAM is a probabilistic robotics technique because it depends on a detailed accounting of the stochastic expectation of noise and error in both the vehicle pose predictions and in its sensor measurements of the environment.

Much of the research on SLAM involves using feature extraction to build a map and to navigate off of physical point features in the environment. See, for example, the research done by Durrant-Whyte and his labs, first at the University of Oxford and then at the University of Sydney, and the related probabilistic localization and mapping research by Thrun and his lab at Stanford University [94, 82, 83]. Another recent SLAM example using underwater feature extraction is the work done by Ribas et al. [74]. They conducted underwater field experiments in a marina where an AUV navigated with a SLAM algorithm using the marina walls as vertical planar features in the environment.

However, in some realizations of SLAM, the navigational aids are acoustic transponders like those used in LBL navigation, but without *a priori* known locations. In-air

research on the range-only SLAM problem was done, for example, by Kanto et al. [43, 49]. They present a comparison of different filtering techniques that can be used for range-only SLAM. Early undersea work in this field was done, for example, by Newman and Leonard [68]. Using a large-scale nonlinear optimization algorithm, they were able to simultaneously determine transponder and vehicle locations. However, their solution would sometimes diverge from reality when the vehicle crossed over the baseline between two transponders.

The range-only beacon localization (ROBL) method of Olson et al. [69] is another example using underwater acoustic transponders. They used a spectral clustering method to partition out and reject outlier data points in order to converge upon the true location of each acoustic transponder. ROBL was shown to be an effective method of determining relative transponder locations as long as the navigating vehicle periodically changed course to solve observability concerns. In order to determine the absolute transponder locations in global coordinates, some type of external reference is necesary to locate and orient the relative solution.

Two prevalent filtering techniques for estimation in probabilistic robotic localization are extended Kalman filters (EKFs) and particle filters. Although they are important in the SLAM problem [19], they are more generally applicable for a wide variety of localization and navigation applications. An EKF is a Gaussian state estimator that works through the linearization of a nonlinear process model and/or a nonlinear observation model while making certain assumptions about the characterization of noise in both models. EKFs are widely studied and implemented. For a detailed description of these techniques see, for example, [6, 29, 84]. Another type of state estimator that does not rely on Gaussian assumptions is the nonparametric particle filter. Instead of being defined by specific distribution parameters, such as the mean and standard deviation parameters of a Gaussian distribution, particle filters approximate a probability distribution through a set of samples drawn from the distribution. A primary advantage of particle filters is that they are not bound by the

unimodal constraints of a Gaussian parametric representation, like an EKF. However, they are computationally intensive because the initial state space must be adequately seeded with particles to ensure that the remaining particles approximate the true statistics of the process after iterative resampling [84]. For a detailed explanation of both EKFs and particle filters, see Thrun et al.'s comprehensive text *Probabilistic Robotics* [84].

Interesting research that falls outside the usual boundaries of the filtering techniques used in probabilistic localization was undertaken by Detweiler et al. [18]. He looked at the problem of vehicle localization in a field of navigational nodes of fixed, known locations, similar to LBL. However, instead of having a detailed position prediction, or dead-reckoning, model, he used a geometric approach based on maximum speed of the vehicle. He created regions of possibility of vehicle location based on consecutive ranges from different transponders and the maximum achievable speed of the vehicle. Each additional range further constrained the regions of possibility until the solution converged to the true location. He also proposed an analogous solution using bearing-only observations, but did not implement it. The results of the convergence could be used on their own or in conjunction with a filtering algorithm such as an EKF. This algorithm would not work with successive measurements from a single transponder because geometric separation of the fixed nodes, or external navigational aids, is crucial to the convergence of a solution.

2.3 Terrain Relative Navigation

The idea behind terrain relative navigation is straight-forward. A vehicle correlates *in-situ* terrain measurements with stored terrain maps to localize its position. The implementations of this idea, however, are varied and complex due to the intricacies of the problem. Fundamentally, several factors affect how well a terrain relative navigation algorithm performs. First, the variability of the terrain itself is important.

Second, the accuracy and resolution of the terrain map for comparison affects performance. Although feature-based SLAM is effectively a terrain relative navigation algorithm with no *a priori* map, in the context of this discussion of terrain-relative navigation, it is assumed that the terrain map is known. Finally, the quality of the sensors for measuring the terrain and for making system state pose predictions are all important.

Terrain relative navigation (TRN) was first developed in a military context for the navigation of airborne missiles over mapped terrain, in a scheme called terrain contour matching (TERCOM), as presented in Golden's seminal article [30]. Since then, the idea of terrain relative navigation has been adapted for underwater vehicles using many different approaches. Rock and his associates at Stanford University and the Monterey Bay Aquarium Research Institute (MBARI) have conducted extensive research in this area. One recent paper from this group that is particularly applicable to the research of this thesis focuses on the use of low-cost alternatives to onboard multibeam sonars. Meduna et al. conduct a detailed sensitivity analysis on the effectiveness of their TRN algorithm due to attitude error using, alternatively, a multibeam sonar, a doppler velocity log (DVL), and an altimeter as their organic onboard sensor [61].

The most common TRN approaches navigate with a level of precision that is the same or lower resolution than that of the available preexisting terrain maps. However, a small subset of TRN literature is highly applicable to the research of this thesis because it addresses the inverse problem. Lucido et al. [57, 58, 59, 60] have looked at the idea of matching a high-resolution *in-situ* local depth map with a larger, lower-resolution, *a priori* terrain map using two different approaches. Their first approach uses a point-based matching algorithm based on extracted depth contours. The second uses a correspondence method based on discriminant parameters in which *in-situ* measurements are transformed into a two-dimensional grid. Local parameter vectors are then pulled off of this grid and compared to vectors on the reference map.

2.4 Acoustic Multipath Identification

Traditional underwater acoustic positioning systems incorporate only direct path acoustic returns between vehicle and any external transponders into their navigation solutions. However, multiple returns often exist which are the result of the sound following alternative eigenray paths, such as bouncing off of the water surface, sea bottom, or other reflective object. Since the invention of underwater acoustic positioning systems, much research has been dedicated to finding ways to eliminate these multipath data outliers and select only the true direct path returns out of the acoustic data. For example, see the general discussion by Milne [63], the specific presentation of both spatial and temporal outlier rejection techniques by Vaganay et al. [87], or the overview in the AUV navigation survey by Leonard et al. [53]. However, during AUV operations, situations often exist in which the direct path returns between a transponder and a vehicle are not received due either to physical obstructions, acoustic propagation characteristics in a given underwater environment, or nonideal acoustic transducer characteristics. These situations are sometimes referred to as fading multipath environments [16]. Using the alternate multipath returns in these fading multipath environments would increase the robustness of an acoustic positioning system. Since *in-situ* acoustic path identification and utilization is the most important contribution of this thesis, this specific area of research is highly applicable, yet the existing body of research is limited in scope.

One serious effort to use *in-situ* multipath returns in an acoustic positioning system was undertaken by Deffenbaugh et al. in the early 1990's [13, 15, 16]. Instead of recording only the first arrival time per transponder in a given navigation cycle, they collected all the returns in every cycle. They used an arrival matching algorithm based on a branch-and-bound methodology to match all the measured arrival times with the predicted arrival times for a given transponder. The eigenrays considered in their analysis were direct path, surface bounce, and bottom bounce. If none of the measured arrival times was matched to a predicted arrival time for a given eigenray,

the expected value was assigned to that eigenray for that navigation cycle. For this system to work well, the vehicle must routinely receive multiple acoustic returns for each beacon in every navigation cycle because the returns are inverted to create an accurate sound velocity profile, which in turn allows for better arrival time predications. The original problem addressed by this research was shallow-water under-ice AUV missions, which is an environment rich in acoustic multipaths. The method was extended, in simulation, to other shallow water environments which could also be expected to be rich in acoustic multipaths [13, 15, 16]. Deffenbaugh's methodology is not ideal for the operating environments assumed within this thesis for two major reasons. First, in a deep water environment with greater distances involved in sound traversing to the surface and back, a vehicle cannot always expect to receive multiple acoustic returns for each transponder in every navigation cycle. Second, the complicated underwater terrains assumed in this research often preclude a clean bottom bounce return and instead create many unexpected bounce paths. Excessive numbers of unpredicted acoustic returns would increase the computational complexity while at the same time degrading the performance of Deffenbaugh's methodology.

A more recent effort to explicitly identify acoustic multipath returns in an LBL framework was undertaken by Bingham [7, 8]. He used a hypothesis grid approach to identify acoustic returns as belonging to one of three categories: direct path, multipath, or outlier. Within this approach, a mixed measurement model is assumed with Gaussian distributions for the ranges of direct path and multipath returns and a uniform distribution for outliers. An expectation-maximization (EM) iterative routine is then undertaken to associate each observed range with one of the assumed eigenray paths. Finally, this information is reorganized spatially into a hypothesis grid of prior probabilities. EM techniques are incompatible with real-time *in-situ* implementation. Instead the purpose of Bingham's research is to increase the prior probability information for acoustic multipath returns in order to improve the performance of navigation methods based on stochastic representations.

2.5 Single Transponder Navigation

Over the past several decades, the idea of navigating an underwater vehicle using information from a single external acoustic transponder instead of an entire LBL acoustic net has been repeatedly revisited. Research has focused both on using a single fixed-location acoustic transponder and on using a moving transponder located on some type of mobile platform. A precursor to single transponder navigation research was work done in the field of tracking a maneuvering target using only range measurements from a single observer. See, for example, the research by Song [79].

The benefits of achieving the goal of single transponder navigation are clear when one considers the costs associated with the deployment, survey, and recovery of each fixed acoustic transponder in an LBL network. Research vessel day rates can be in the range of tens of thousands of dollars and transponder handling operations can consume multiple days of ship time on a typical research cruise. See, for example, the cost-benefit analysis presented by LaPointe [51]. However, despite the individual solutions presented by different researchers, there is still no single transponder navigation method in widespread use today. The primary obstacle to effective single transponder navigation is the fundamental problem of observability based on relative geometry between vehicle and transponder. Analyses of observability and methods to overcome the problems thereof are addressed in a large portion of the existing research.

A common approach to single transponder navigation presented in existing literature is to use an EKF estimator. Although exact techniques vary, each single transponder EKF incorporates some method of vehicle position initialization and some method of acoustic time-of-flight data preprocessing. Then, the standard EKF steps of prediction, observation, and update are performed using each author's particular state and observation model formulations. See, for example, Vaganay et al. [86, 1, 2]. Their experimental setup assumed a low-cost AUV with no organic DVL sensor.

An extensive observability analysis based on an EKF framework was conducted by Gadre et al. [25, 26, 27]. In addition to discussions of observability in the presence of unknown currents and during vehicle crabbing, the major conclusion of their research was that straight-line trajectories passing through the transponder position are not locally observable. This important result was echoed by the research of Ross et al. [75]. They also presented another important conclusion that a straight-line vehicle trajectory is not directly observable between the actual track and its mirror image without good position initialization.

The synthetic long baseline (SLBL) approach to single transponder navigation, developed by Larsen [52], inputs temporally separated range measurements from a single transponder into an error state Kalman filter framework. The requisite spatial separation between transponder locations in a traditional LBL network is replaced with temporal separation of the ranges from a single transponder at the expense of position update rate.

There have also been a number of single transponder methods based on geometric approaches not utilizing a Gaussian primary navigation filter. One such method was described by Scherbatyuk [77], who developed a set of nonlinear parameters to model vehicle location using measured ranges between vehicle and transponder, the fixed transponder position, vehicle-relative velocity and yaw, and current velocity. The nonlinear parameters are estimated using a least-squares root method.

Another geometric approach to single transponder navigation is the virtual long baseline (VLBL) algorithm developed by LaPointe [51]. Like the aforementioned SLBL, VLBL uses the temporal range separation between consecutive ranges of a single transponder in lieu of spatial separation among multiple transponders. VLBL combines the temporally-separated ranges from this virtual long baseline with Doppler-aided velocity information to produce positional fix updates using a nonlinear least-squares methodology.

More recently, an algebraic estimator for single transponder navigation was pro-

posed by Jouffoy et al. [42]. Using the measured ranges between a vehicle and a single transponder, they developed an algebraic time-derivative estimation technique using data from a moving window of fixed length. They conducted an observability analysis which reflected the same result of earlier analyses that the system is unobservable when the vehicle is traveling on a radial trajectory toward or away from the transponder and when the vehicle is not moving. Their calculations involve an inverse cosine function. When the argument of this inverse cosine function falls outside the interval of $[-1, 1]$ because of noise in the signal, then the result is imaginary. They circumvented this problem pragmatically by filtering the argument with a saturation function in which any values outside of the defined argument interval of the inverse cosine function are reset to the maxima or minima of this interval commensurate with the parity of the value. This saturation function makes the mathematics work at every time frame, but the resulting degradation of the quality of the algebraic estimator is apparent in their results whenever the argument of the inverse cosine function approaches or reaches the extrema of the defined interval.

A completely different approach to single transponder navigation incorporates a moving transponder mounted on a GPS-enabled ship, such as the research conducted by Eustice et al. [21, 22]. Using an acoustic modem, the transponder periodically broadcasts a data packet containing its current location. AUVs within range of the transmission use the one-way travel time (OWTT) pseudo-range along with their organic Doppler velocity sensor information to compute their positions. Since the AUVs are not required to communicate with the moving transponder, this is a passive system that allows multiple AUVs to navigate without the position fix frequency dilution created by multiple vehicles using a common LBL network because of sequential vehicle interrogations in a time division multiple access mode. Sensor fusion between the ship's GPS, the pseudo-ranges, and the autonomous vehicle's Doppler velocity information is accomplished using a maximum likelihood estimate optimization.

A second form of moving single transponder navigation is the single transponder

range-only navigation (STRONG) method, developed by Hartsfield [32]. STRONG uses a nonlinear least-squares error approach that seeks to mitigate geometric in-observabilities and errors through strict operational constraints. In other words, STRONG is a piecewise navigator that is able to determine vehicle speed corrections only in regions of radial, or near-radial, tracklines and course corrections only in regions of tangential, or near-tangential, tracklines. As with the OWTT approach, the instantaneous location of the moving transponder must be conveyed to the underwater vehicle with every ranging acoustic time-of-flight. Hartsfield leaves the actual implementation of this problem to future work.

2.6 Data Association Techniques

Data association is an important concept within probabilistic robotics. Although data association has been studied extensively in the context of target tracking applications, such as in [6], it has also become an increasingly important field of research for localization applications. For example, due to its repeated requirement to correspond sensor measurements with features in the environment, the SLAM problem is fundamentally akin to a multisensor multitarget tracking problem [92]. More generally, navigation is essentially the process of continually estimating a vehicle's position with periodic updates from an external navigational aid to limit the growth of position estimate error. Therefore, in any situation where a sensor measurement relating the vehicle to an external navigational aid is not uniquely identifiable, a data association problem results.

The following discussion presents a brief overview of a noncomprehensive list of existing data association techniques which are either directly applicable or in some manner related to this research. For a succinct yet effective overview of existing techniques, see the discussion in the introduction by Wijesoma et al. [92]. For a comprehensive explanation of any of the following techniques, see the works of Bar-

Shalom [4, 5, 6].

The individual compatibility nearest neighbor (ICNN), or nearest neighbor (NN), data association technique corresponds a single entity (e.g., a target or physical feature) with the closest observation based on some type of distance metric and subject to threshold gating. The most common distance metrics are either a Euclidean distance or a Mahalanobis distance which accounts for error in the form of defined covariances. The primary advantage of the NN approach is its simplicity in implementation, but its effectiveness degrades rapidly in the presence of clutter [5, 92, 111]. A good explanation of the NN technique using Mahalanobis distances can be found in [65].

When multiple entities are present, a common data association technique is the joint compatibility branch and bound (JCBB) method. It takes into account the spatial correlations between multiple entities when corresponding those entities to *in-situ* measurements. This improves the data association performance at the cost of additional computational complexity [5, 66, 92].

Furthermore, a disadvantage of all single-time frame data-association methods like NN and JCBB is that they ignore temporal information and make hard decisions in every given time frame. This means that once a correspondence between an entity and a measurement has been determined, it cannot be revised later in the presence of new information. Therefore, any incorrect data associations made can degrade the overall estimation process into which they are input [92].

In order to leverage the benefits of temporal observation trends over multiple time frames, multiple hypothesis data association methods have been developed. In the presence of data association ambiguity in a given time frame, multiple hypothesis tracking (MHT) algorithms will delay the correspondence decision-making in order to incorporate the additional information gained through repeated measurements in future time frames. Although theoretically effective, the optimal approach to this solution, where all hypotheses are maintained at all time frames, quickly becomes

computationally intractable and is therefore not suitable for real-time implementation. Therefore, a number of suboptimal MHT methods have been proposed to use the information provided by temporal observation records while limiting the computational requirements to levels feasible for real-time implementation [6, 92].

2.7 Multiple Model Estimation Techniques

An extension of MHT data association methods are multiple model (MM) estimators which present alternatives to the Gaussian EKF and nonparametric particle filter state estimators discussed previously in Section 2.2. MM estimators are adaptive estimators that use parallel banks of filters to account for multimodal system state possibilities. Since the filters run in parallel, there are no hard, irreversible, decisions made. Instead, there is soft switching between the modes depending on which mode is associated with the highest mode probability at the end of any given estimation cycle. There are three types of MM estimators, including static, dynamic and interactive. The following descriptions are all paraphrased from Bar-Shalom [6].

2.7.1 Static Multiple Model Estimation

Static multiple model (SMM) estimators are made up of a bank of filters, each representing a different state 'mode' or 'model' [6]. In parallel with each other, each individual filter runs recursively using its own estimates. At the end of each time frame, there is an update of all mode probabilities, which are the probabilities that the mode represented by each filter is the true system model. The basic idea is that eventually the mode probability of the true model will converge to unity and the mode probabilities of all of the incorrect models will converge to zero. For this to happen, two major assumptions must be met. The first is that one of the filters in the estimator represents the true system model. The second assumption is that the system remains in the same mode throughout the entire process and does not mode

50

jump between time frames. In other words, the state must be consistently represented by a single process model throughout the estimation duration and that model must be represented by one of the filters in the SMM architecture.

2.7.2 Dynamic Multiple Model Estimation

In order to accurately represent a system in which mode jumping does occur, dynamic multiple model (DMM) estimators were created [6]. Using DMM estimators, the system state is allowed to jump from one mode to another between the individual time frames. It is assumed that mode jumping, or 'mode switching', is a Markov process for which the mode transition probabilities are known. In practical implementation, these mode transition probabilities are design parameters that are established during the design of the DMM estimator. Optimal DMM estimators suffer from the same deficiency as the MHT data association methods previously mentioned in that the computations involved in maintaining all the possible histories grow exponentially and quickly become intractable. Therefore, suboptimal approaches have been designed to create DMM estimators that are feasible to implement.

One suboptimal DMM estimator is the generalized pseudo-Bayesian estimator of the first order (GPB1) [6]. In this estimator for a system with r possible modes or hypotheses, there is a filter bank of r filters. At the beginning of each cycle, a single lumped hypothesis is input into each of the r filters. At the end of each cycle, the r different estimates are lumped into a new single estimate using a weighted average based on their relative probabilities. This new single lumped estimate is then the input to all the filters in the following cycle.

A second suboptimal DMM estimator is the generalized pseudo-Bayesian estimator of the second order (GPB2) [6]. It differs from GPB1 in that it considers all possible models in the last two time frames before reducing the number of hypotheses. Therefore, GPB2 consists of r^2 filters into which r estimates are input at the beginning of the cycle. At the end of the cycle, the r^2 estimates output by the r^2 filters are

Table 2.1: Comparison of types of multiple model estimators given r hypothesis modes for filter cycle n.

MM Estimator	SMM	Optimal DMM	GPB1	GPB2	IMM
Number of estimate inputs	r	$r^{2^{n-1}}$	1	r	r
Number of filters	r	r^{2^n}	r	r^2	r
Hypothesis merging	None	None	r to 1	r^2 to r	r to r
Merging point in cycle	N/A	N/A	End	End	Start
Computational burden	Low	Intractable	Low	High	Low
Performance	Limited	Optimal	Low	High	High

merged into r new lumped estimates again using a weighted-average methodology. This increases the performance of the estimator above that of the GPB1, but it also exponentially increases the computational complexity.

2.7.3 Interacting Multiple Model Estimation

The interacting multiple model (IMM) estimator was designed to achieve similar performance to the GPB2 estimator but with reduced computational complexity on the order of that required by the GPB1 estimator [6]. The IMM achieves this by inputting a mixed initial condition input into each of r filters. In other words, the r estimates that are output at the end of a cycle are weighted and combined in r different ways to create a set of r new estimates at the beginning of the next cycle. Each of these r mixed estimates is then fed into one of the r parallel filters. For a comparison of these multiple model estimators, see Table 2.1. The relative computational complexity comparison pertains only to these multiple model estimators. As a whole, multiple model methods involve far greater complexity than other types of estimators.

2.7.4 Subsea Implementations of Multiple Hypothesis Filters

Many of the subsea implementations of multiple hypothesis estimators, like the multiple hypothesis extended Kalman filters (MHEKF), are for the purpose of target tracking such as passive target motion analysis (TMA). For example, see the MHEKF TMA design presented by Wilbur et al. [93]. Another example is the combined MHEKF and joint probabilistic data association (JPDA) method for TMA of multiple targets presented by Guo et al. [31].

One of the few examples of MHEKF-based AUV navigation uses an MHEKF to accomplish low-speed autonomous bottom following by an AUV operating in close proximity to the sea floor. Each of the multiple hypothesis filters assumes a different seabed profile gradient value. The MHEKF then arbitrates between the different assumed gradients to choose the correct, or closest, gradient. The AUV is then able to perform avoidance maneuvers as necessary to prevent a bottom collision [10].

2.8 Summary of Research Context

The PH method draws upon all of the research fields discussed in this chapter. The instantaneous localization method of acoustic LBL provides the initial departure point for the PH research. The open-architecture structure of the PH method allows it to incorporate elements from robotic localization research, such as the possibility of implementing an EKF as the primary navigation filter in the update step. The terrain relative navigation research provides the theoretical background for the grid arbitration step of the PH method. The acoustic multipath identification literature is relevant to one of the primary contributions of this research, which is the *in-situ* identification and incorporation of acoustic multipaths into the navigation solution. The single-transponder navigation literature is relevant to the development of the single transponder parallel hypothesis building block of the PH method. Finally, existing data association research provides the techniques used in the primary arbiter.

Chapter 3

Parallel Hypothesis Navigation Methodology

3.1 Existing Operational Paradigm

Understanding the existing operational paradigm upon which this research problem is founded is critical to understanding the capabilities gap that motivates this research. The existing paradigm is based on the specific, but representative, operational scenario typically used by the ABE and Sentry vehicles. When a research vessel enters its operating theater to complete a mission, the first step is to obtain pre-operation conductivity and temperature data throughout the water column and calculate the local sound velocity profile (SVP). Next, an acoustic network of transponders for LBL navigation is deployed and the fixed location of each transponder is surveyed by the host vessel. The multiple transponders of the LBL net may or may not provide coverage for the entire operating area.

A sophisticated AUV is then deployed, where the term *sophisticated* assumes the inclusion of accurate heading and depth sensors, a DVL, and an acoustic transceiver among the organic sensor suite of the vehicle. The sound velocity profile and transponder locations are uploaded to the AUV before it deploys. The AUV descends through

the water column to a predetermined altitude above the sea floor, initializes its position from the LBL network, and begins its dive plan. During the AUV mission, the ship is available to depart the immediate operating area to accomplish other missions in other locales.

During the dive, the AUV navigates using direct path two-way travel times from external acoustic transponders in a complementary LBL/DVL algorithm. When the survey mission is complete, the vehicle anchors itself on the bottom until a pre-arranged time when the AUV returns to the surface. The host ship then returns to theater to recover the AUV. After the first dive in a given operating area, the transponder survey is refined in post-processing and the new transponder positions are uploaded to the AUV prior to subsequent dives.

3.2 Identification of Capabilities Gap

The aforementioned paradigm works well when the mission of the AUV is to perform repeated dive operations in the same vicinity with clear lines of sight to all the transponders on the deployed LBL network. However, the functionality of this operational paradigm breaks down in several scenarios.

The first such scenario is when potential areas of scientific interest are discovered on the edge or outside of the effective boundaries of the LBL transponder network. If this occurs, additional transponders must be deployed and surveyed or some of the original transponders must be recovered, redeployed and resurveyed prior to AUV dive operations in those areas.

The existing operational paradigm also breaks down in the presence of shadowing in which a vehicle is operating in a rough underwater terrain and its line of sight with one or more of the transponders is physically obstructed. The increased risk of shadowing in rough terrain makes it difficult to construct an acoustic transponder network in which all transponders will be observable from all locations of the AUV

during dive operations. To maintain an adequate number of line-of-sight observable transponders at any given time in these conditions, the LBL acoustic network must be densely constructed with many transponders for a given area.

A third scenario in which the existing operational paradigm is inadequate is when planned AUV operations will cover an extensive area of seafloor. Due to the physical properties of underwater acoustic propagation, AUV communication with external transponders is limited to distances on the order of ten kilometers for typical LBL frequencies. Therefore, in order to have constant LBL coverage over an extended operating area, a large number of transponders must be deployed.

All three of these scenarios require additional transponder handling operations including deployment, surveying and recovery of each transponder. However, transponder handling operations require extensive amounts of devoted ship time. Therefore, depending on the day rate of the particular host vessel, resetting the acoustic transponder network for every dive can become prohibitively expensive.

3.3 Parallel Hypothesis Navigation Algorithm

The PH navigation algorithm presented in this thesis was designed to push the limits of effective AUV operation into these fringe scenarios without requiring additional transponders. Therefore, the operational expenses of a cruise can be reduced by limiting the amount of ship time devoted to transponder handling operations.

The motivating inspiration for the PH algorithm stems from the author's experience as the navigator on two United States Navy destroyers. The navigator on a surface ship uses all information available to identify, or *fix*, the location of the ship at any given time. This information could include, among other things, visual bearings to charted physical features, radar ranges to features of known location, the Global Positioning System (GPS), azimuths to celestial bodies, and depth soundings. During any given navigation cycle, the navigator assimilates the measurements of

any available types of information into a single best estimate of ship position. If the available information does not meet certain quality and quantity thresholds, the ship location estimate is classified as an *estimated position* instead of a true *position fix*. Until the next position fix is calculated, the working estimate of the ship's position is maintained by dead reckoning using knowledge of the ship's course and speed.

The steps in the AUV navigation process are analogous to those of surface ship navigation with one major exception. Most AUV navigation algorithms are designed to incorporate a predetermined set of observations from onboard sensors. If observations from all of those predetermined sensors are not available, the algorithm breaks down and the navigation process reverts to dead reckoning until the required observations become available again. Furthermore, if other types of external navigation information happen to be available to the AUV, they are not incorporated in the navigation process.

The PH algorithm is designed to mimic a human navigator by assimilating all available information into the navigation solution in real-time. It achieves this through a building block filter architecture. Individual building blocks are designed for every type of information that may be available to a vehicle *in situ*. These building blocks are then assembled into an overall filter architecture as described in Section 3.5 below. For any given navigation cycle during the dive, the building blocks corresponding to available information will be used and any building block for which there are no observations will be omitted.

3.4   Types of External Navigational Information

Within the scope of this research, external navigation information available *in situ* to an AUV is classified as one of two types. The first type, hereafter referred to as a line of position (LOP), is any relative measurement between the vehicle and a specific external object. The second type is the instantaneous measurement of any physical

parameter at the vehicle's location which can be compared to an *a priori* map of that parameter. This type of information is referred to as gridded information.

3.4.1 Lines of Position

An LOP is a relative measurement of range or bearing to a specific external object. The external object can be either in a fixed position or moving on some host platform. Existing research addresses the problem of vehicle navigation using LOP measurements to objects of unknown locations, most significantly the simultaneous localization and mapping (SLAM) problem and its offshoots. See for example [3, 19, 54, 82]. However, in its current form the PH algorithm deals only with external objects of known location.

The location of fixed objects can be relayed to the vehicle prior to dive operations, such as with long baseline navigation [63, 88]. If the location of any object is not passed to the vehicle prior to the dive, that information must be transmitted to the vehicle during the dive. For external moving objects, the instantaneous location of that object must be transmitted to the vehicle concurrently with the relative measurement, as done in the recent research by Eustice et al. on one-way synchronous-clock travel times [21, 22]. Examples of lines of position include, *inter alia*:

- Ranges to single fixed transponders,

- Ranges to moving transponders,

- One-way synchronous-clock travel times, and

- Bearings to a fixed landmark.

3.4.2 Gridded Information

Gridded information is any physical property which can be measured by a vehicle *in situ* and compared to an *a priori* map of the distribution of that property in

the operating area. Terrain relative navigation algorithms are founded on this type of information. There is a large body of literature on the design of terrain relative navigations based on high-resolution maps of altitude contours or bathymetry using various types of correlation methods. A smaller field of existing research approaches the multiscale terrain navigation problem where maps of relatively low resolution are used in higher resolution AUV navigation [57, 58, 59, 60]. For bathymetric gridded information, vehicle altitude measurements from onboard sensors such as doppler velocity logs or multibeam sonars can be used for comparison in conjunction with vehicle depth information. Other types of gridded information could be used, such as gravity or magnetic variations across an operating area, if *a priori* information exists and the vehicle is equipped with the appropriate sensors. Examples of gridded information include, *inter alia*:

- High-resolution bathymetry,

- Low-resolution bathymetry,

- Gravity, and

- Magnetics.

3.5 Parallel Hypothesis Filter Architecture

The PH filter architecture combines line of position and gridded information into parallel hypothesis and grid arbiter building blocks, respectively, as shown in Figure 3-1. As a proof of concept, a parallel hypothesis filter block was built to incorporate ranges to a single transponder and a grid arbiter block was built to incorporate *a priori* low-resolution bathymetric maps. Each navigation cycle in the PH method is represented by the horizontal progression across the flow chart depicted in Figure 3-1. During each cycle, the prediction, hypothesis generation, arbitration and update processes occur in that order. The horizontal blocks running through the hypothesis
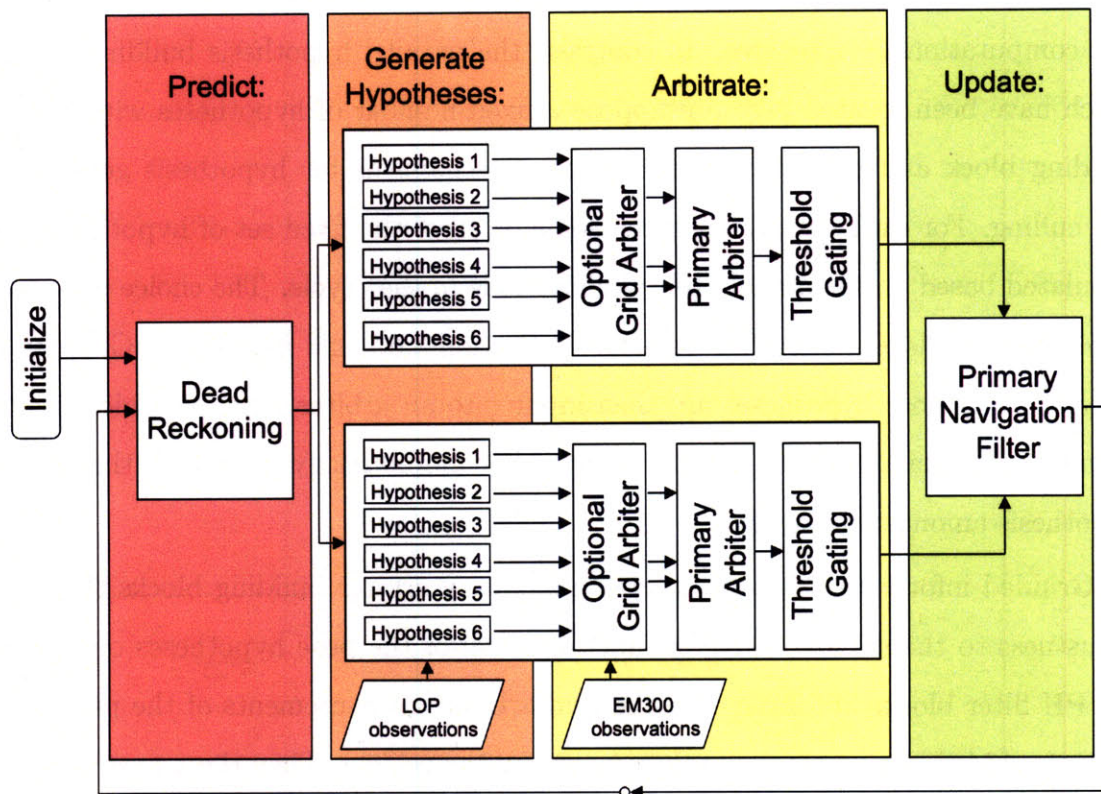
Figure 3-1: Architecture of the parallel hypothesis navigation algorithm.

generation and arbitration steps represent individual navigational aids that generate LOP information, such as a single acoustic transponder. In the illustration, there are two transponders depicted. In practice, however, the number of horizontal blocks will be equal to the number of transponders, or other LOP navigational aids.

PH filter blocks are created for LOP information. The LOP information is collected along with any other requisite sensor measurements. These measurements are the inputs to the PH filter block, where they are assimilated into multiple vehicle pose hypotheses. The term *parallel hypothesis* has been used instead of *multiple hypothesis* because the term *multiple hypothesis* refers to a specific field of study within robotics. Multiple hypothesis tracking or localization requires mechanisms for active hypothesis generation and culling during real-time operations. See for example Bar-Shalom

[6]. As a result, these multiple hypothesis algorithms can be exceedingly complex and computationally intensive. In contrast, the parallel hypothesis building blocks which have been created here presuppose a fixed number of hypotheses within each building block and therefore do not require mechanisms for hypothesis generation and culling. For each navigation cycle, some or all of the fixed set of hypotheses are populated based on the actual observations made in that cycle. The choice of potential hypotheses is discussed briefly below in Section 3.6.2 and in detail in Chapter 4. The resulting pose hypotheses are then input into an arbiter function which uses a form of individual compatibility nearest neighbor methodology to identify the correct hypothesis amongst the group.

Gridded information is used to create auxiliary arbiter building blocks that add robustness to the standard arbiter functions. All of the pose hypotheses output by the PH filter blocks are input into the grid arbiter. Measurements of the particular type of gridded information are taken *in situ* by the vehicle. Then the *a priori* map is used to determine the expected values of this particular physical quantity at each of the pose hypotheses. Any hypothesis whose expected value diverges from the *in-situ* measurements by more than an error threshold, as discussed in Section 3.6.3.3, are rejected in a hard decision process. In other words, those hypotheses are discarded irrevocably. The remaining pose hypotheses are then passed to the primary arbiter function. See Chapter 5 for a detailed explanation of the development of the low-resolution bathymetric grid arbiter.

3.6 Parallel Hypothesis Navigation Process Steps

The steps in the PH algorithm are similar to a unimodal state estimation process but with an added arbitration step. A unimodal state estimation process goes through a loop of prediction, observation and update. The PH algorithm also generates a unimodal prediction of vehicle pose for each navigation cycle. However, during the

Traditional Navigation Process   Parallel Hypothesis Navigation Process

```
     ┌─────────────────────┐              ┌─────────────────────┐
     │      Initialize      │              │      Initialize      │
     └─────────────────────┘              └─────────────────────┘
                │                                      │
                ▼                                      ▼
     ┌─────────────────────┐              ┌─────────────────────┐
  ┌─▶│       Predict        │          ┌─▶│       Predict        │
  │  └─────────────────────┘          │  └─────────────────────┘
  │             │                     │             │
  │             ▼                     │             ▼
  │  ┌─────────────────────┐          │  ┌─────────────────────┐
  │  │       Observe        │          │  │  Generate Hypotheses │
  │  └─────────────────────┘          │  │  from LOP observations│
  │             │                     │  └─────────────────────┘
  │             │                     │             │
  │             │                     │             ▼
  │             │                     │  ┌─────────────────────┐
  │             │                     │  │      Arbitrate       │
  │             │                     │  │ using gridded observations│
  │             ▼                     │  └─────────────────────┘
  │  ┌─────────────────────┐          │             │
  │  │        Update        │          │             ▼
  │  └─────────────────────┘          │  ┌─────────────────────┐
  │             │                     │  │        Update        │
  └─────────────┘                     │  └─────────────────────┘
                                      │             │
                                      └─────────────┘
```
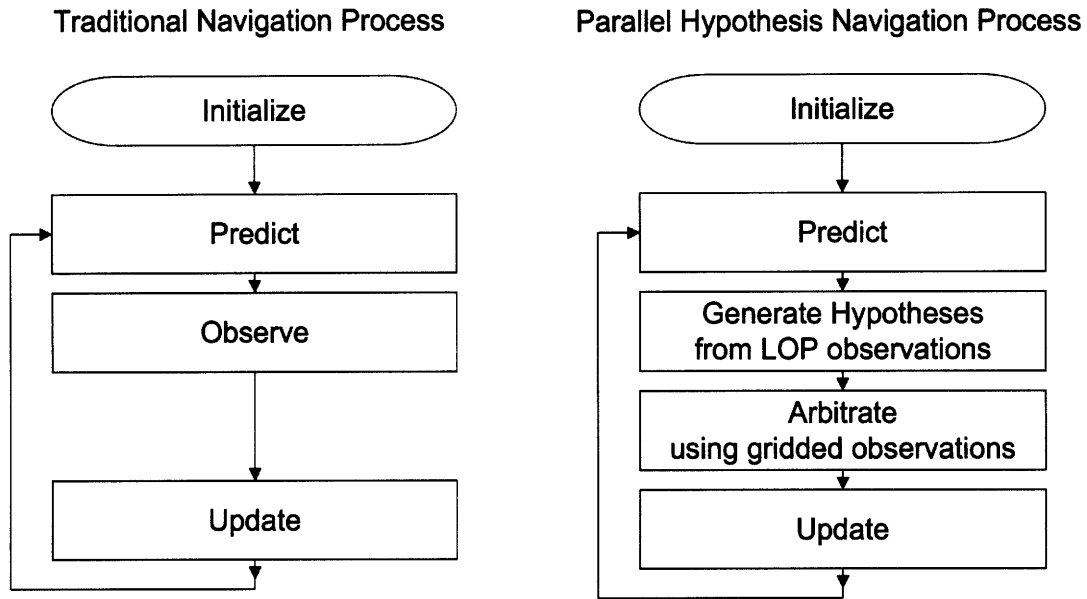
Figure 3-2: Steps in a standard unimodal navigation algorithm versus in the multi-modal PH method.

observation process, up to six hypotheses are formed based on the synthesis of measurements from multiple onboard sensors. As shown in Figure 3-2, an additional arbitration step is required to discern the correct pose hypothesis and use that information to update the unimodal vehicle pose estimate.

3.6.1 Predict

The prediction step of the PH algorithm is the dead reckoning process. From the best vehicle pose estimate at one timestep, or frame, the vehicle predicts its location at the next frame based on its course and speed. In this research, the dead reckoning process is modeled with a kinematic model that assumes constant velocity from one

time frame to the next. The only inputs to the model are the vehicle's prior frame pose coordinates, speed vectors, the length of the time interval between frames, and prior knowledge of the variance of the system process noise.

3.6.1.1 The System Model

The system model used in the prediction step of the PH algorithm is a standard direct discrete-time kinematic model under the assumption of white noise acceleration. See, for example, Bar-Shalom [6] for further details on the derivation of this type of model. This is a basic kinematic model that is based on several simplifying assumptions, such as assuming a constant velocity during every transition from one frame to the next. This assumption allows the model to be two-dimensional per coordinate. Therefore, for the two-coordinate problem of horizontal location, the model is four-dimensional as given by

$$\mathbf{x}(k|k-1) = \mathbf{F}(k-1)\,\mathbf{x}(k-1|k-1) + \mathbf{\Gamma}(k-1)\,\nu(k-1) \tag{3.1}$$

where

$$\mathbf{x}(k|k-1) \equiv \text{Vehicle state prediction at frame } k,$$

$$\mathbf{x}(k-1|k-1) \equiv \text{Vehicle state estimate at frame } k-1,$$

$$\mathbf{F} \equiv \text{State transition matrix,}$$

$$\mathbf{\Gamma} \equiv \text{Vector gain multiplying the scalar process noise,}$$

$$\nu \equiv \text{Scalar process noise, and}$$

$$\Delta T(k) \equiv \text{Timestep from frame } k-1 \text{ to frame } k.$$

$$\mathbf{x} = \begin{bmatrix} x \\ y \\ \dot{x} \\ \dot{y} \end{bmatrix} \tag{3.2}$$

$$\mathbf{F} = \begin{bmatrix} 1 & 0 & \Delta T & 0 \\ 0 & 1 & 0 & \Delta T \\ 0 & 0 & 1 & 0 \\ 0 & 0 & 0 & 1 \end{bmatrix} \tag{3.3}$$

$$\mathbf{\Gamma} = \begin{bmatrix} \frac{(\Delta T)^2}{2} & 0 & 0 & 0 \\ 0 & \frac{(\Delta T)^2}{2} & 0 & 0 \\ 0 & 0 & \Delta T & 0 \\ 0 & 0 & 0 & \Delta T \end{bmatrix} \tag{3.4}$$

The process noise covariance matrix, Q, is then given by Equation 3.5.

$$\mathbf{Q} = E[\Gamma \nu \nu \Gamma'] = \begin{bmatrix} \frac{(\Delta T)^4}{4} & 0 & 0 & 0 \\ 0 & \frac{(\Delta T)^4}{4} & 0 & 0 \\ 0 & 0 & (\Delta T)^2 & 0 \\ 0 & 0 & 0 & (\Delta T)^2 \end{bmatrix} * \sigma_\nu^2 \tag{3.5}$$

where

$\sigma_\nu^2 \equiv$ Variance of the scalar system model process noise.

According to Bar-Shalom [6], a good design guideline for assigning a value to the process noise standard deviation is to use a value between 50 and 100 percent of the maximum vehicle acceleration. This guideline was adopted in this research, with the understanding that this may be a conservative estimate for survey operations.

$$0.5 * a_M \leq \sigma_\nu \leq a_M \tag{3.6}$$

where

$$a_M \equiv \text{Maximum vehicle acceleration.}$$

3.6.1.2 The Vehicles

The vehicles used in this research are the two AUVs of the Deep Submergence Lab of the Woods Hole Oceanographic Institution (WHOI), ABE and Sentry. They were both designed and built at WHOI for exploring the ocean at depths up to 6000 meters. Primary operations include conducting sea floor data collection and bathymetric mapping operations often in the vicinity of deep-sea hydrothermal vent sites. For a detailed description of the vehicles, see Section 6.1.

In order to determine the maximum vehicle acceleration of each of these vehicles, the temporal records of forward acceleration during dive operations were examined. Other than a few outlier data points, the maximum of the absolute value of acceleration is less than 0.1 $\frac{m}{s^2}$ for all ABE dives included within this research. Vehicle accelerations from a representative ABE dive are shown in Figure 3-3. Therefore, a value of 0.05 $\frac{m}{s^2}$ was assigned for the standard deviation of the process noise for ABE.

The vehicle accelerations of Sentry were more diverse and the maximums were larger in magnitude than those of ABE. During two of the three dives used in the research, Sentry experienced erratic speed changes as it attempted to conduct bottom following over rough terrain, as discussed later in Section 6.2.2. The resulting temporal records of Sentry vehicle acceleration for the three dives used in this research are shown in Figures 3-4, 3-5, and 3-6. Note that the scale of the vertical axis is an order of magnitude larger in the plots of the first two dives, when Sentry was experiencing erratic speed changes, than it is for the plot of the third dive. Other than a few outlier data points, the maximum of the absolute value of acceleration for Sentry is less than 2.2 $\frac{m}{s^2}$. Therefore, again following Bar-Shalom's suggested design guidelines, a value of 1.1 $\frac{m}{s^2}$ was assigned for the standard deviation of the process noise for Sentry.
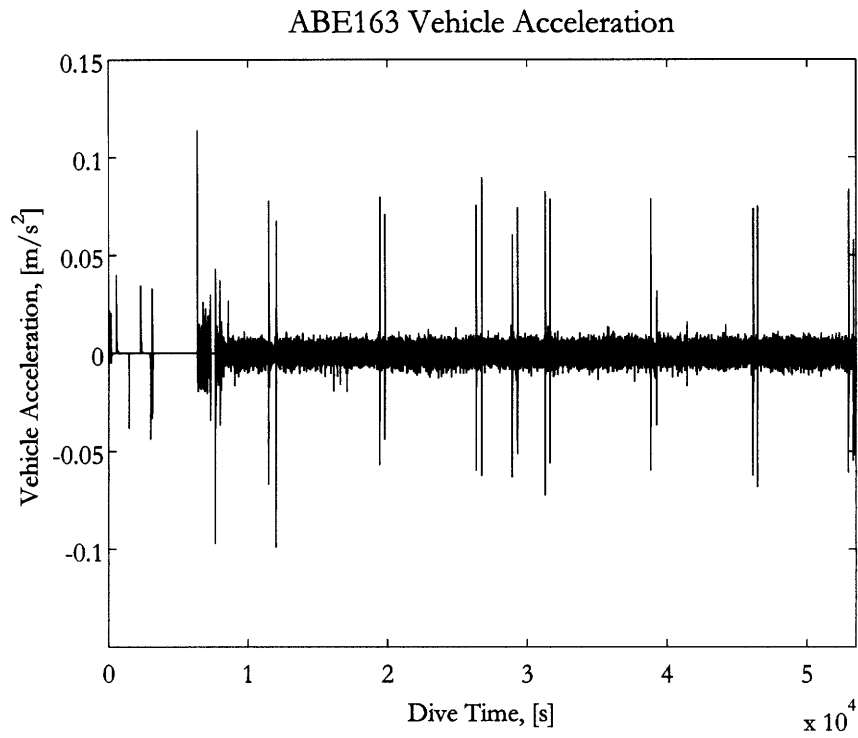
Figure 3-3: Vehicle forward accelerations for ABE163.
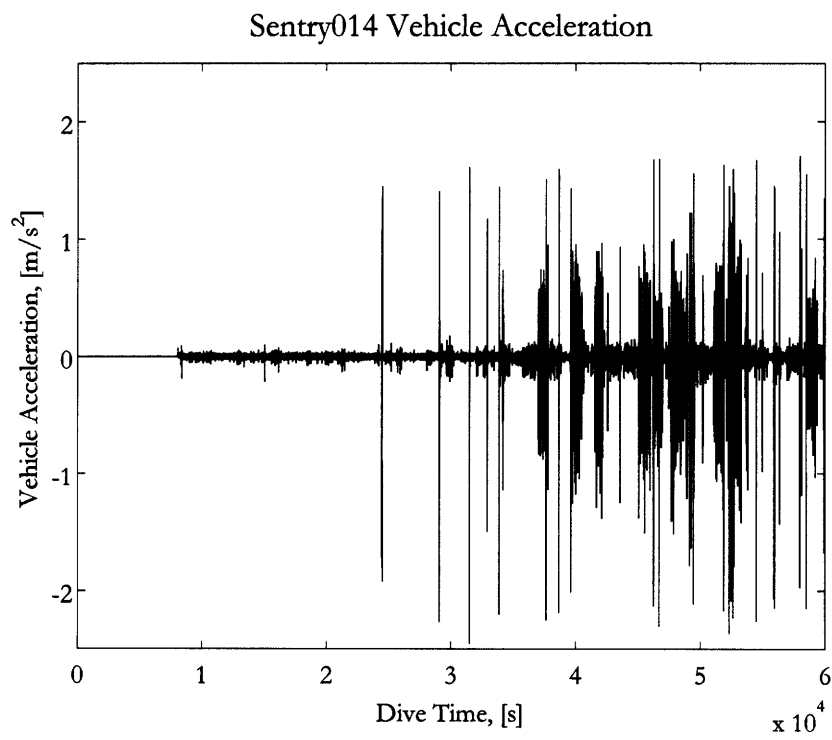
Figure 3-4: Vehicle forward accelerations for Sentry014.
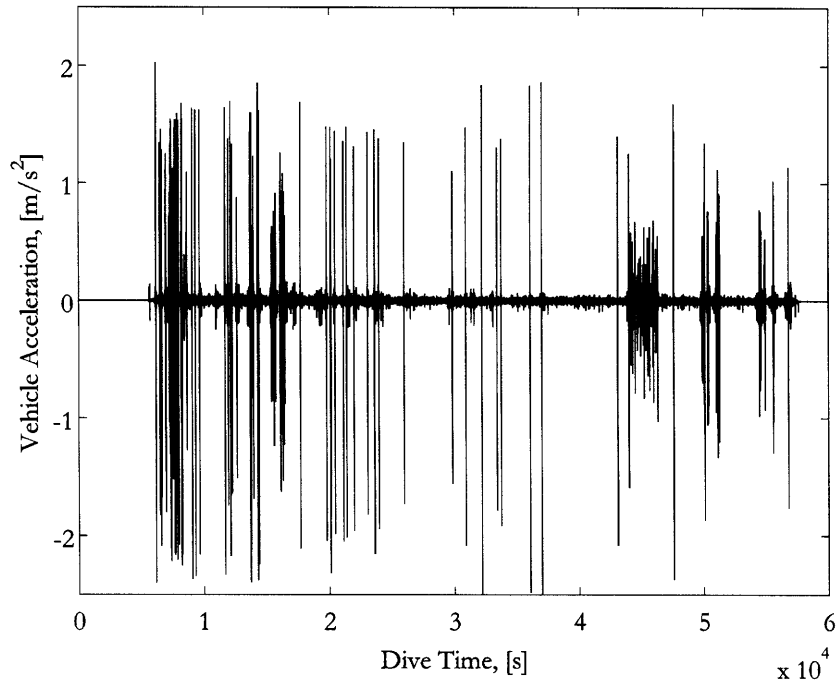
Figure 3-5: Vehicle forward accelerations for Sentry015.
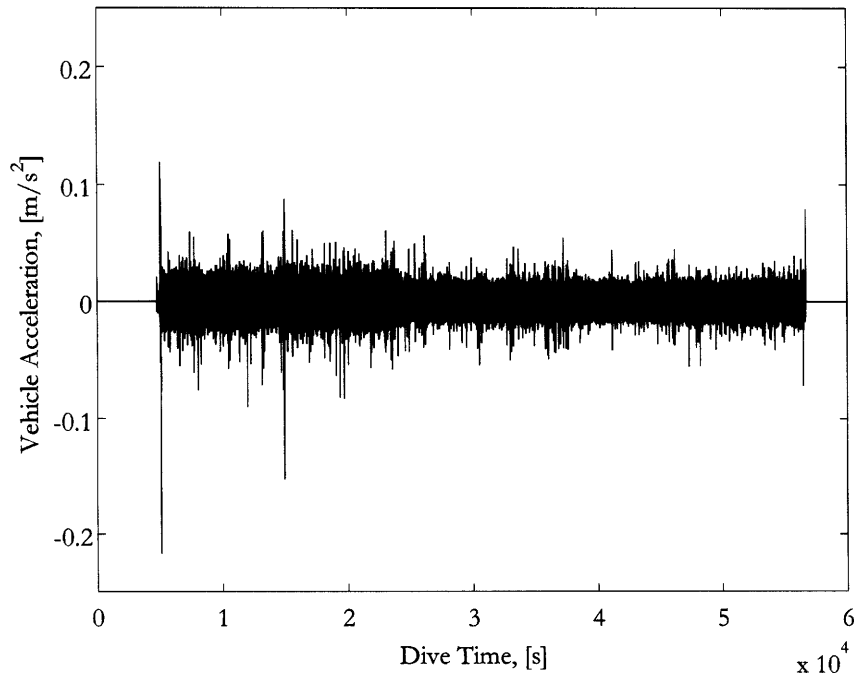
Figure 3-6: Vehicle forward accelerations for Sentry016.

3.6.2 Generate Hypotheses

In the hypothesis generation step, the vehicle takes measurements of the external environment with its onboard sensors. The information from these measurements is then synthesized into multiple vehicle pose hypotheses. The PH algorithm architecture is designed so that different parallel hypothesis filter blocks can be designed and used in the hypothesis generation step using different LOP types of sensor information. Each filter block inputs relevant sensor measurements and outputs several vehicle pose hypotheses. As shown in Figure 3-1, multiple PH filter blocks can also be used in conjunction with one another to form a comprehensive set of multiple pose hypotheses which will then be passed to the arbiter.

As part of this research, a proof of concept was done in which a PH filter block was developed for acoustic time-of-flight measurements. This filter uses measurements of

- Vehicle depth,

- Vehicle heading,

- Vehicle speed over ground,

- Acoustic time-of-flight measurements to a single external transponder, and

- Prior knowledge of the three-dimensional location of the external transponder.

These measurements are used to form multiple hypotheses of the vehicle's location for a given time frame as shown in Figure 3-7. The existence of multiple hypotheses arises from the fact that two key parameters are not directly observable from the measurement process. These parameters are the acoustic multipath traveled by the two-way signal and the general orientation of the transponder location with respect to the vehicle's track. Therefore, up to six hypotheses are determined at every time frame for every combination of three possible acoustic paths and two relative orientations between transponder and vehicle course. The possible acoustic paths considered in

the single transponder PH filter are direct path (DP), triangle path (TP) and double bounce (DB). The two possible relative orientations between transponder and vehicle course are that the transponder is located either to the left or to the right of the vehicle's course over ground. All of Chapter 4 is devoted to a detailed explanation of the development of the single transponder PH filter block.

3.6.3 Arbitrate

In the arbitration process, the data association problem between the multimodal pose hypotheses and the unimodal predicted vehicle pose is addressed. The multiple pose hypotheses are input into the arbiter function. First, any definitively erroneous hypotheses based on the *a priori* knowledge of gridded information are eliminated from consideration. Then, the primary arbiter function identifies the best among the remaining pose hypotheses using a nearest neighbor algorithm. If the chosen hypothesis meets the acceptable threshold criteria, then that hypothesis is forwarded to the primary navigation filter for the vehicle pose estimate update.

Depending upon the availability of *a priori* maps of gridded information, there are either two or three steps in the arbitration process, as follows:

1. Grid Arbiter (Optional)

2. Nearest Neighbor Identification

3. Threshold Gating

3.6.3.1 Grid Arbiter

If some type of *a priori* gridded information map is available to compare to *in-situ* measurements taken by the vehicle, then the first level in the arbitration process is a grid arbiter. The grid arbiter compares *in-situ* measurements of the given variable with the *a priori* mapped values of that variable at each of the hypothesis locations.
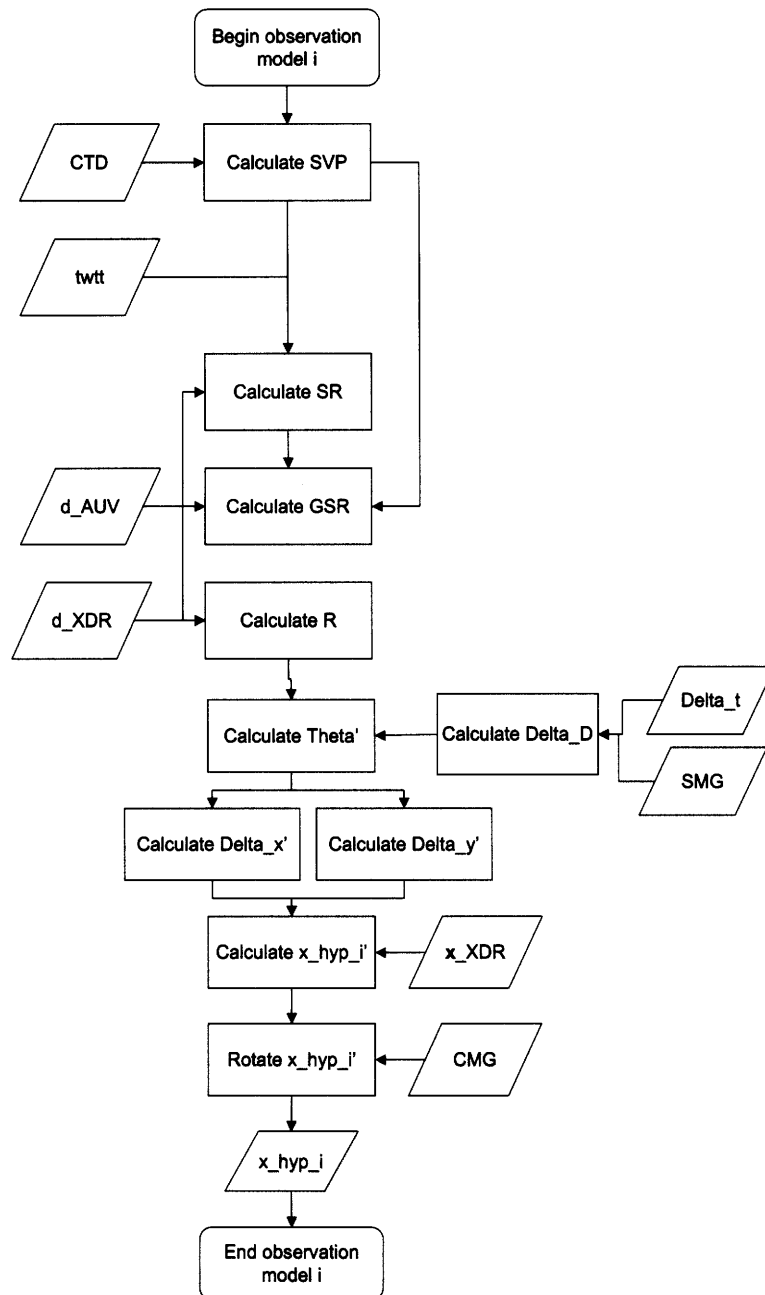
Figure 3-7: Detailed flow chart of the hypothesis generation process.

Any hypothesis locations that have mapped values that diverge from the *in-situ* measurements more than the error tolerance, as discussed in Section 5.2.3, are disqualified from consideration for the nearest neighbor calculations. For this proof of concept research, a grid arbiter was developed based on *a priori* low-resolution bathymetric data from ship-deployed multibeam sonars. The use of low-resolution *a priori* maps in a high-resolution navigation process creates a multiscale problem. The development of this multiscale bathymetry grid arbiter filter block is discussed in detail in Chapter 5.

3.6.3.2 Nearest Neighbor Identification

The individual compatibility nearest neighbor (ICNN), or nearest neighbor (NN), method is a standard data association technique which corresponds a single entity with the closest observation based on some type of distance metric and subject to threshold gating. The single entity can be many things such as a physical feature, a moving target, or the mean value of a sample population. The most common distance metrics used are either a standard Euclidean distance, as in Equation 3.7, or a Mahalanobis distance, as in Equation 3.8, which accounts for error in the form of defined covariances. The primary advantage of the NN approach is its simplicity in implementation, but its effectiveness degrades rapidly in the presence of clutter [5, 92, 111].

The Euclidean and Mahalanobis distances between the pose estimate and hypothesis i are given, respectively, by

$$
\begin{aligned}
d_{E_i} &= ||\tilde{\mathbf{x}}_i(k) - \mathbf{x}(k|k-1)||_2 \\
&= \sqrt{[\tilde{x}_i(k) - x(k|k-1)]^2 + [\tilde{y}_i(k) - y(k|k-1)]^2},
\end{aligned}
\tag{3.7}
$$

and

$$
d_{M_i} = \sqrt{[\tilde{\mathbf{x}}_i(k) - \mathbf{x}(k|k-1)]^T \Sigma_i^{-1} [\tilde{\mathbf{x}}_i(k) - \mathbf{x}(k|k-1)]},
\tag{3.8}
$$

where

$$d_{E_i} \equiv \text{Euclidean distance of hypothesis } i,$$

$$d_{M_i} \equiv \text{Mahalanobis distance of hypothesis } i,$$

$$\tilde{\mathbf{x}}_i(k) = \begin{bmatrix} \tilde{x}_i(k) \\ \tilde{y}_i(k) \end{bmatrix} \equiv \text{Vehicle pose hypothesis } i \text{ at frame } k,$$

$$\mathbf{x}(k|k-1) = \begin{bmatrix} x(k|k-1) \\ y(k|k-1) \end{bmatrix} \equiv \text{Vehicle state prediction at frame } k, \text{ and}$$

$$\Sigma_i = \begin{bmatrix} \sigma_{\tilde{x}}^2 & \sigma_{\tilde{x}\tilde{y}}^2 \\ \sigma_{\tilde{x}\tilde{y}}^2 & \sigma_{\tilde{y}}^2 \end{bmatrix} \equiv \text{Vehicle pose hypothesis } i \text{ covariance matrix.}$$

The NN method was used as the primary arbiter function in this research based on comparing the distance between the predicted vehicle pose and each of the observed vehicle pose hypotheses for each transponder at every time frame. The clutter problem is generally not a significant issue for the PH method because the geometry of deep ocean vehicle operations dictates that the pose hypotheses generated using different acoustic path assumptions are separated by large distances. The PH method was implemented using both Euclidean and Mahalanobis distance metrics. The Euclidean metric has a significantly lower computational burden due to the matrix inversion in the Mahalanobis metric so it is advantageous to use the Euclidean metric whenever the pose uncertainties in the x and y directions are similar.

3.6.3.3 Threshold Gating

Threshold gating is the process of eliminating outliers that survived the arbitration process. If the acoustic return at a given timeframe did not follow one of the three modeled two-way acoustic paths, then none of the resulting pose hypotheses from that timestep will correspond with the vehicle's true pose. The main arbiter selects

73

one pose hypothesis regardless of the magnitude of the appropriate distance metric for that hypothesis. The function of the threshold gate is to reject any arbitrated pose hypothesis whose distance metric exceeds an acceptable level. The acceptable level is a parameter subject to the design aspect of the process. In other words, there is no unique solution to the threshold gating level. With a Mahalanobis metric, the square of the Mahalanobis distance corresponds to the Chi-squared distribution. Therefore, the threshold gate can be set for a desired confidence interval using the Chi-squared value determined by that confidence interval and the number of degrees of the system. In the PH method, a 95-percent confidence interval was selected which corresponds to a Chi-squared value of 5.991 for the two degree problem of horizontal plane navigation.

3.6.4 Update

The update step of any navigation process is where the new information from the observations is combined in some way with the vehicle pose prediction based on prior information. The mechanism used to accomplish this combination will herein be referred to as the primary navigation filter. Many different types of primary navigation filters exist in practice. The choice of an exact primary navigation filter dictates the balance that will be achieved between observation and prediction.

In the most simplistic sense, this problem can be looked at as a weighting spectrum in which at one end prediction is weighted at unity and observations at zero and vice versa at the other end. If one were to weight predictions at unity and observations at zero, this is just the dead-reckoning process. At the other end of the spectrum, observations are weighted at unity and the pose prediction based on prior information is given no weight. In other words, all prior estimates of vehicle position are discarded after a new observation is made. Unless the position observations are precise and accurate at a high resolution, this type of update process results in a navigation solution that is discontinuous as it jumps from predicted to observed position at every

observation. The inherent sensor and computational errors that arise when the vehicle is operating near the limits of observability make this process inappropriate for use as a primary navigation filter using only ranges from a single transponder in the PH method. However, as part of this research this update process was implemented with ranges from a single transponder to examine some of the qualitative characteristics inherent in the PH method. This update process was also implemented with ranges from multiple transponders with the expected increase in accuracy that derives from using observations from multiple transponders.

All other primary navigation filters are located somewhere on the spectrum between the prediction and observation. The Kalman gain term is the crux of the ubiquitous family of Gaussian filters which includes the Kalman filter and all of its derivatives. The Kalman gain term dynamically assigns the balance between prediction and observation at every timestep based on covariance calculations of the instantaneous levels of error in each. This dynamic weighting function makes Kalman filters very successful in situations where the basic assumptions of the method are strictly adhered to. However, many real-world situations violate the linearity and noise characterization assumptions in the state and observation processes. The nonlinear adaptations of the Kalman filter, extended Kalman filters, are commonly used as primary navigation filters in underwater navigation applications, including several single transponder EKF solutions [1, 2, 86]. The PH method could incorporate an EKF as the primary navigation filter; however this refinement is left to future work. One unique contribution of the PH method is that it incorporates multimodalities in an architecture which does not violate the necessary assumption of a Gaussian primary navigation filter.

The type of primary navigation filter used on ABE and Sentry for real-world operations is an LBL/DVL complementary filter. A fundamental aspect of integrating acoustic time-of-flight measurements from external transponders into any navigation algorithm is the update rate discrepancy between acoustic returns and internal sen-
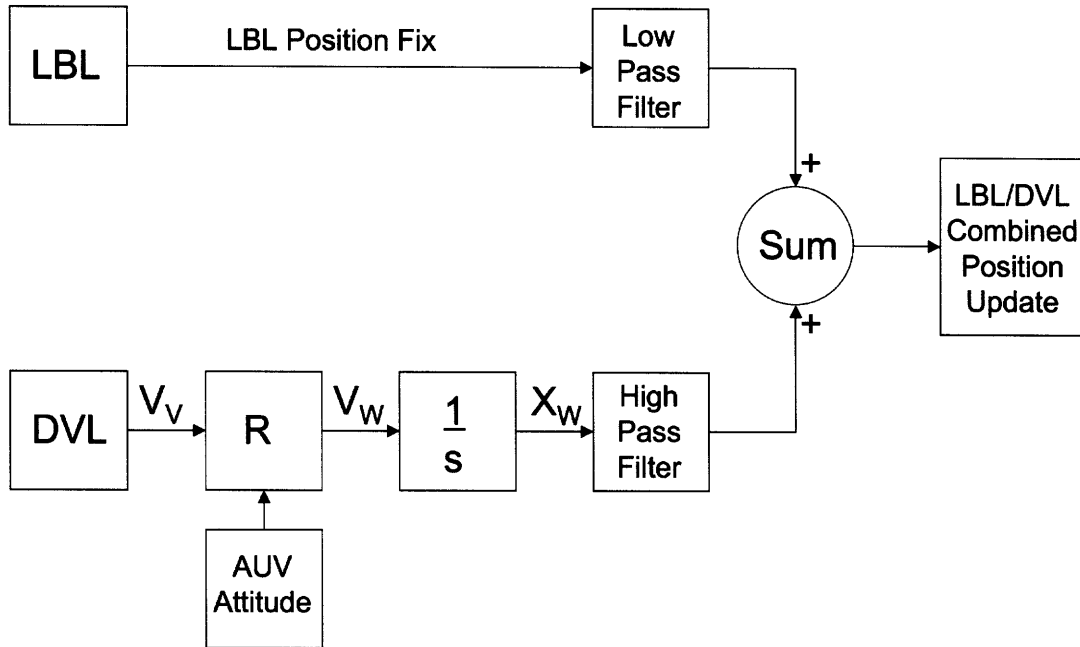
Figure 3-8: Block diagram of an LBL/DVL complementary filter adapted from Whitcomb et al. [89].

sors. The vehicle's organic sensors sample upwards of once per second while the transponder returns usually update only once every ten seconds or less. Complementary filters are an effective method of fusing asynchronous data. A complementary filter was implemented in this research similar to an LBL/DVL configuration as illustrated in Figure 3-8, but with the addition of incorporating *in-situ* multipath returns into each of the observed position fixes.

3.7   Research Assumptions

Any research that involves modeling real-world phenomena necessarily incorporates certain assumptions into the process. Some of the assumptions made in the course of this research include:

Design element In this research, there is an inherent design aspect to the development of the PH method. Throughout the architecture, there are non-unique choices made by the author based on belief of best design principles. One example is the assignment of the error threshold for the Euclidean variation of the primary arbiter. Also, the choice of system model process noise variance in the prediction step was chosen for each vehicle following the design guidelines presented by Bar-Shalom [6].

Position initialization A specific assumption made in this research is that multiple transponders are observable by the vehicle after initial descent in order to initialize vehicle position with conventional multiple transponder methods.

Environmental modeling Several assumptions are made during the process of modeling the environment and they are listed explicitly in Sections 4.1.4 and 5.2.4.

Chapter 4

The Hypothesis Generation Step: Incorporating Acoustic Travel Times from a Single Transponder

The hypothesis generation step in this proof of concept uses observed acoustic travel times from a single external transponder. Based on sensor observations of several physical quantities made *in-situ* by an AUV, the PH filter block develops up to six hypotheses of the horizontal plane position of the AUV. The overall process is shown in Figure 4-1.

4.1 Modeling the Underwater Environment

Accurately modeling the environment is a fundamental step in any system based on sensor readings of that environment. Modeling the underwater acoustic environment is a vast field of study in its own right with numerous subdisciplines. The underwater modeling used in this research is done with existing and widely used methods. It is left to future design iterations of the PH method to incorporate other advances from the dynamic field of underwater acoustics. The key steps of the underwater
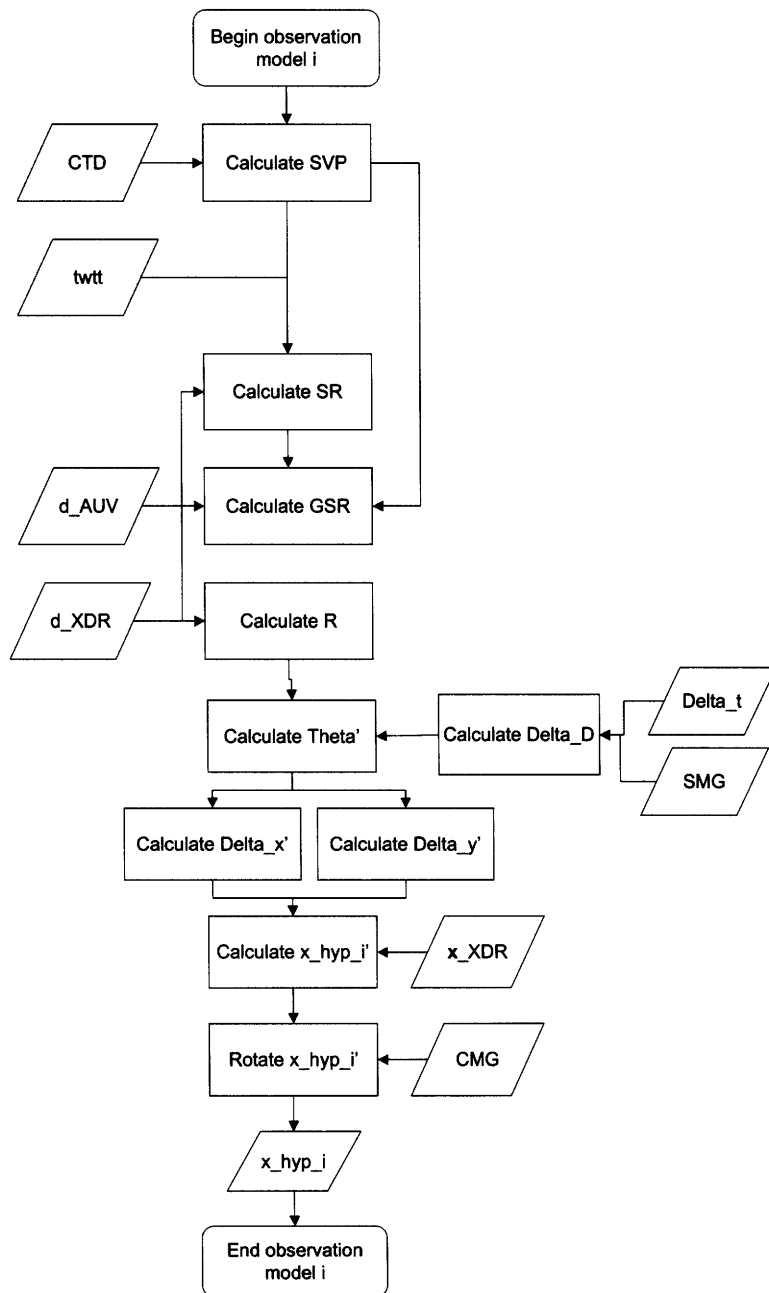
Figure 4-1: Detailed flow chart of the hypothesis generation process.
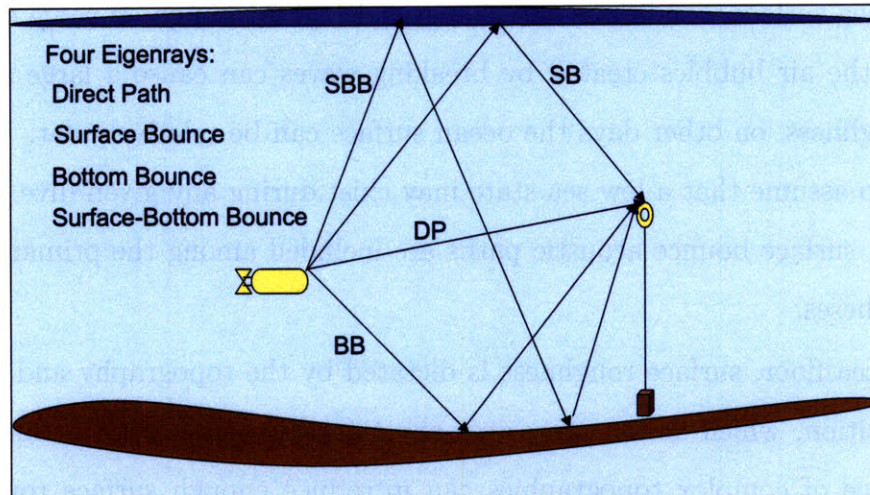
Figure 4-2: Four basic types of one-way eigenrays between vehicle and transponder.

environment modeling process used in this research are highlighted below, but see Appendix B for a detailed explanation of the process.

4.1.1 Acoustic Multipaths

4.1.1.1 One-Way Acoustic Paths

An acoustic ray traveling between any two points in the ocean can take many different paths depending on the local environment. The acoustic path taken between a source and a receiver is generally referred to as an eigenray. Neglecting refracted paths, four basic types of reflected one-way eigenrays are direct path (DP), surface bounce (SB), bottom bounce (BB), and surface-bottom bounce (SBB) as illustrated in Figure 4-2.

Clean reflection of acoustic eigenrays along bounce paths assumes smooth, flat conditions at both the water surface and the sea floor. In the real world, surface roughness at either of these boundaries could scatter acoustic signals and degrade the

81

reflective performance of each. It is necessary, therefore, to address the likelihood of encountering surface roughness at the sea surface and at the sea floor.

At the sea surface, conditions can change quickly. Although on some days, large waves and the air bubbles created by breaking waves can cause a large amount of surface roughness, on other days the ocean surface can be relatively flat. Therefore, it is valid to assume that a low sea state may exist during any given dive operation. As a result, surface bounce acoustic paths are included among the primary acoustic path hypotheses.

At the sea floor, surface roughness is dictated by the topography and the material composition, which do not vary over any timescale of interest in this research. The presence of complex topographies can introduce enough surface roughness to completely invalidate the assumption of a smooth, flat bottom [20]. Sophisticated mapping AUVs such as ABE and Sentry usually operate in regions of complex underwater features. Therefore, for the scope of this research, bottom bounce eigenray paths are not considered among the primary acoustic paths. If bottom bounces do occur, this methodology will reject the associated acoustic returns as outliers.

As a result, only direct path (DP) and surface bounce (SB) eigenrays are considered to be dominant modes of one-way acoustic travel within the context of this research.

4.1.1.2 Two-Way Acoustic Paths

When an AUV interrogates an external transponder and receives a reply, the resulting information recorded by the AUV is a two-way time-of-flight measurement. Therefore, with two primary one-way eigenrays, there are four primary acoustic multipaths for a two-way cycle. Since time-of-flight measurements correspond to the two-way range traveled by the acoustic signal, the difference between an outbound direct path with inbound surface bounce and an outbound surface bounce with an inbound direct path is not observable to the AUV. Therefore, the primary acoustic paths can be classified
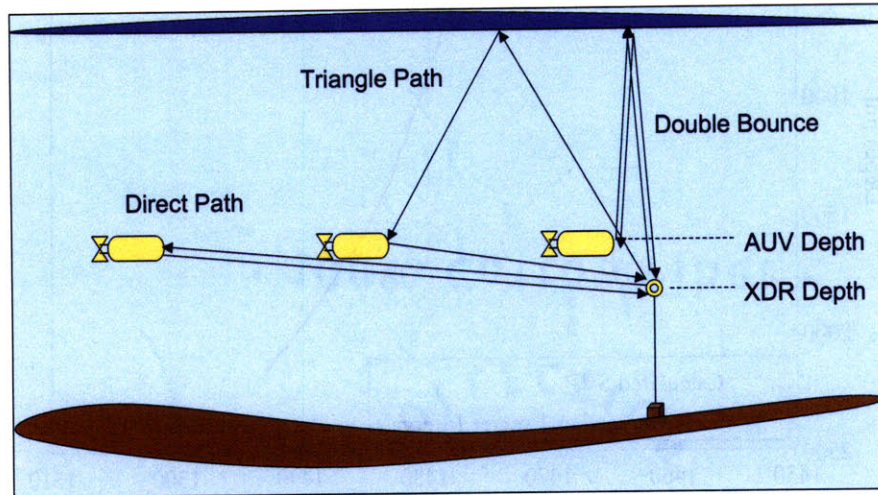
Figure 4-3: Three primary two-way acoustic paths between vehicle and transponder.

Table 4.1: Primary two-way acoustic paths.

One-Way		Outbound Eigenray	
Raypath		Direct Path	Surface Bounce
Inbound	Direct Path	Direct Path	Triangle Path
Eigenray	Surface Bounce	Triangle Path	Double Bounce

in three modes: **direct path** (DP), **triangle path** (TP) and **double bounce** (DB) as shown in Table 4.1 and illustrated in Figure 4-3.

4.1.2 Sound Velocity Profile

The speed of sound in seawater varies dramatically throughout the water column based on the salinity, temperature and pressure of the seawater at any given point [17, 24]. Knowledge of the sound velocity profile is crucial for any acoustic range calculations. Therefore, before any other operations are undertaken in a given operating
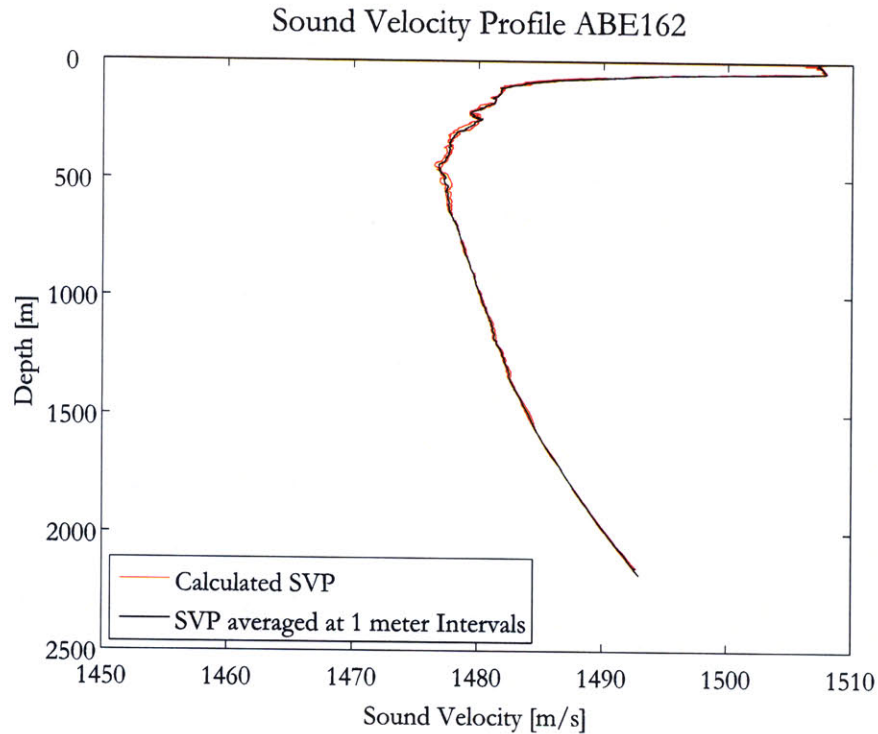
Figure 4-4: ABE162 sound velocity profile.

area, one or more conductivity, temperature and depth sensor (CTD) casts are taken with a ship-deployed sensor package. The sound velocity profile is then calculated as a function of the CTD measurements. For use in the PH algorithm, the calculated sound velocity profile is then discretized in one-meter vertical layers throughout the water column. For example, see the sound velocity profiles calculated for the dives ABE162 and ABE163 in Figures 4-4 and 4-5 respectively. The original sound velocity profiles are shown calculated at every depth where CTD data was taken. Also shown are the discretized versions where sound velocity is averaged for every one-meter layer of water.

4.1.3   Ray Tracing

The bending of acoustic rays due to the nonuniform sound velocity throughout the water column complicates the calculation of underwater distances from time-of-flight
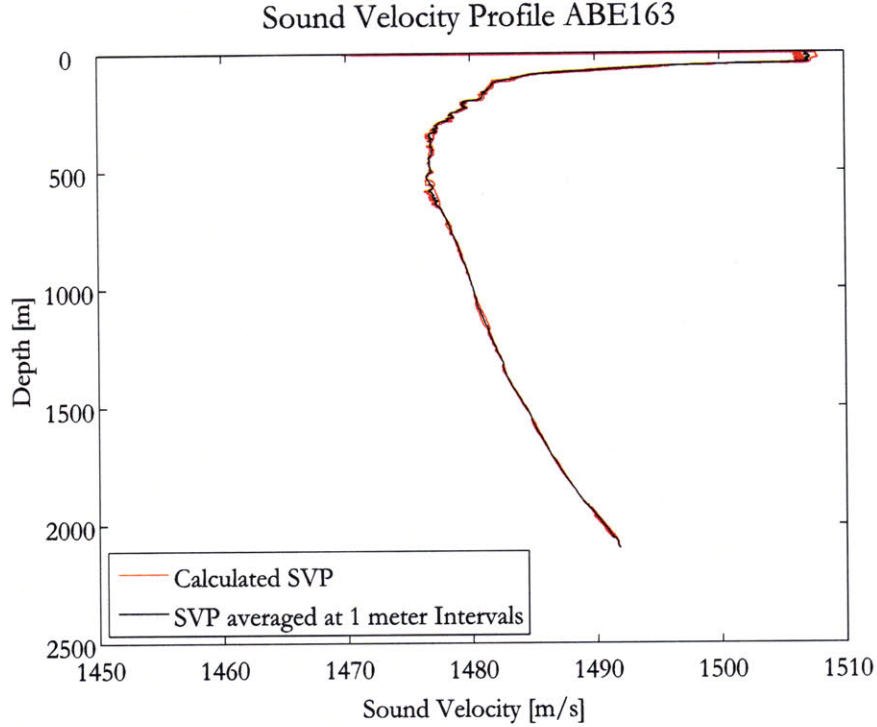
Figure 4-5: ABE163 sound velocity profile.

measurements. Through ray tracing, a relationship can be developed between the true source-to-receiver range and the observed range that the sound actually traveled along the bending eigenrays based on Snell's Law. This research incorporates a ray-tracing method which uses a version of Snell's Law based on a parallel gradient assumption where the water column is discretized in vertical layers [36]. The resulting relationship between the observed slant range (OSR) and the geometric slant range (GSR) is given by Equation 4.1.

$$GSR(OSR) = p_1 * OSR^3 + p_2 * OSR^2 + p_3 * OSR^1 + p_4 \qquad (4.1)$$

where the p values are polynomial coefficients that are a function of the depths of the AUV and the transponder. Prior to each dive, the polynomial coefficients are calculated as a function of AUV depth for each transponder.

In order to calculate this relationship between OSR and GSR for any acoustic
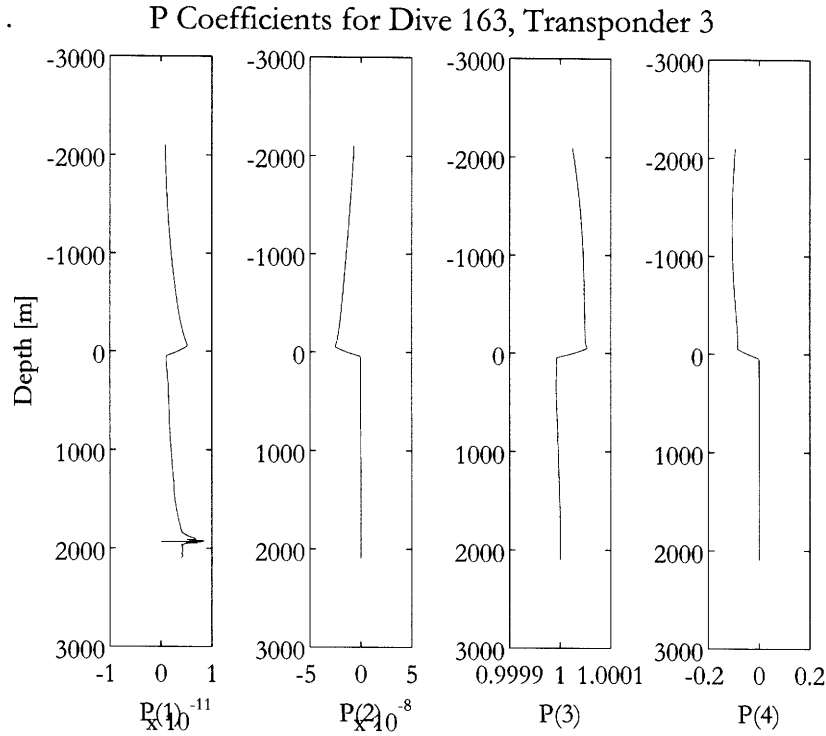
Figure 4-6: Representative ray tracing polynomial coefficients.

paths including a surface bounce, the sound velocity profile is inverted at the surface of the water. Polynomial coefficients are also then calculated for negative depths. To calculate the GSR for a bounce path, the polynomial coefficients corresponding to the depth equal to the negative of the vehicle depth are used. To illustrate, the polynomial coefficients for ABE163 Transponder 3 are shown in Figure 4-6. The resulting error between the OSR and GSR is shown for ABE163 Transponder 3 in Figure 4-7. The error is highest for DP returns where the sound travels nearly normal to the sound velocity gradient. The low-frequency temporal variation is a result of the changing physical geometry between the vehicle and the transponder during the dive due to the vehicle's motion. The high-frequency noise comes from the noise in the raw acoustic data either due to multipath returns or to true outliers.

Ray Bending Error in Slant Range for Each Acoustic Path
ABE163 Transponder 3
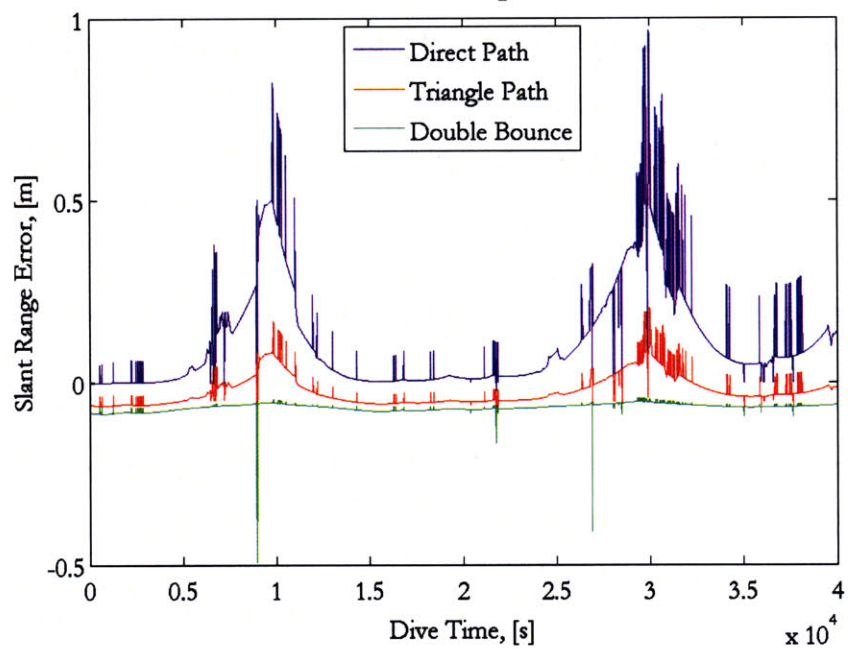
Figure 4-7: Representative error between geometric and observed slant ranges corrected by ray tracing.

4.1.4 Modeling Assumptions

As with the creation of any model of a real environment or system, certain assumptions must be made in the modeling process. Some of the specific assumptions used in this research include:

Range-independence The horizontal gradients in the speed of sound underwater are ignored and sound velocity is spatially considered to be a function only of depth.

Temporal stability of the sound velocity profile The sound velocity profile is considered constant throughout the duration of a dive, and for the Sentry operations on the Axial Seamount, the sound velocity profile is assumed to be constant throughout all three dives.

Smooth ocean surface The effects of surface roughness are ignored and the ocean surface is considered to be a smooth, reflective surface.

Rough ocean bottom The effects of surface roughness are assumed to be significant and the ocean bottom is not considered to be a smooth, reflective surface.

Parallel layer earth The curvature of the earth is ignored in these calculations due to the limited operating range of the vehicles relative to the earth's radius, so the water column is modeled as a vertical stack of parallel flat layers.

4.2 Algorithm Inputs

The PH algorithm requires inputs from multiple onboard vehicle sensors as well as the location of any external acoustic transponders in the operating area. The onboard sensor measurements required include vehicle depth, heading, attitude, speed over ground, and observed two-way travel times to an external transponder.

4.2.1 Vehicle Depth

Knowledge of the vehicle and transponder depths allows AUV localization to be easily transformed from a three-dimensional problem into a two-dimensional, horizontal plane problem. Furthermore, since the sound velocity profile gradients can be so dramatic throughout the water column, an accurate estimation of the average sound speed between the AUV and a transponder depends on the depths of both. Vehicle depth on both vehicles is measured *in situ* by a Paroscientific Inc. sensor. Depth is inferred from observed gauge pressure using a standard calculation as explained in Appendix B.

4.2.2 Vehicle Course and Speed

An important component of the single transponder building block is the calculation of the vehicle speed and course over ground, or speed made good (SMG) and course made good (CMG). Each platform uses an RDI Instruments Workhorse Navigator Doppler Velocity Log (DVL) to determine the speed of the vehicle with a long term accuracy of 0.4% [72]. Using a pattern of four downward-looking beams, the DVL records SMG in instrument-frame velocities. The instrument-frame velocities are then transformed into body-frame velocities using a constant rotation matrix based on the fixed orientation of the instrument on the vehicle. The resulting body-frame velocities provide forward speed, u, and cross body speed, v, where positive values are to starboard and negative values to port. Finally, the body-frame velocities are transformed into global-frame velocities via another rotation matrix using measurements from internal heading and attitude sensors. However, this rotation matrix is time-varying because it depends on the instantaneous orientation of the vehicle. The attitude information provided by a calibrated flux-gate compass for ABE and by an IXSEA Phins INS for Sentry is used to build this time-varying rotation matrix to provide velocity information in a global cardinal Cartesian framework [71].

After the appropriate rotation matrix transformations have been performed, the

velocity data are available in the globally-referenced Cartesian coordinate framework and are used to determine the course over ground. The global-frame velocities are integrated to calculate the distance traveled by the vehicle as given by

$$\Delta Distance = \int V(\tau) \, d\tau \tag{4.2}$$

Since the velocity information is available as a discrete data set, numerical integration is used to calculate the distance traveled. The composite trapezoidal quadrature method is used for this numerical integration as in the general Equation 4.3.

$$\int_{t_1}^{t_n} f(t) \, dt = \sum_{i=1}^{n-1} \frac{1}{2} * (f(i) + f(i-1)) * (t(i+1) - t(i)) \tag{4.3}$$

More complex methods of quadrature exist for discrete data that involve higher-order polynomial fitting and adaptive quadrature sampling. However, the complexity introduced by these methods is extreme compared to the small incremental improvement in accuracy of the quadrature [11, 64, 73]. Therefore, composite trapezoidal quadrature is the standard for numerical integration calculations of discrete data sets and is used in this research.

4.2.3 Transponder Location

Prior to launching an AUV for scientific operations in a given operating area, any acoustic transponders that will be used for navigation are deployed in predetermined areas. Once the transponders are anchored in position, their precise horizontal locations and depth must be determined by personnel on the ship. This is done by surveying each transponder's location individually. During the survey process, the ship drives in a semicircle around the transponder and repeatedly interrogates it with ship-mounted transducers. The resulting time-of-flight measurements, r_i, are used in conjunction with precise knowledge of the ship's location from GPS, x_i, to calculate the exact location of each transponder, x_{XDR}, according to Equation 4.4.

90

$$\mathbf{x}_{XDR} = \text{argmin}_{\mathbf{x}_{XDR}} \sum_{i=1}^{n} \left(\|\mathbf{x}_{XDR} - \mathbf{x}_i\| - r_i^2 \right) \tag{4.4}$$

In reality, the location of each transponder can vary over the course of dive operations, for example due to currents. However, once the transponders are surveyed, it is general practice to assume that these locations are fixed and known. In postprocessing, it is possible to adjust these locations slightly to better fit the acoustic data. However, since the goal of the PH algorithm is real-time implementation, this research uses the surveyed locations of the transponders.

4.2.4 Acoustic Two-Way Time-of-Flight Measurements

The acoustic time-of-flight measurements between an AUV and external acoustic transponders provide the basis for acoustic baseline vehicle navigation. A two-way time-of-flight measurement is converted to a range by using an average value for the sound velocity between the AUV and the transponder. In LBL navigation, the vehicle uses multiple calculated direct path ranges in a given navigation cycle to triangulate its horizontal position, as described in Milne's seminal work [63]. The locations of all transponders are preloaded into the AUV prior to the dive. A single navigation cycle is the period of time in which an AUV collects acoustic time-of-flight measurements from the transponders to calculate a single position fix or pose estimate.

At the beginning of the navigation cycle, the AUV will interrogate the transponders by pinging them on a master frequency. Upon hearing the master frequency ping, each transponder replies after a preset delay. The returns from the different transponders are either made on distinct frequencies or with distinct codes for unique identification. For LBL transponders, the frequencies used are usually in the range of 7 to 12 kHz. The length of the navigation cycle should be set based on the anticipated operating distance of the AUV from the transponders so that the reply pings from the transponders are received by the AUV during the correct navigation cycle. If

the cycle is set too short, then the AUV can experience wrap-around returns where it hears returns in one cycle from a previous cycle's interrogation. However, a long navigation cycle limits the update rate of the acoustic baseline system. ABE and Sentry use ten second navigation cycles. For discussion of LBL navigation, see, for example, [41, 45, 108]. A PH single transponder filter uses the two-way travel times from a single transponder collected during each navigation cycle.

4.3   Calculating the Possible Range Rings

During every navigation cycle, the vehicle collects a two-way travel time of the acoustic return from a given transponder. This two-way travel time is then converted into an observed slant range measurement as in Equation 4.5.

$$OSR = \frac{\bar{c} * (twtt - \epsilon)}{2} \tag{4.5}$$

where

OSR = Observed slant range between vehicle and transponder,

$\bar{c}$ = Average sound velocity,

$twtt$ = Observed acoustic two-way travel time, and

ϵ = Known transponder response time delay.

This observed slant range is then transformed into a geometric slant range as described in Section 4.1.3 with Equation 4.1. Since both the transponder depth and the vehicle depth are known, the geometric slant range is then converted into a horizontal range (HR) between the two using equations of relative geometry.
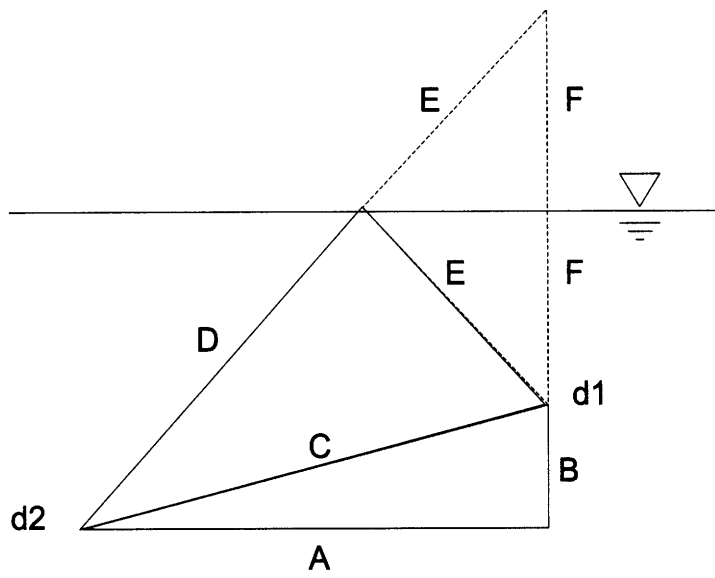
Figure 4-8: Relative geometry between transponder and vehicle for acoustic multi-paths.

4.3.1 Direct Path

For direct path returns, the relative geometry between transponder and vehicle is a simple Pythagorean relationship. In Figure 4-8, the horizontal range between the vehicle and transponder is shown as A and the one-way direct path GSR is represented by C. The depth $d1$ represents the minimum of the transponder and vehicle depths, while $d2$ represents the maximum of the two depths. The horizontal range is given by

$$A = (C^2 - B^2)^{\frac{1}{2}} \qquad (4.6)$$

where

$A = $ Horizontal range, HR,

$B = |d1 - d2|$, and

$C = $ One-way direct path geometric slant range, GSR.

Recall that Figure 4-7 shows that ignoring ray bending produces errors on the order of one meter.

4.3.2 Double Bounce Path

For double bounce returns, the relative geometric relationships are simplified using the mirror method as shown in Figure 4-8. Once again, the horizontal range between the vehicle and transponder is given as A, but here the one-way GSR is represented by $D + E$. The horizontal range is found using the Pythagorean theorem on a triangle whose uppermost vertex is at a point that is the reflection of $d1$ across the water surface like a mirror, as given by

94

$$A = ((D + E)^2 - (B + 2F)^2)^{\frac{1}{2}} \tag{4.7}$$

where

A = Horizontal range, HR,

$B + 2F = d1 + d2$, and

$D + E$ = One-way double bounce path geometric slant range, GSR.

Figure 4-7 shows that ignoring ray bending produces errors that are typically much less than one meter.

4.3.3 Triangle Path

Calculating the horizontal range from the triangle path GSR is more complicated. In Figure 4-8, the two-way triangle path GSR is given by $C + D + E$. Since the acoustic signal follows different outbound and inbound paths, the idea of a one-way triangle path GSR does not correspond to any exact physical quantity depicted in Figure 4-8. Therefore, it is defined as a purely mathematical concept as one half of the round trip, or two-way, GSR. The relative geometry requires a series of complicated calculations to determine the exact mathematical relationship between horizontal range and triangle path GSR. These calculations are dependent upon the assumption of a flat ocean surface that creates equal angles of incidence and reflection of the sound off of this surface. The results are given by Equation 4.8.

$$A = (\frac{C1^2 - C3}{C2 + 2C1})^{\frac{1}{2}} \tag{4.8}$$

95

where

$$A = \text{Horizontal range, HR,}$$

$$C + D + E = \text{Two-way triangle path geometric slant range, 2*GSR,}$$

$$C1 = \frac{(C + D + E)^2 - C2}{2},$$

$$C2 = B^2 + (B + 2F)^2 \text{ , and}$$

$$C3 = B^2 * (B + 2F)^2.$$

Figure 4-7 shows that ignoring ray bending produces errors that are typically much less than one meter.

4.3.4 Range Calculation Paradigm

In typical LBL navigation schemes, the assumption is made that every received acoustic return has followed a two-way direct path between vehicle and transponder. Therefore, Equation 4.6 is used at every timestep to determine the horizontal range. If the acoustic signal in any given timestep actually did follow a direct path through the water, then the horizontal range determined by Equation 4.6 will be correct. However, if the acoustic signal at that timestep followed any other acoustic path, then the horizontal range determined with Equation 4.6 will be incorrect. The apparent horizontal range for any type of bounce path will be greater than the actual horizontal range. This effect is illustrated from a side view in Figure 4-9 and from a planar or bird's eye view in Figure 4-10.
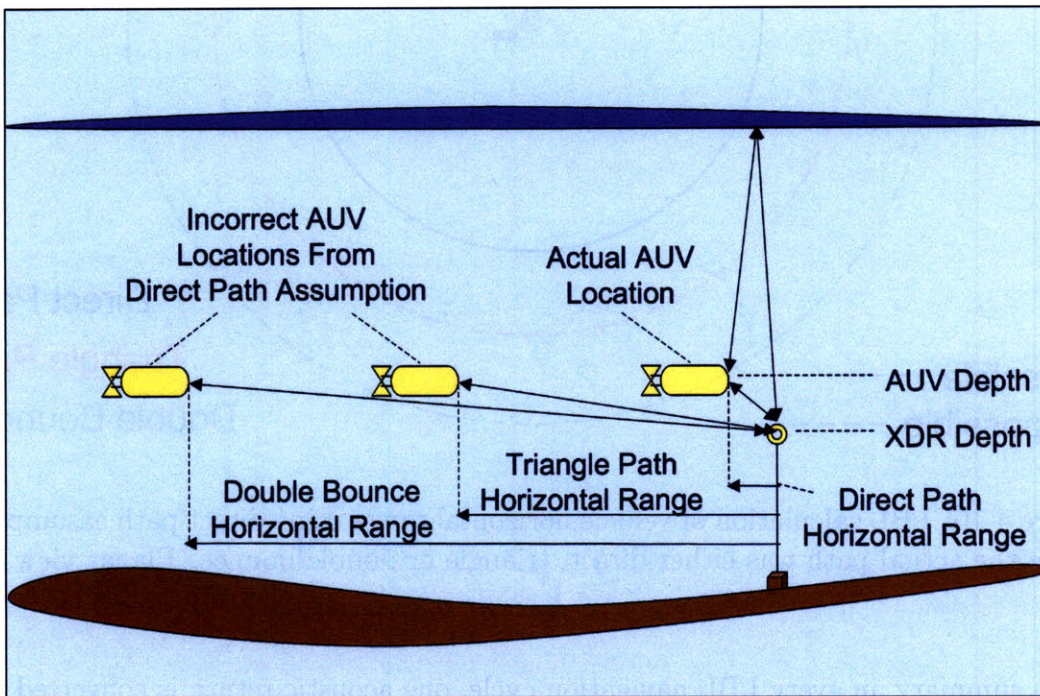
Figure 4-9: LBL calculation of vehicle horizontal range using direct path assumption where the actual path was either direct, triangle or double bounce. Side view.
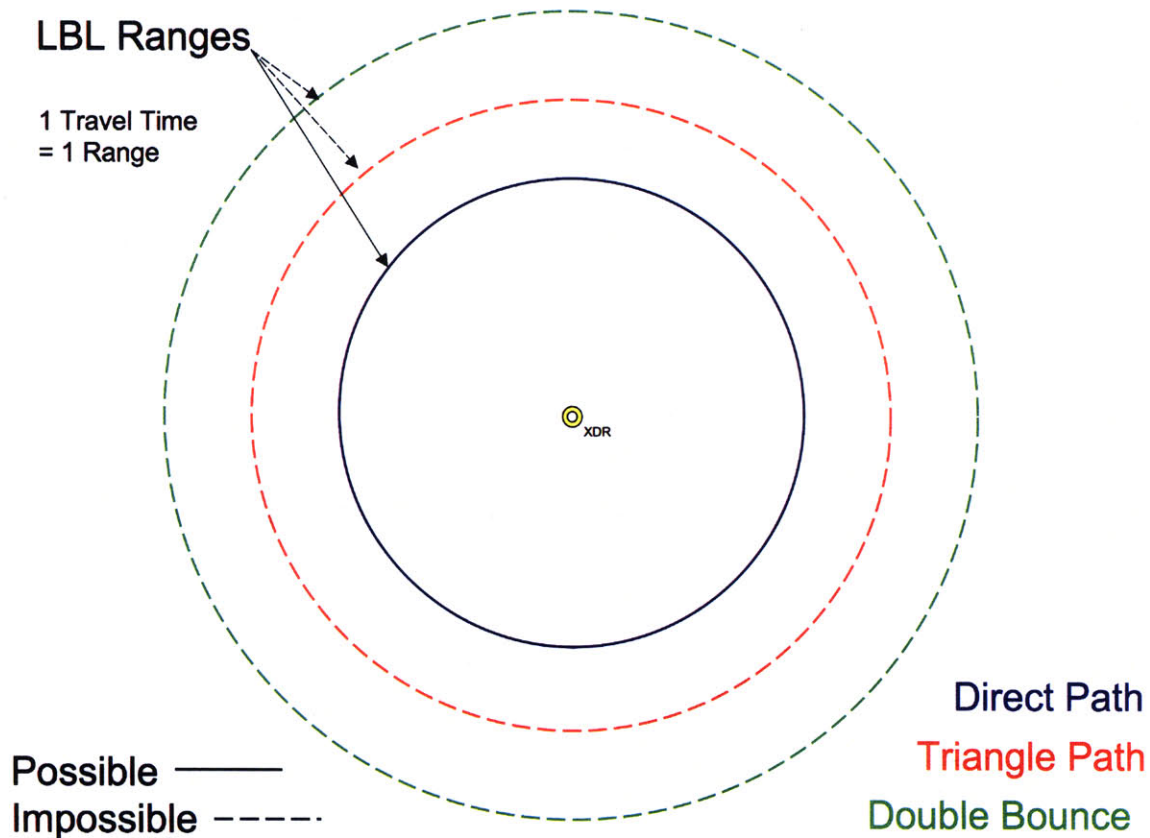
Figure 4-10: LBL calculation of vehicle horizontal range using direct path assumption where the actual path was either direct, triangle or double bounce. Planar view.

In summary, in every LBL navigation cycle, one acoustic return is converted to a horizontal range using a direct path assumption. If that acoustic return followed any path other than the direct path, the calculated horizontal range will be incorrect and will be rejected as an outlier. Therefore, the only returns that are used in a typical LBL solution are those that followed a two-way direct path.

In PH navigation, a different paradigm is employed with respect to possible range calculations. The acoustic return received in any given timestep is processed three separate times. First, the acoustic return is used to calculate a direct path horizontal range using Equation 4.6. As with LBL, if the acoustic signal actually followed a two-way direct path, then this calculated direct path horizontal range will be the

true horizontal range between vehicle and transponder. Next, the acoustic return is used to calculate a triangle path horizontal range using Equation 4.8. If the acoustic signal had actually followed a triangle path through the water, then this calculated triangle path horizontal range will be the same as the true horizontal range between vehicle and transponder. Finally, the acoustic signal is converted to a double bounce path horizontal range using Equation 4.7. Once again, if the given acoustic signal actually did follow a double bounce path, then this calculation will yield the true horizontal range between vehicle and transponder. This paradigm is illustrated in Figures 4-11 and 4-12 in side and planar views, respectively.
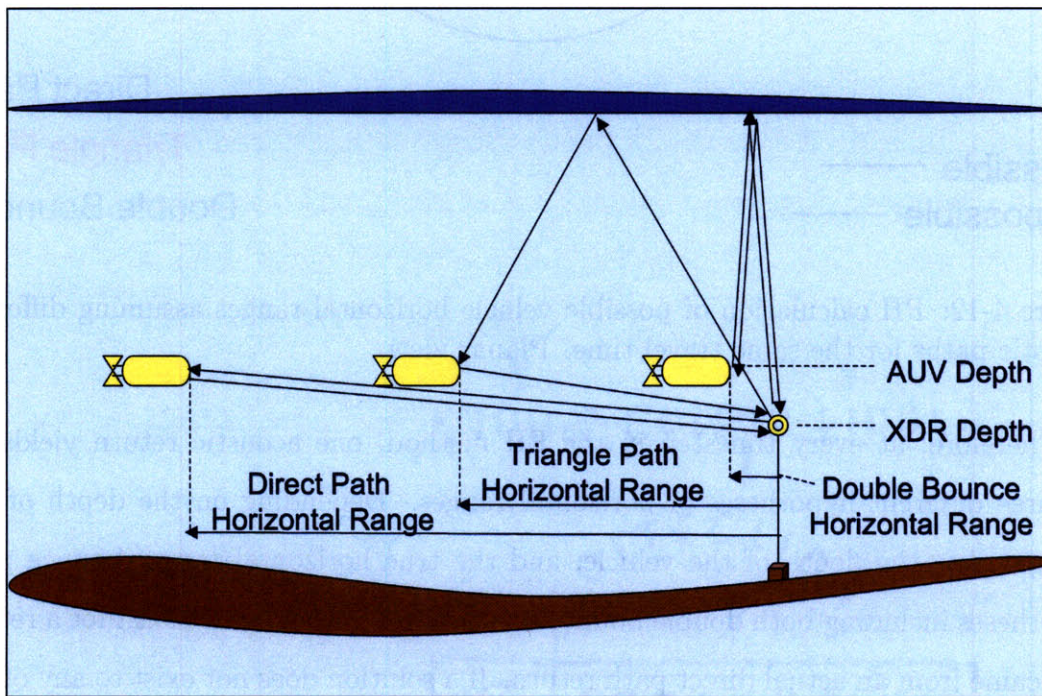
Figure 4-11: PH calculation of possible vehicle horizontal ranges assuming different acoustic paths for the same travel time. Side view.
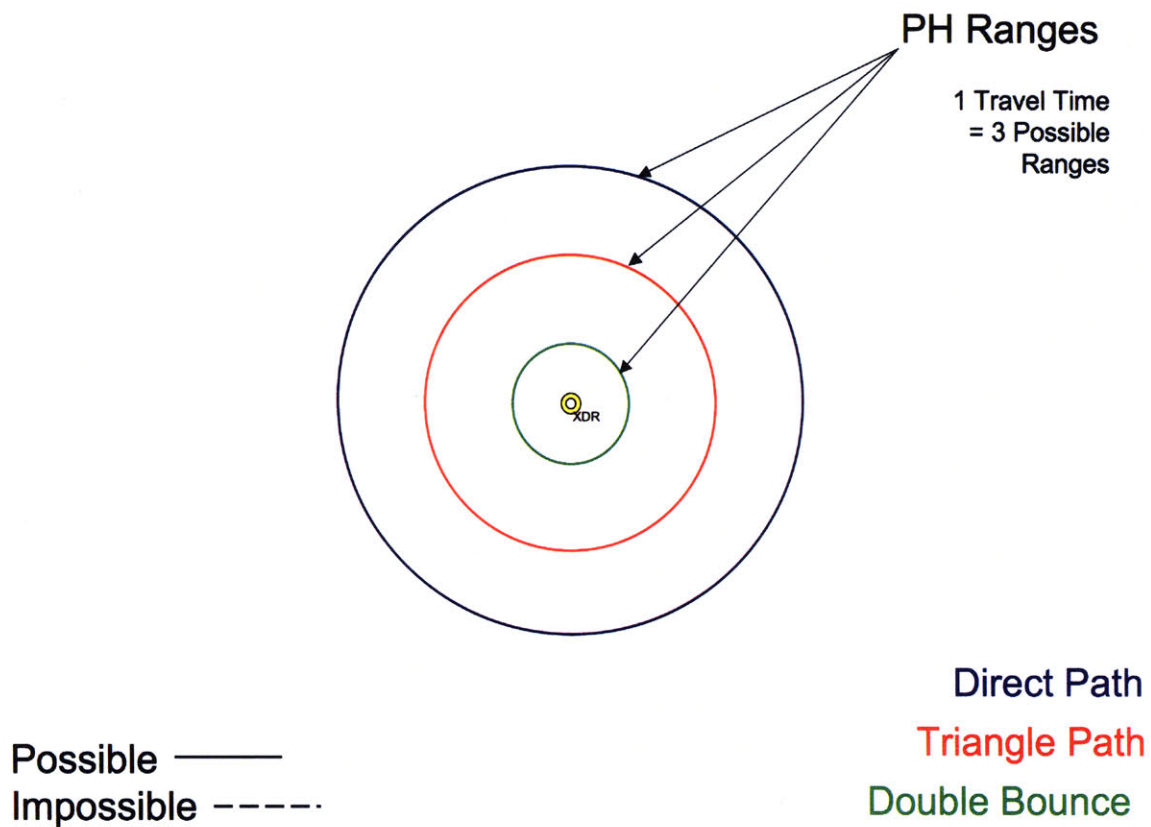
Figure 4-12: PH calculation of possible vehicle horizontal ranges assuming different acoustic paths for the same travel time. Planar view.

Therefore, at every timestep in the PH method, one acoustic return yields up to three different hypotheses of horizontal ranges. Depending on the depth of the transponder, the depth of the vehicle, and the true horizontal range, bounce path hypotheses including both double bounce and triangle path may not exist for a return that came from an actual direct path return. If a solution does not exist to any of the horizontal range equations, then the respective acoustic path assumption was invalid anyway.

Figure 4-13 shows the relative magnitudes of the horizontal distances calculated by the LBL and PH range calculation paradigms.
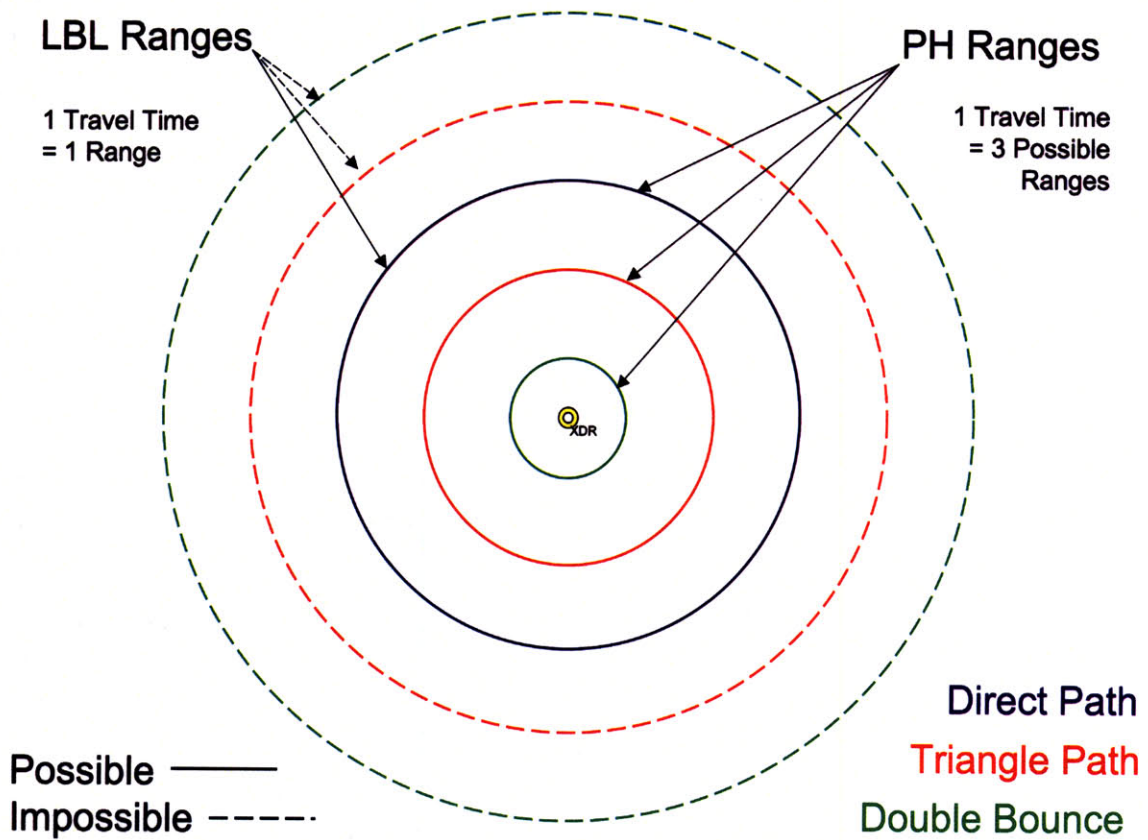
Figure 4-13: Comparison of LBL and PH calculations of possible vehicle horizontal ranges. Planar view.

4.4 Locating the Position Hypotheses on Each Range Ring

After the range rings have been calculated for each of the three possible acoustic paths, two vehicle position hypotheses are located on each of these possible range rings, as illustrated in Figure 4-14. There are two possible vehicle locations on each range ring because the relative orientation of the transponder with respect to vehicle course is not directly observable.
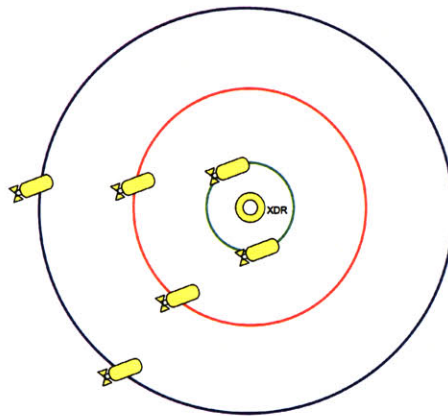
Figure 4-14: Illustration of PH calculation of vehicle pose hypotheses for a single navigation cycle. While all positions on each ring are consistent with the observed travel time and the acoustic path assumption, only two positions on each ring are consistent with the observed range rate, CMG and SMG.

The notation used in these calculations is shown in Figure 4-15.

The first step in identifying the vehicle pose hypotheses is to locate the range ring of the horizontal range between vehicle and transponder at time t in relation to the transponder location, as shown in Figure 4-16.
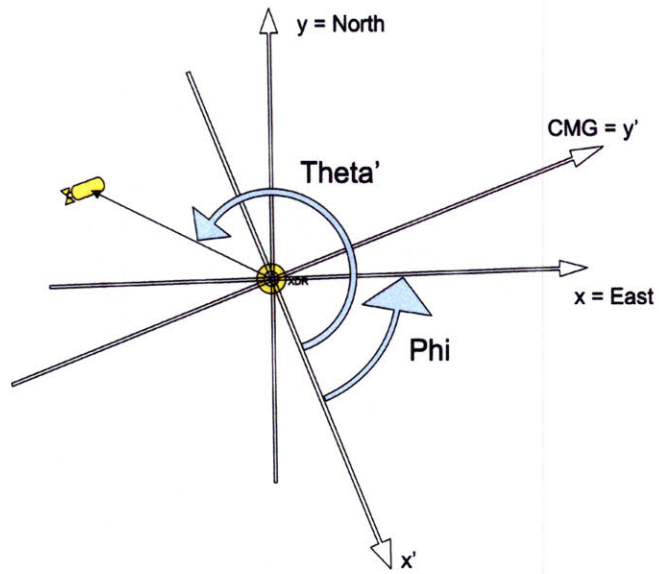
Figure 4-15: Nomenclature for vehicle poses.
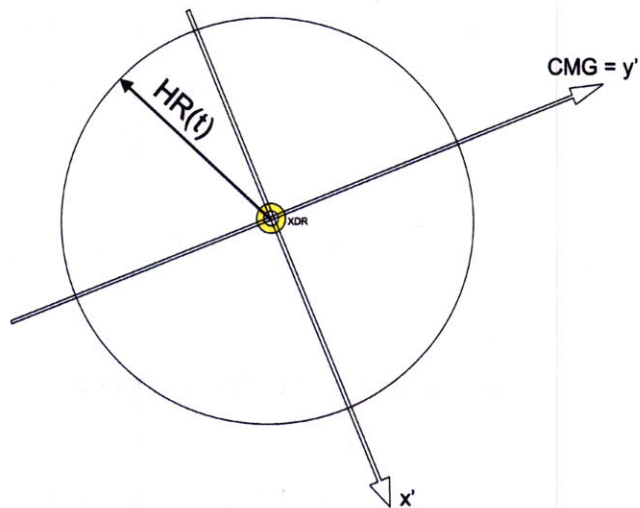
Figure 4-16: Range ring of possible vehicle poses at time t based on horizontal range.
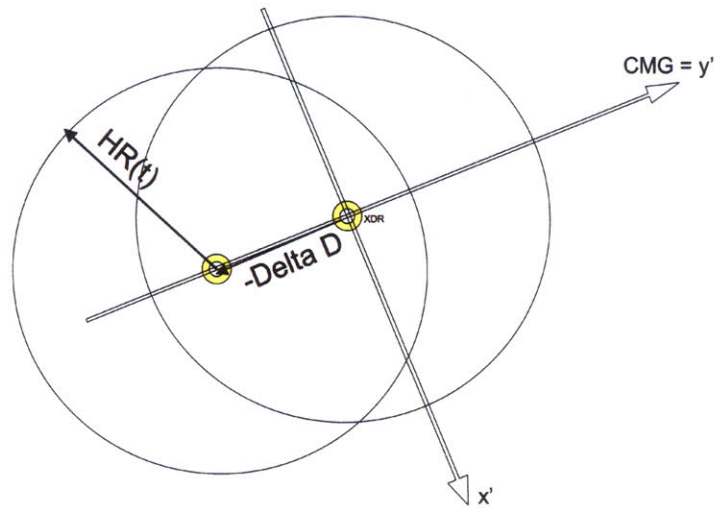
Figure 4-17: Possible vehicle poses at time $t - n$ based on backwards propagation of horizontal range from time t.

The next step is to use the information about CMG and SMG from the DVL to calculate a vector of direction and distance traveled between the current timestep and a timestep in the past. The range ring at time t is then propagated backwards along the negative of the distance traveled vector, as shown in Figure 4-17. At time $t - n$, the vehicle must have been located somewhere on this backwards propagated range ring.

Next, the horizontal range calculated at time $t - n$ is superimposed on the previous visualization. The possible vehicle locations at time $t - n$ are located at the intersection between the range ring at $t - n$ and the backwards propagated range ring, as shown in Figure 4-18. There are two location hypotheses because the relative location of the transponder with respect to the vehicle's course is not directly observable from a single set of measurements.
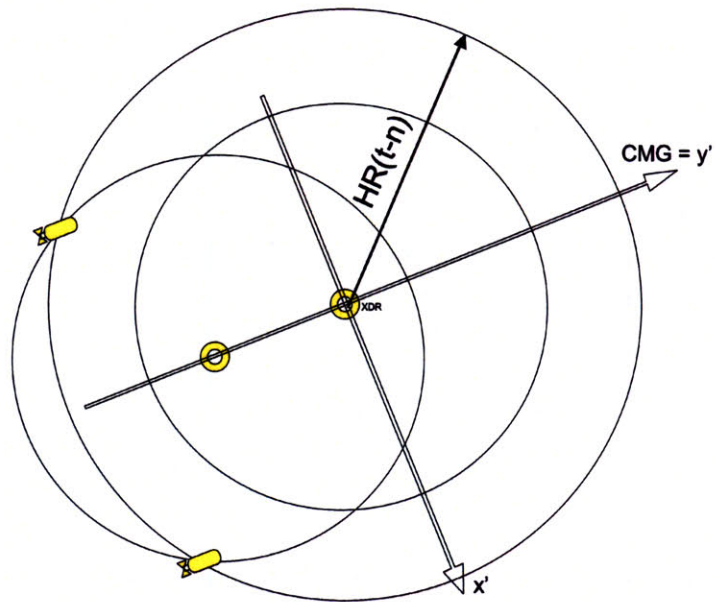
Figure 4-18: Possible vehicle poses at time $t - n$ based on intersection with horizontal range at time $t - n$.
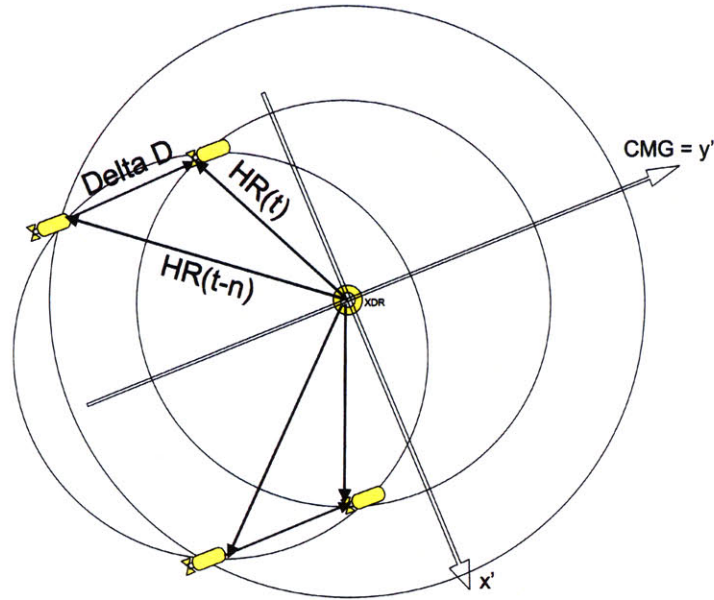
Figure 4-19: Possible vehicle poses at time t forward propagated from time $t - n$ with the distance traveled vector.

The vehicle pose hypotheses at time t are found by forward propagating the possible vehicle locations at time $t - n$ using the distance traveled vector, as shown in Figure 4-19.

θ' is the bearing to the vehicle from the transponder with respect to the vehicle-frame coordinate system with axes x' and y' which is orientated such that the CMG is the y' axis, as shown in Figure 4-20. It is given by

$$\theta' = \frac{\pi}{2} - \arccos\left[\frac{\Delta D(t)^2 + HR(t)^2 - HR(t-n)^2}{2\Delta D(t)HR(t)}\right] \qquad (4.9)$$

106
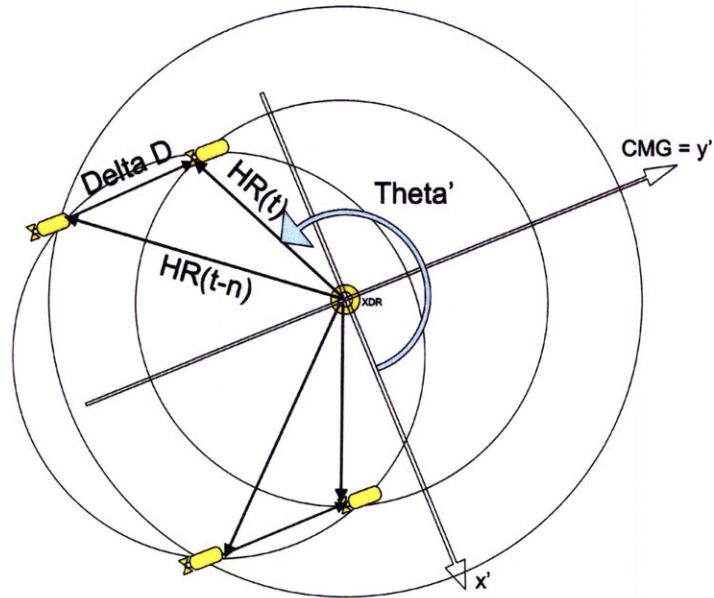
Figure 4-20: Calculating the bearing from the transponder to the vehicle pose hypotheses on the prime axes.

where

$$\theta' \equiv \text{Bearing to vehicle from transponder in prime coordinate system,}$$

$$\Delta D(t) \equiv \text{Vector of distance traveled by vehicle from time } t - n \text{ to } t,$$

$$HR(t) \equiv \text{Horizontal range between vehicle and transponder at time } t, \text{ and}$$

$$HR(t - n) \equiv \text{Horizontal range between vehicle and transponder at time } t - n.$$

The displacement of each pose hypothesis from the transponder with respect to the prime coordinate system is calculated, as shown in Figure 4-21.

The prime coordinate system is then rotated into a cardinal coordinate system with the y axis pointing to the North, as shown in Figure 4-22. ϕ is the rotation angle between the vehicle-frame Cartesian coordinate system and the global-frame cardinal Cartesian coordinate system. It is given by
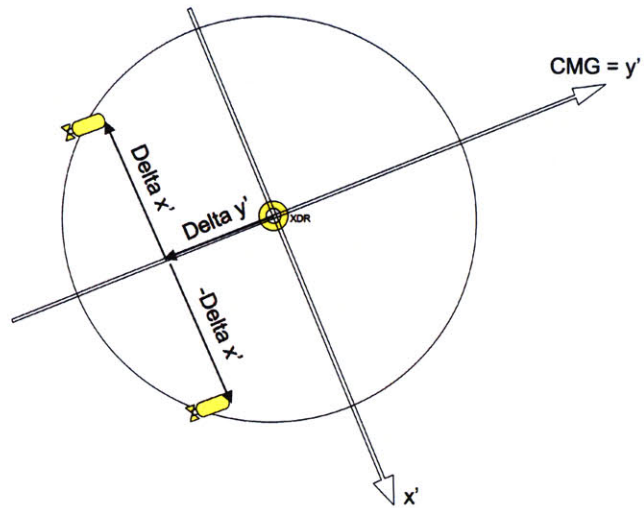
Figure 4-21: Calculating the coordinates of the vehicle pose hypotheses in the prime coordinate system.

$$\phi = \frac{\pi}{2} - CMG \tag{4.10}$$

where

$CMG =$ Course made good, measured in radians counterclockwise from due East.
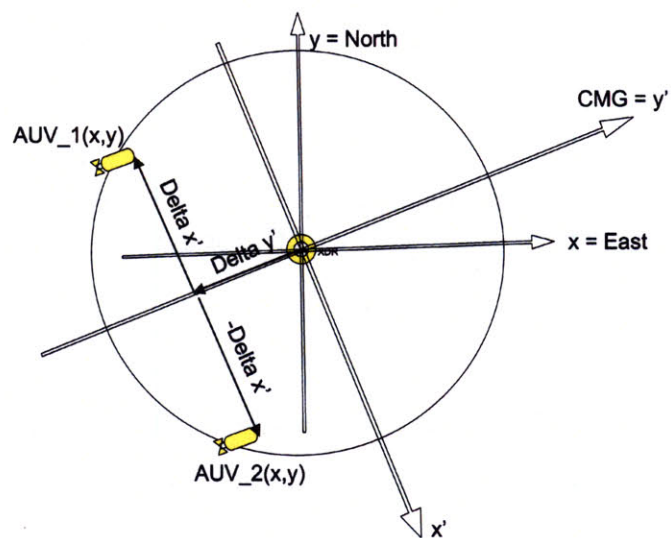
Figure 4-22: Rotating solution from the prime coordinate system to the cardinal coordinate system.
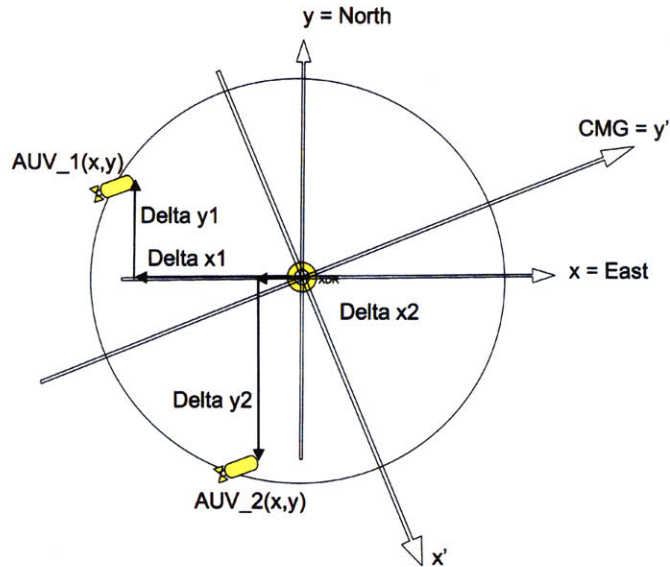
Figure 4-23: Calculating the coordinates of the vehicle pose hypotheses in a cardinal coordinate system with the transponder at the origin.

The displacements of the vehicle from the transponder are recalculated in the cardinal coordinate system, as shown in Figure 4-23.

Then the coordinates of the pose hypotheses are found in the local grid cardinal Cartesian coordinate system by displacing the system origin from the transponder to the local Cartesian origin for each operating area as shown in Figure 4-24.

The equations governing the process shown in Figures 4-16 to 4-24 are as follows. The pose hypotheses for the different possible range rings under the assumption that the transponder lies to the left of the vehicle's course are given by Equation 4.11.

$$
\begin{bmatrix} \tilde{x}_{odd} \\ \tilde{y}_{odd} \end{bmatrix} = \begin{bmatrix} \cos\phi & \sin\phi \\ -\sin\phi & \cos\phi \end{bmatrix} \begin{bmatrix} r(k) * \cos\theta' \\ r(k) * \sin\theta' \end{bmatrix} + \begin{bmatrix} x_{XDR} \\ y_{XDR} \end{bmatrix} \tag{4.11}
$$
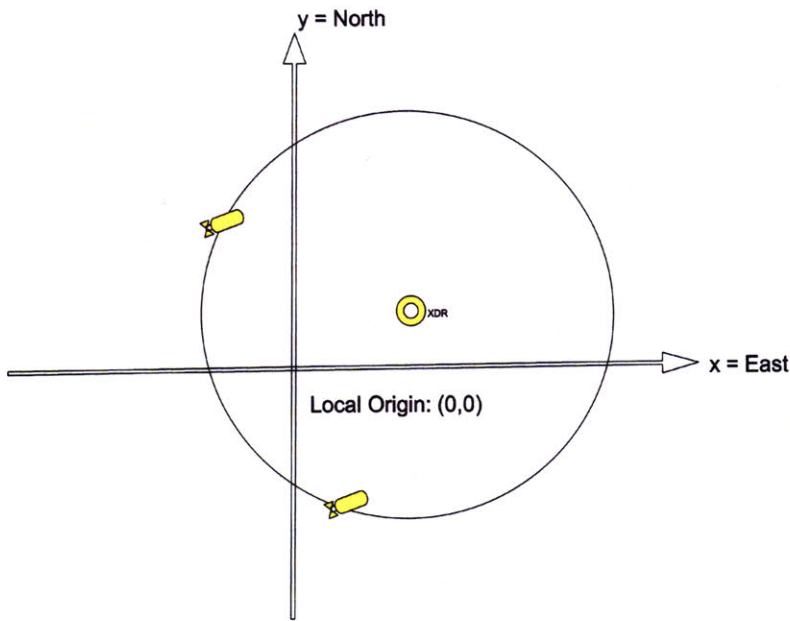
Figure 4-24: Calculating the coordinates of the vehicle pose hypotheses using the local Cartesian origin.

where

$(\tilde{x}_1, \tilde{y}_1)$ = Direct path pose hypothesis with transponder left of course,

$(\tilde{x}_3, \tilde{y}_3)$ = Triangle path pose hypothesis with transponder left of course, and

$(\tilde{x}_5, \tilde{y}_5)$ = Double bounce pose hypothesis with transponder left of course.

The pose hypotheses for the different possible range rings under the assumption that the transponder lies to the right of the vehicle's course are given by Equation 4.12.

$$\begin{bmatrix} \tilde{x}_{even} \\ \tilde{y}_{even} \end{bmatrix} = \begin{bmatrix} \cos\phi \ \sin\phi \\ -\sin\phi \ \cos\phi \end{bmatrix} \begin{bmatrix} -r(k)*\cos\theta' \\ r(k)*\sin\theta' \end{bmatrix} + \begin{bmatrix} x_{XDR} \\ y_{XDR} \end{bmatrix} \tag{4.12}$$

where

$(\tilde{x}_2, \tilde{y}_2)$ = Direct path pose hypothesis with transponder right of course,

$(\tilde{x}_4, \tilde{y}_4)$ = Triangle path pose hypothesis with transponder right of course, and

$(\tilde{x}_6, \tilde{y}_6)$ = Double bounce pose hypothesis with transponder right of course.

4.5   Uncertainty Analysis

The covariance of each pose hypothesis is calculated using uncertainty analysis as shown in Figure 4-25 .
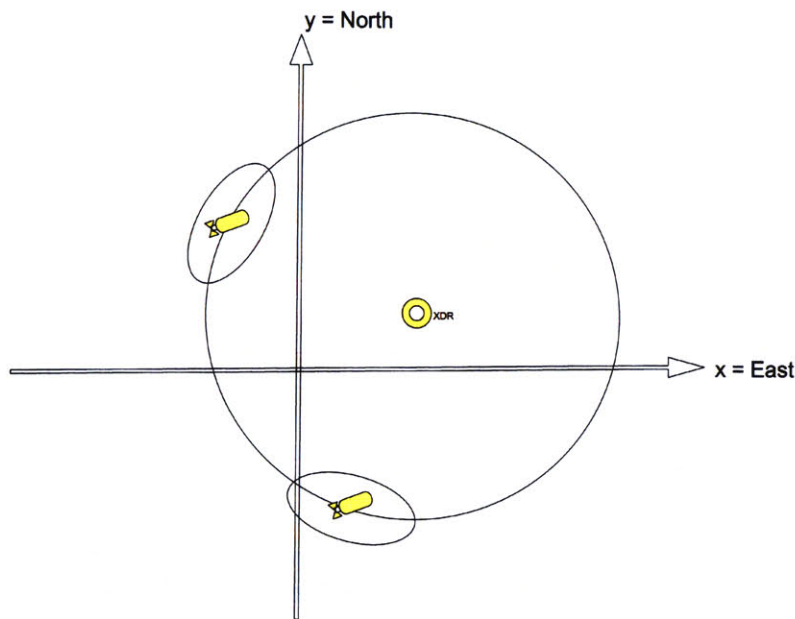
Figure 4-25: Calculating the covariance of the vehicle pose hypotheses.

The entire process is repeated for each range ring until a total of up to six position hypotheses are generated, as shown in Figure 4-26. The position hypotheses are then ready to input into the Arbiter.
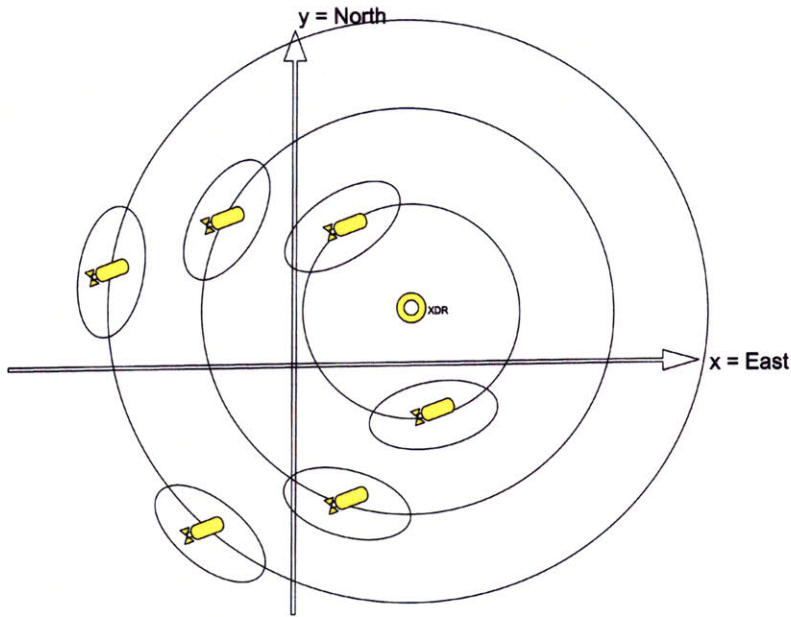
Figure 4-26: Repeating the entire process for all possible ranges.

An example from actual data is shown for one timestep in Figure 4-27 and for a series of six consecutive timesteps in Figure 4-28. The blue markers represent direct path hypothesis locations and the red markers represent triangle path hypothesis locations. The acoustic return shown in Figure 4-27 was actually a triangle path return, while Figure 4-28 shows a combination of actual direct path and triangle path returns over the six timesteps. In this particular geometry, the vehicle was operating too close to the transponder to get any double bounce location hypotheses using these travel times, that happened to all be either direct path or triangle path.
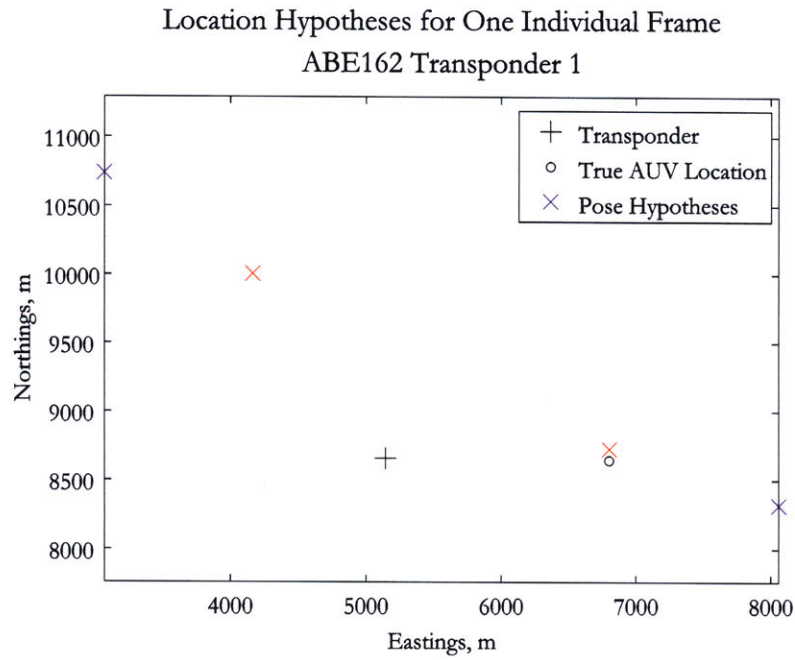
Figure 4-27: ABE162 pose hypotheses for a single timestep.
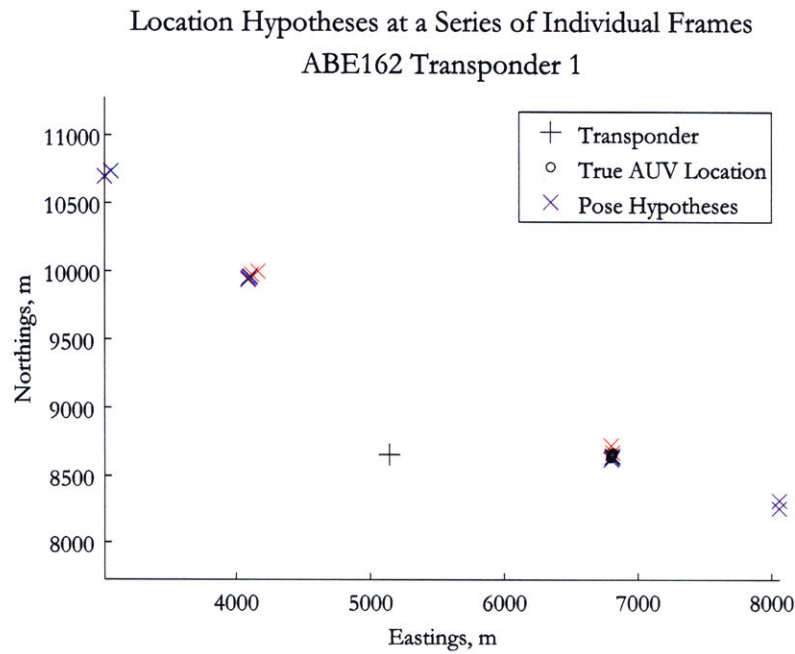
Figure 4-28: ABE162 pose hypotheses for a series of six consecutive timesteps.
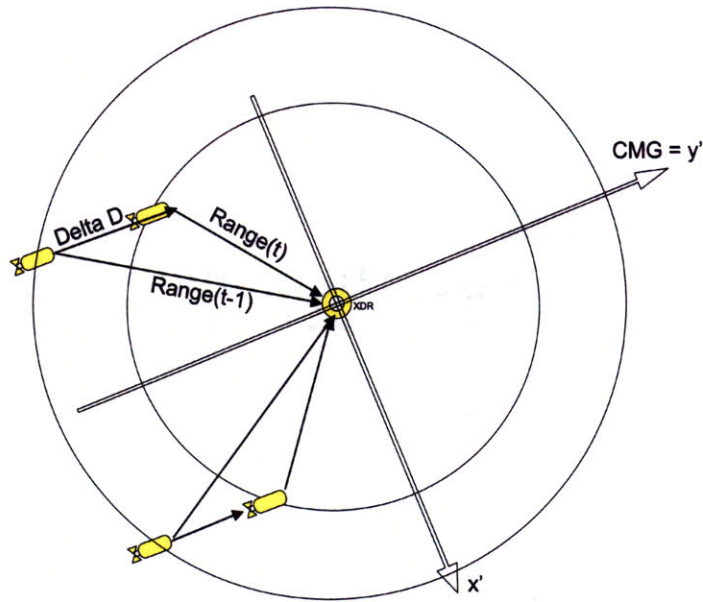
Figure 4-29: Successful pose localization geometry.

4.6 Dynamic Temporal Window

Generating a pose hypothesis is only possible if the triangle between the range at time t, the range at time $t - n$, and the vector of distance traveled between $t - n$ and t exists, as shown in Figure 4-29.

If the range at time t is generated from one acoustic path and the range at time $t - n$ is generated from a different acoustic path, their difference will be so great that no triangle exists, as in Figure 4-30.

As a result, the two acoustic travel times used to calculate each set of pose hypotheses in any given navigation cycle must have followed the same acoustic path. Therefore, a dynamic temporal window filter was designed to select *in situ* two acoustic travel times of the same type for every given navigation cycle. This process is repeated for each of the three range hypotheses at every navigation cycle.

An illustration of the filter is shown in Figure 4-31. At time t, there is a range that is calculated from the two-way travel time using one of the three possible acoustic
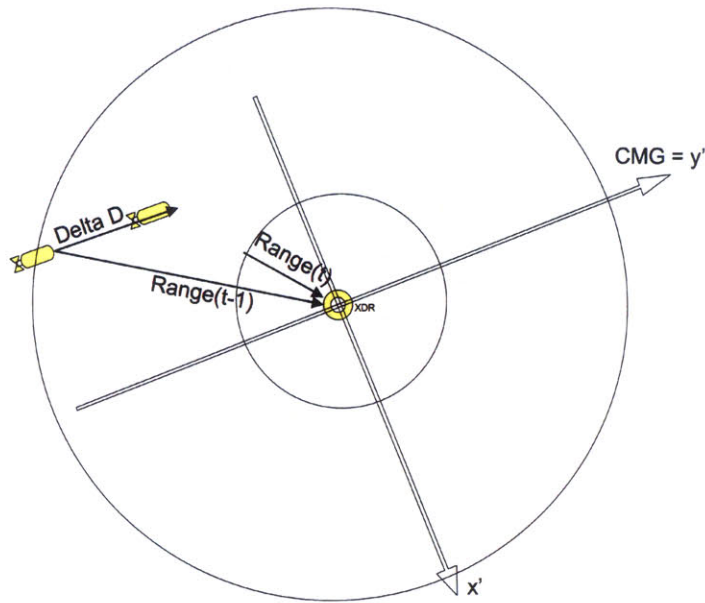
Figure 4-30: Example illustration of the failure of the pose localization equations in the presence of acoustic outliers or interspersed multipath returns.

path hypotheses. Assume for this illustration that the range is calculated with the direct path assumption. The dynamic temporal window filter then looks back at the range calculated with the direct path assumption during the previous timestep, time $t - 1$. The filter compares the $t - 1$ range to the time t range plus or minus the maximum possible distance traveled by the vehicle from time $t - 1$ to time t. If the direct path range from time $t - 1$ falls outside of this realm, then it is rejected as shown in Figure 4-31. The filter then looks back at the next earlier timestep, time $t - 2$, and performs a similar comparison. If the direct path range at $t - 2$ falls within the filter threshold boundaries, as shown in the illustration, then it is selected and the number of timesteps in the dynamic temporal window for that navigation cycle, $n_W(t)$, is 2. If the direct path range had fallen outside of the filter threshold boundaries, then the filter would have continued to step backwards in time until it found an acceptable range to use in the hypothesis generation process. The maximum number of timesteps that the filter will look at is set to 30, based on the judgment

116
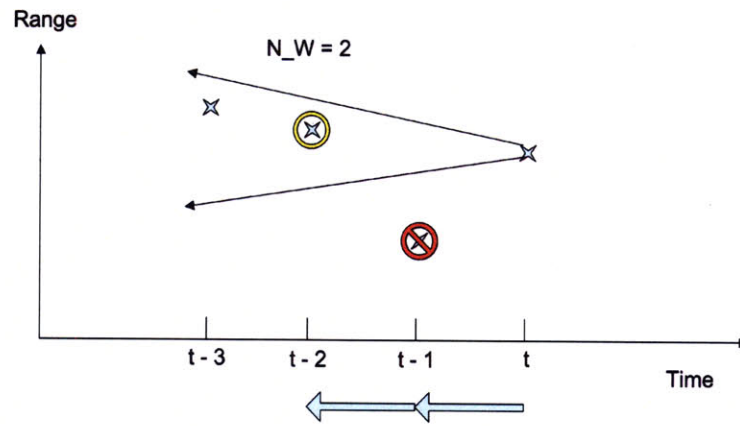
Figure 4-31: Design of a dynamic temporal window filter to reduce failures in pose localization equations.

of the author. For a ten-second navigation cycle, this corresponds to five minutes in time. As shown in Figure 4-31, the filter threshold boundaries grow as the filter looks backwards in time because the possible distance traveled by the vehicle is greater for a larger intervening time interval.

Chapter 5

The Arbitration Step: Incorporating Low-Resolution Bathymetric Data

The parallel hypothesis method uses a multi-level arbitration process. A nearest neighbor data association algorithm is implemented as the primary arbiter. However, if gridded information is available to the vehicle, an additional level is added on to the front end of the arbiter using this information. The grid arbiter block is based on a real-time comparison of *in-situ* values of some type of gridded information to *a priori* maps of the distribution of that type of information within the operating environment. Possible examples of gridded information include maps of bathymetry, magnetic field anomalies, gravitational constant variations, and seafloor composition.

The grid arbiter block designed as part of the proof of concept conducted for this research is based on bathymetry obtained using a ship-mounted Kongsberg-Simrad EM300 Multibeam Echo Sounder. The horizontal resolution of the EM300 bathymetric data available for the given operating areas is on the order of 50 meters, which is lower than the resolution of the vehicle's navigation solution. Therefore, this grid arbiter addresses the multiscale problem of navigating at a high resolution relative to

the lower resolution *a priori* depth maps. The approach used to address this problem within this research is to incorporate the relatively low-resolution bathymetric data into the PH architecture as negative information. In other words, instead of using the EM300 information to determine exactly where the vehicle is located, this information is used to determine where the vehicle is not located. As with the overall design of the PH method, this approach directly mimics the manner in which bathymetric data and depth soundings are assimilated into the navigation solution calculated by a human navigator.

5.1 Modeling the Environment

5.1.1 Low-Resolution Bathymetric Data

The *a priori* bathymetric data used within this research was collected with a Kongsberg-Simrad EM300 Multibeam Echo Sounder. The EM300 is a hull-mounted nominally 30 kHz multibeam sonar with an angular coverage sector of 150 degrees using 135 individual beams. The system has a maximum operating depth of 5000 meters, and the resolution provided by the one degree by one degree beams is 2% of water depth. The transducer arrays are arranged in a Mills Cross geometry with a longitudinal transmit array and a latitudinal receive array. The transmit fan has a piecewise attitude compensation mechanism that actively steers each discrete sector of the transmit fan to achieve a best-fit line perpendicular to the survey line. The two major components of the data collected by an EM300 system are bathymetry and backscatter [47, 28].

5.1.1.1 Bathymetry

Bathymetric measurements are computed by the EM300 using phase detection. The two-way travel time (TWTT), depression angle and azimuth of each individual beam are used to compute the water depth within that beam's seafloor footprint [55]. The EM300 system is calibrated to compensate for many of the errors inherent to the

transmission of acoustic signals in seawater. However, even a calibrated system's response does not always match the calibration curve due to a number of additional possible error sources.

One possible source of error is the presence of seabed targets that are smaller than the footprint of an individual EM300 beam and the effect of those small targets on water depth measurements. Clark et al. [12] have shown that the phase distortion created by these small targets is generally averaged out in the bathymetric calculations.

As with the acoustic time-of-flight range measurements, another possible source of error is the sound velocity profile information that is input into the system prior to operations. A CTD cast is taken prior to EM300 operations, but CTD casts are linear measurements in a complex three-dimensional environment and the resulting sound velocity profiles cannot capture the full range of variability within the environment. Furthermore, the ray bending problem discussed in Chapter 4 can also distort the phase difference calculations of a multibeam sonar. Therefore, another source of possible error is that the real-time SVP information required for accurate beamforming is not available *in situ* [81].

Within the scope of this research, there was no capability to empirically test the achieved accuracy of the EM300 bathymetry data. A field test report on the EM300 by Kasantsev et al. [44] lists the root-mean-square accuracy of the EM300 under ideal conditions to be 0.2% of water depth for beams from vertical to 45 degrees, 0.3% of water depth for beams up to 60 degrees, and 0.5% of water depth for beams from 60 degrees to 70 degrees. However, since it is unknown under what exact conditions the *a priori* EM300 data used in this research were obtained, a conservative root-mean-square measurement accuracy of < 1% of water depth was adopted for this research. It is left to future research to test and refine this assumption.

5.1.1.2 Backscatter

One major component of the data collected by an EM300 is backscatter strength which is computed through amplitude detection. Backscatter strength is the ratio of the intensity in the received return acoustic wave over the intensity of the original transmitted acoustic signal. Backscatter strength is a useful metric because it provides information regarding the geometry of rough interfaces and the material properties of the ocean floor [55, 81]. This information could be incorporated into future grid arbiters, however the scope of this research focused solely on the bathymetric data obtained through the EM300.

5.1.2 Vehicle Depth and Altitude

Depth of the water column at any instantaneous location of the vehicle is measured as the sum of vehicle depth, vehicle altitude and an offset based on the relative location of the sensors, as given by Equation 5.1.

$$WD_{obs}(t) = Alt_{AUV}(t) + d_{AUV}(t) + \delta(t) \tag{5.1}$$

where

$WD_{obs}(t) \equiv$ Depth of the water column observed by the vehicle,

$Alt_{AUV}(t) \equiv$ Altitude of the vehicle,

$d_{AUV}(t) \equiv$ Depth of the vehicle, and

$\delta(t) \equiv$ Vertical offset between vehicle depth and altitude sensors.

The offset term due to the relative equipment installation heights, $\delta(t)$, is time varying based on the instantaneous vehicle attitude. However, the resulting sub-meter time-varying error is at least an order of magnitude smaller than the root-mean-square
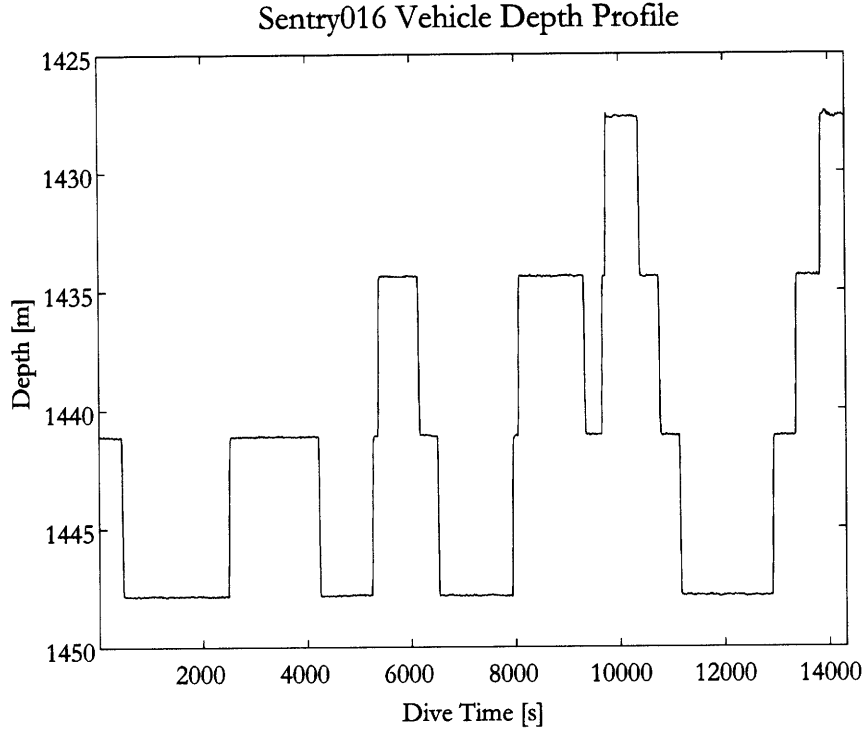
Figure 5-1: Sentry016 vehicle depth profile.

errors in the bathymetric data as discussed below in Section 5.2.3. Therefore, the additional error introduced by the time variability of this offset term is neglected and the offset term is assumed to be constant, δ, within the scope of this research.

Vehicle depth on both vehicles is measured *in situ* by a Paroscientific Inc. sensor. See, for example, the Sentry016 depth profile shown in Figure 5-1. The sensor calculates the depth as a function of the observed gauge pressure. See Appendix B for a detailed explanation of this calculation. The error in this depth measurement is on the order of 0.01% of overall depth. For the 6000-meter rated sensors used on ABE and Sentry, this corresponds to errors on the order of less than one meter which is again insignificant in comparison to the error in the EM300 bathymetric data.

Each platform uses an RDI Instruments Workhorse Navigator DVL to determine the *in-situ* altitude of the vehicle over ground. Using a pattern of four downward-looking beams, the DVL measures range to the bottom from the vehicle. See, for example, the Sentry016 altitude profile shown in Figure 5-2. Each of the AUVs
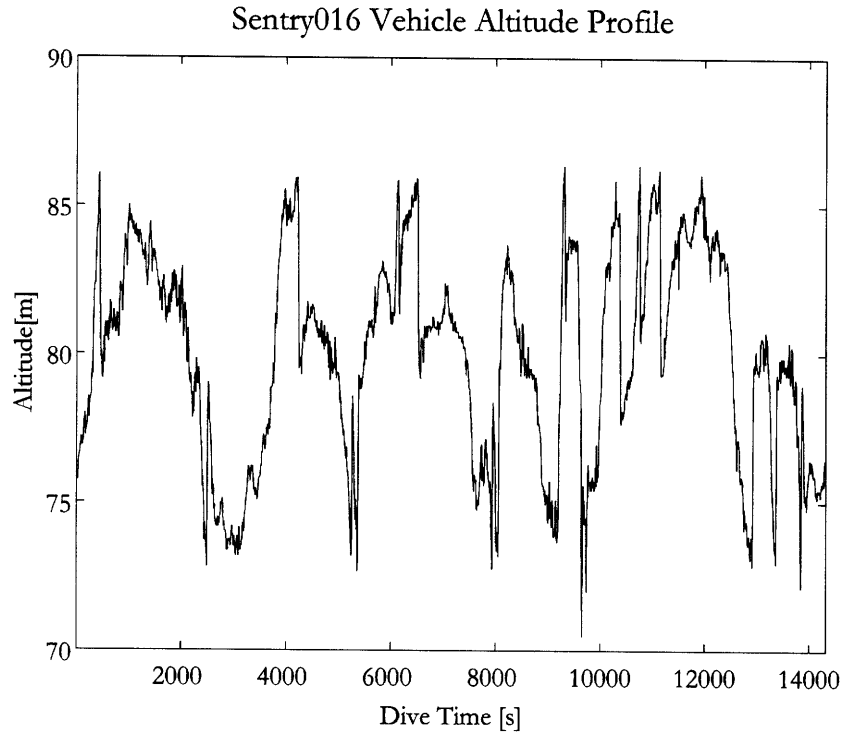
Figure 5-2: Sentry016 vehicle altitude profile.

is equipped with a high-resolution multibeam sonar which could also be used to determine the *in-situ* vehicle altitude, but this adaptation is left to future work. Once again, the errors of the altitude measurement are on the order of less than one meter and are therefore neglected within the scope of this research.

An example of the observed water column depth calculated using Equation 5.1 is shown in Figure 5-3.

5.2 Designing the Grid Arbiter Block

The goal of the grid arbiter is two-fold. First, it reduces the *in-situ* computational burden by quickly eliminating any hypothesis whose mapped water depth falls outside the acceptable depth range given the *in-situ* observations of water depth. The computational complexity of the grid arbiter is minimal. With a single point comparison, at each timestep for each hypothesis, only seven computations are required.

124
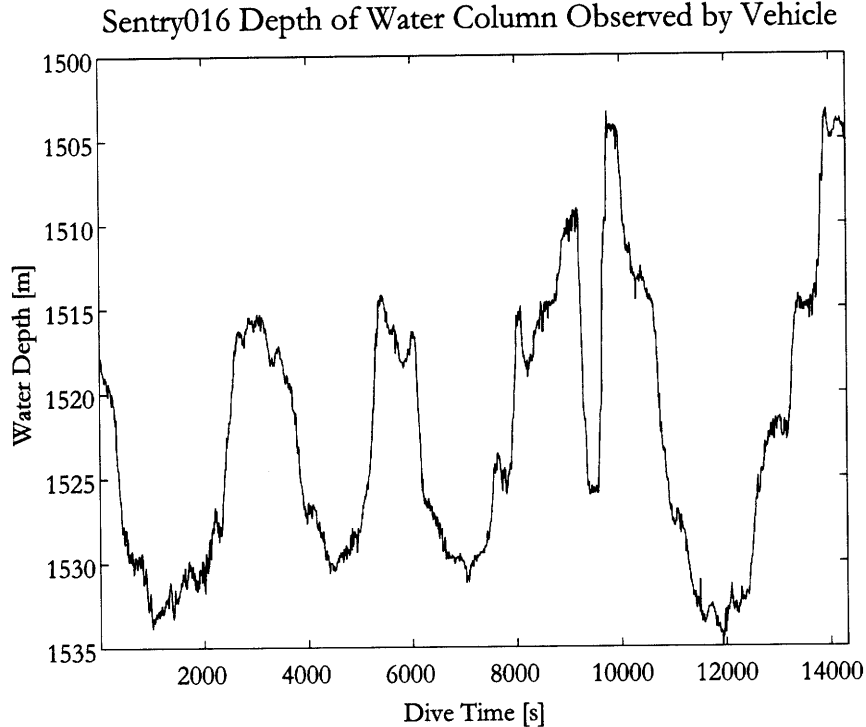
Figure 5-3: Sentry016 depth of water column as observed *in situ* by the vehicle.

Even with the inclusion of the nine-point voting scheme, the computational burden per hypothesis is still only sixteen total computations.

The second goal of the grid arbiter is the long-term objective of having enough grid arbiter filters to completely decouple the arbitration and the pose estimation processes. By correctly eliminating all the erroneous hypotheses while preserving the true hypothesis via the grid arbiter process, the nearest neighbor data association becomes unnecessary except for the threshold gating process.

5.2.1   Basic Design

The vehicle pose parallel hypotheses generated using the LOP observations are input directly into the grid arbiter, as shown in Figure 5-4. As shown in Equation 5.2, the grid arbiter eliminates any of the hypotheses whose *a priori* mapped EM300 water depth value differs from the *in-situ* observed water depth by more than an acceptable

125
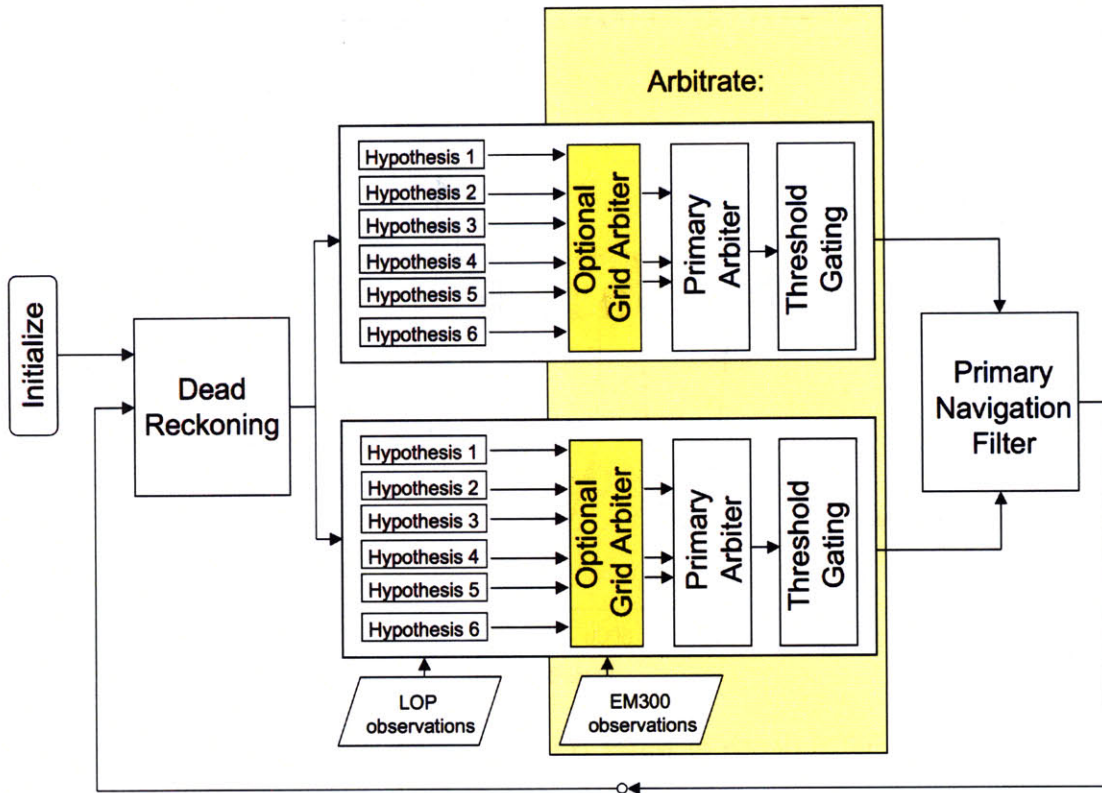
Figure 5-4: Grid arbiter location within the architecture of the parallel hypothesis navigation algorithm.

error threshold as discussed in Section 5.2.3.

$$\varepsilon(t, \tilde{\mathbf{x}}_i(t)) = |WD_{obs}(t) - WD_{EM300}(\tilde{\mathbf{x}}_i(t))| \qquad (5.2)$$

where

$$\varepsilon(t, \tilde{\mathbf{x}}_i(t)) \equiv \text{Difference between observed and mapped water depths,}$$

$$WD_{obs}(t) \equiv \text{Depth of the water column observed by the vehicle,}$$

$$WD_{EM300}(\tilde{\mathbf{x}}_i(t)) \equiv \text{Mapped water depth at hypothesis } i \text{ vehicle pose, and}$$

$$\tilde{\mathbf{x}}_i(t) \equiv \text{Vehicle pose hypothesis } i.$$

To mitigate the errors created when a pose hypothesis is located adjacent to the edge of a particular depth cell of the EM300 map, a nine-point voting scheme is used to calculate $WD_{EM300}(\tilde{\mathbf{x}}_i(t))$, as shown in Figure 5-5. $WD_{EM300}(\tilde{\mathbf{x}}_i(t))$ is calculated as the mean of the charted EM300 water depths at each of these nine points.

5.2.2   Modeling the Uncertainty

Research into quantitative seafloor characterization by Stewart et al. [81] concluded that high-frequency components of the seafloor can often be characterized by Gaussian statistics. They conducted their research in three distinct geological provinces of the Juan de Fuca Ridge, which incidentally is the same operating area for the real-world AUV data used within this research. Stewart et al. found that the statistical distribution of the bathymetry of relatively flat-bottomed areas could be satisfactorily described by Gaussian statistics. Areas with more complex underwater terrain resulted in multimodal stochastic distributions, but when this data was detrended to remove the low-spatial-frequency components, the detrended data followed Gaussian distributions. Therefore, for this research, a Gaussian error model is assumed for the high-frequency variability of bathymetric data.

Any multibeam data contains bad detections, or fliers, that are typically removed by automated or hand editing. Any fliers that pass the filters are mitigated by the gridding process. Therefore, for this analysis, these errors are ignored.

127
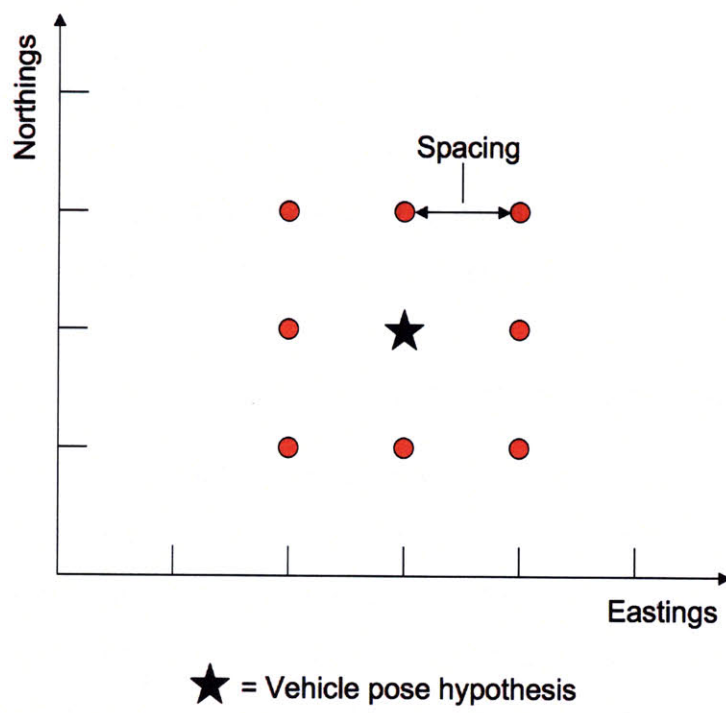
Figure 5-5: Illustration of the nine-point voting scheme centered on the vehicle pose hypothesis.

Table 5.1: Gaussian distribution confidence intervals.

Number of Standard Deviations	Confidence Interval Percentage
1	68.2689
2	95.4499
3	99.7300
4	99.9936
5	99.9999

5.2.3   Choosing an Error Threshold

The high-variability error of the EM300 bathymetric data is assumed to follow a Gaussian distribution as discussed in the previous section. Therefore, the selection of an appropriate allowable error factor within the grid arbiter is made using standard Gaussian distribution error function tables, as excerpted in Table 5.1.

The purpose of the grid arbiter is to eliminate definitively erroneous position hypotheses while ensuring that the true hypothesis is among the group of hypotheses that successfully pass from the grid arbiter into the main arbiter. Therefore, the design decision was made to allow an error factor of five standard deviations to achieve a 99.9999% confidence interval, as shown in Table 5.1. Based on the assumed root-mean-square system accuracy for the EM300 of 1% of water depth, as discussed in Section 5.1.1.1, the acceptable error threshold in the current design of the grid arbiter is within five percent of mapped water depth.

The following series of figures illustrates the threshold choice for two Sentry dives. Sentry016 was conducted over relatively flat terrain, as shown in Figure 5-6. The *in-situ* observed water depth compared to the corresponding EM300 *a priori* depths are shown in Figures 5-7 and 5-8 along with 3σ and 5σ error thresholds, respectively.

In comparison, Sentry014 and Sentry015 were conducted over terrain with a steep gradient, as shown in Figure 5-9. The *in-situ* observed water depth compared to the corresponding EM300 *a priori* depths for Sentry015 are shown in Figures 5-10 and

5-11 along with 3σ and 5σ error thresholds, respectively.

5.2.4 Research Assumptions

Assumptions were made about the EM300 system vertical accuracy as discussed in Section 5.1.1.1. Furthermore, the assumption was made that the horizontal error in the EM300 data was negligible. Future design iterations of the grid arbiter could test these assumptions and improve upon the error model.

Another assumption implicit in this research is that whatever type of gridded information is used, the local distribution of that information remains constant between the *a priori* map generation through the completion of dive operations within the fixed error tolerance. Dynamic predictions of temporal variability are not included in the current design of the grid arbiter and would be left to future work. This work could be done in conjunction with the design of the grid arbiter blocks for other types of gridded information that experience a higher rate of temporal variability.
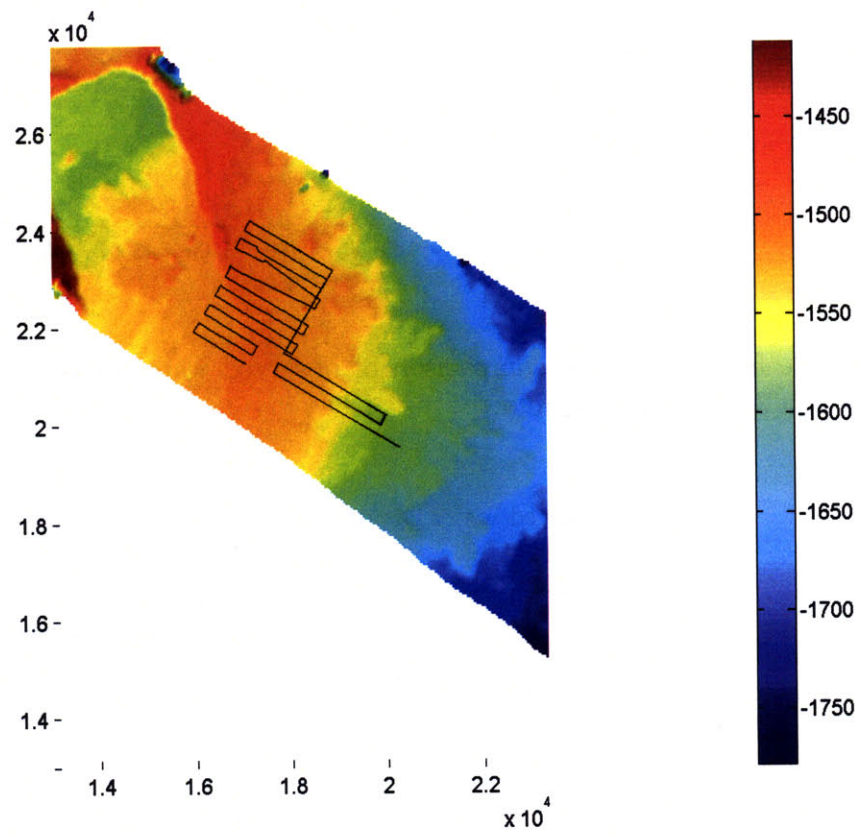
Figure 5-6: Sentry016 tracklines and the *a priori* EM300 bathymetric map.

Observed Water Depth Compared to EM300 Water Depth
Sentry016, 3 c Threshold
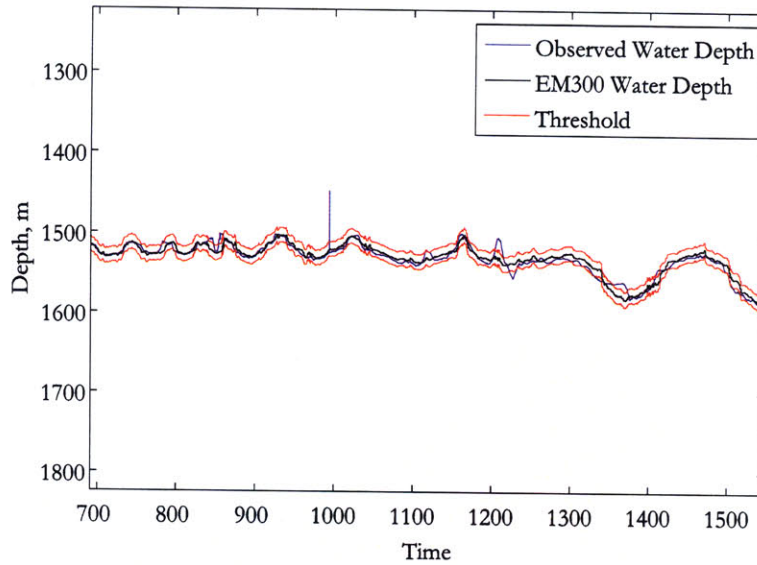
Figure 5-7: Sentry016 comparison of observed water depth to EM300 water depth with a 3σ gating threshold.

Observed Water Depth Compared to EM300 Water Depth
Sentry016, 5 c Threshold
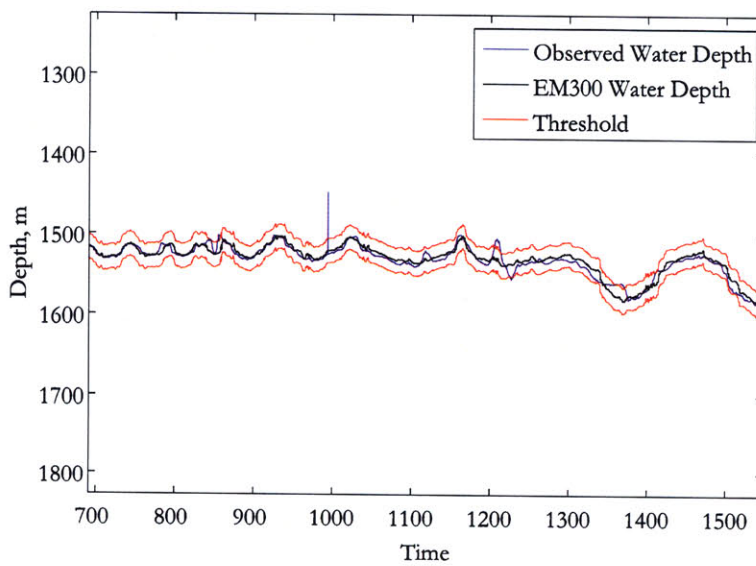
Figure 5-8: Sentry016 comparison of observed water depth to EM300 water depth with a 5σ gating threshold.
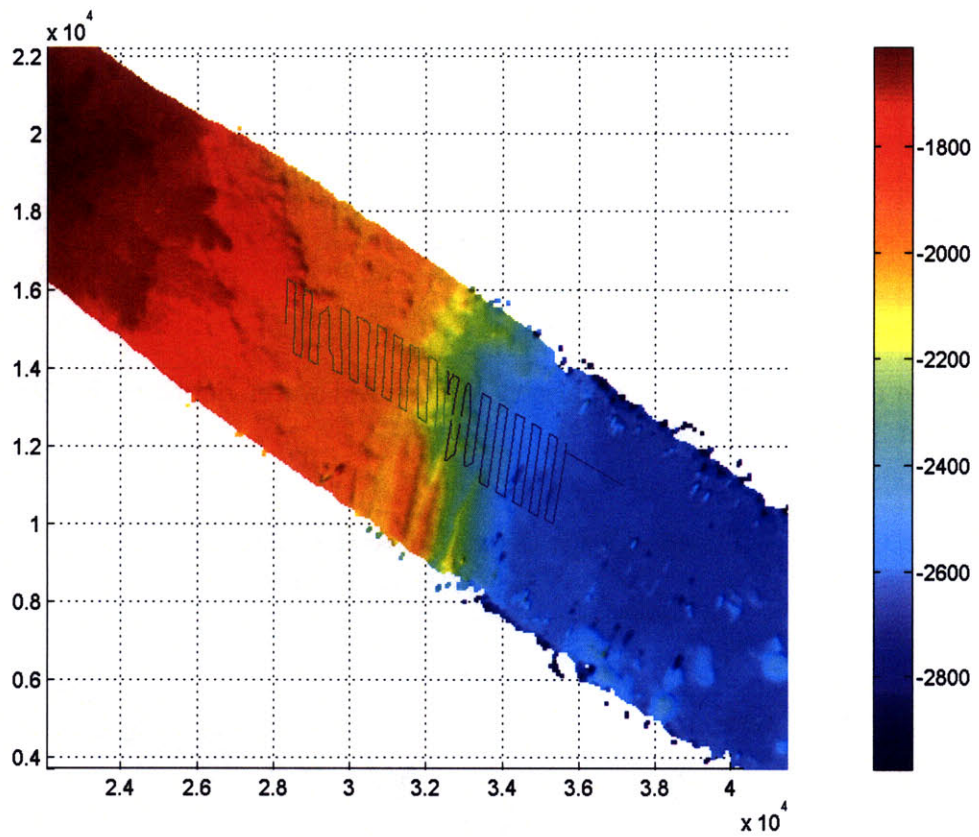
Figure 5-9: Sentry014 and Sentry015 tracklines and the *a priori* EM300 bathymetric map.
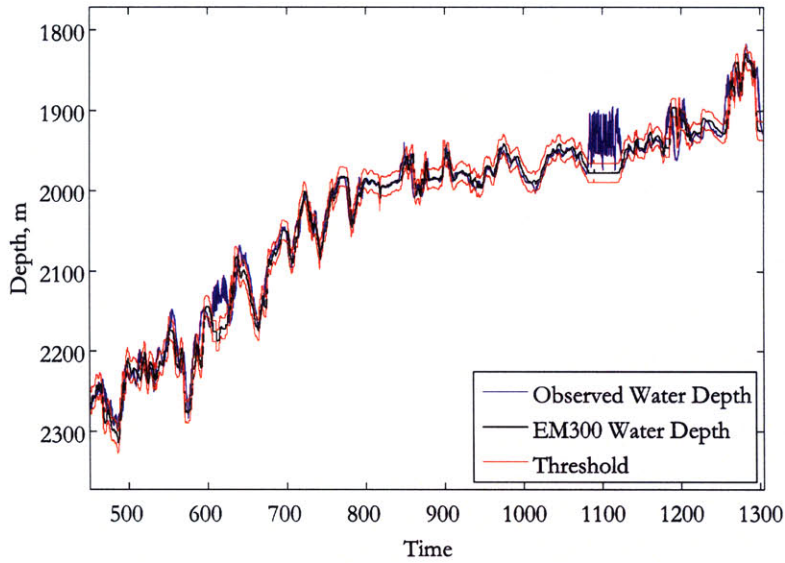
Figure 5-10: Sentry015 comparison of observed water depth to EM300 water depth with a 3σ gating threshold.
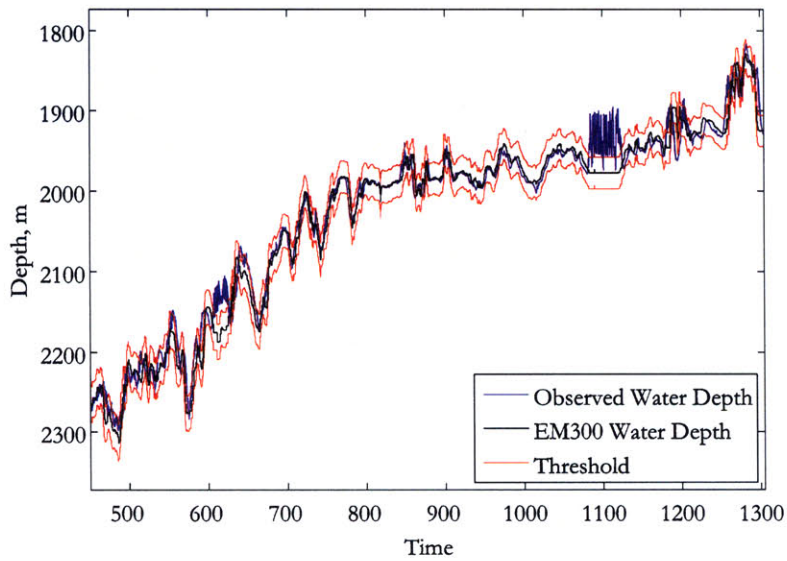
Figure 5-11: Sentry015 comparison of observed water depth to EM300 water depth with a 5σ gating threshold.

Chapter 6

Real-World Data Collection

A proof of concept of the PH navigation algorithm was conducted using data from real-world operations of the AUVs, ABE and Sentry, on the Juan de Fuca Ridge in 2005 and 2008, respectively.

6.1 Platforms

6.1.1 ABE

6.1.1.1 History

The Autonomous Benthic Explorer (ABE) AUV was designed to conduct precise sea bottom survey work at ocean depths in excess of 4000 meters. ABE was created to meet the scientific need of conducting repeated surveys of deep ocean hydrothermal vent regions. To fulfill this capabilities requirement, ABE was built and tested in the early 1990's at the Woods Hole Oceanographic Institution (WHOI) under National Science Foundation (NSF) sponsorship. As seen in Figure 6-1, ABE is a tri-body vehicle with thrusters on the aft of each body. This vehicle configuration gives it good controllability and makes ABE a good platform to conduct precision bathymetric mapping missions. Additionally, its low power consumption allows it to conduct
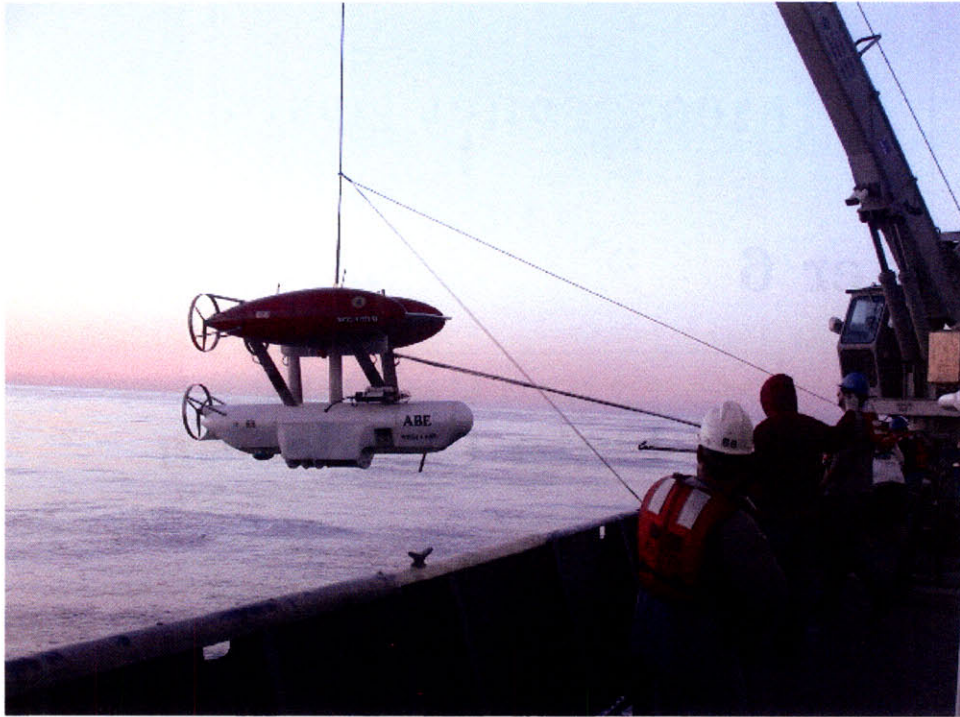
Figure 6-1: ABE being recovered after a dive on the Juan de Fuca Ridge. Photo by D. Yoerger.

long-duration dives that can last more than a day. Since conducting its first scientific mission at the Juan de Fuca Ridge in 1996, ABE has successfully completed 220 operational dives to date in operating areas worldwide and is part of the National Deep Submergence Facility (NDSF) at WHOI [96, 97, 98, 99, 100, 101, 102, 103, 104, 105, 106, 108, 109].

6.1.1.2 Sensors

During the scientific dives of 2005 used in this research, ABE was outfitted with the following, noncomprehensive list of sensors: [107].

- SIMRAD SM2000 200 kHz multibeam sonar

- RDI 300 kHz Workhorse Navigator Doppler Velocity Log (DVL)

- TCM2 magnetic compass

- SeaBird SBE3 and SBE4 conductivity/temperature sensors

- Paroscientific pressure sensor

- SeaPoint optical backscatter (OBS) sensor

- Acoustic transceiver

6.1.2   Sentry

6.1.2.1   History

The Sentry AUV was designed and built at WHOI as a successor to ABE. It was created to continue the precision bathymetric mapping mission with increased performance provided by a greater depth limit, longer endurance, more powerful multibeam sonar, and an improved bottom-following capability. As seen in Figure 6-2, Sentry is a single-body vehicle with four thrusters mounted on fore and aft rotating control planes, or foils. The fore and aft foils rotate independently of each other, thus providing excellent dynamic maneuverability. The unique and hydrodynamically-efficient hull design of the Sentry AUV was initially inspired by the *mola mola*, or ocean sunfish, that are often seen basking at the ocean's surface. After undergoing its at-sea engineering trials in 2007 and 2008, Sentry deployed for its first scientific cruise in July 2008, completing sixteen ocean dives to date [91].

6.1.2.2   Sensors

During the relevant dives for this research, Sentry was outfitted with the following, noncomprehensive list of sensors: [110]

- Reson 7125 400 kHz multibeam sonar

- RDI 300 kHz Workhorse Navigator Doppler Velocity Log (DVL)

- IXSEA Phins Inertial Navigation System (INS)
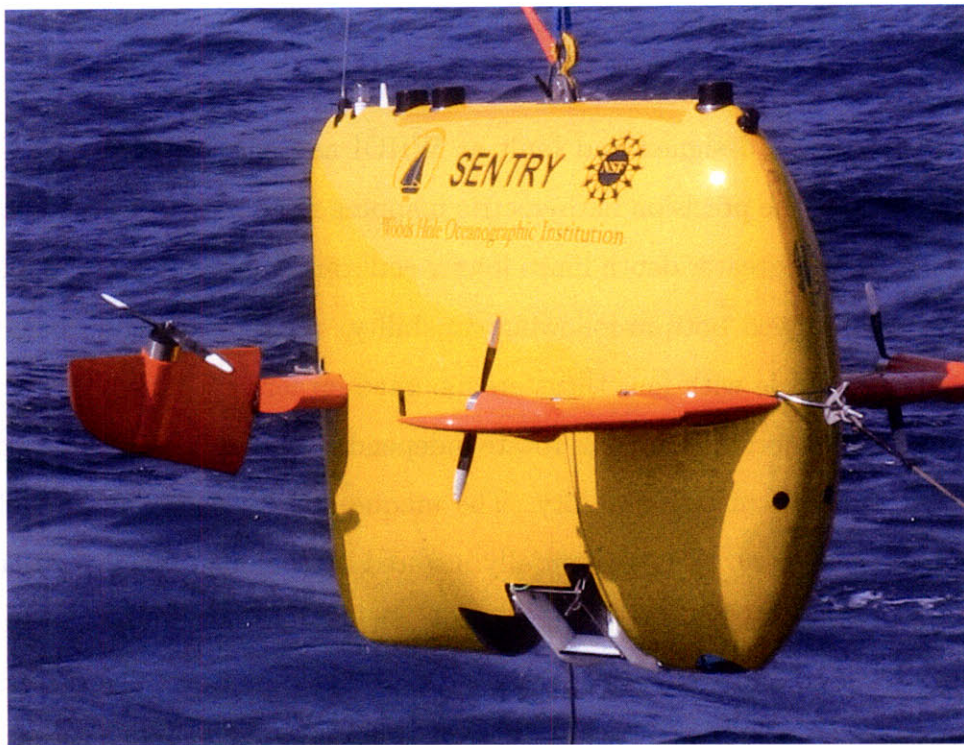
Figure 6-2: Sentry during at-sea engineering trials in August 2008. Photo by C. LaPointe.

- TCM2 magnetic compass

- Neil Brown Ocean Sensors Inc. Conductivity and Temperature sensors

- ParoScientific 8B7000-I Digiquartz pressure sensor

- Dual 3-Axis Honeywell smart digital magnetometers

- Acoustic transceiver

6.2 Missions

6.2.1 ABE Visions05 Cruise

In October 2005, ABE was deployed aboard the R/V *Thomas G. Thompson* on the Visions05 expedition to the Juan de Fuca Ridge with chief scientists John Delaney and Deborah Kelley. ABE made a total of ten dives during the expedition for the purpose of creating detailed bathymetric maps of the Endeavour region of the Juan de Fuca Ridge. The Endeavour region is volcanic in nature with water depth varying between approximately 1900 and 2350 meters. It is a diverse underwater terrain with the bathymetry varying from extreme depth gradients to swaths of relatively flat bottom. The remotely operated vehicle (ROV) Jason2 was also embarked on the Visions05 expedition. During most of the ABE dives on this cruise, Jason2 was also in the water. Occasionally this resulted in acoustic travel time interference when either Jason2 or its elevator were interrogating the same transponder network off of which ABE was navigating [107].

6.2.1.1 ABE160

The dive tracklines for ABE160 are shown in Figure 6-3, where these tracklines were determined as the best estimate of vehicle location through post-processing of the LBL and DVL information. The raw acoustic two-way travels times are shown in Figure 6-4 and the observed water depth profile is shown in Figure 6-5.

During most of this dive, two of the transponders were too far away to get direct path returns during the correct navigation cycle as shown in Figure 6-4. Also during ABE160 Jason2 or its elevator were periodically interrogating the LBL network creating the appearance of structured noise in the acoustic data [107].

ABE160 Transponder Positions

Figure 6-3: ABE160 tracklines and transponder locations.

Raw Two Way Acoustic Times of Flight
ABE160

Figure 6-4: ABE160 raw two-way acoustic travel times.

ABE160 Depth of Water Column Observed by Vehicle
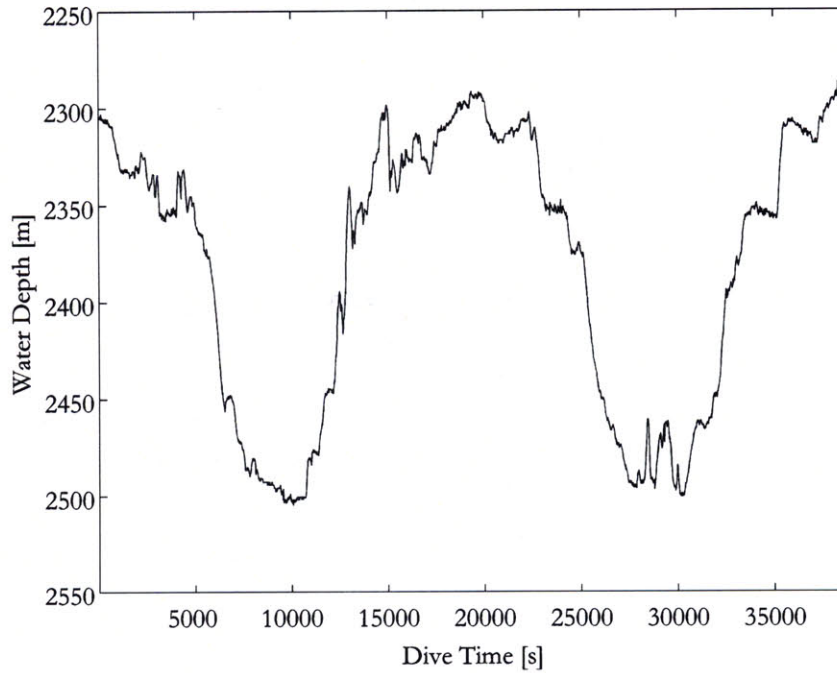
Figure 6-5: ABE160 observed water depth profile.

6.2.1.2 ABE161

The dive tracklines for ABE161 are shown in Figure 6-6, where these tracklines were determined as the best estimate of vehicle location through post-processing of the LBL and DVL information. The raw acoustic two-way travels times are shown in Figure 6-7 and the observed water depth profile is shown in Figure 6-8.

All systems worked well for ABE161 with relatively clean acoustic returns through the dive. There were extended periods where no direct path returns were available on the different transponders and triangle and double bounce path returns were prevalent, as seen in Figure 6-7 [107].

Figure 6-6: ABE161 tracklines and transponder locations.

Raw Two Way Acoustic Times of Flight
ABE161

Figure 6-7: ABE161 raw two-way acoustic travel times.

ABE161 Depth of Water Column Observed by Vehicle
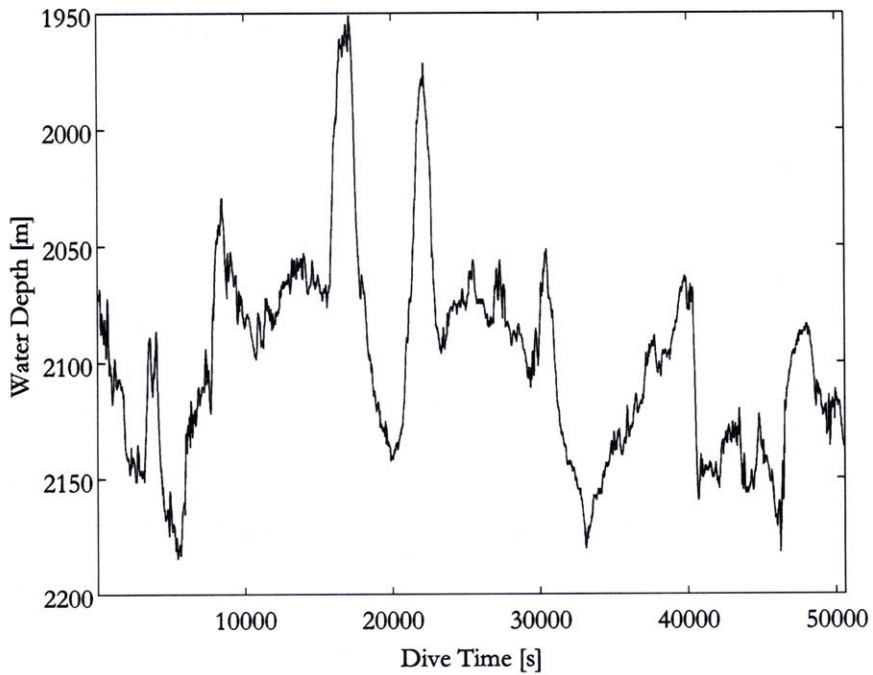
Figure 6-8: ABE161 observed water depth profile.

6.2.1.3 ABE162

The dive tracklines for ABE162 are shown in Figure 6-9, where these tracklines were determined as the best estimate of vehicle location through post-processing of the LBL and DVL information. The raw acoustic two-way travels times are shown in Figure 6-10 and the observed water depth profile is shown in Figure 6-11.

ABE162 was a multipurpose dive with a complicated trackline, designed to fill a gap in the coverage from earlier dives; to survey a large area on the south side of the Summit Seamount; and finally to do a detailed, low-altitude survey over a small area to the east. The dive went smoothly with no engineering failures, however there was some acoustic interference due to Jason2 operations as discussed previously [107].
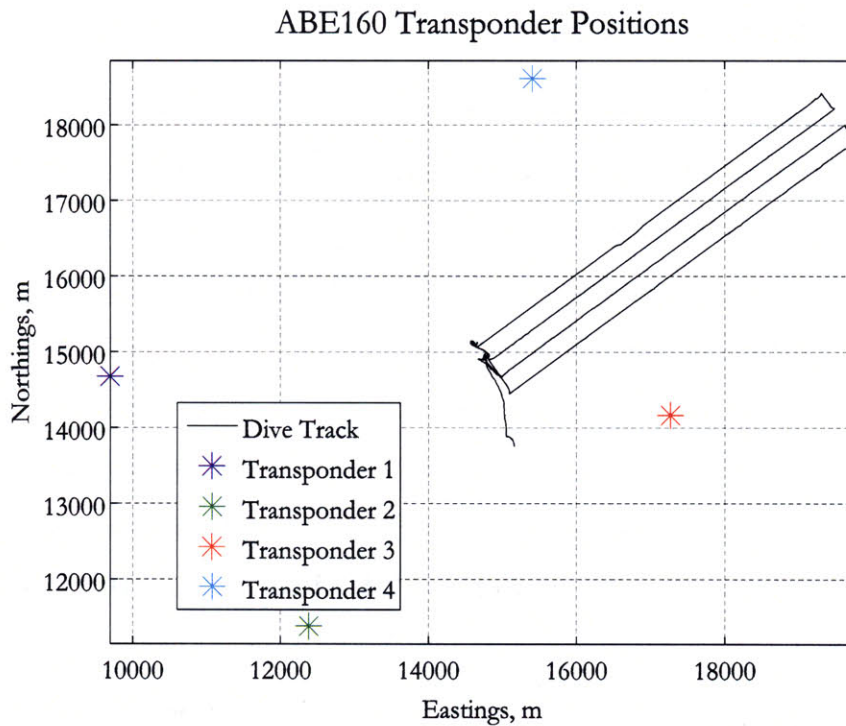
ABE162 Transponder Positions

Figure 6-9: ABE162 tracklines and transponder locations.

Raw Two Way Acoustic Times of Flight
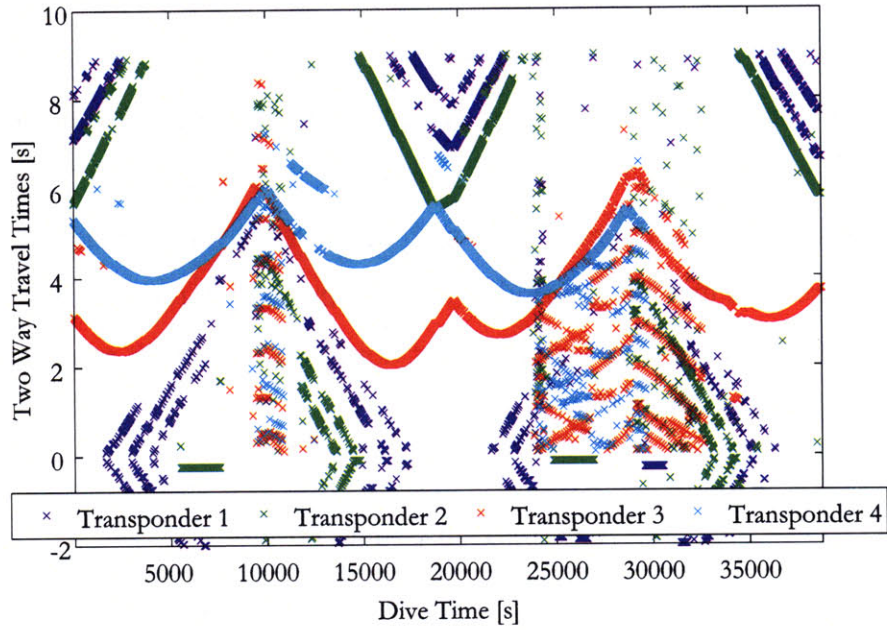## ABE162

Figure 6-10: ABE162 raw two-way acoustic travel times.

## ABE162 Depth of Water Column Observed by Vehicle
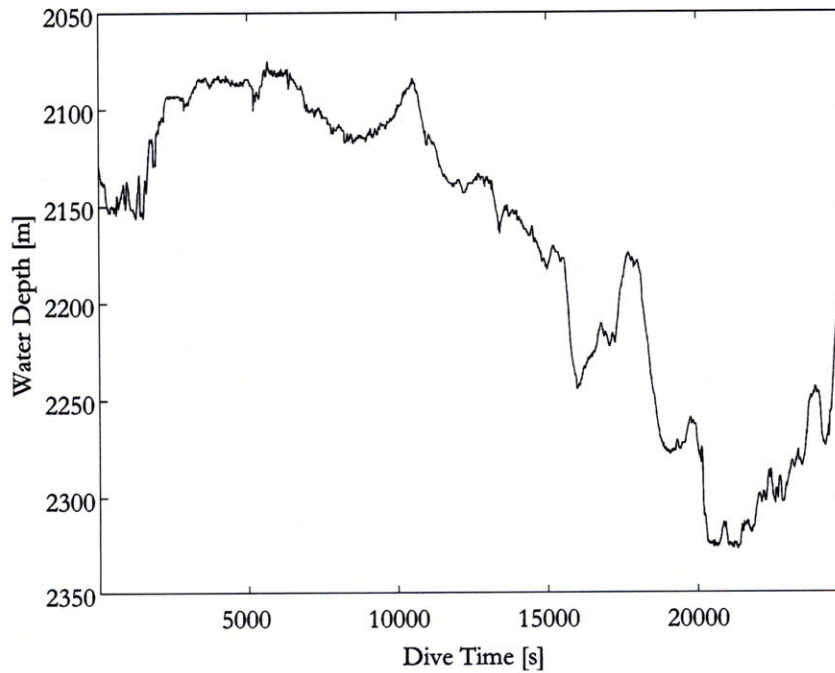
Figure 6-11: ABE162 observed water depth profile.

145

6.2.1.4 ABE163

The dive tracklines for ABE163 are shown in Figure 6-12, where these tracklines were determined as the best estimate of vehicle location through post-processing of the LBL and DVL information. The raw acoustic two-way travels times are shown in Figure 6-13 and the observed water depth profile is shown in Figure 6-14.

ABE163 was a dive with long tracklines running parallel to the depths contours on either side of an axial valley south of the Summit Seamount. This dive was smooth and successful with near-continuous acoustic returns from all transponders and no engineering failures during the dive. There was no noticeable acoustic interference from Jason2 operations [107].
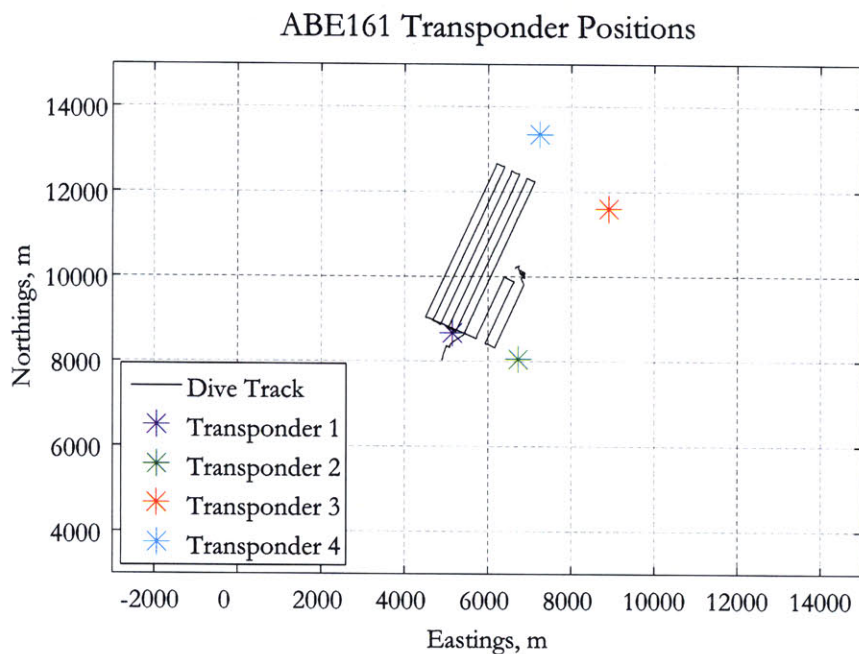
Figure 6-12: ABE163 tracklines and transponder locations.

146

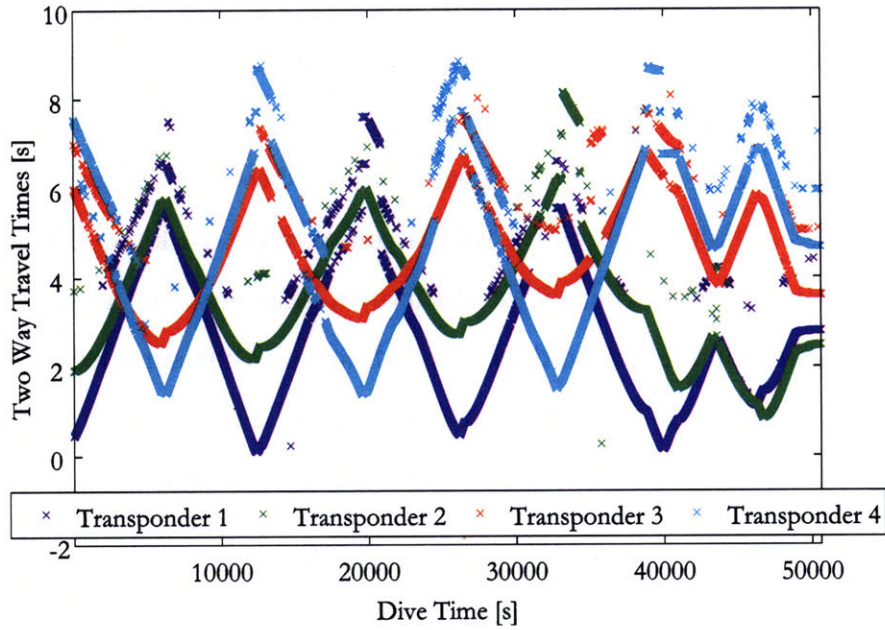## Raw Two Way Acoustic Times of Flight
ABE163

Figure 6-13: ABE163 raw two-way acoustic travel times.

ABE163 Depth of Water Column Observed by Vehicle
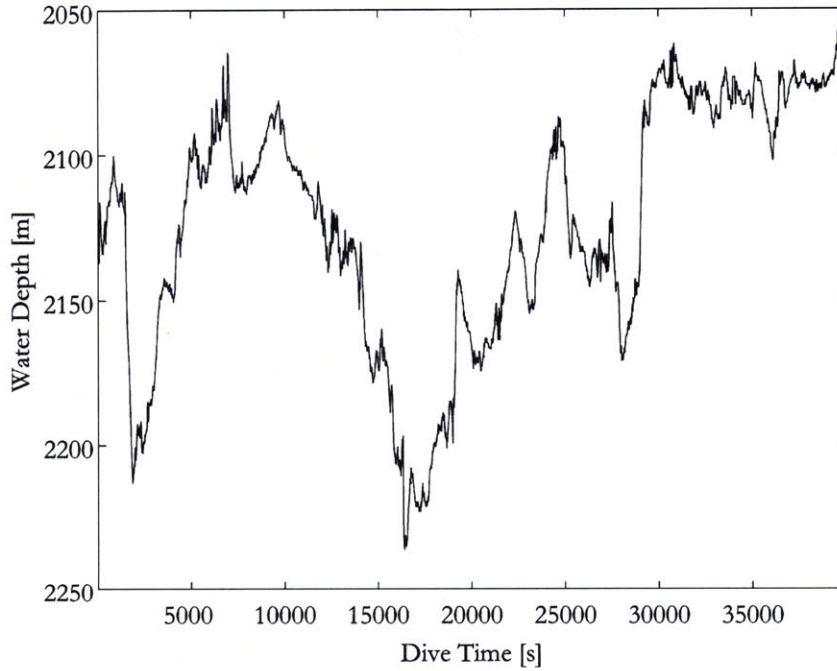
Figure 6-14: ABE163 observed water depth profile.

147

6.2.1.5   ABE164

The dive tracklines for ABE164 are shown in Figure 6-15, where these tracklines were determined as the best estimate of vehicle location through post-processing of the LBL and DVL information. The raw acoustic two-way travels times are shown in Figure 6-16 and the observed water depth profile is shown in Figure 6-17.

The ABE164 survey dive ended early because ABE became entangled in a piece of 1/4" polypropylene line that was anchored to the sea floor. The acoustic returns that were received during the dive are shown in Figure 6-16 [107].

Figure 6-15: ABE164 tracklines and transponder locations.

Raw Two Way Acoustic Times of Flight
ABE164

Figure 6-16: ABE164 raw two-way acoustic travel times.

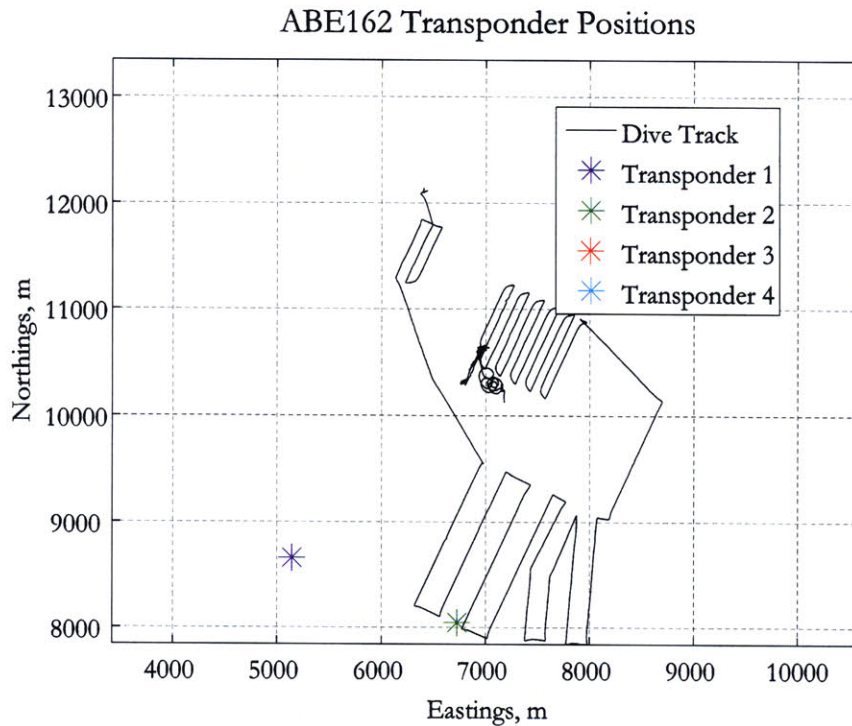ABE164 Depth of Water Column Observed by Vehicle
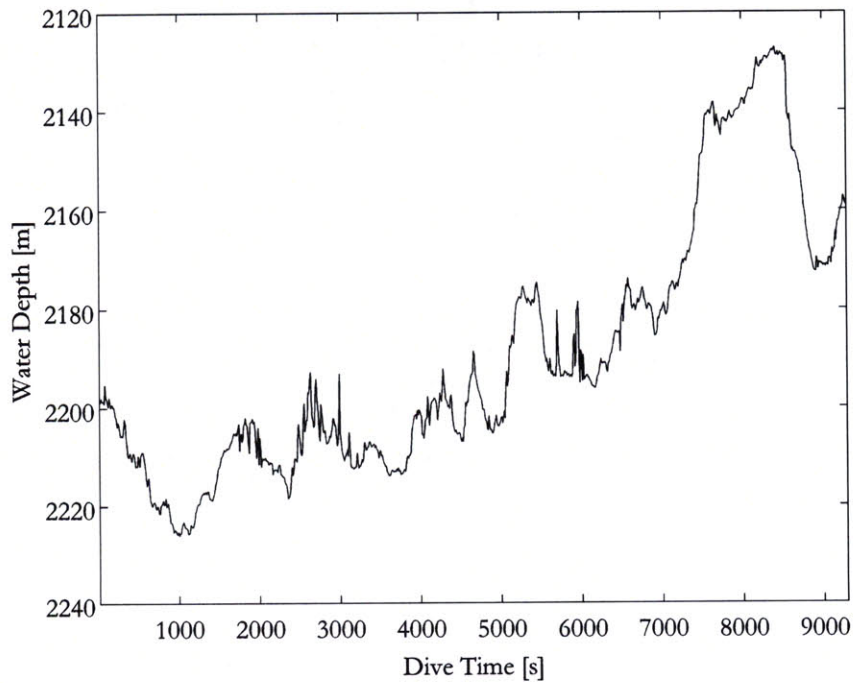
Figure 6-17: ABE164 observed water depth profile.

6.2.1.6 ABE165

The dive tracklines for ABE165 are shown in Figure 6-18, where these tracklines were determined as the best estimate of vehicle location through post-processing of the LBL and DVL information. The raw acoustic two-way travels times are shown in Figure 6-19 and the observed water depth profile is shown in Figure 6-20.

During most of ABE165, the acoustic returns were relatively clean. However, there were periods of structured noise when Jason2 or its elevator were interrogating the same LBL net. These interrogations were made on a regular cycle time so the noise that they created appears structured rather than random in the ABE data [107].
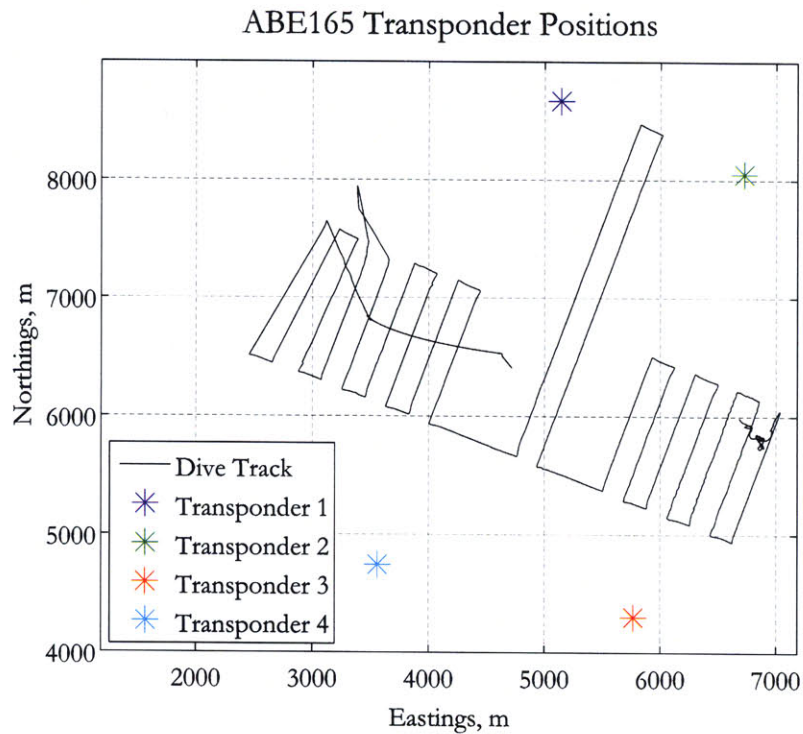
Figure 6-18: ABE165 tracklines and transponder locations.

150

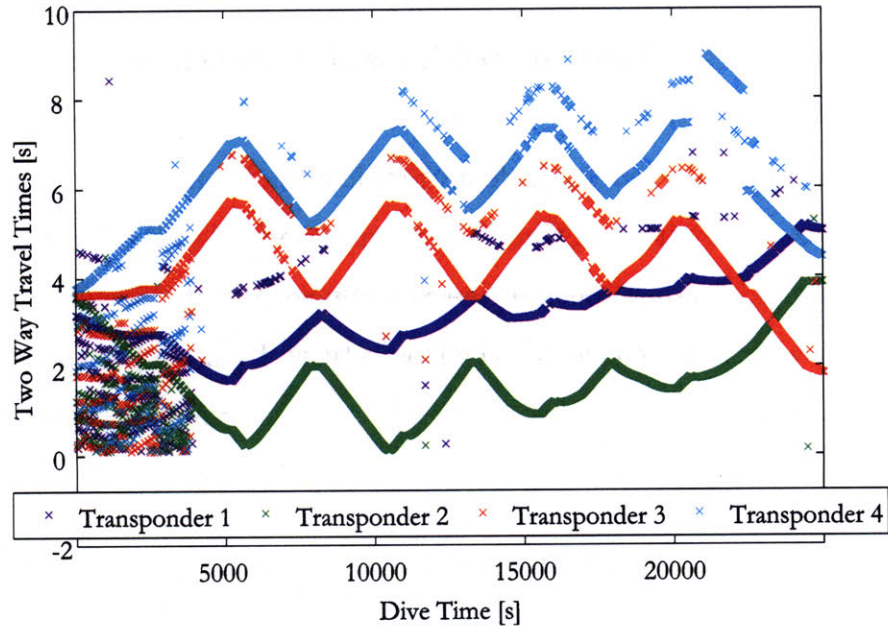## Raw Two Way Acoustic Times of Flight
ABE165
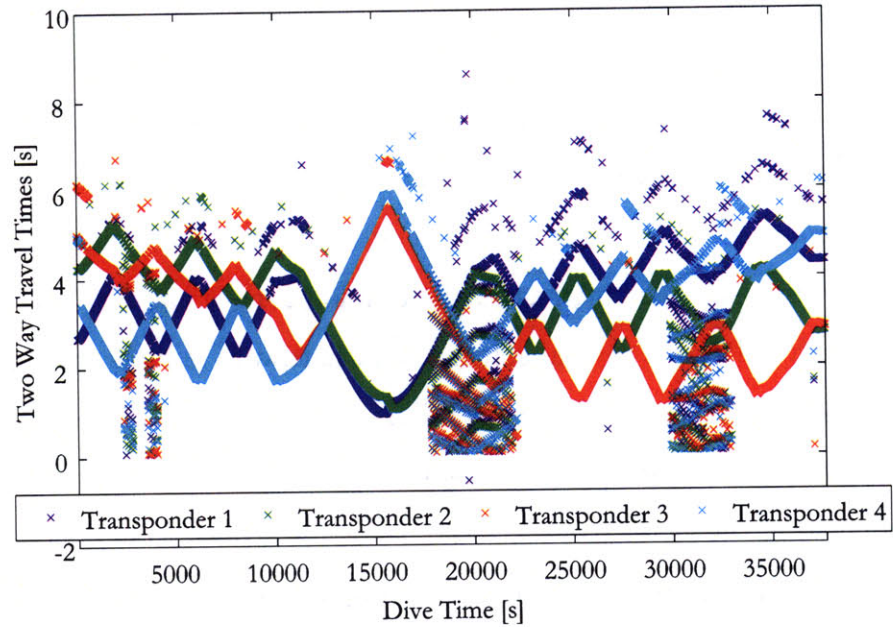
Figure 6-19: ABE165 raw two-way acoustic travel times.

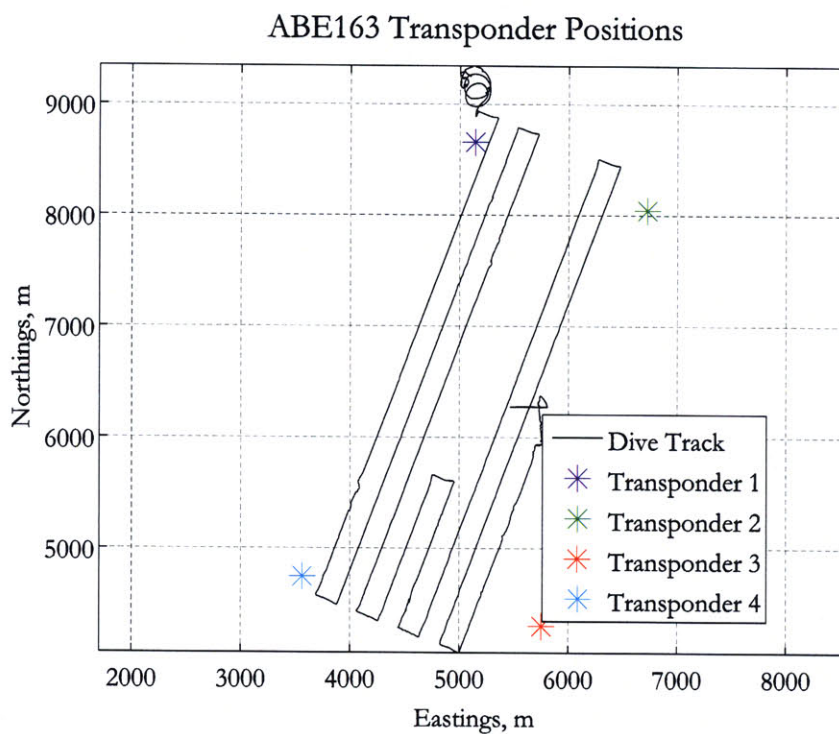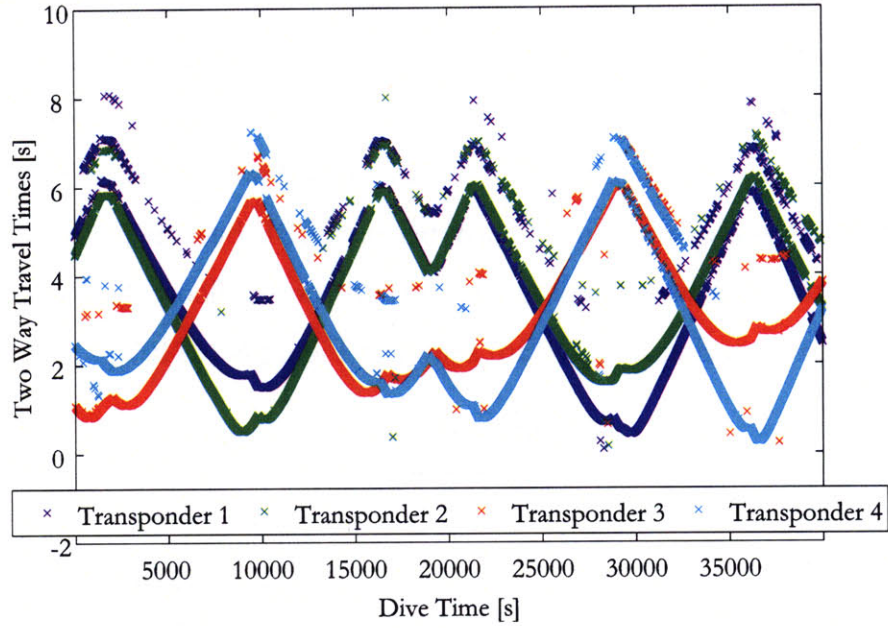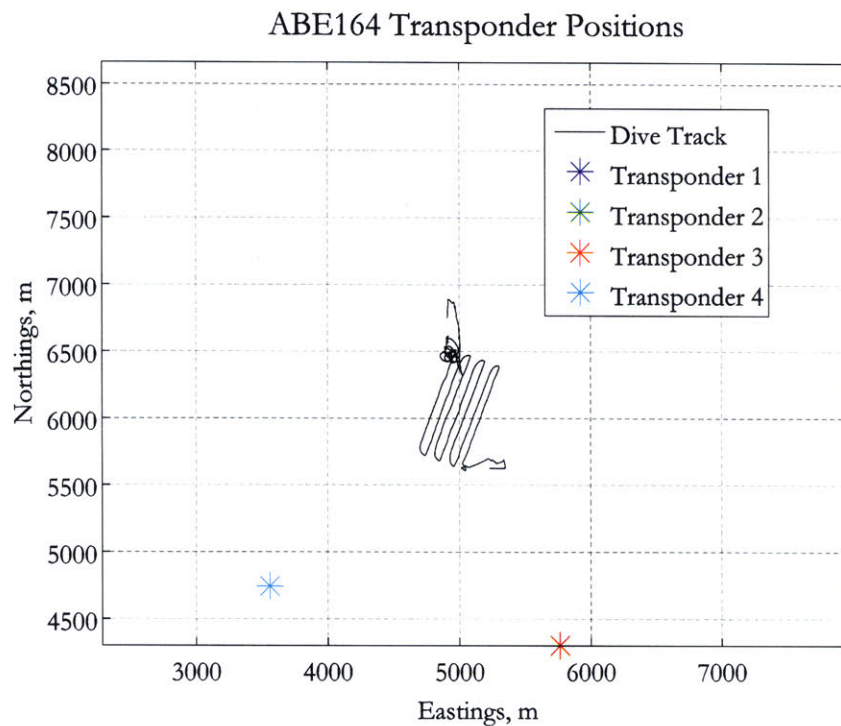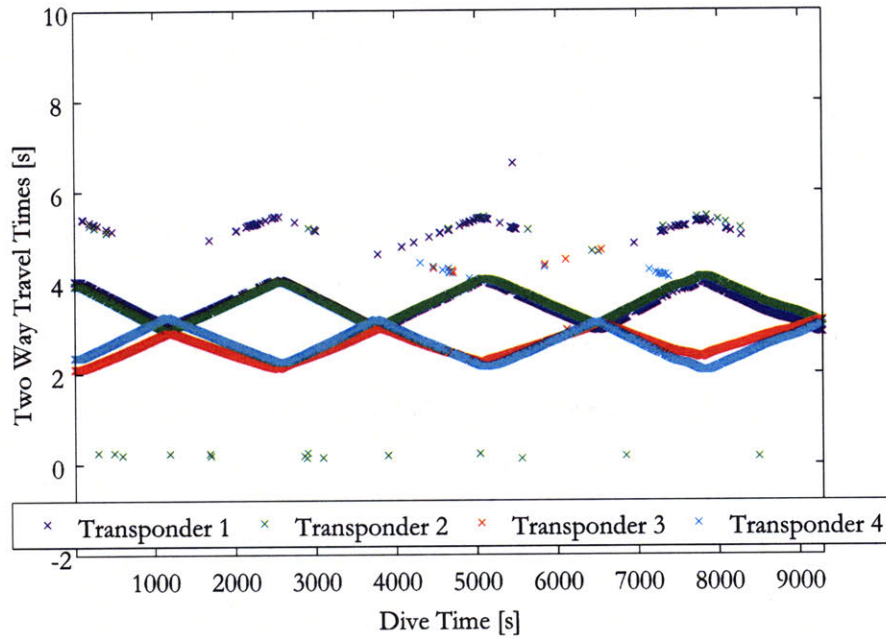## ABE165 Depth of Water Column Observed by Vehicle
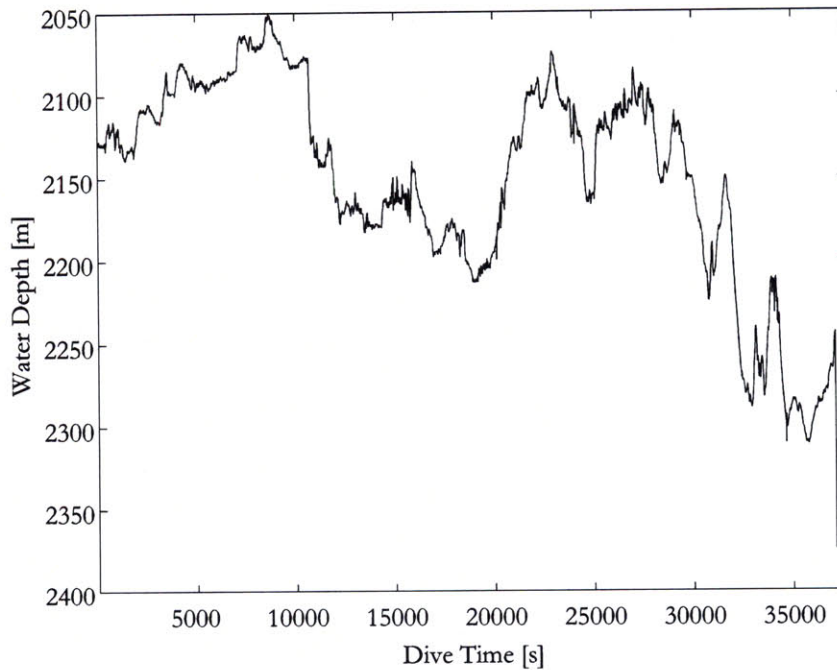
Figure 6-20: ABE165 observed water depth profile.

6.2.2 Sentry Insite08 Cruise

From July to August 2008, Sentry was deployed aboard the R/V *Thomas G. Thompson* on the Insite08 research cruise to the Juan de Fuca Ridge again with chief scientists John Delaney and Deborah Kelley. Insite08 was the first oceanographic research cruise for Sentry. The main goal of the cruise was to have Sentry make detailed bathymetric maps of the seafloor in the vicinities of Hydrate Ridge and Axial Volcano, areas of high scientific interest in the development of the NSF's Ocean Observatories Initiative. Despite several software and hardware failures during the cruise, Sentry completed a total of six scientific dives on these sites conducting more than 200 km of survey tracklines. The data used in this research was taken from the three dives conducted in the vicinity of the Axial Seamount, which is an area of rough bottom terrain with water depth varying between approximately 1500 and 2700 meters. Similar to the Endeavour region, the Axial Seamount is a diverse underwater terrain with the bathymetry varying from extreme depth gradients to swaths of relatively flat bottom. The accurate heading information from all three dives was intermittent due to repeated failures of the INS and miscalibration of the backup heading sensors [110].

6.2.2.1 Sentry014

The first dive done at the Axial Seamount was Sentry014. Sentry began the dive over flat terrain to the East of the seamount, then proceeded to climb up the seamount on tracklines that ran roughly parallel to the contours of the slope. Towards the end of the dive, the extreme roughness of the terrain created problems for Sentry as its bottom-following behaviors began to dominate its maneuvering. The forward progress of the dive slowed during these vertical manuevers and at one point stopped altogether as Sentry stalled in one location while trying to achieve the correct bottom-following altitude. The result was a high-frequency variability in the depth and altitude data recorded by Sentry during this dive. At the beginning of the dive, the

water depth was approximately 2700 meters. By the end of the dive, Sentry had climbed to a region where the water depth was approximately 2150 meters [110]. The dive tracklines for Sentry014 are shown in Figure 6-21, where these tracklines were determined as the best estimate of vehicle location through post-processing of the LBL and DVL information. The raw acoustic two-way travels times are shown in Figure 6-22. Acoustic returns from only two transponders were available during this dive.

Figure 6-21: Sentry014 tracklines and transponder locations.
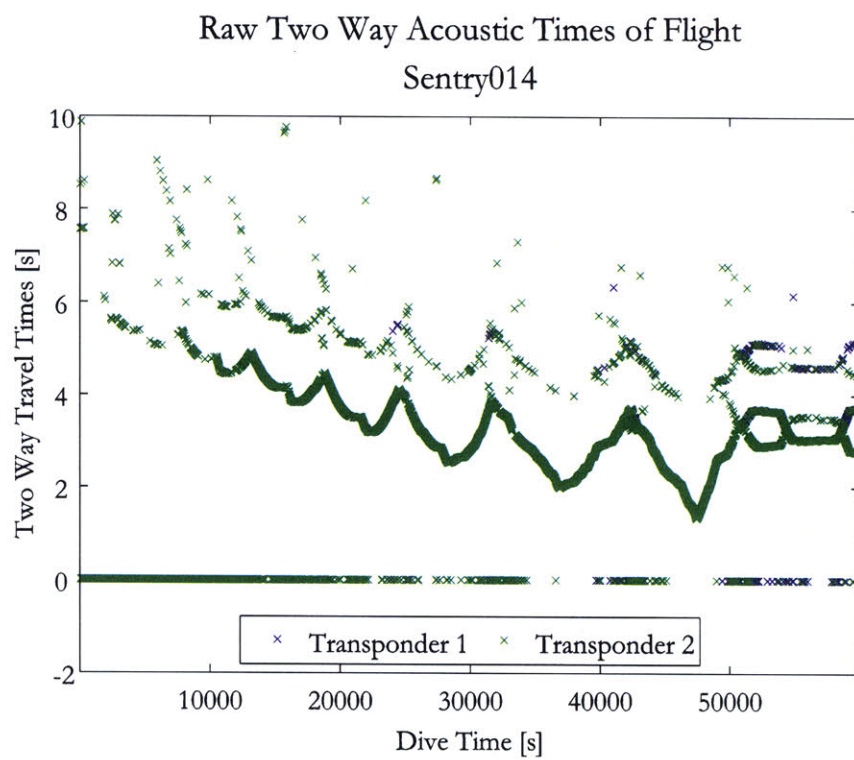
Figure 6-22: Sentry014 raw two-way acoustic travel times.

Figure 6-23: Sentry014 observed water depth profile.

6.2.2.2 Sentry015

The next dive at Axial Seamount, Sentry015, started near the end of the previous dive and continued the survey westward up the slope. Sentry experienced similar problems with forward progress being slowed during bottom-following maneuvers which was once again reflected in the depth and altitude data. Additionally, Sentry experienced three failures and resets of the onboard INS which negatively affected navigation performance [110]. For use with the PH algorithm, subsets of data were extracted between the failures of the INS. Over the course of the dive, Sentry traversed areas with water depths of approximately 2350 meters up to 1800 meters.

The dive tracklines for Sentry015 are shown in Figure 6-24, where these tracklines were determined as the best estimate of vehicle location through post-processing of the LBL and DVL information. The raw acoustic two-way travels times are shown in Figure 6-25 and the observed water depth profile is shown in Figure 6-26.
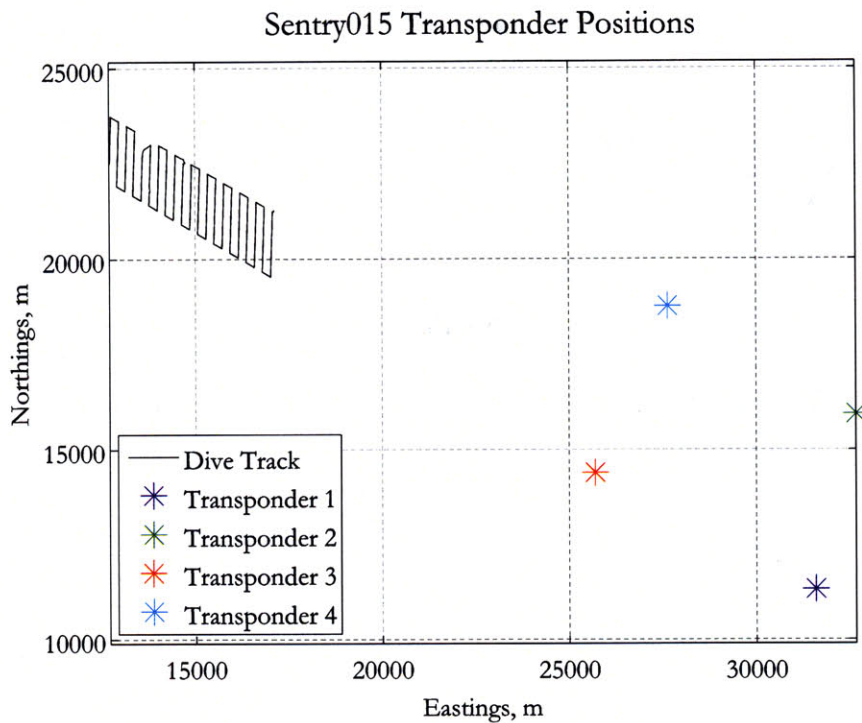
Figure 6-24: Sentry015 tracklines and transponder locations.
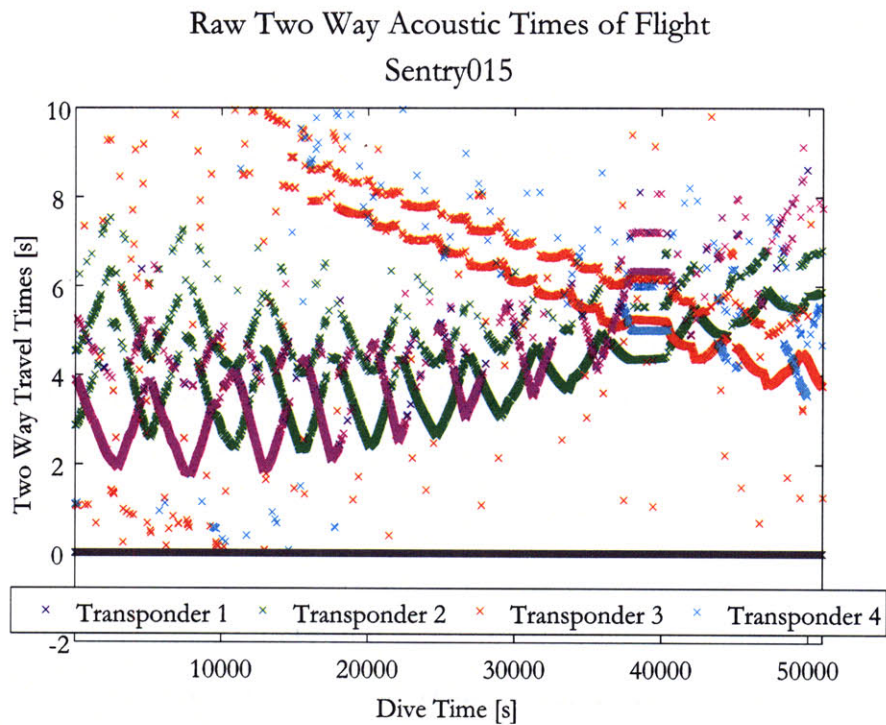
Figure 6-25: Sentry015 raw two-way acoustic travel times.
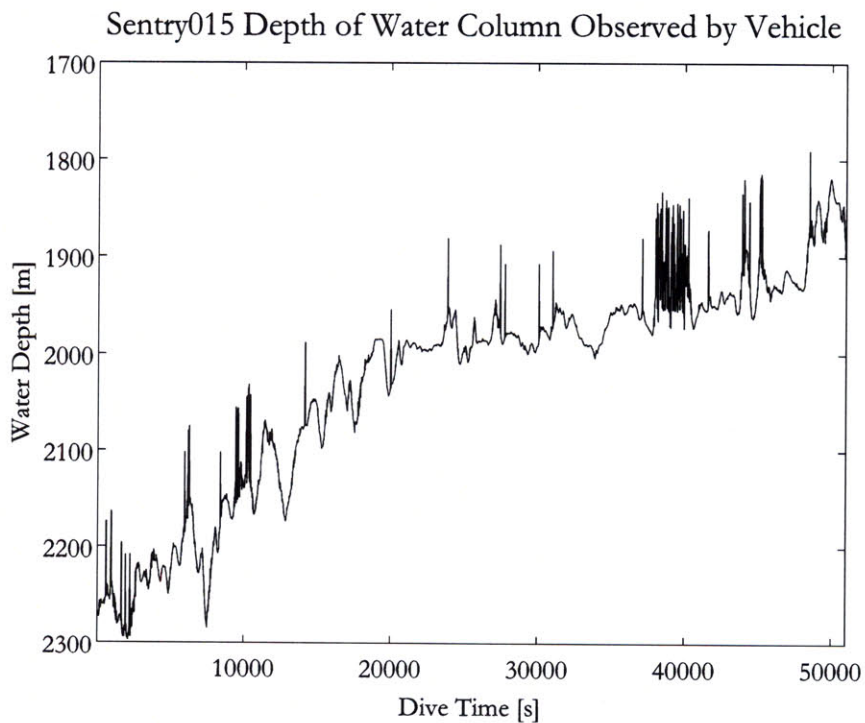
Figure 6-26: Sentry015 observed water depth profile.

157

6.2.2.3 Sentry016

The final dive of the cruise was Sentry016. Sentry began this dive on the southeastern slope of the Axial Seamount and descended toward flatter areas farther east. As opposed to the two previous dives, the tracklines of this dive were roughly perpendicular to the depth contours. During the dive, the INS again failed and reset four times. Additionally, a shear pin failed on one of the aft thrusters five hours into the fourteen hour dive. Sentry was able to continue the dive using the remaining aft thruster to keep on course, but the heading control was adversely affected. On this dive, water depths along the survey track varied from approximately 1500 meters down to 1600 meters [110].

The dive tracklines for Sentry016 are shown in Figure 6-27, where these tracklines were determined as the best estimate of vehicle location through post-processing of the LBL and DVL information. The raw acoustic two-way travels times are shown in Figure 6-28 and the observed water depth profile is shown in Figure 6-29.
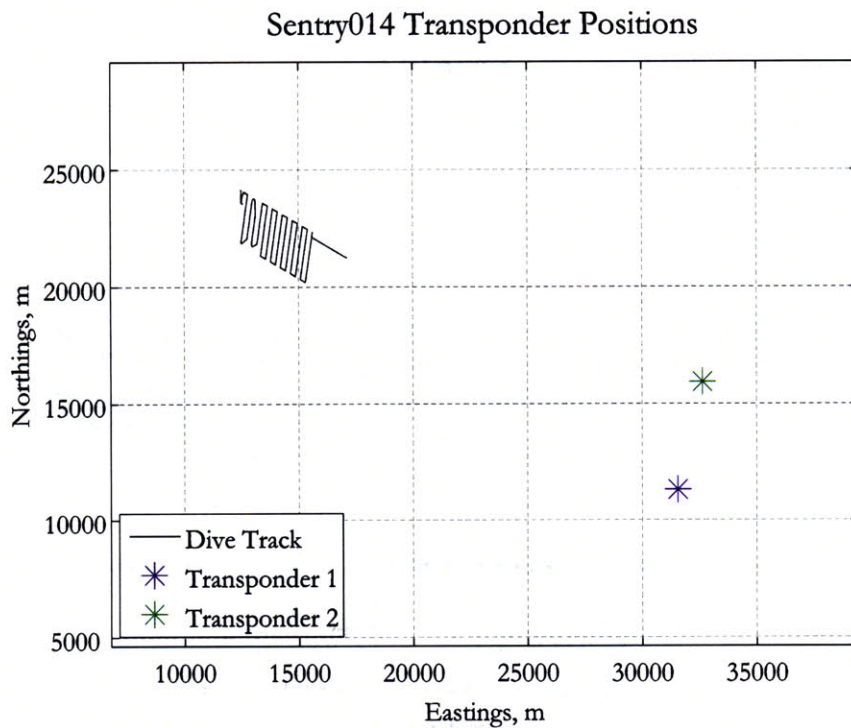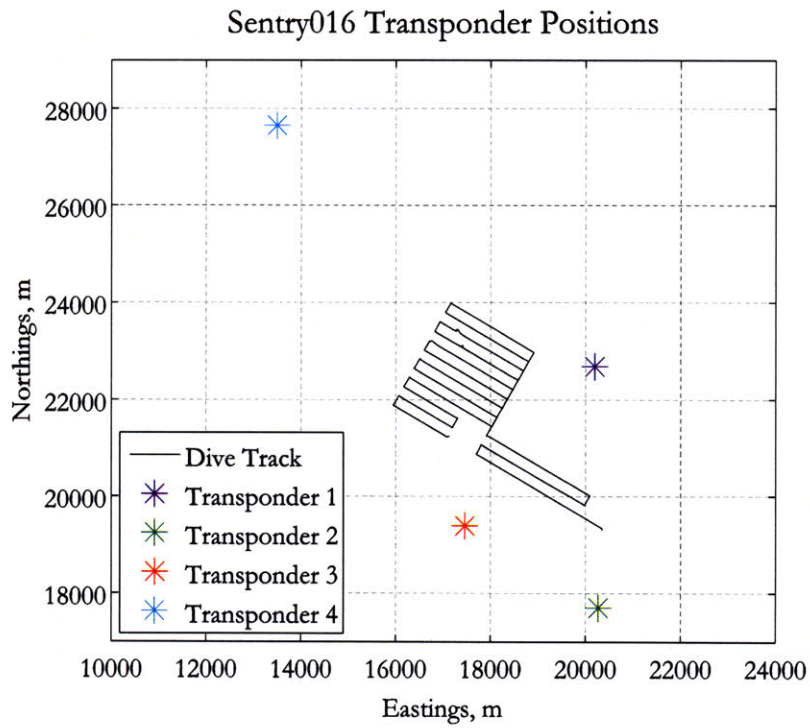
Figure 6-27: Sentry016 tracklines and transponder locations.
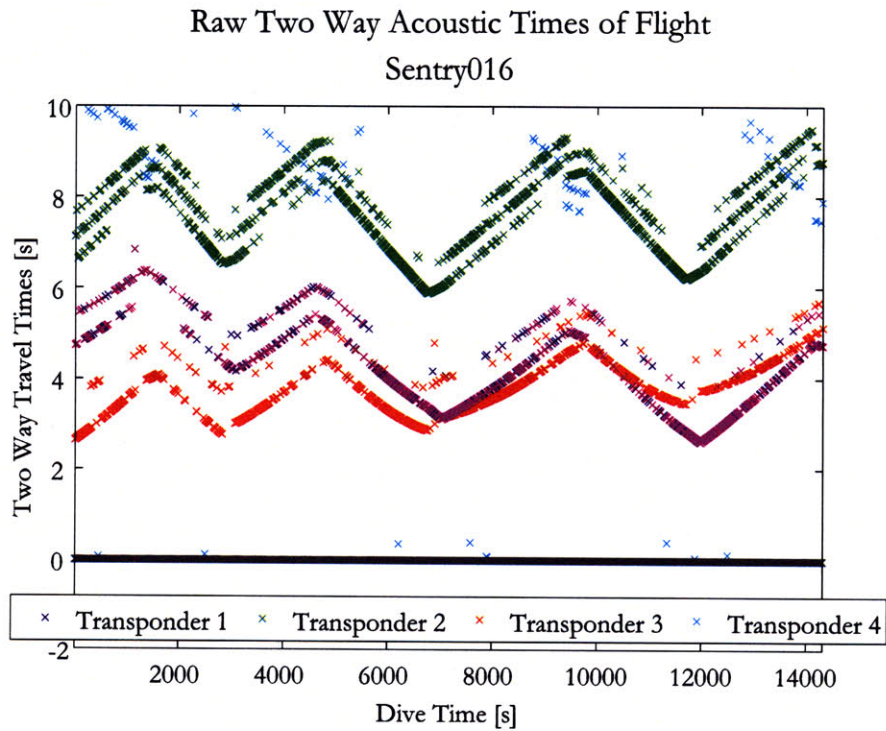
Figure 6-28: Sentry016 raw two-way acoustic travel times.

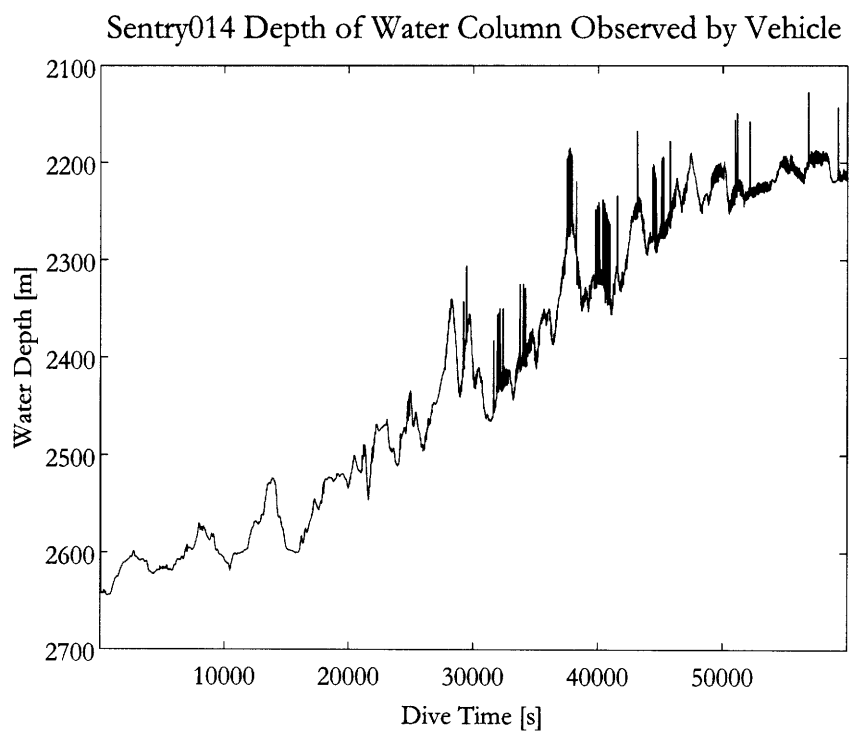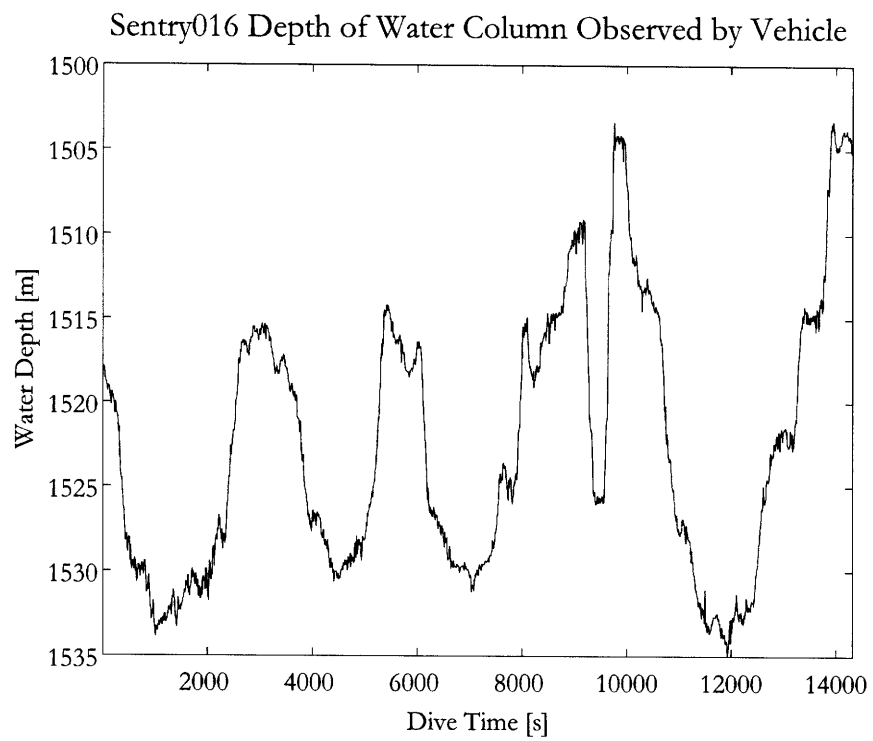Figure 6-29: Sentry016 observed water depth profile.

Chapter 7

Proof of Concept

The proof of concept of the PH navigation algorithm was conducted using data from real-world operations of the ABE and Sentry AUVs. Data from multiple external acoustic transponders were available during each dive. The proof of concept was performed using a data-denial methodology in which subsets of the available information were selected and post-processed using the PH algorithm. Although this research was done through post-processing, the only information required by the PH method is generally available to a vehicle real-time during its dive and all the techniques involved are causal and therefore feasible for real-time implementation.

7.1 Parallel Hypothesis Navigation with ABE161

This section will illustrate the PH navigation method in detail using dive ABE161 as an example. For this dive, the acoustic returns were relatively free from random noise, but there were significant periods of direct path dropouts in which only triangle or double bounce path returns were present. The locations of the transponders with respect to the tracklines are shown in Figure 7-1. The tracklines represents the best post-processed calculation of vehicle actual position using LBL and DVL data. Acoustic data from four transponders were available for this dive as shown in Figure

7-2. The location of the tracklines with respect to the EM300 *a-priori* map is shown in Figure 7-3.

The result of the PH algorithm is shown in Figure 7-4. In this plot, the blue markers indicate fixes that include only direct path returns. The red markers indicate fixes that used at least one triangle path return and any available direct path returns. The green markers indicate fixes that used at least one double bounce path return and any available direct path and triangle path returns.

ABE161 Transponder Positions
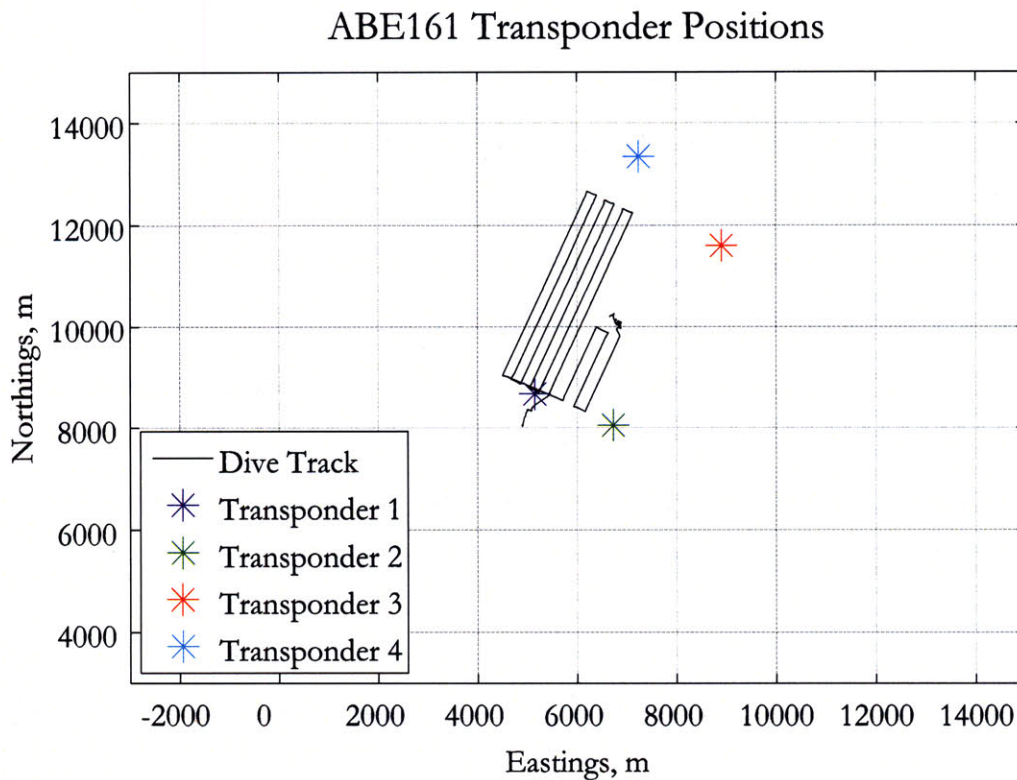
Figure 7-1: ABE161 tracklines and transponder locations.

Over the following pages, the intermediate steps of the process will be illustrated in detail to demonstrate how the result was obtained. First, the hypothesis generation and arbitration steps will be looked at individually for each transponder. Then, at the end, the update step and performance metrics are discussed for the dive overall.

162
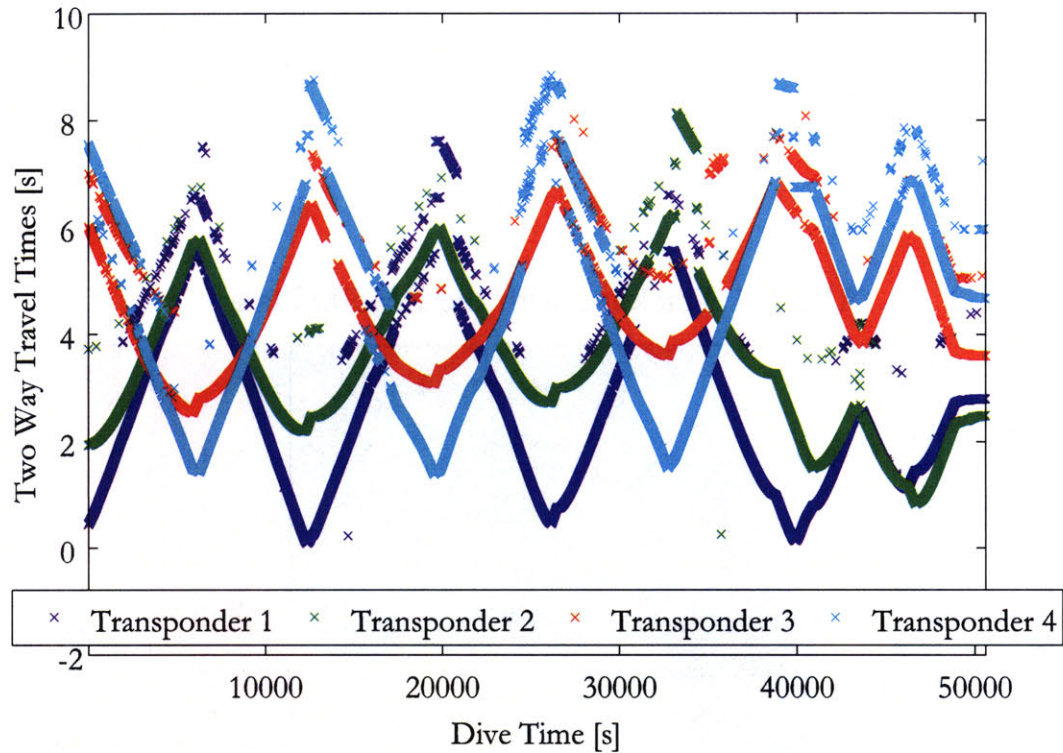
Figure 7-2: ABE161 raw acoustic two-way travel times.

In the navigation algorithm, the steps of the process are done iteratively in a loop for each time frame. Therefore, the cumulative plots of hypotheses that are shown for each step in the process for each transponder represent data that has been picked out of the loop during each navigation cycle at the appropriate stage.

Legends were omitted from the plots in this section and a common color scheme was used throughout for visual simplicity. In the common color scheme, blue markers represent direct path data, red markers represent triangle path data, and green markers represent double bounce data. The only exception to this color scheme is in the plots of raw acoustic two-way travel times where the colors corresponded to different transponders as shown in the legend of Figure 7-1.

ABE161 Trackline with the EM300 Data
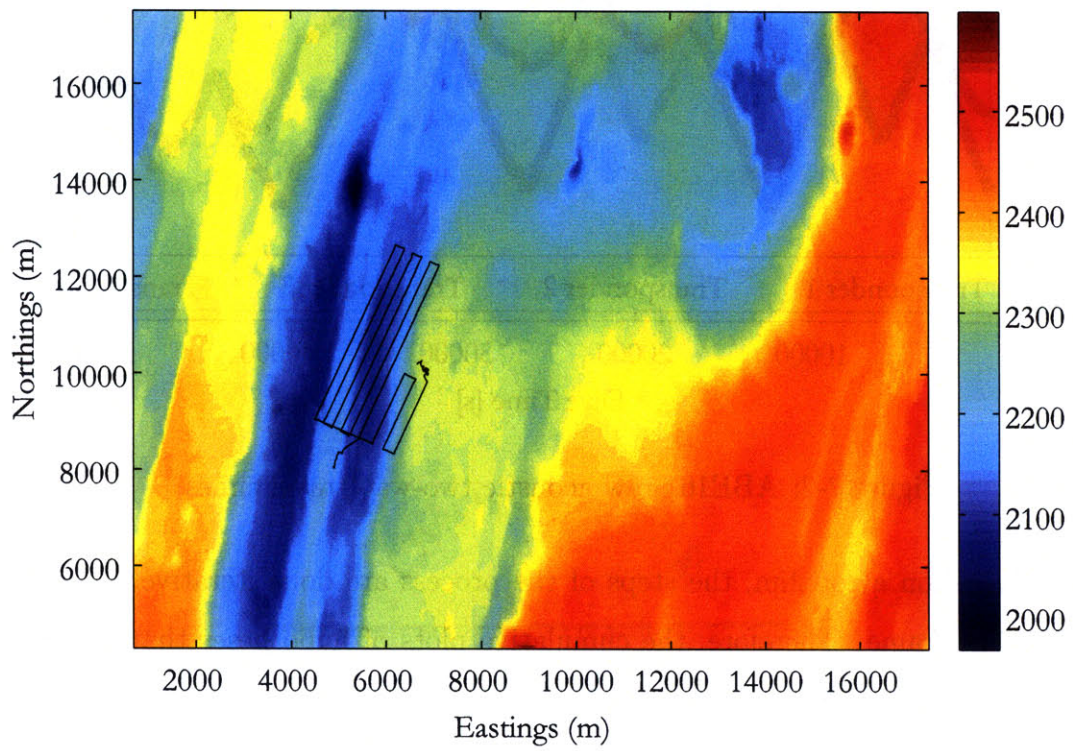
Figure 7-3: ABE161 tracklines and the *a priori* EM300 bathymetric map.
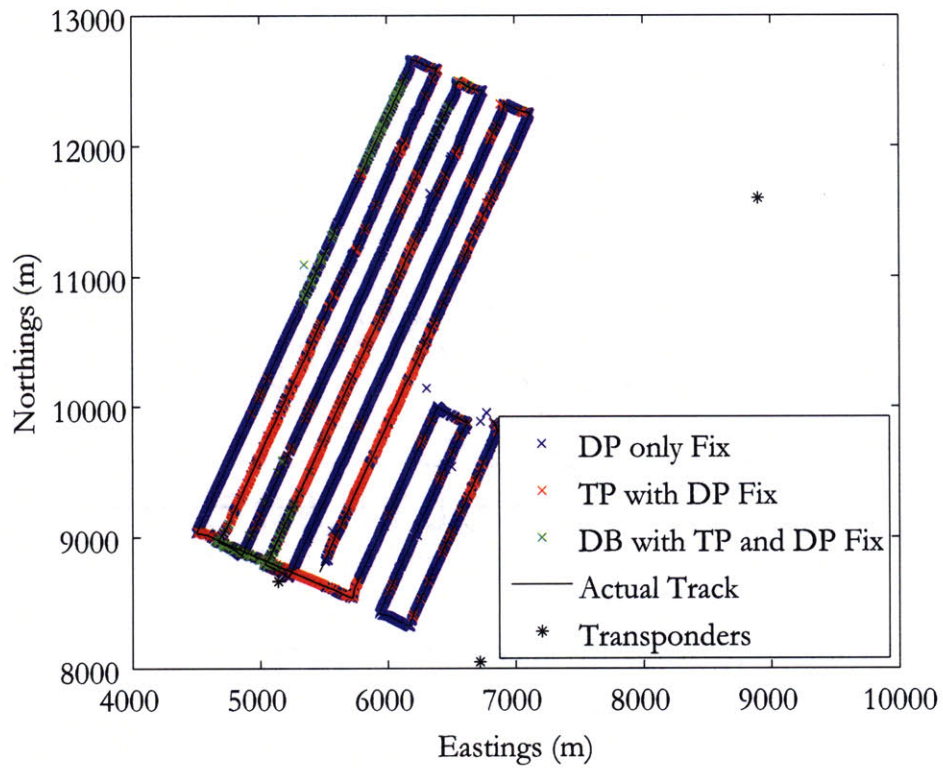
Figure 7-4: ABE161 results of the PH navigation algorithm.

7.1.1 ABE161 Transponder 1

The position of Transponder 1 with relation to the trackline for ABE161 is shown in Figure 7-5. The raw two-way travel times of the Transponder 1 returns observed by the vehicle are shown in Figure 7-6. The data is relatively clean with some periods of bounce returns evident.
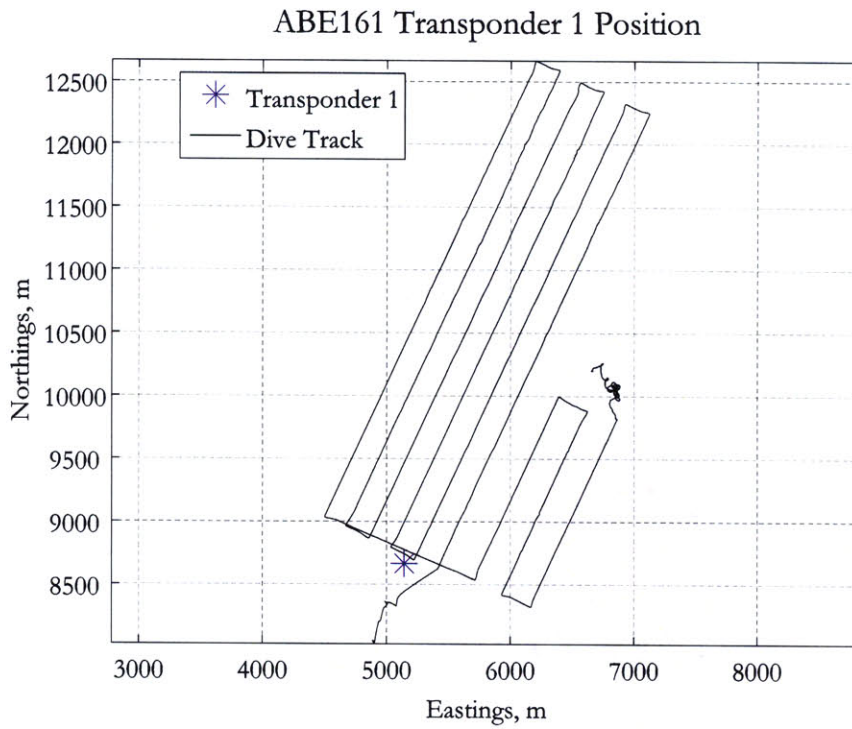
Figure 7-5: ABE161 tracklines and Transponder 1 location.

Raw Two Way Acoustic Times of Flight
ABE161 Transponder 1
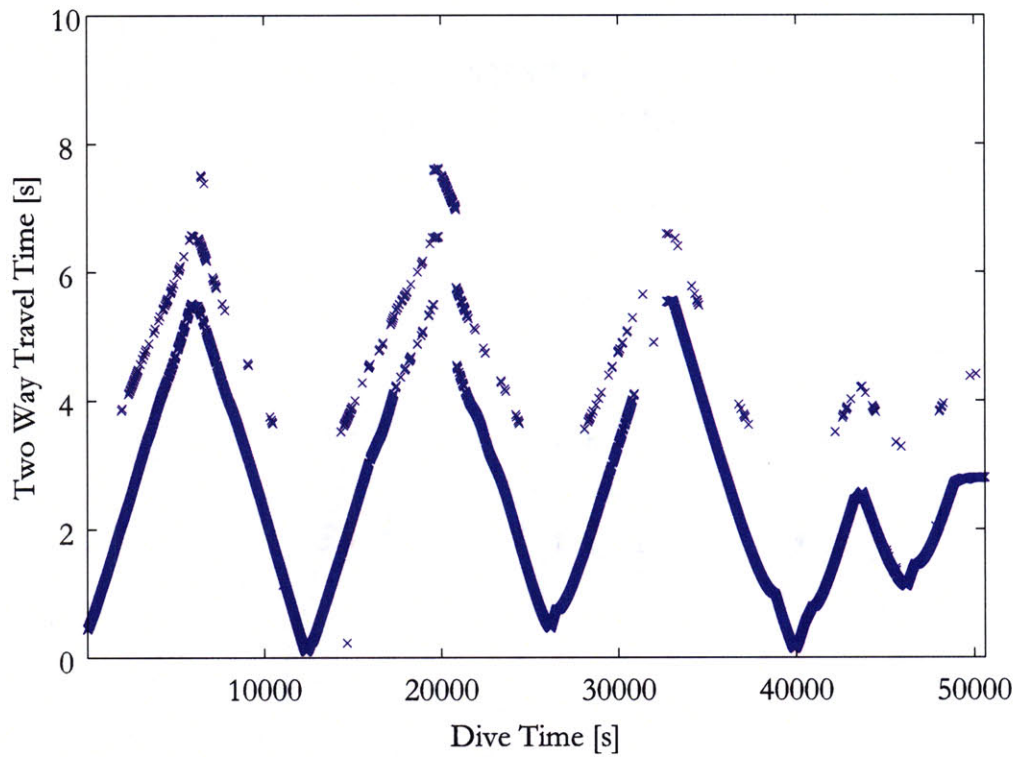
Figure 7-6: ABE161 Transponder 1 raw two-way acoustic travel times.

7.1.1.1 ABE161 Transponder 1 Hypothesis Generation Step

Figure 7-7 shows the raw acoustic data after it has been transformed into horizontal ranges for each of the three possible acoustic paths. For each travel time received by ABE, the corresponding range if the signal was direct path is shown in blue, for triangle path is shown in red, and double bounce is shown in green. The black line indicates the actual distance between vehicle and transponder throughout the dive. Therefore, the ranges that fall along that line indicate which acoustic path the received acoustic signal actually followed for each navigation cycle.
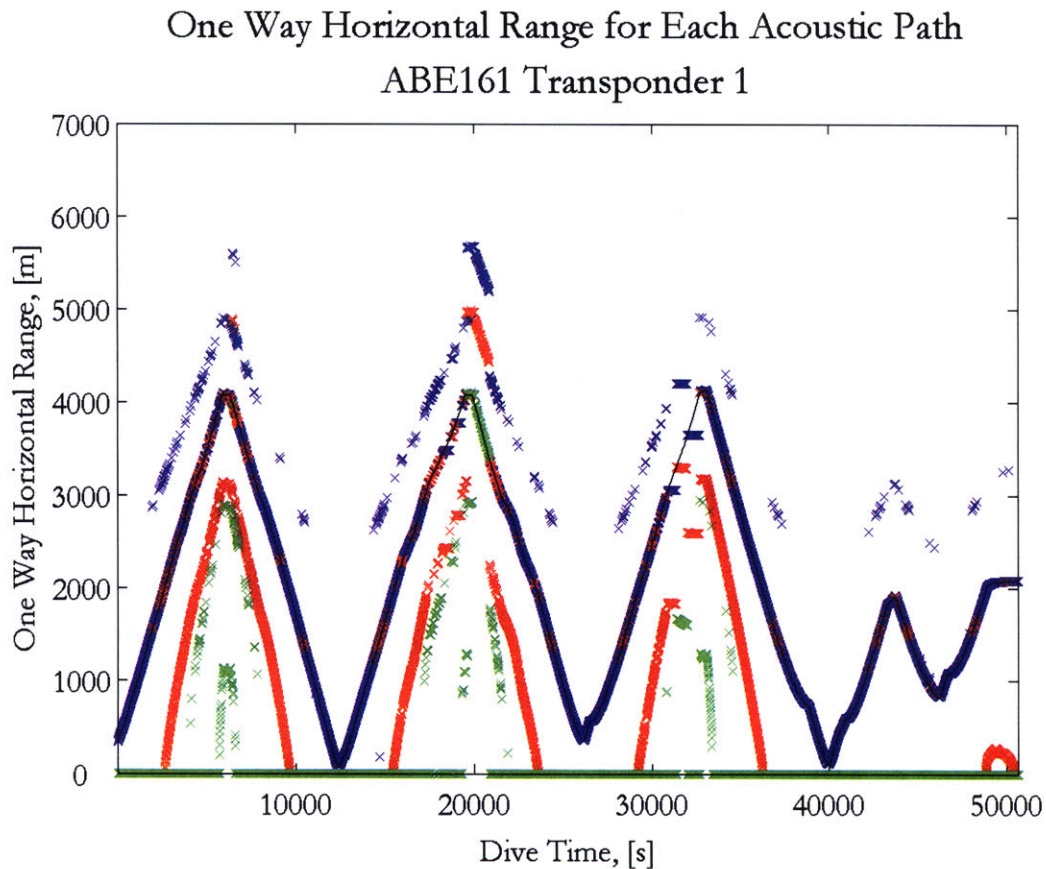
Figure 7-7: ABE161 Transponder 1 horizontal ranges for possible acoustic paths.

For Transponder 1, there was significant dropout of the direct path data when the vehicle was operating farthest from the transponder. At the end of the first two outbound legs, triangle path and double bounce path returns were received that filled

Cumulative Location Hypotheses Before Arbitration
ABE161 Transponder 1
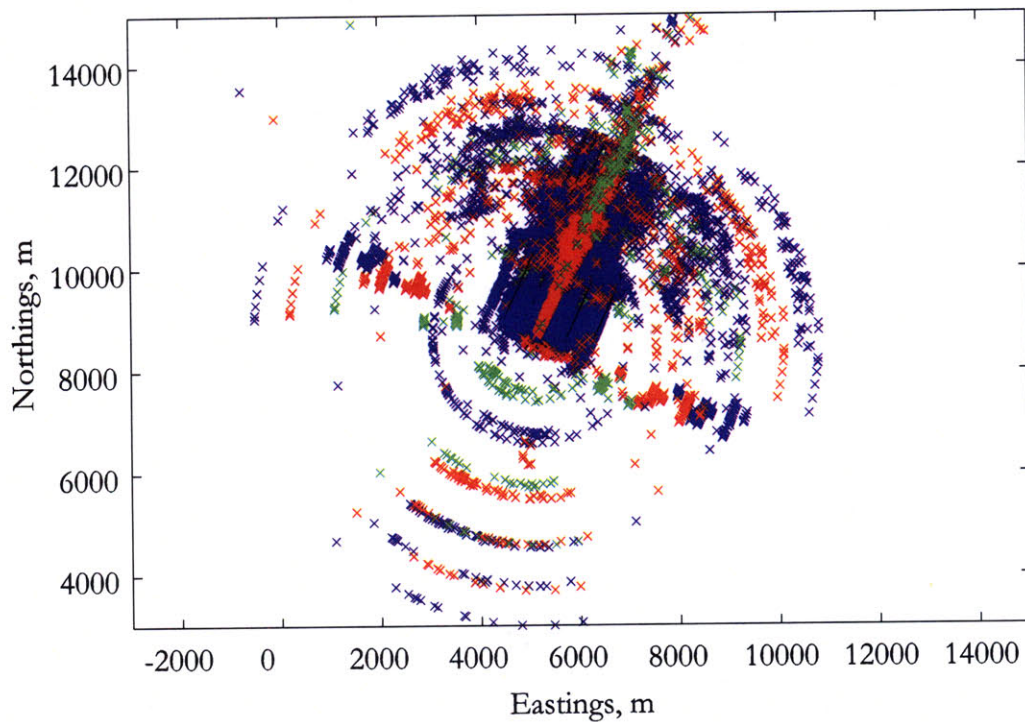
Figure 7-8: ABE161 Transponder 1 generated pose hypotheses, plotted cumulatively over the entire course of the dive.

in much of this dropout. At the end of the third outbound leg there was significant loss of data from all multipaths. From these horizontal range hypotheses, up to six pose hypotheses were created for the vehicle in each navigation cycle. Figure 7-8 shows a cumulative plot of all of the pose hypotheses created from the observed horizontal ranges over the course of the entire dive before any arbitration was conducted.

7.1.1.2 ABE161 Transponder 1 Grid Arbitration Step

The first level of the arbitration process is the grid arbiter. Figure 7-9 shows all the pose hypotheses that survived the grid arbitration process, again plotted cumulatively over the course of the whole dive.

Table 7.1 presents a performance metric for the grid arbiter based on the percentage of the total navigation cycles in which each type of pose hypothesis was eliminated by the grid arbiter. A cumulative statistic is also presented representing the percentage of total navigation cycles in which at least one pose hypothesis was eliminated by the grid arbiter. The cumulative number does not equal the sum of the individual statistics because more than one pose hypothesis may have been eliminated in any given navigation cycle.

It is important to understand that the performance metric used is a percentage of total navigation cycles, not a percentage of total pose hypotheses. Depending on the travel time recorded in each navigation cycle, not all six of the possible types of pose hypotheses were necessarily generated. For example, if the distance between the transponder and vehicle was less than the water depth and a direct path return was received for a given navigation cycle, there is no physical way for a triangle path or double bounce path range hypothesis to be generated with that information. Therefore, only direct path hypotheses would be generated total in that navigation cycle. For Transponder 1 on this dive, there were relatively few double bounce hypotheses generated over the course of the dive, as evident in Figure 7-7. Therefore, even though the statistics for double bounce paths in Table 7.1 appear low, they actually represent a high percentage of the double bounce hypotheses generated over the course of the dive.

Figure 7-9: ABE161 Transponder 1 pose hypotheses after grid arbitration, plotted cumulatively over the entire course of the dive.

Table 7.1: ABE161 Transponder 1 grid arbiter performance metrics.

	Percentage of navigation cycles in which an elimination occurred
Direct path 1	17.28
Direct path 2	18.12
Triangle path 1	13.56
Triangle path 2	15.26
Double bounce path 1	4.70
Double bounce path 2	4.92
Cumulative	24.22

7.1.1.3 ABE161 Transponder 1 Primary Arbitration Step

The pose hypotheses that survive the grid arbiter process are input into the primary arbiter, which selects the single nearest neighbor hypothesis for every navigation cycle. Figure 7-10 depicts the acoustic range at every time frame corresponding to each chosen nearest neighbor pose hypotheses. Figure 7-11 shows the same information spatially by depicting a cumulative plot over the course of the whole dive of the nearest neighbor pose hypotheses from each navigation cycle.
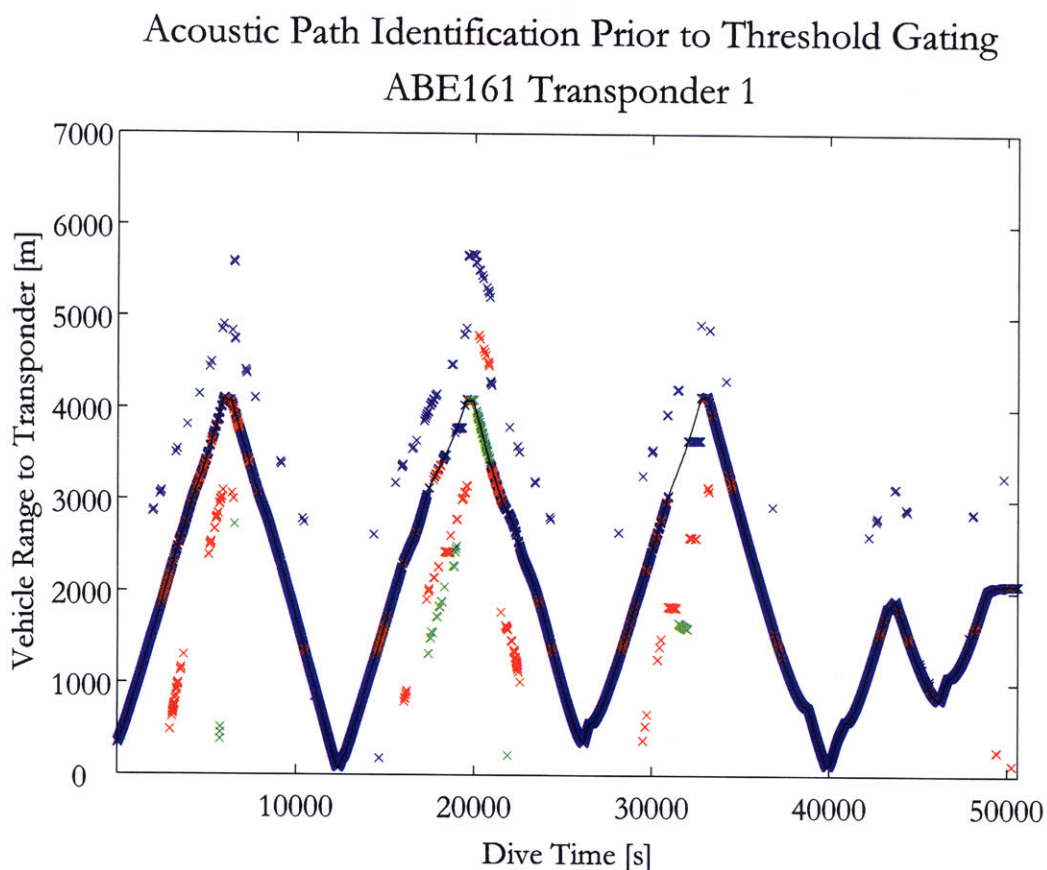
Figure 7-10: ABE161 Transponder 1 horizontal ranges corresponding to pose hypotheses after primary arbitration.

Cumulative Location Hypotheses After Arbitration
ABE161 Transponder 1

Figure 7-11: ABE161 Transponder 1 pose hypotheses after primary arbitration, plotted cumulatively over the entire course of the dive.

7.1.1.4 ABE161 Transponder 1 Threshold Gating Step

The single pose hypothesis that is output from the primary arbiter at each navigation cycle is subject to threshold gating to ensure that it is a valid hypothesis. Figure 7-12 depicts the acoustic ranges corresponding to the pose hypotheses that survived the threshold gating process. Figure 7-13 shows the same information spatially by depicting a cumulative plot of the threshold-gated hypotheses from each navigation cycle.
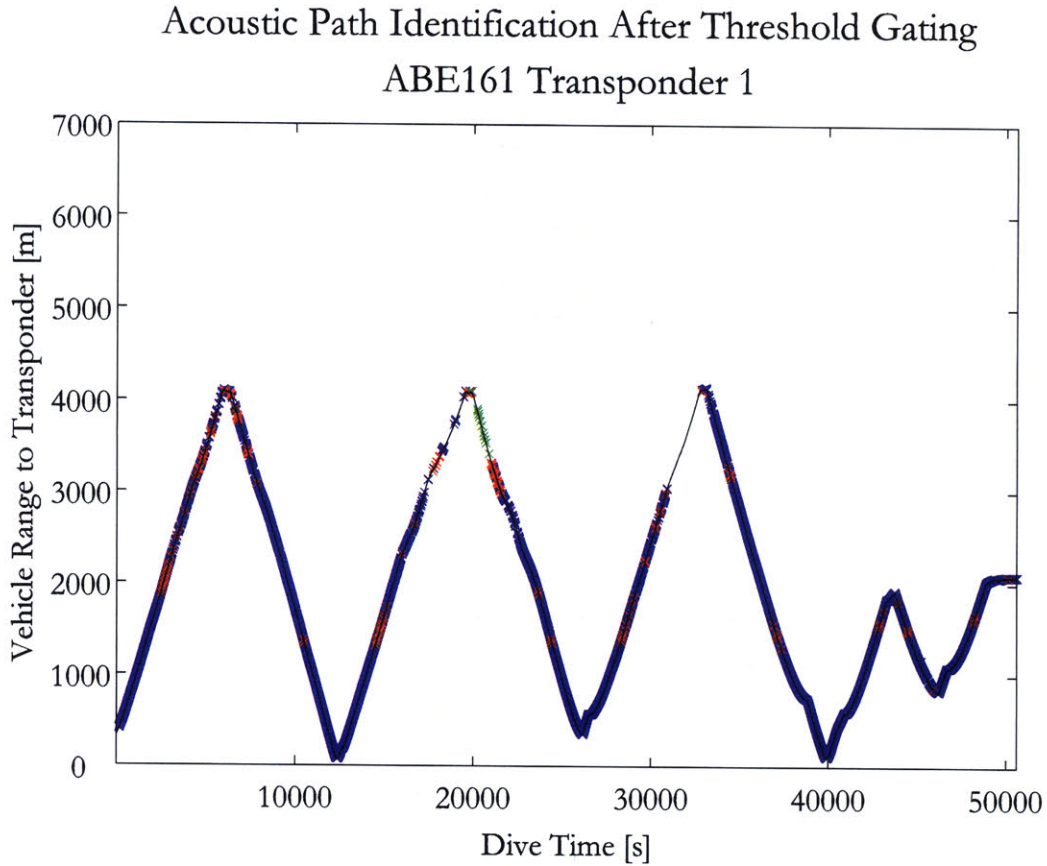
Figure 7-12: ABE161 Transponder 1 horizontal ranges corresponding to pose hypotheses after threshold gating.

Cumulative Location Hypotheses After Threshold Gating
ABE161 Transponder 1
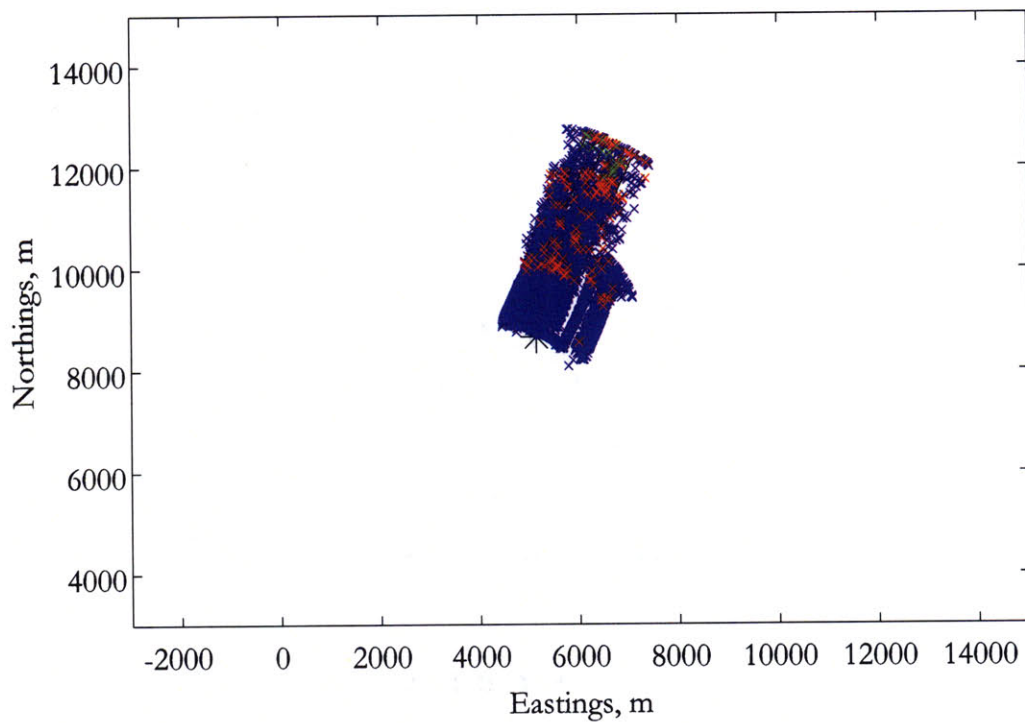
Figure 7-13: ABE161 Transponder 1 pose hypotheses after threshold gating, plotted cumulatively over the entire course of the dive.

7.1.2 ABE161 Transponder 2

The position of Transponder 2 with relation to the tracklines for ABE161 is shown in Figure 7-14. The raw two-way travel times of the Transponder 2 returns observed by the vehicle are shown in Figure 7-15. The data is relatively clean with good direct path data throughout most of the dive and occasional bounce path returns.
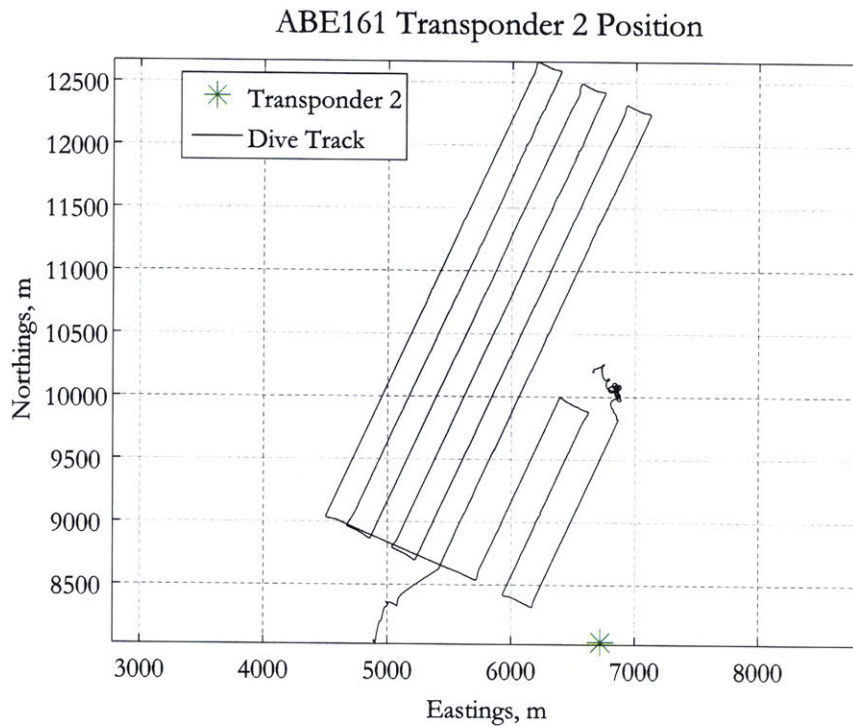
Figure 7-14: ABE161 tracklines and Transponder 2 location.

Raw Two Way Acoustic Times of Flight
ABE161 Transponder 2
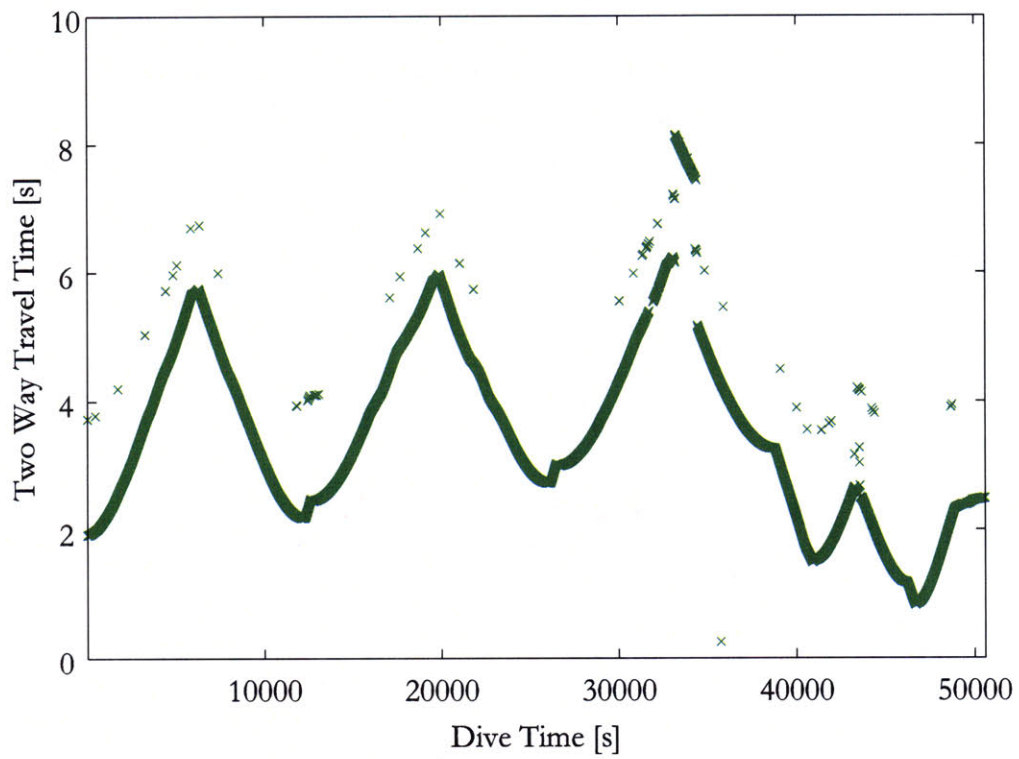
Figure 7-15: ABE161 Transponder 2 raw two-way acoustic travel times.

7.1.2.1 ABE161 Transponder 2 Hypothesis Generation Step

Figure 7-16 shows the raw acoustic data after it has been transformed into horizontal ranges for each of the three possible acoustic paths. For each travel time received by ABE, the corresponding range if the signal was direct path is shown in blue, for triangle path is shown in red, and double bounce is shown in green. The black line indicates the actual distance between vehicle and transponder throughout the dive. Therefore, the ranges that fall along that line indicate which acoustic path the received acoustic signal actually followed for each navigation cycle.
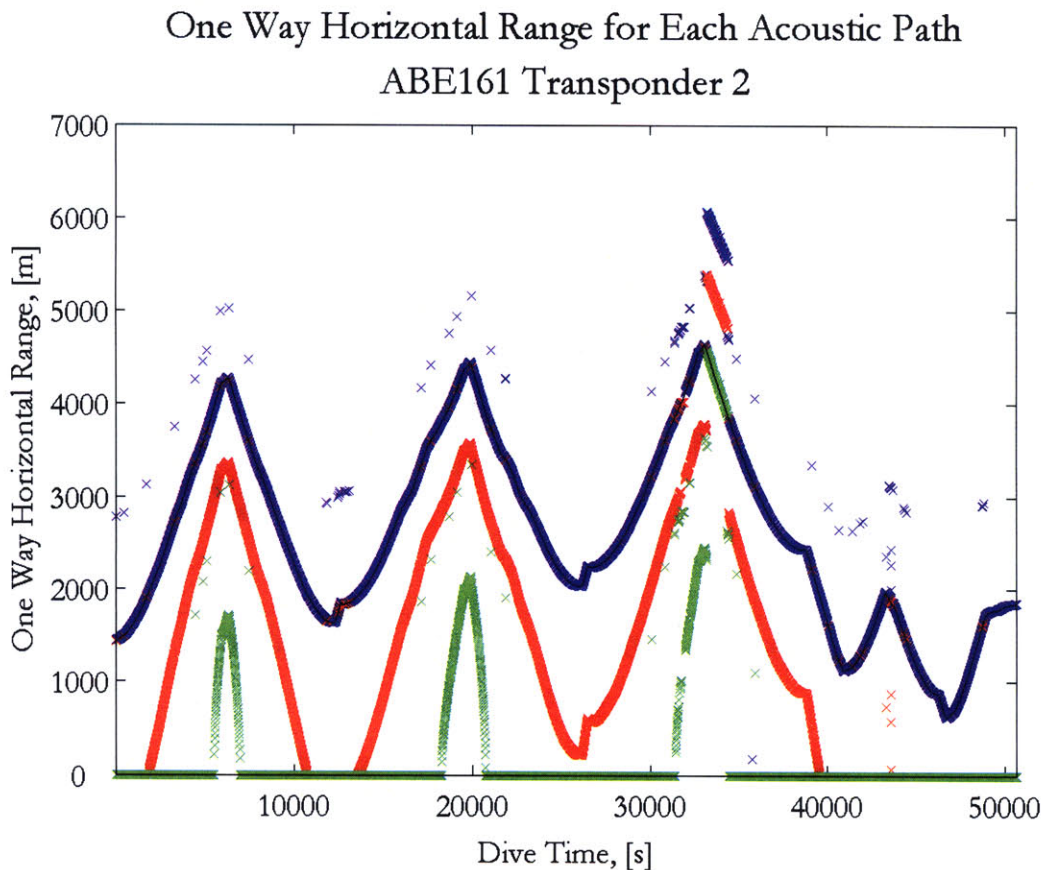
Figure 7-16: ABE161 Transponder 2 horizontal ranges for possible acoustic paths.

For Transponder 2, there was good direct path data throughout most of the dive. At the beginning of the third inbound leg there was a period of direct path dropout when only double bounce returns were received. This is a good indication of shad-

178

Cumulative Location Hypotheses Before Arbitration
ABE161 Transponder 2
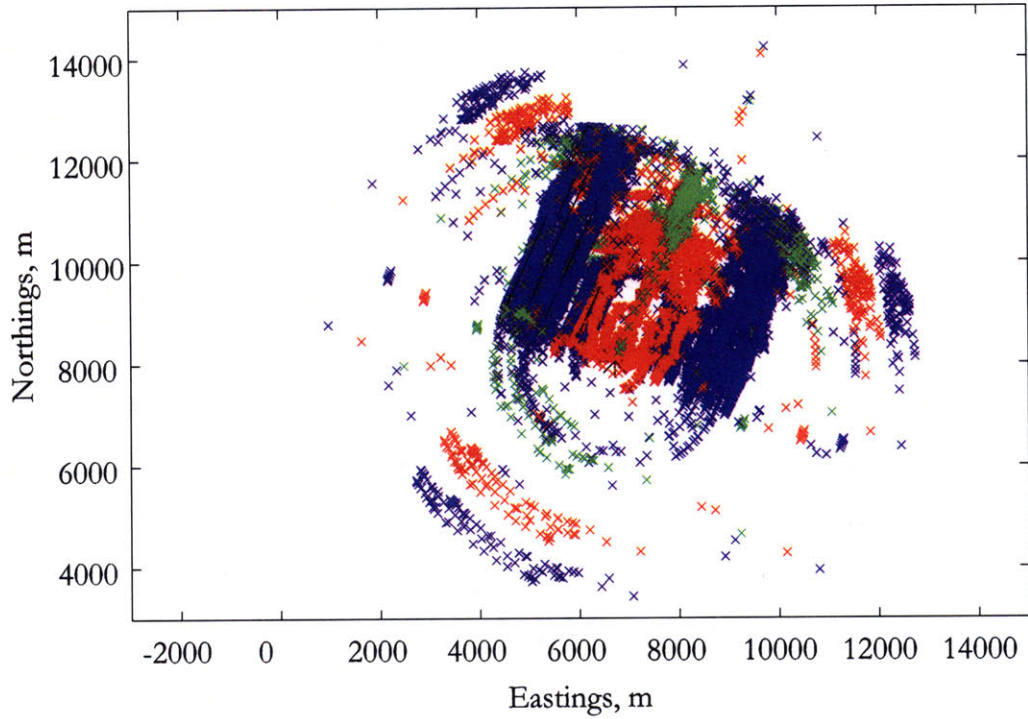
Figure 7-17: ABE161 Transponder 2 generated pose hypotheses, plotted cumulatively over the entire course of the dive.

owing during this period. From these horizontal range hypotheses, up to six pose hypotheses were created for the vehicle in each navigation cycle. Figure 7-17 shows a cumulative plot of all of the pose hypotheses created from the observed horizontal ranges over the course of the entire dive before any arbitration was conducted.

7.1.2.2 ABE161 Transponder 2 Grid Arbitration Step

The first level of the arbitration process is the grid arbiter. Figure 7-18 shows all the pose hypotheses that survived the grid arbitration process, again plotted cumulatively over the course of the whole dive.

Table 7.2 presents a performance metric for the grid arbiter based on the percentage of the total navigation cycles in which each type of pose hypothesis was eliminated by the grid arbiter. A cumulative statistic is also presented representing the percentage of total navigation cycles in which at least one pose hypothesis was eliminated by the grid arbiter. The cumulative number does not equal the sum of the individual statistics because more than one pose hypothesis may have been eliminated in any given navigation cycle.

Again, it is important to understand that the performance metric used is a percentage of total navigation cycles, not a percentage of total pose hypotheses. Depending on the travel time recorded in each navigation cycle, not all six of the possible types of pose hypotheses were necessarily generated. For example, if the distance between the transponder and vehicle was less than the water depth and a direct path return was received for a given navigation cycle, there is no physical way for a triangle path or double bounce path range hypothesis to be generated with that information. Therefore, only direct path hypotheses would be generated total in that navigation cycle. For Transponder 2 on this dive, again there were relatively few double bounce hypotheses generated over the course of the dive, as evident in Figure 7-16. Therefore, even though the statistics for double bounce paths in Table 7.2 appear low, they actually represent a high percentage of the double bounce hypotheses generated over the course of the dive. Overall, the grid arbiter had a significant effect for Transponder 2.

Cumulative Location Hypotheses After Grid Arbitration ABE161 Transponder 2
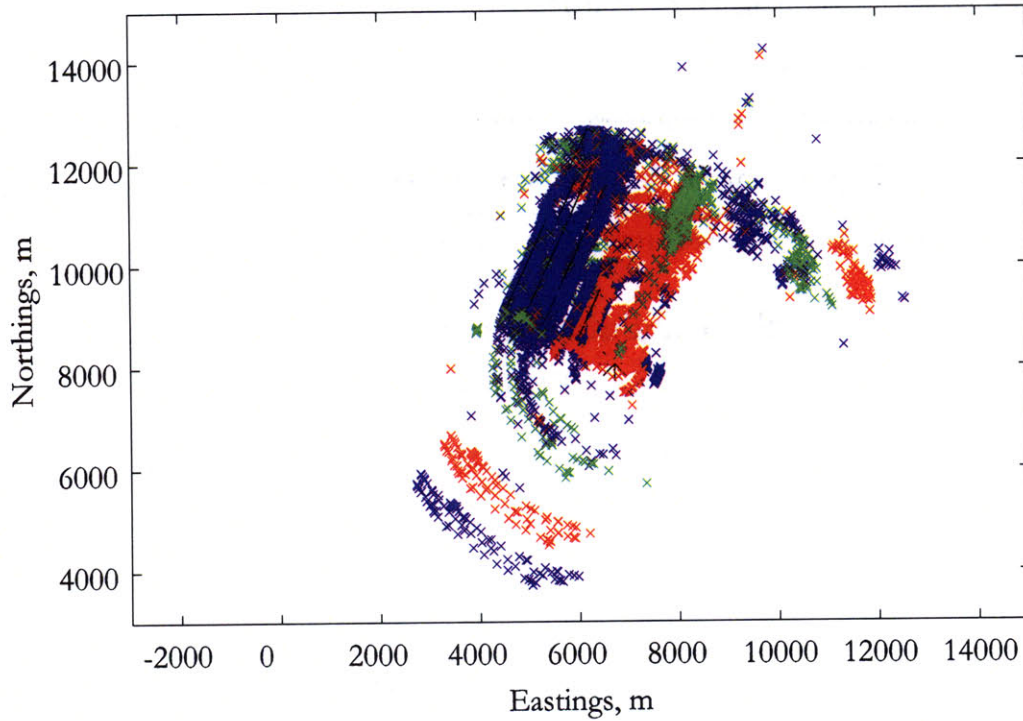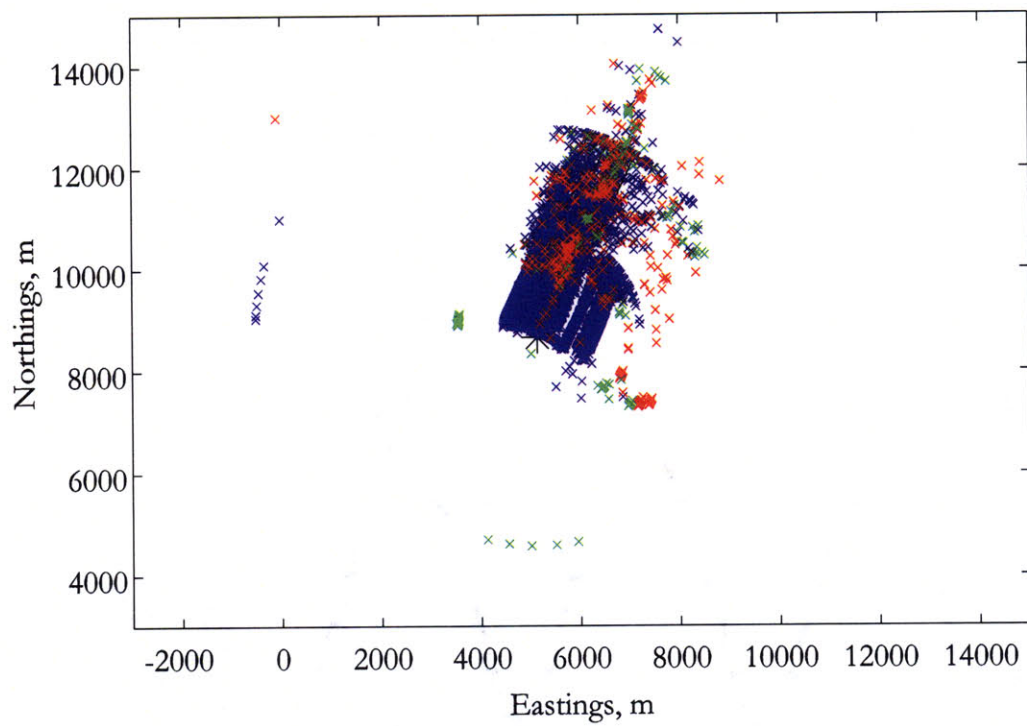
Figure 7-18: ABE161 Transponder 2 pose hypotheses after grid arbitration, plotted cumulatively over the entire course of the dive.

Table 7.2: ABE161 Transponder 2 grid arbiter performance metrics.

	Percentage of navigation cycles in which an elimination occurred
Direct path 1	47.43
Direct path 2	41.37
Triangle path 1	17.40
Triangle path 2	17.86
Double bounce path 1	1.96
Double bounce path 2	2.06
Cumulative	83.20

7.1.2.3   ABE161 Transponder 2 Primary Arbitration Step

The pose hypotheses that survive the grid arbiter process are then input into the primary arbiter, which selects the single nearest neighbor hypothesis for every navigation cycle. Figure 7-19 depicts the acoustic range at every time frame corresponding to each chosen nearest neighbor pose hypotheses. Figure 7-20 shows the same information spatially by depicting a cumulative plot over the course of the whole dive of the nearest neighbor pose hypotheses from each navigation cycle.
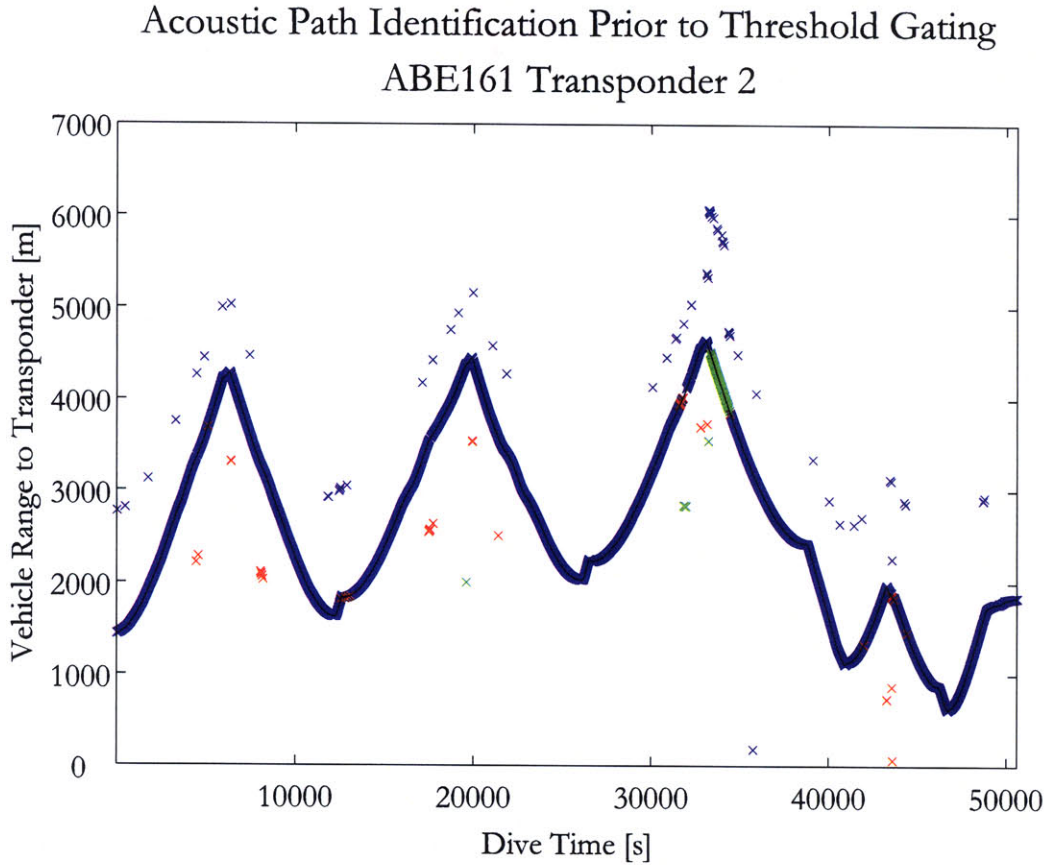
Figure 7-19: ABE161 Transponder 2 horizontal ranges corresponding to pose hypotheses after primary arbitration.

Cumulative Location Hypotheses After Arbitration
ABE161 Transponder 2

Figure 7-20: ABE161 Transponder 2 pose hypotheses after primary arbitration, plotted cumulatively over the entire course of the dive.

7.1.2.4 ABE161 Transponder 2 Threshold Gating Step

The pose hypothesis that is output from the primary arbiter at each navigation cycle is subject to threshold gating to ensure that it is a valid hypothesis. Figure 7-21 depicts the acoustic ranges corresponding to the pose hypotheses that survived the threshold gating process. Figure 7-22 shows the same information spatially by depicting a cumulative plot of the threshold-gated hypotheses from each navigation cycle.
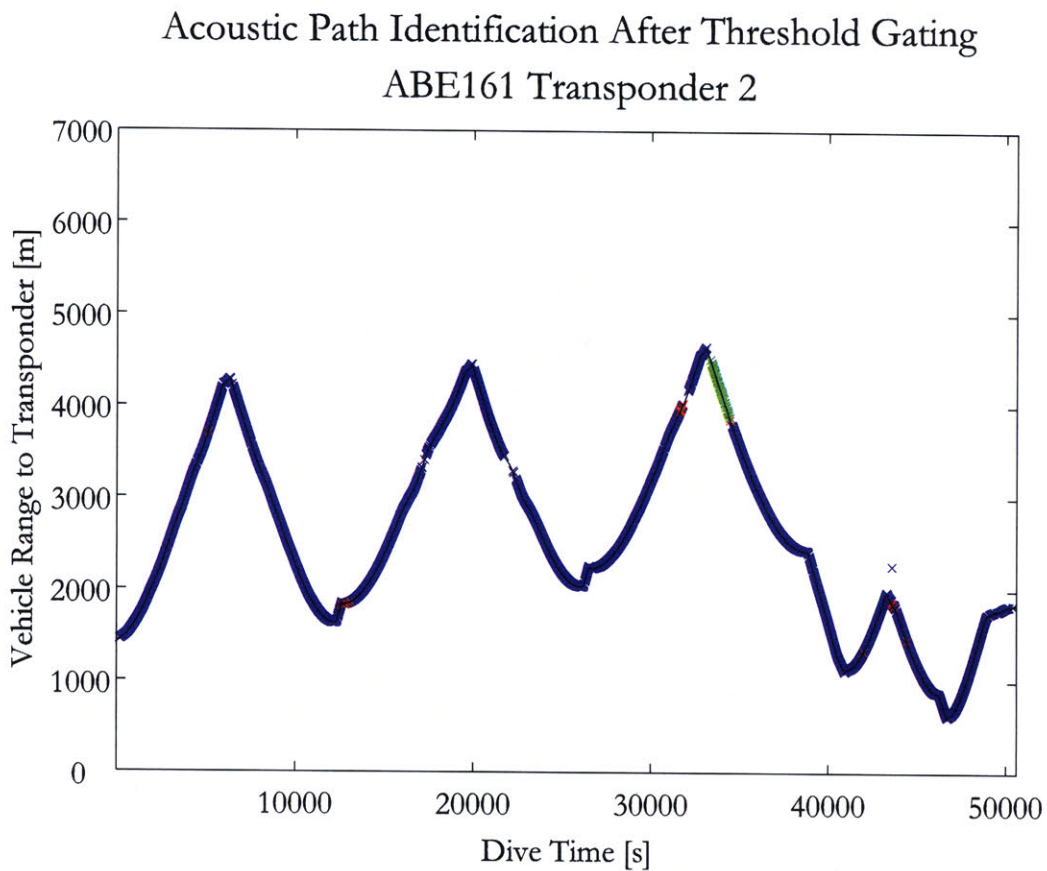
Figure 7-21: ABE161 Transponder 2 horizontal ranges corresponding to pose hypotheses after threshold gating.

Cumulative Location Hypotheses After Threshold Gating
ABE161 Transponder 2

Figure 7-22: ABE161 Transponder 2 pose hypotheses after threshold gating, plotted cumulatively over the entire course of the dive.

7.1.3 ABE161 Transponder 3

The position of Transponder 3 with relation to the tracklines for ABE161 is shown in Figure 7-23. The raw two-way travel times of the Transponder 3 returns observed by the vehicle are shown in Figure 7-24. The data is relatively clean with good direct path data throughout most of the dive except for periods of bounce path returns at the beginning of each inbound trackline.
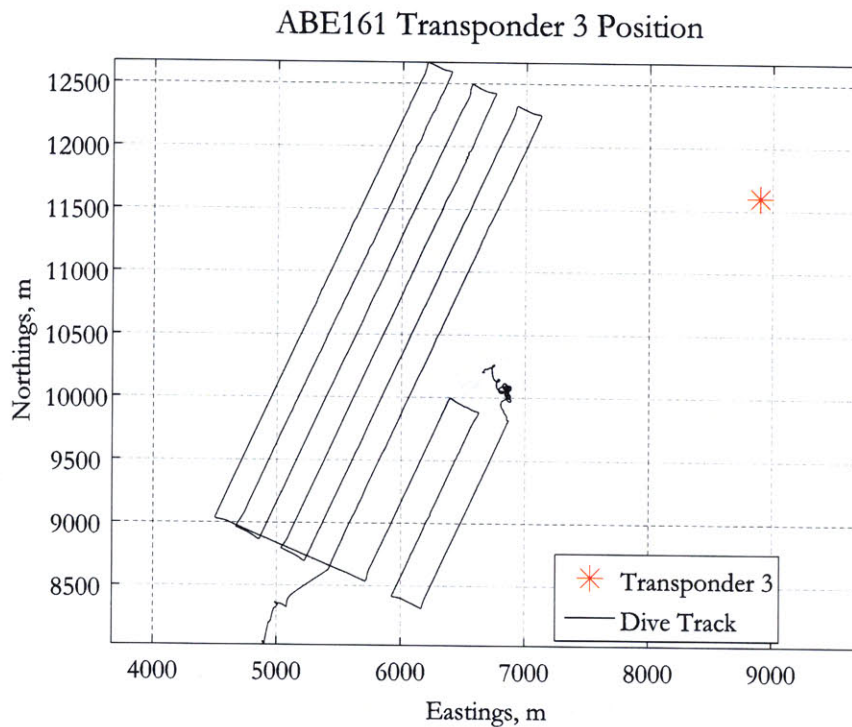
Figure 7-23: ABE161 tracklines and Transponder 3 location.

Raw Two Way Acoustic Times of Flight
ABE161 Transponder 3
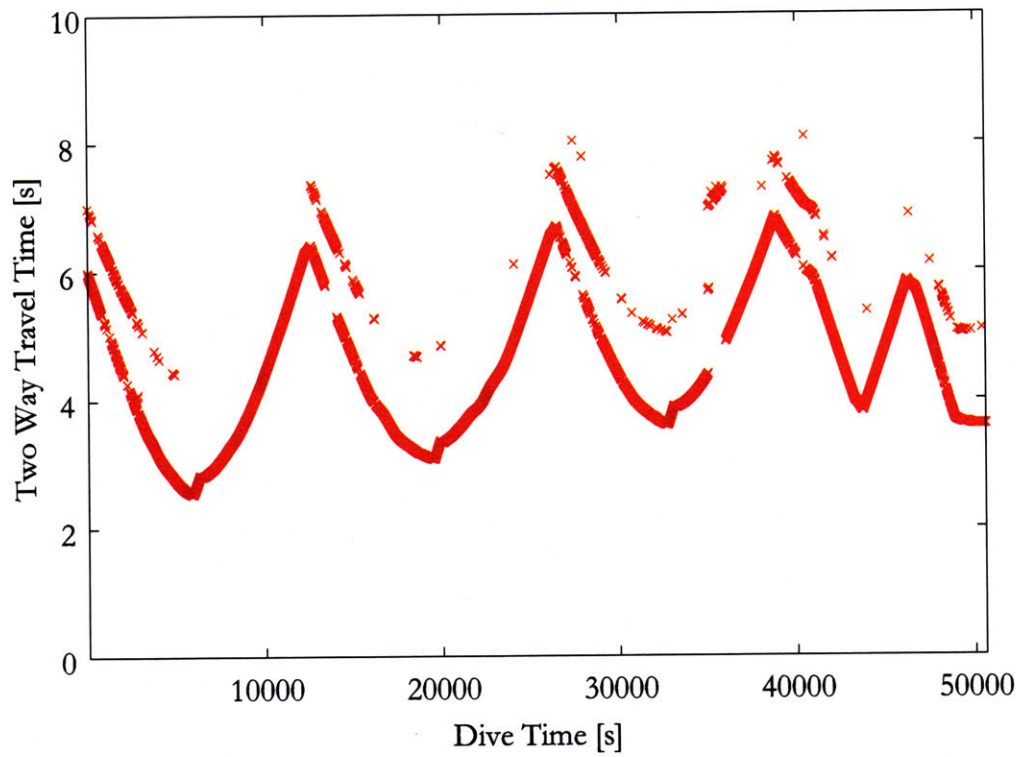
Figure 7-24: ABE161 Transponder 3 raw two-way acoustic travel times.

7.1.3.1 ABE161 Transponder 3 Hypothesis Generation Step

Figure 7-25 shows the raw acoustic data after it has been transformed into horizontal ranges for each of the three possible acoustic paths. For each travel time received by ABE, the corresponding range if the signal was direct path is shown in blue, for triangle path is shown in red, and double bounce is shown in green. The black line indicates the actual distance between vehicle and transponder throughout the dive. Therefore, the ranges that fall along that line indicate which acoustic path the received acoustic signal actually followed for each navigation cycle.
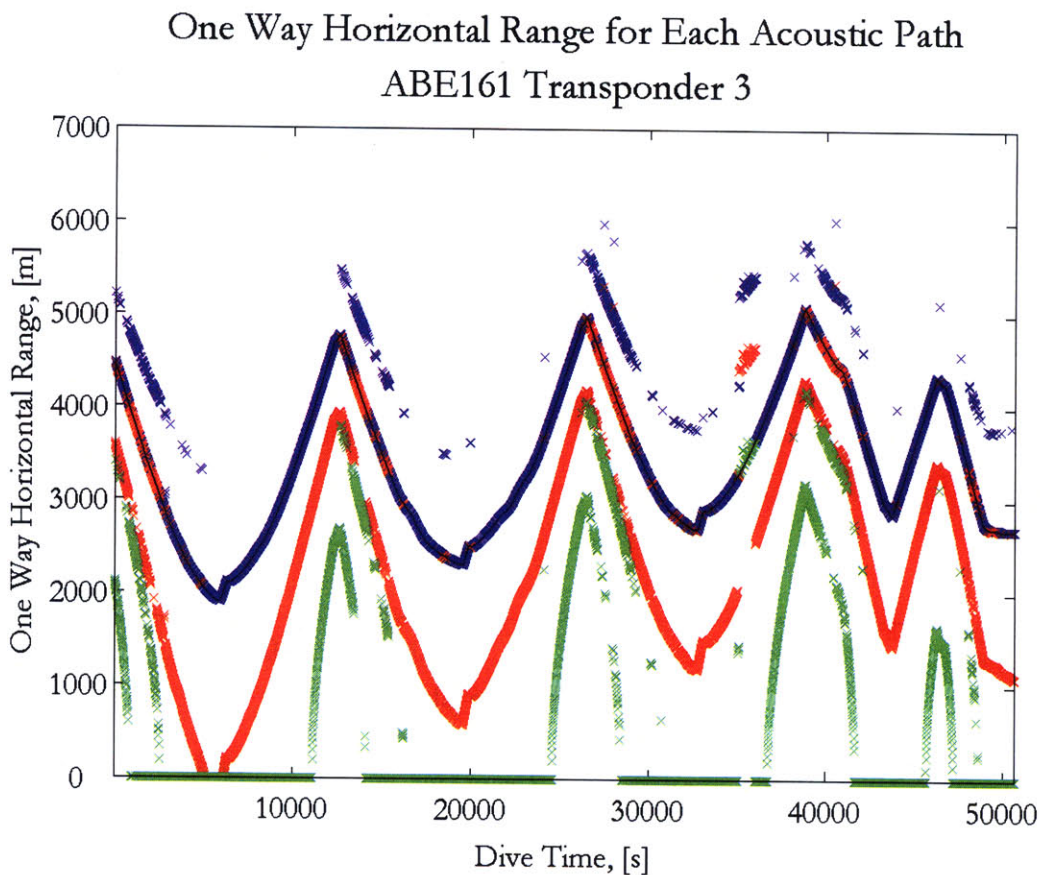
Figure 7-25: ABE161 Transponder 3 horizontal ranges for possible acoustic paths.

For Transponder 3, there was good direct path data throughout most of the dive except for periods of triangle path returns at the beginning of each inbound trackline. From these horizontal range hypotheses, up to six pose hypotheses were created for

Cumulative Location Hypotheses Before Arbitration
ABE161 Transponder 3

Figure 7-26: ABE161 Transponder 3 generated pose hypotheses, plotted cumulatively over the entire course of the dive.

the vehicle in each navigation cycle. Figure 7-26 shows a cumulative plot of all of the pose hypotheses created from the observed horizontal ranges over the course of the entire dive before any arbitration was conducted.

7.1.3.2   ABE161 Transponder 3 Grid Arbitration Step

The first level of the arbitration process is the grid arbiter. Figure 7-27 shows all the pose hypotheses that survived the grid arbitration process, again plotted cumulatively over the course of the whole dive.

Table 7.3 presents a performance metric for the grid arbiter based on the percentage of the total navigation cycles in which each type of pose hypothesis was eliminated by the grid arbiter. A cumulative statistic is also presented representing the percentage of total navigation cycles in which at least one pose hypothesis was eliminated by the grid arbiter. The cumulative number does not equal the sum of the individual statistics because more than one pose hypothesis may have been eliminated in any given navigation cycle.

Again, it is important to understand that the performance metric used is a percentage of total navigation cycles, not a percentage of total pose hypotheses. Depending on the travel time recorded in each navigation cycle, not all six of the possible types of pose hypotheses were necessarily generated. For example, if the distance between the transponder and vehicle was less than the water depth and a direct path return was received for a given navigation cycle, there is no physical way for a triangle path or double bounce path range hypothesis to be generated with that information. Therefore, only direct path hypotheses would be generated total in that navigation cycle. For Transponder 3 on this dive, again there were relatively few double bounce hypotheses generated over the course of the dive, as evident in Figure 7-25. Therefore, even though the statistics for double bounce paths in Table 7.3 appear low, they actually represent a high percentage of the double bounce hypotheses generated over the course of the dive. Overall, the grid arbiter had a significant effect for Transponder 3.

Cumulative Location Hypotheses After Grid Arbitration
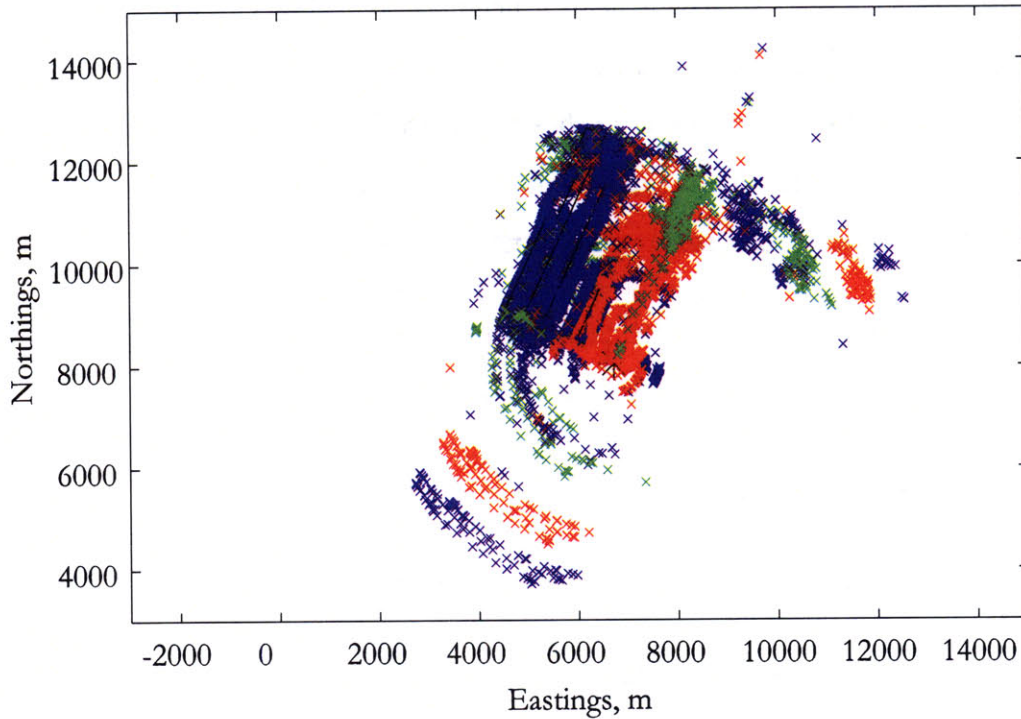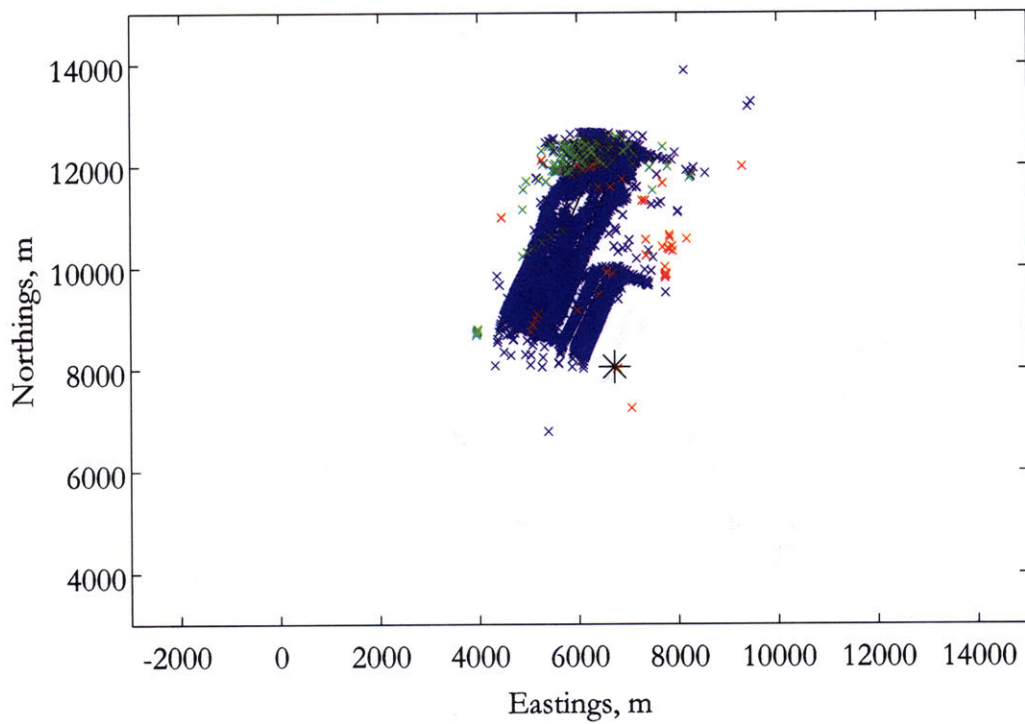ABE161 Transponder 3

Figure 7-27: ABE161 Transponder 3 pose hypotheses after grid arbitration, plotted cumulatively over the entire course of the dive.

Table 7.3: ABE161 Transponder 3 grid arbiter performance metrics.

	Percentage of navigation cycles in which an elimination occurred
Direct path 1	48.29
Direct path 2	51.43
Triangle path 1	43.31
Triangle path 2	42.45
Double bounce path 1	13.14
Double bounce path 2	15.86
Cumulative	91.24

7.1.3.3 ABE161 Transponder 3 Primary Arbitration Step

The pose hypotheses that survive the grid arbiter process are then input into the primary arbiter, which selects the single nearest neighbor hypothesis for every navigation cycle. Figure 7-28 depicts the acoustic range at every time frame corresponding to each chosen nearest neighbor pose hypotheses. Figure 7-29 shows the same information spatially by depicting a cumulative plot over the course of the whole dive of the nearest neighbor pose hypotheses from each navigation cycle.
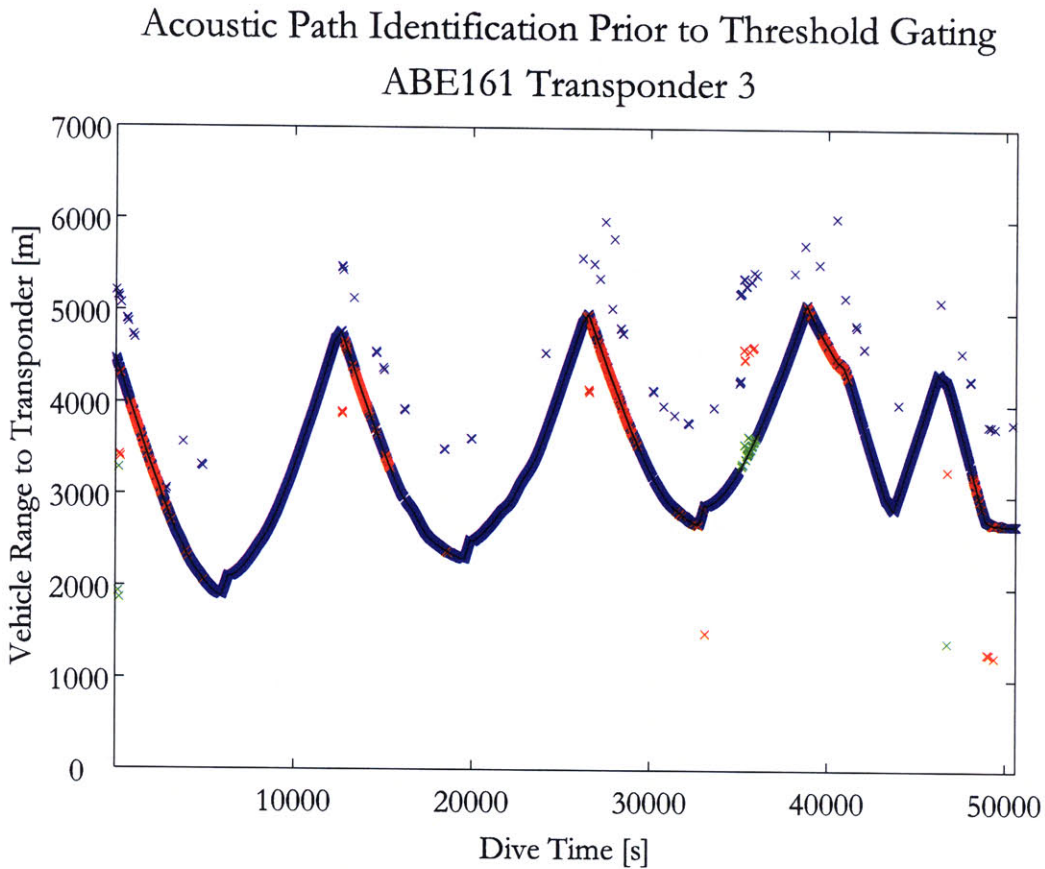
Figure 7-28: ABE161 Transponder 3 horizontal ranges corresponding to pose hypotheses after primary arbitration.
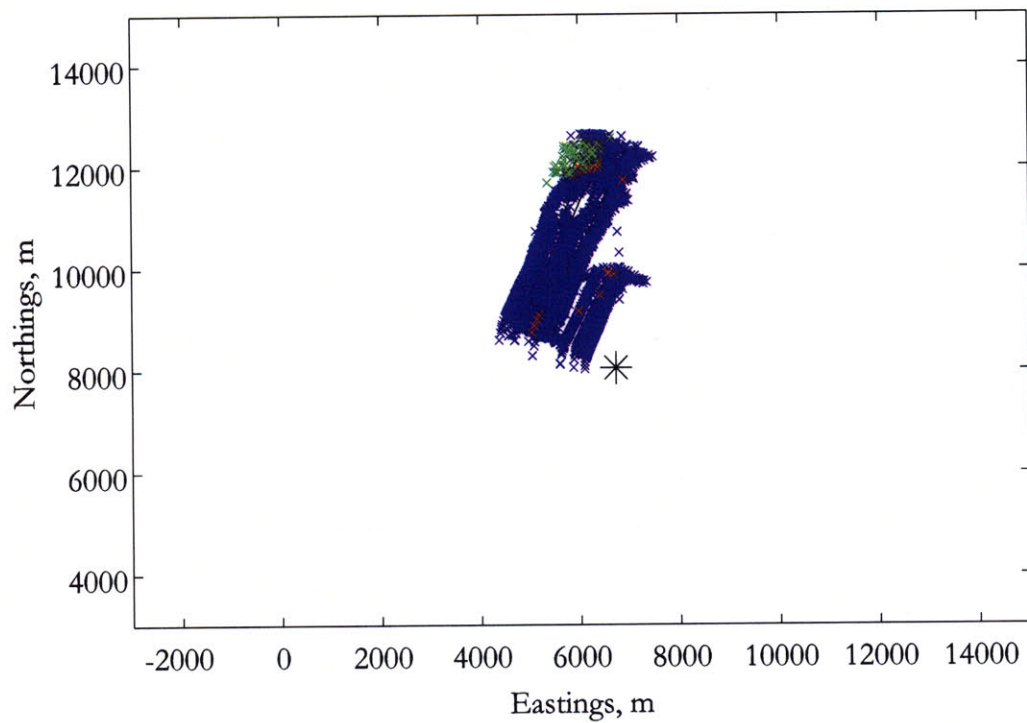
Figure 7-29: ABE161 Transponder 3 pose hypotheses after primary arbitration, plotted cumulatively over the entire course of the dive.

7.1.3.4 ABE161 Transponder 3 Threshold Gating Step

The pose hypothesis that is output from the primary arbiter at each navigation cycle is subject to threshold gating to ensure that it is a valid hypothesis. Figure 7-30 depicts the acoustic ranges corresponding to the pose hypotheses that survived the threshold gating process. Figure 7-31 shows the same information spatially by depicting a cumulative plot of the threshold-gated hypotheses from each navigation cycle.

Figure 7-30: ABE161 Transponder 3 horizontal ranges corresponding to pose hypotheses after threshold gating.

Cumulative Location Hypotheses After Threshold Gating
ABE161 Transponder 3

Figure 7-31: ABE161 Transponder 3 pose hypotheses after threshold gating, plotted cumulatively over the entire course of the dive.

7.1.4 ABE161 Transponder 4

The position of Transponder 4 with relation to the tracklines for ABE161 is shown in Figure 7-32. The raw two-way travel times of the Transponder 4 returns observed by the vehicle are shown in Figure 7-33. The data is again relatively clean with good direct path data is some of the dive. However, there were extended periods of only bounce path returns as well.
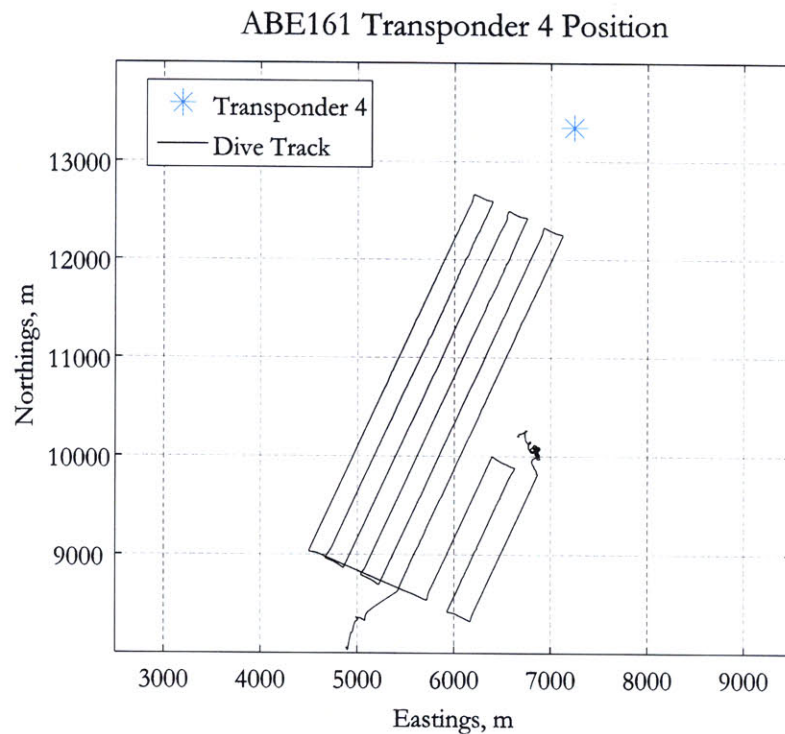
Figure 7-32: ABE161 tracklines and Transponder 4 location.

Raw Two Way Acoustic Times of Flight
ABE161 Transponder 4
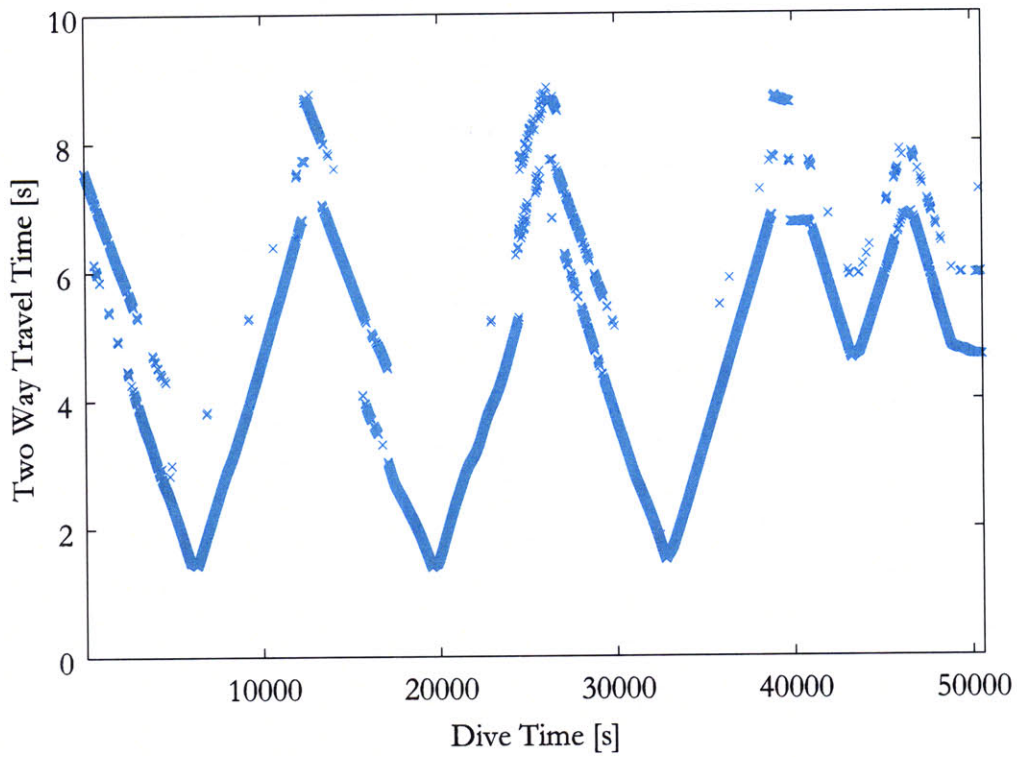
Figure 7-33: ABE161 Transponder 4 raw two-way acoustic travel times.

7.1.4.1 ABE161 Transponder 4 Hypothesis Generation Step

Figure 7-34 shows the raw acoustic data after it has been transformed into horizontal ranges for each of the three possible acoustic paths. For each travel time received by ABE, the corresponding range if the signal was direct path is shown in blue, for triangle path is shown in red, and double bounce is shown in green. The black line indicates the actual distance between vehicle and transponder throughout the dive. Therefore, the ranges that fall along that line indicate which acoustic path the received acoustic signal actually followed for each navigation cycle.

One Way Horizontal Range for Each Acoustic Path
ABE161 Transponder 4
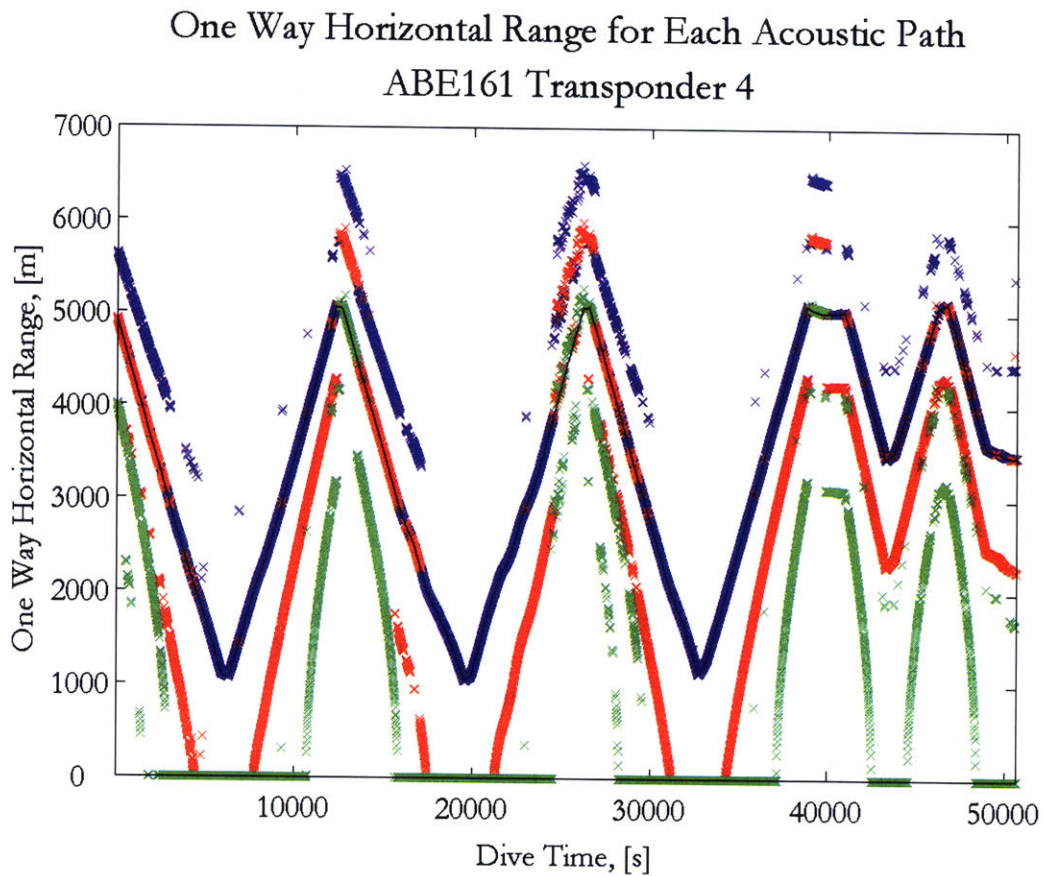
Figure 7-34: ABE161 Transponder 4 horizontal ranges for possible acoustic paths.

For Transponder 4, there were some periods with good direct path data and other periods with consistent triangle or bounce path returns. From these horizontal range hypotheses, up to six pose hypotheses were created for the vehicle in each navigation
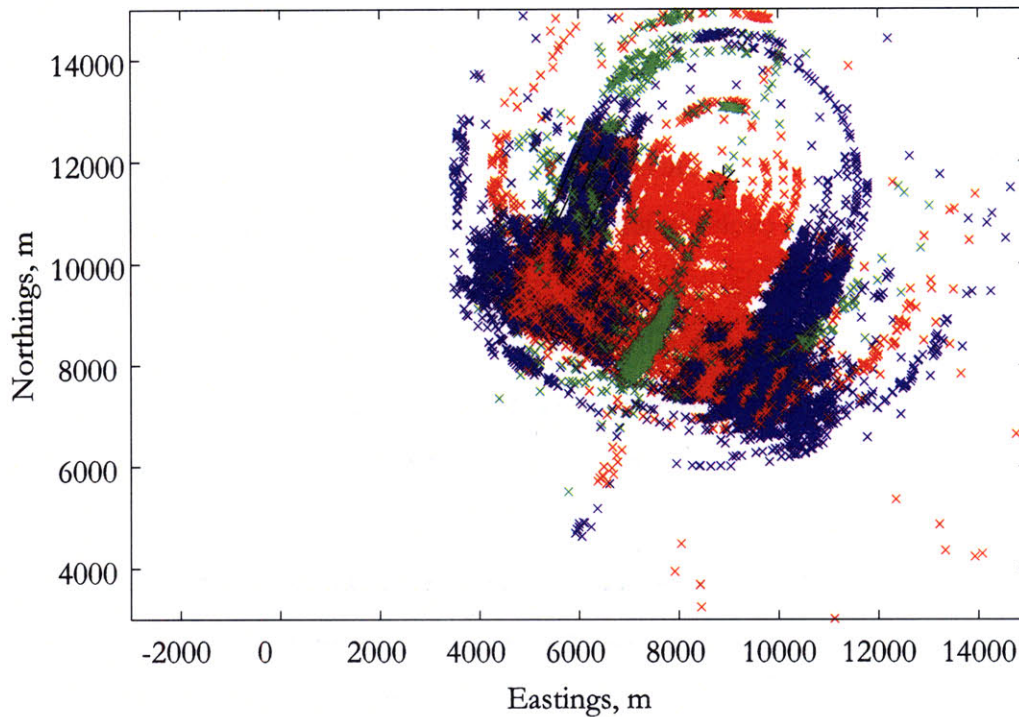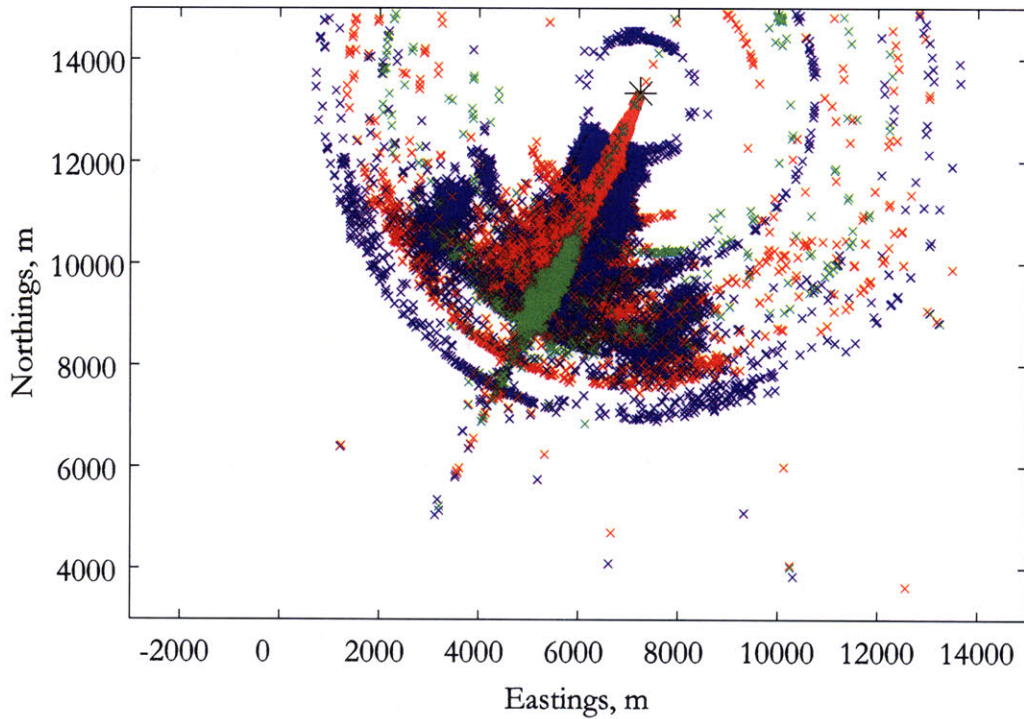
Figure 7-35: ABE161 Transponder 4 generated pose hypotheses, plotted cumulatively over the entire course of the dive.

cycle. Figure 7-35 shows a cumulative plot of all of the pose hypotheses created from the observed horizontal ranges over the course of the entire dive before any arbitration was conducted.

7.1.4.2 ABE161 Transponder 4 Grid Arbitration Step

The first level of the arbitration process is the grid arbiter. Figure 7-36 shows all the pose hypotheses that survived the grid arbitration process, again plotted cumulatively over the course of the whole dive.

Table 7.4 presents a performance metric for the grid arbiter based on the percentage of the total navigation cycles in which each type of pose hypothesis was eliminated by the grid arbiter. A cumulative statistic is also presented representing the percentage of total navigation cycles in which at least one pose hypothesis was eliminated by the grid arbiter. The cumulative number does not equal the sum of the individual statistics because more than one pose hypothesis may have been eliminated in any given navigation cycle.

Again, it is important to understand that the performance metric used is a percentage of total navigation cycles, not a percentage of total pose hypotheses. Depending on the travel time recorded in each navigation cycle, not all six of the possible types of pose hypotheses were necessarily generated. For example, if the distance between the transponder and vehicle was less than the water depth and a direct path return was received for a given navigation cycle, there is no physical way for a triangle path or double bounce path range hypothesis to be generated with that information. Therefore, only direct path hypotheses would be generated total in that navigation cycle. For Transponder 4 on this dive, again there were relatively few double bounce hypotheses generated over the course of the dive, as evident in Figure 7-34. Therefore, even though the statistics for double bounce paths in Table 7.4 appear low, they actually represent a high percentage of the double bounce hypotheses generated over the course of the dive. Overall, the grid arbiter had a moderate effect for Transponder 4.

Cumulative Location Hypotheses After Grid Arbitration
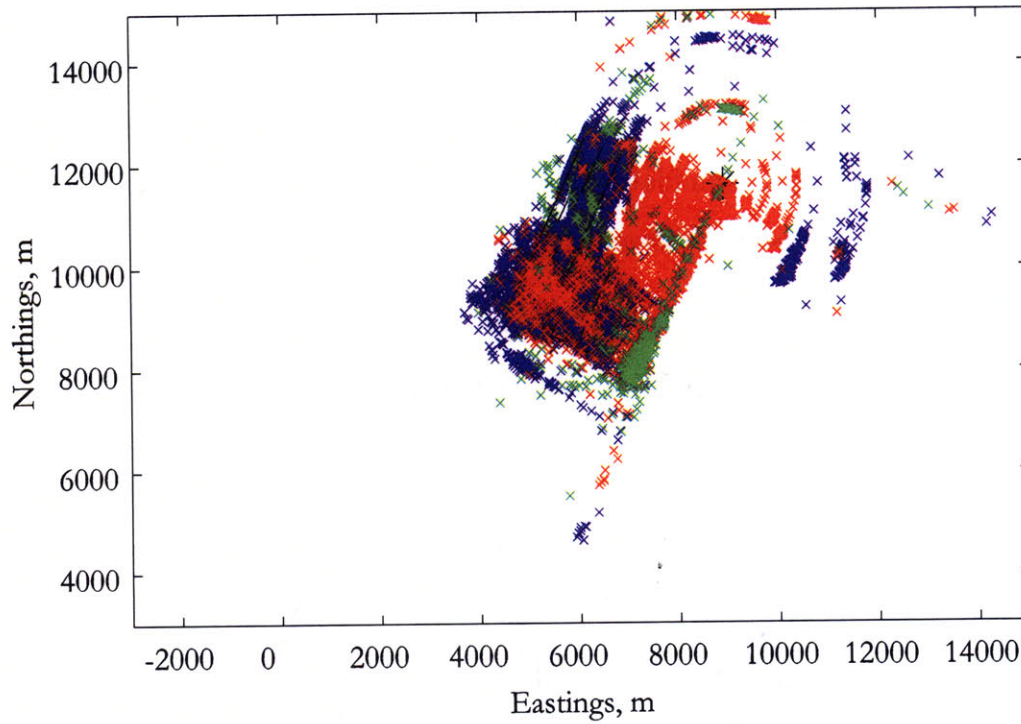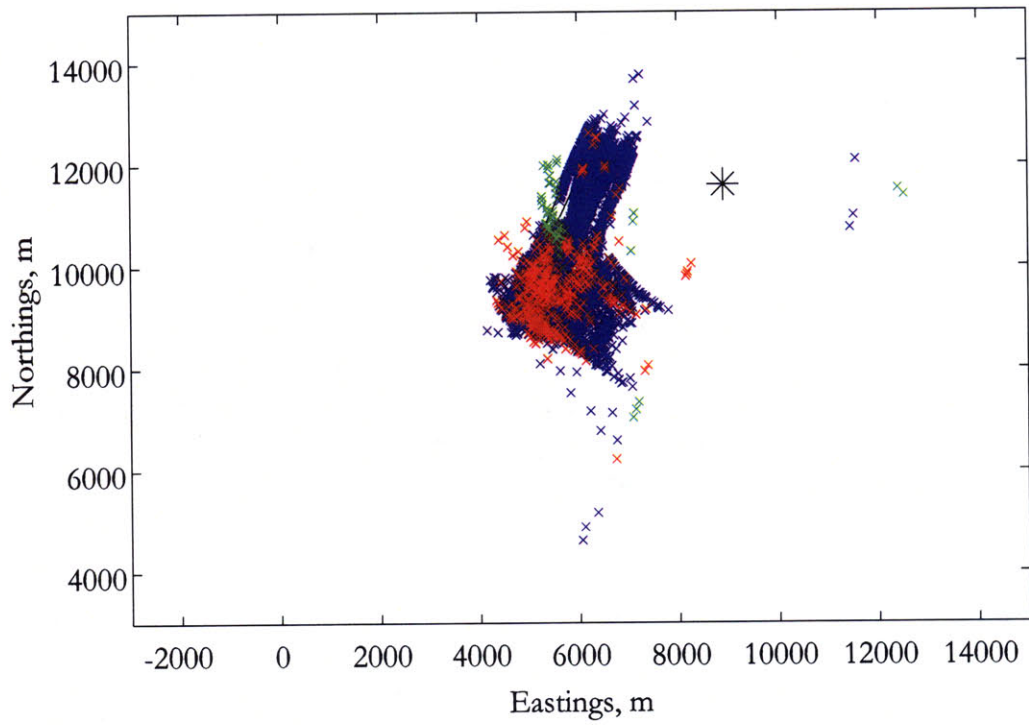ABE161 Transponder 4
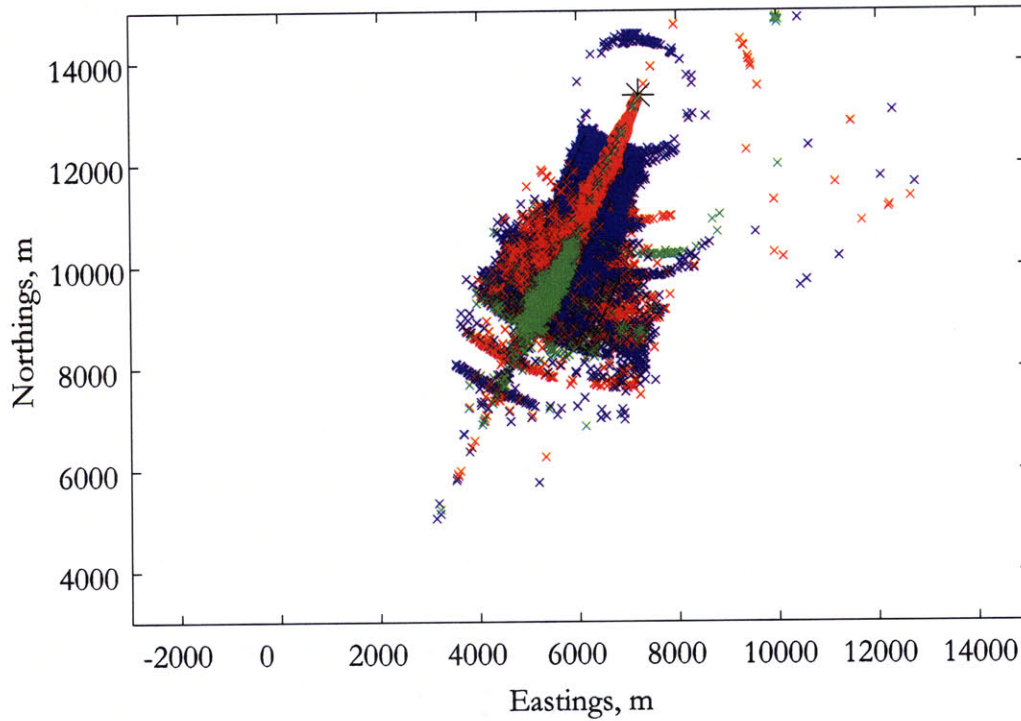
Figure 7-36: ABE161 Transponder 4 pose hypotheses after grid arbitration, plotted cumulatively over the entire course of the dive.

Table 7.4: ABE161 Transponder 4 grid arbiter performance metrics.

	Percentage of navigation cycles in which an elimination occurred
Direct path 1	25.61
Direct path 2	32.05
Triangle path 1	16.50
Triangle path 2	21.76
Double bounce path 1	9.10
Double bounce path 2	12.62
Cumulative	40.37

7.1.4.3 ABE161 Transponder 4 Primary Arbitration Step

The pose hypotheses that survive the grid arbiter process are then input into the primary arbiter, which selects the single nearest neighbor hypothesis for every navigation cycle. Figure 7-37 depicts the acoustic range at every time frame corresponding to each chosen nearest neighbor pose hypotheses. Figure 7-38 shows the same information spatially by depicting a cumulative plot over the course of the whole dive of the nearest neighbor pose hypotheses from each navigation cycle.
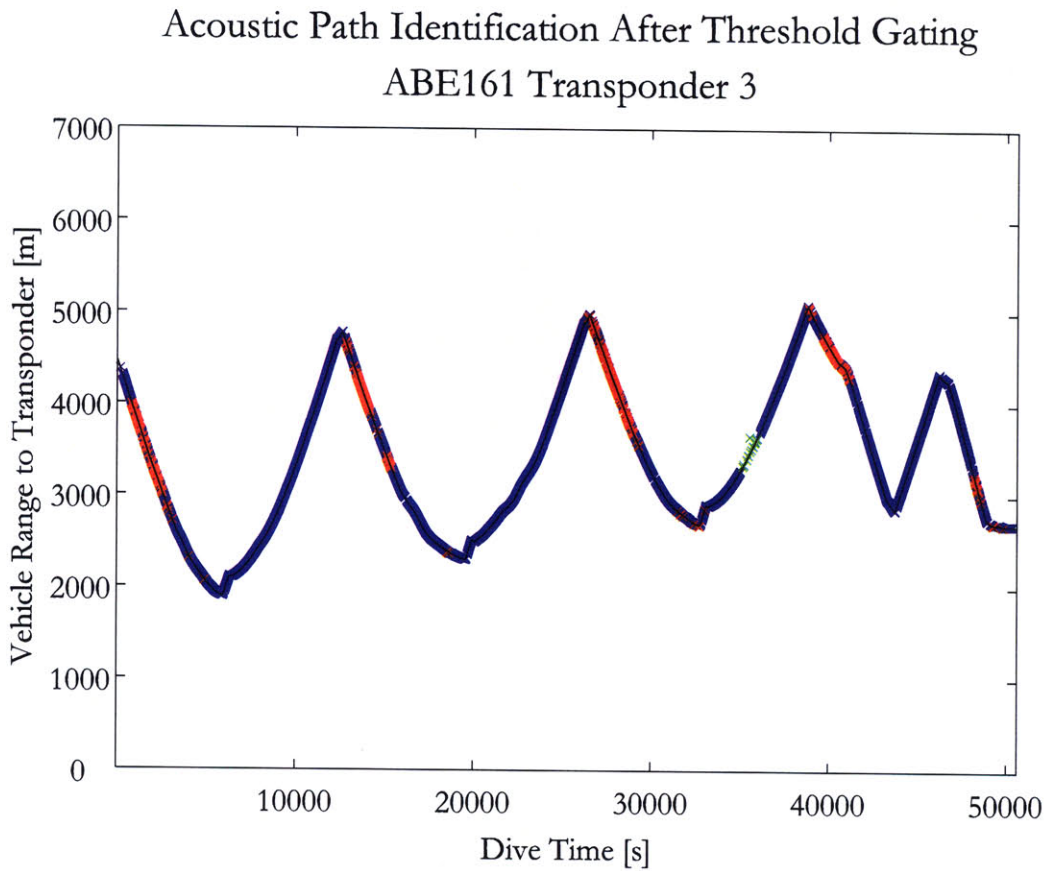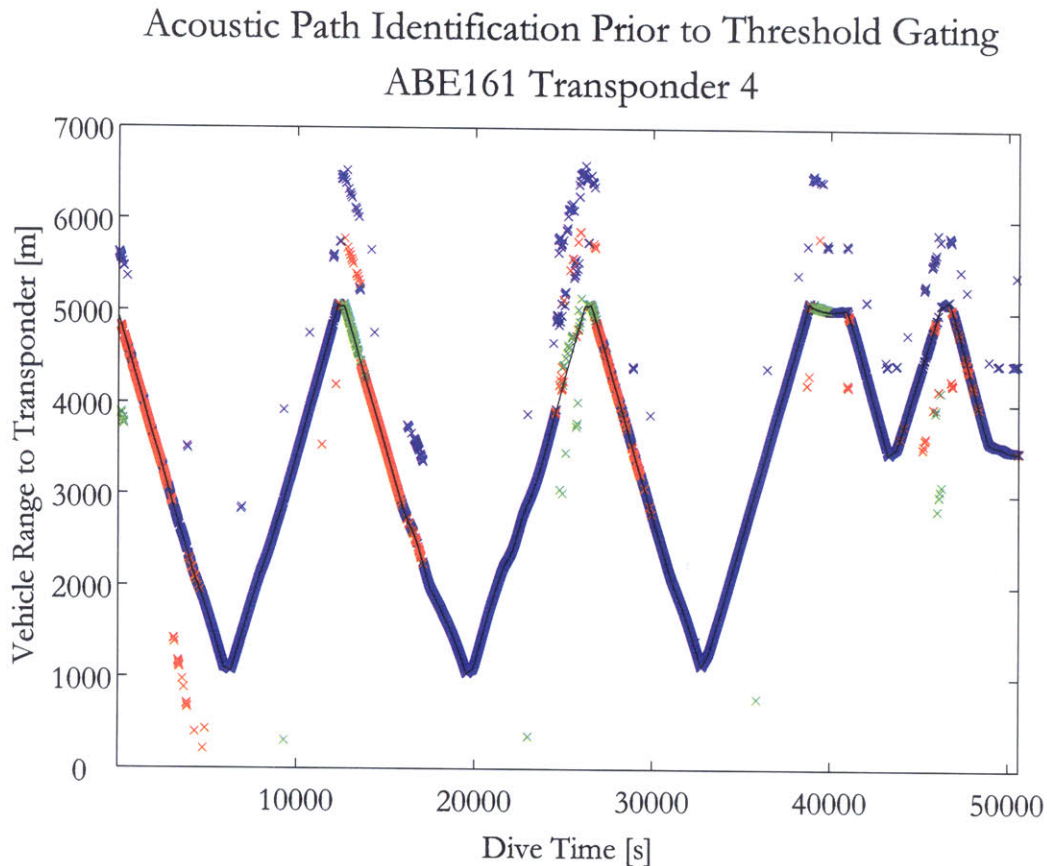

Figure 7-37: ABE161 Transponder 4 horizontal ranges corresponding to pose hypotheses after primary arbitration.

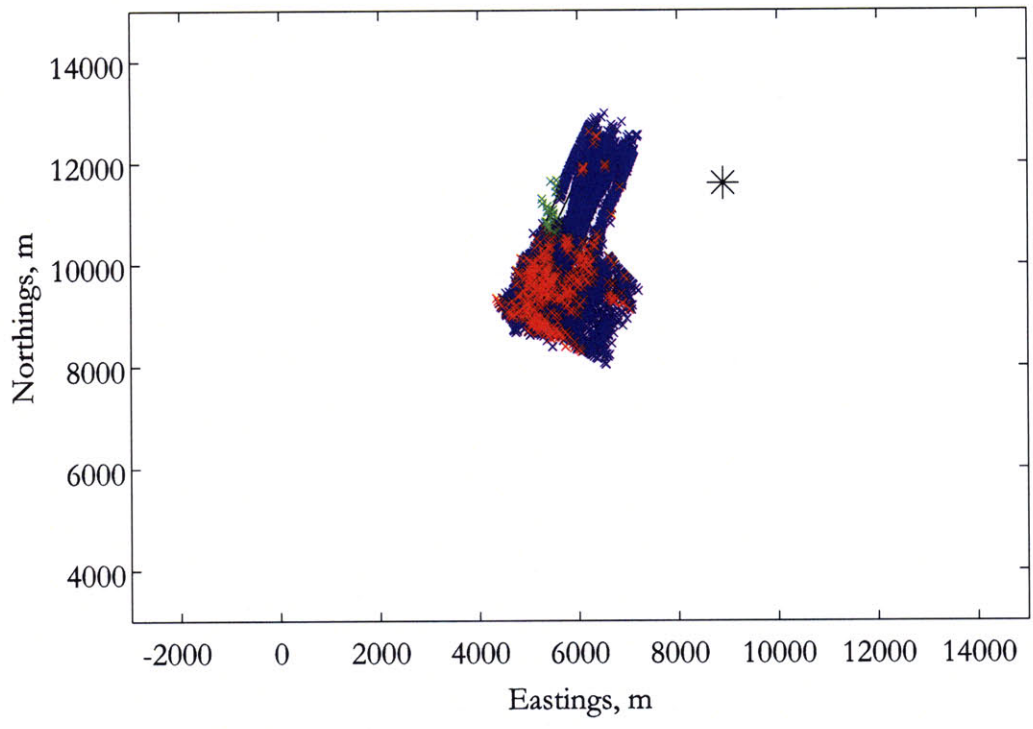## Cumulative Location Hypotheses After Arbitration
ABE161 Transponder 4
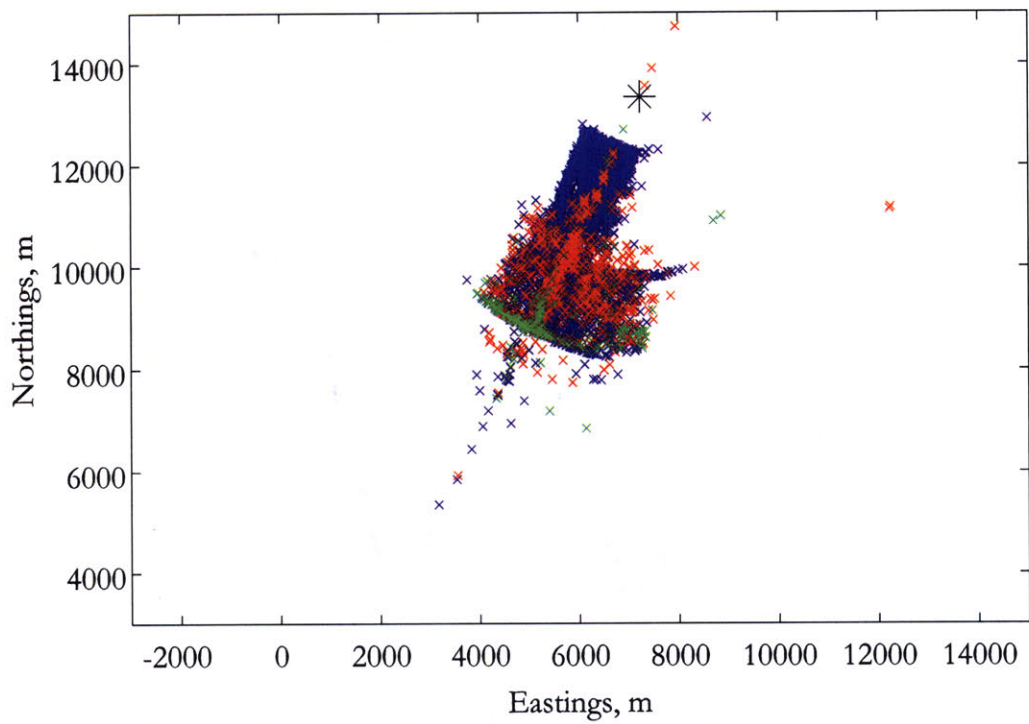
Figure 7-38: ABE161 Transponder 4 pose hypotheses after primary arbitration, plotted cumulatively over the entire course of the dive.

7.1.4.4 ABE161 Transponder 4 Threshold Gating Step

The pose hypothesis that is output from the primary arbiter at each navigation cycle is subject to threshold gating to ensure that it is a valid hypothesis. Figure 7-39 depicts the acoustic ranges corresponding to the pose hypotheses that survived the threshold gating process. Figure 7-40 shows the same information spatially by depicting a cumulative plot of the threshold-gated hypotheses from each navigation cycle.
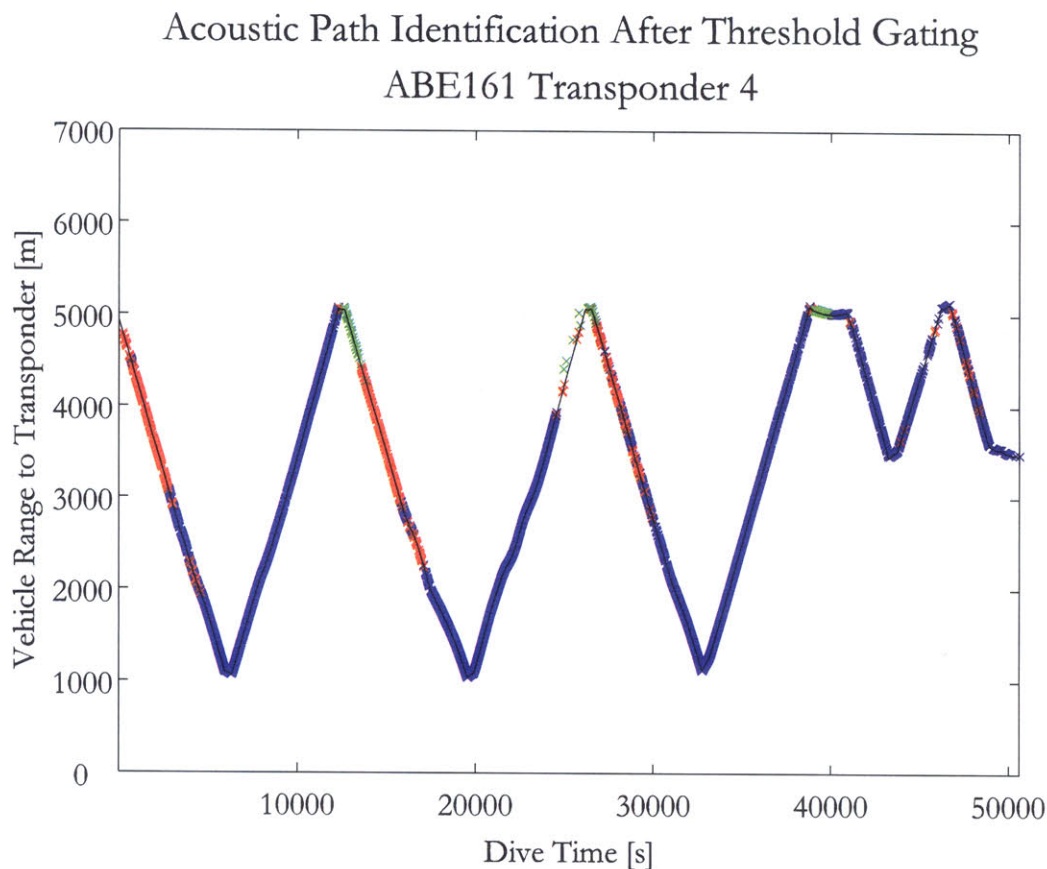
Figure 7-39: ABE161 Transponder 4 horizontal ranges corresponding to pose hypotheses after threshold gating.

Cumulative Location Hypotheses After Threshold Gating
ABE161 Transponder 4
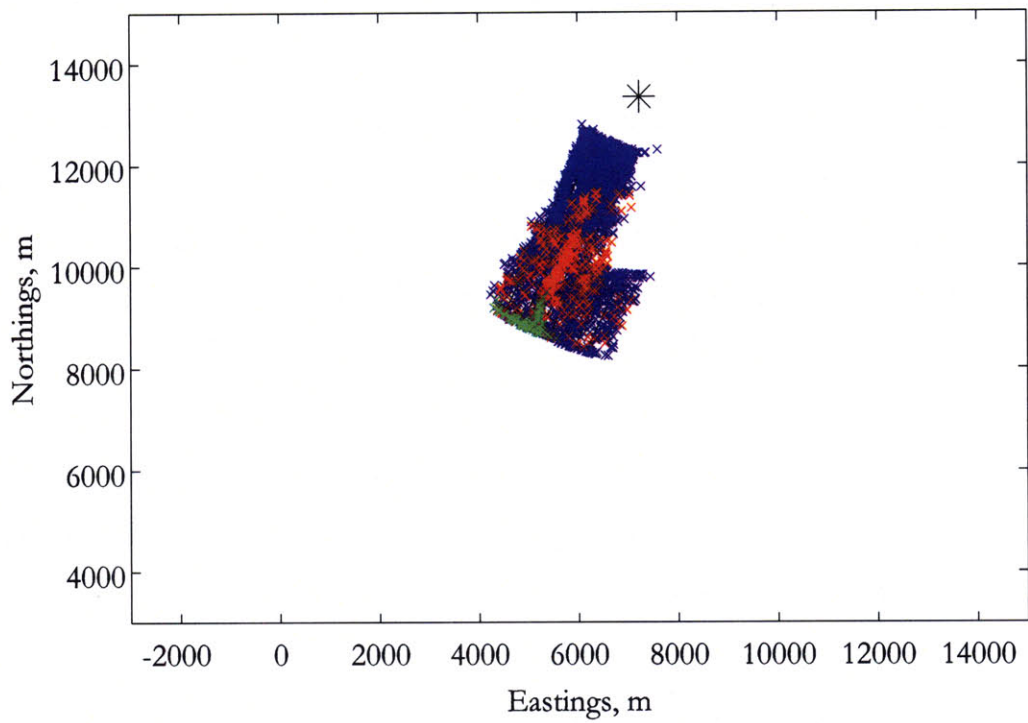
Figure 7-40: ABE161 Transponder 4 pose hypotheses after threshold gating, plotted cumulatively over the entire course of the dive.

7.1.5 ABE161 Update Step and Performance Metrics

In the update step, the primary navigation process combines all the acoustic path returns that were identified *in situ* through each of the single transponder parallel hypothesis filters, as shown in Figure 7-41. Due to excessive noise in the bearing angle information, for reasons discussed below in Section 7.3, only the range and acoustic path identification information is retained for use in the update process. The ranges corresponding to the identified acoustic path hypotheses for each transponder in each navigation cycle are combined in a conventional least-squares trilateration method. For illustration purposes, the results are not filtered in any way to remove outliers. For actual navigation, an outlier rejection filter would be implemented. The blue markers indicate fixes that include only direct path returns. The red markers indicate fixes that used at least one triangle path return and any available direct path returns. The green markers indicate fixes that used at least one double bounce path return and any available direct path and triangle path returns.

As a metric of performance between the PH and LBL methods, total numbers of fixes generated and statistics regarding the time between four transponder fixes are compared in Table 7.5. Due to the fact that the gaps in the direct path data usually come in long intervals, the median time of the LBL method does not adequately illustrate the difference between the two methods. However, the maximum time and mean times are significantly less for the PH method, thus illustrating its real benefit. The minimum times for both the methods are dictated by the length of the navigation cycle. Figures 7-42, 7-43, and 7-44 show the same performance metrics when the data was processed using each combination of three total transponders in a data denial method. Figures 7-45, 7-46, and 7-47 show the same performance metrics when the data was processed using each combination of two total transponders. The same pattern of results is followed in the four, three and two transponder data.

Table 7.5: ABE161 performance metric comparison between the PH and LBL navigation methods using acoustic data from all four transponders.

	PH	LBL
Total number of fixes	2587	1735
Maximum time between fixes	1940 s	3590 s
Mean time between fixes	19.26 s	28.51 s
Median time between fixes	10.19 s	9.78 s
Minimum time between fixes	9.42 s	9.42 s
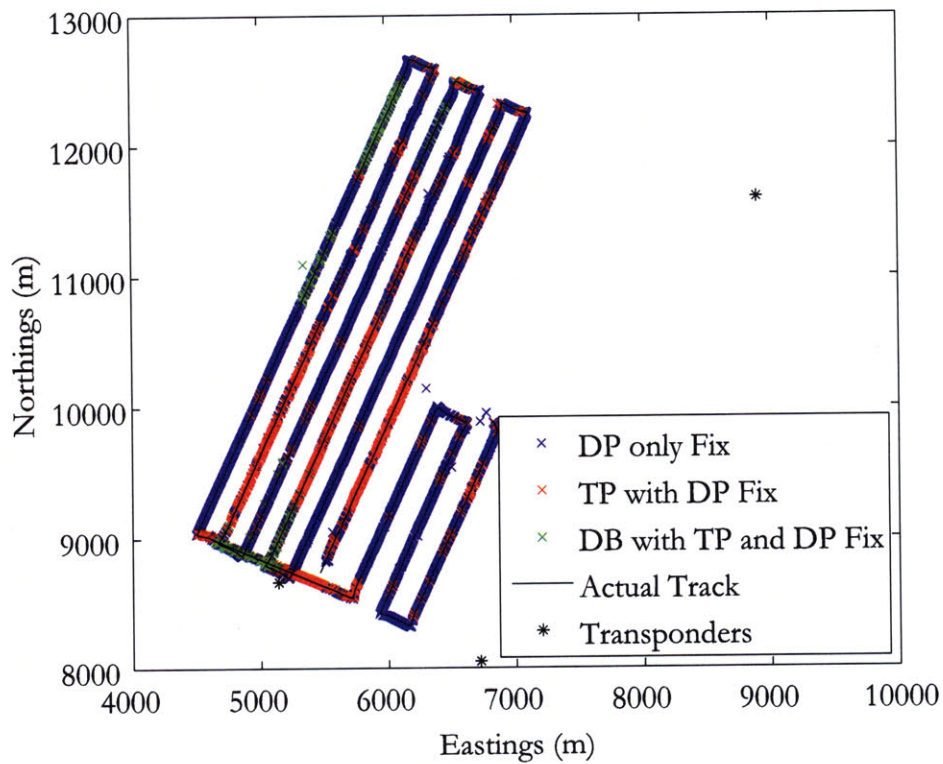
Figure 7-41: ABE161 results of the PH navigation algorithm.
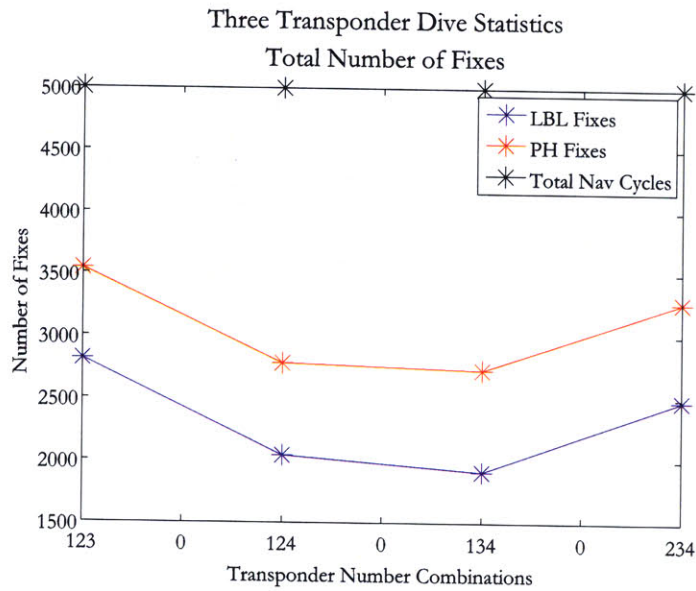
Figure 7-42: ABE161 comparison of total number of fixes between the PH and LBL methods for all possible combinations of three transponders.
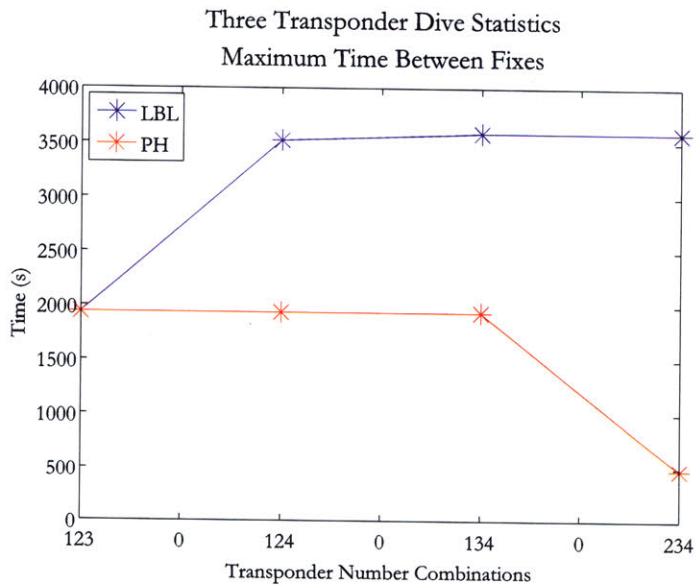
Figure 7-43: ABE161 comparison of maximum time between fixes for the PH and LBL methods for all possible combinations of three transponders.
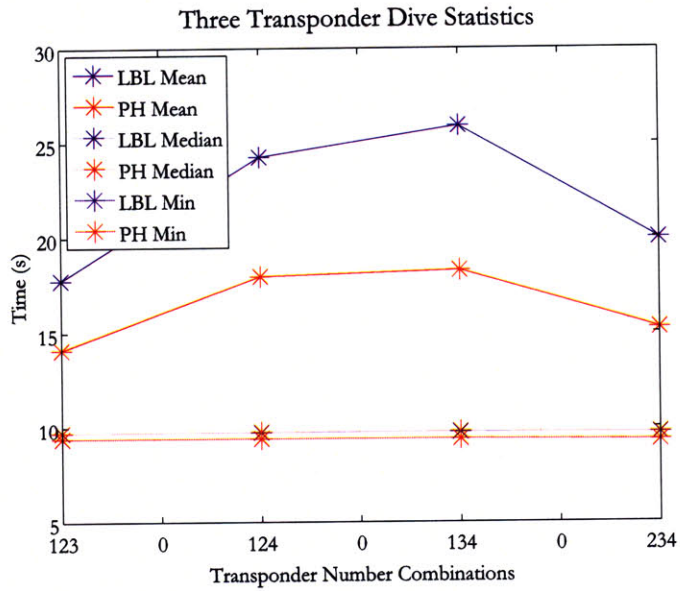
Figure 7-44: ABE161 comparison of mean, median and minimum time between fixes for the PH and LBL methods for all possible combinations of three transponders.
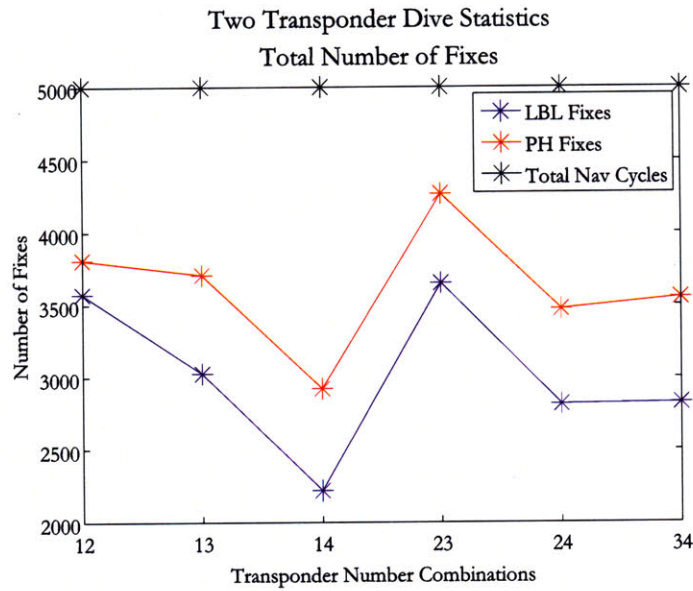
Figure 7-45: ABE161 comparison of total number of fixes between the PH and LBL methods for all possible combinations of two transponders.
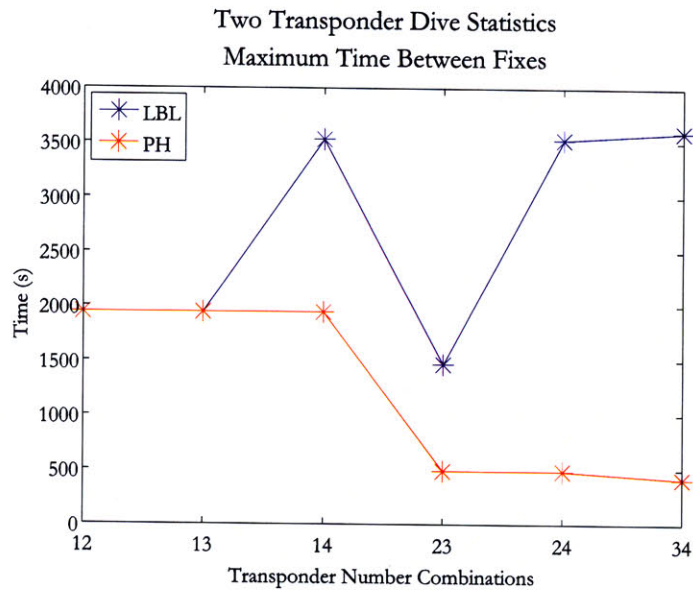
Figure 7-46: ABE161 comparison of maximum time between fixes for the PH and LBL methods for all possible combinations of two transponders.
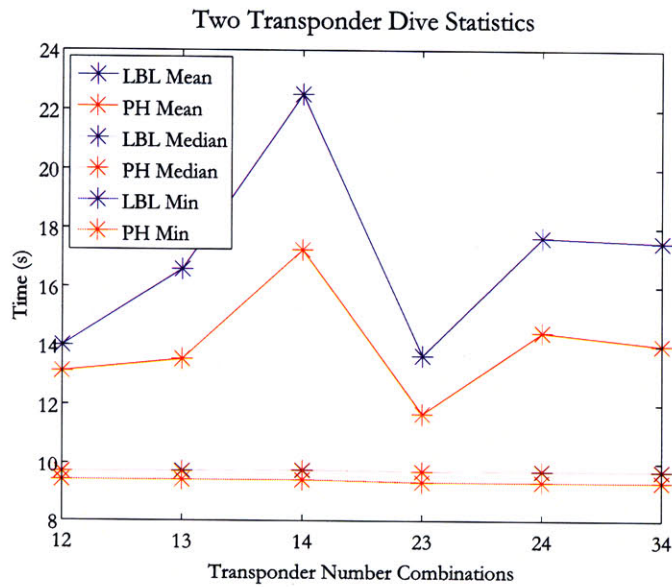
Figure 7-47: ABE161 comparison of mean, median and minimum time between fixes for the PH and LBL methods for all possible combinations of two transponders.

7.2   Parallel Hypothesis Navigation with Sentry016

This section will illustrate the PH navigation method in detail using dive Sentry016 as an example. For this dive, multipaths were present consistently for all transponders. Transponder 4 returns were sparse and intermittent throughout the dive. The locations of the transponders with respect to the tracklines is shown are 7-48. The tracklines represent the best post-processed calculation of vehicle position using LBL and DVL data. Acoustic data from four transponders were available for this dive as shown in Figure 7-49. For this run, the transponders were spaced widely compared to the water depth. The maximum slant range was nearly 7500 meters in water depth of approximately 1450 meters. As a result, the bounce paths were only slightly longer than the direct paths, which challenged the algorithms more than the previous runs.

The result of the PH algorithm is shown in Figure 7-50. In this plot, the blue markers indicate fixes that include only direct path returns. Due to INS dropouts during Sentry016, some non-real-time information was used in this particular result. Also, this result was processed without using the grid arbiter to illustrate the PH method with a two-level arbitration step. As for the previous dive, the red markers again indicate fixes that used at least one triangle path return and any available direct path returns. The green markers indicate fixes that used at least one double bounce path return and any available direct path and triangle path returns.

Over the following pages, the intermediate steps of the process will be illustrated in detail to demonstrate how the result was obtained. First, the hypothesis generation and arbitration steps will be looked at individually for each transponder. Then, at the end, the update step and performance metrics are discussed for the dive overall. In the navigation algorithm, the steps of the process are done iteratively in a loop for each time frame. Therefore, the cumulative plots of hypotheses that are shown for each step in the process for each transponder represent data that has been picked out of the loop during each navigation cycle at the appropriate stage.

Legends were omitted from the plots in this section and a common color scheme
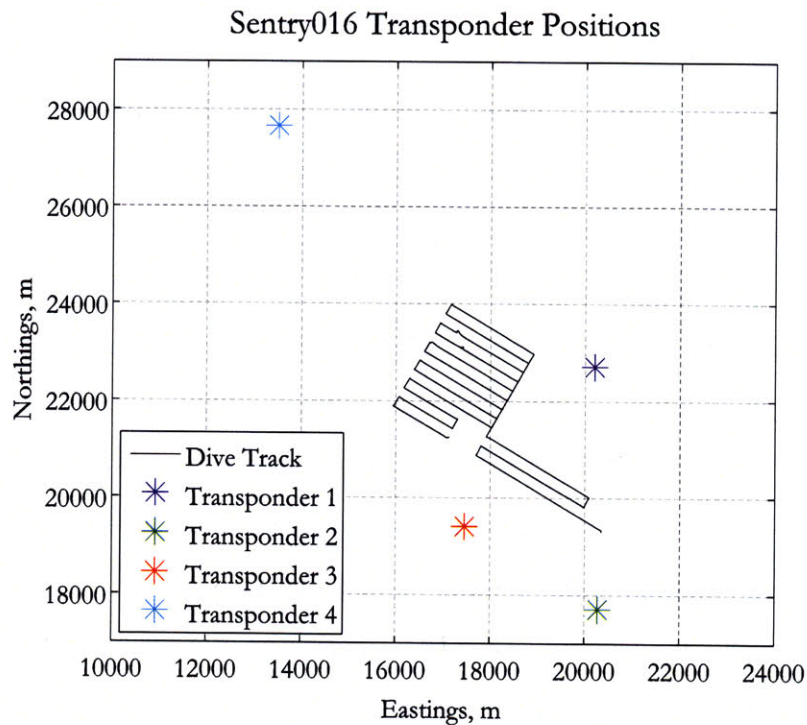
Figure 7-48: Sentry016 tracklines and transponder locations.

was used throughout for visual simplicity. In the common color scheme, blue markers represent direct path data, red markers represent triangle path data, and green markers represent double bounce data. The only exception to this color scheme is in the plots of raw acoustic two-way travel times where the colors corresponded to different transponders as shown in the legend of Figure 7-48.
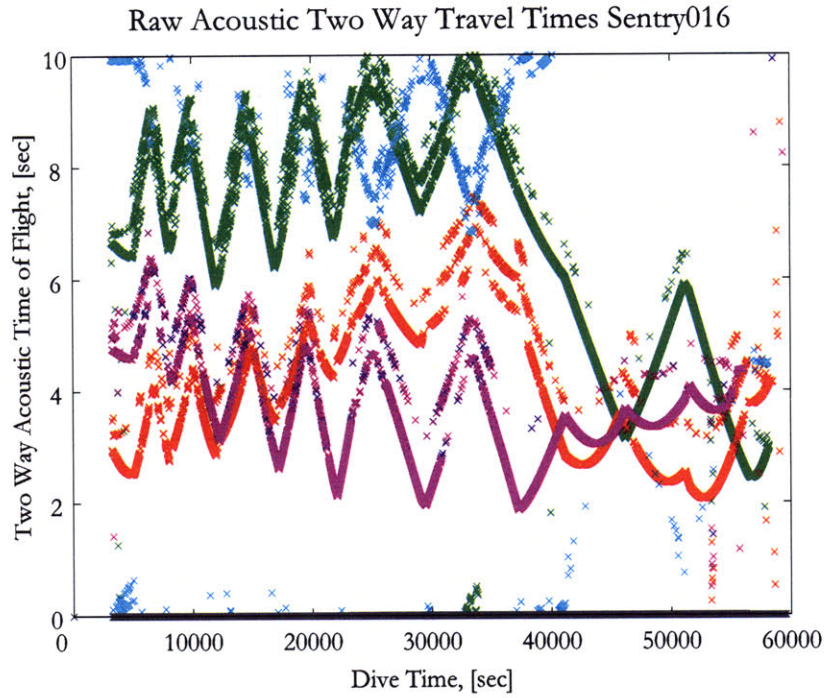
Figure 7-49: Sentry016 raw acoustic two-way travel times. Note that the bounce paths are only slightly longer than the direct paths, especially for the longer ranges.
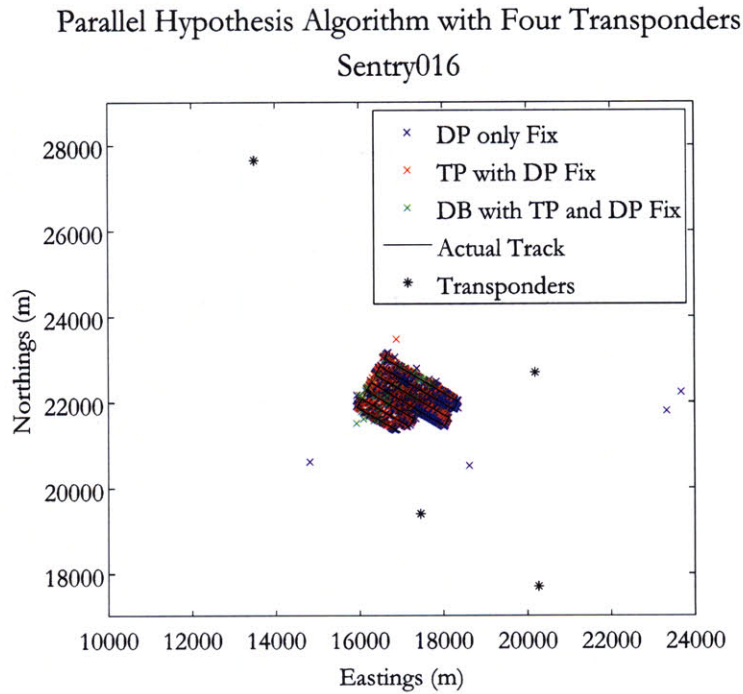
Figure 7-50: Sentry016 results of the PH navigation algorithm.

7.2.1 Sentry016 Transponder 1

The position of Transponder 1 with relation to the tracklines for Sentry016 is shown in Figure 7-51. The raw two-way travel times of the Transponder 1 returns observed by the vehicle are shown in Figure 7-52. There were significant periods without direct path acoustic returns and supplemented only intermittently with triangle path returns.
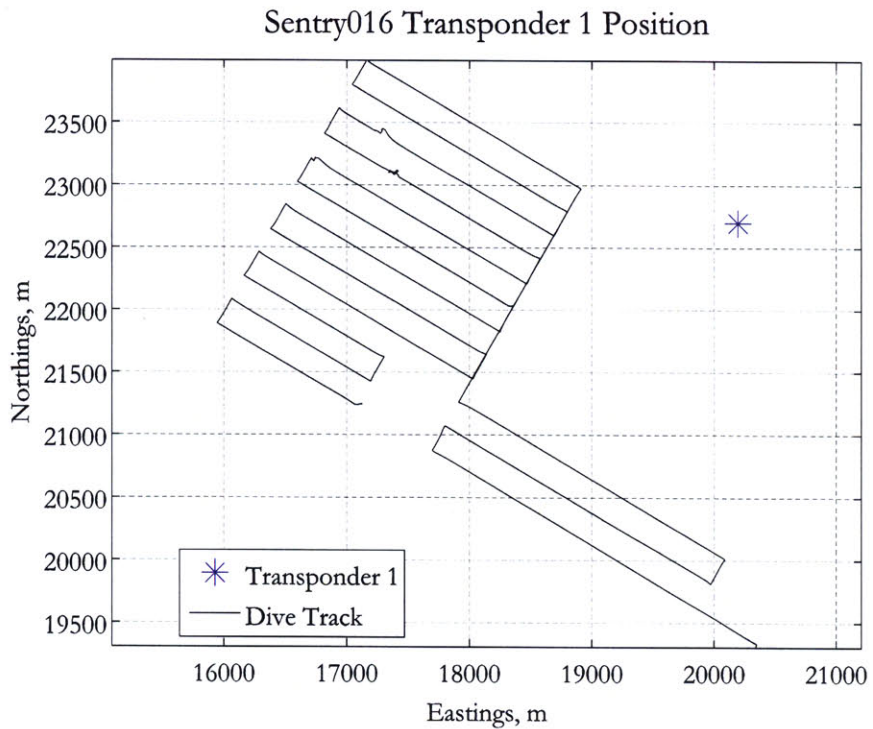
Figure 7-51: Sentry016 tracklines and Transponder 1 location.

Raw Two Way Acoustic Times of Flight
Sentry016 Transponder 1
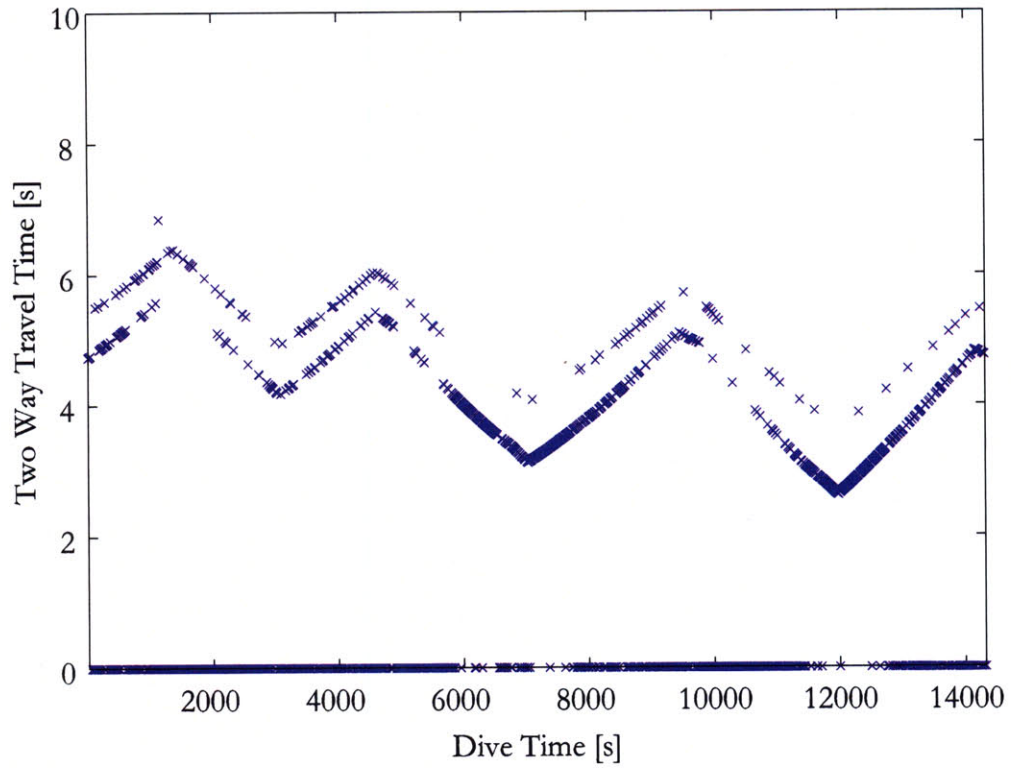
Figure 7-52: Sentry016 Transponder 1 raw two-way acoustic travel times.

7.2.1.1 Sentry016 Transponder 1 Hypothesis Generation Step

Figure 7-53 shows the raw acoustic data after it has been transformed into horizontal ranges for each of the three possible acoustic paths. For each travel time received by Sentry, the corresponding range if the signal was direct path is shown in blue, for triangle path is shown in red, and double bounce is shown in green. The black line indicates the actual distance between vehicle and transponder throughout the dive. Therefore, the ranges that fall along that line indicate which acoustic path the received acoustic signal actually followed for each navigation cycle.
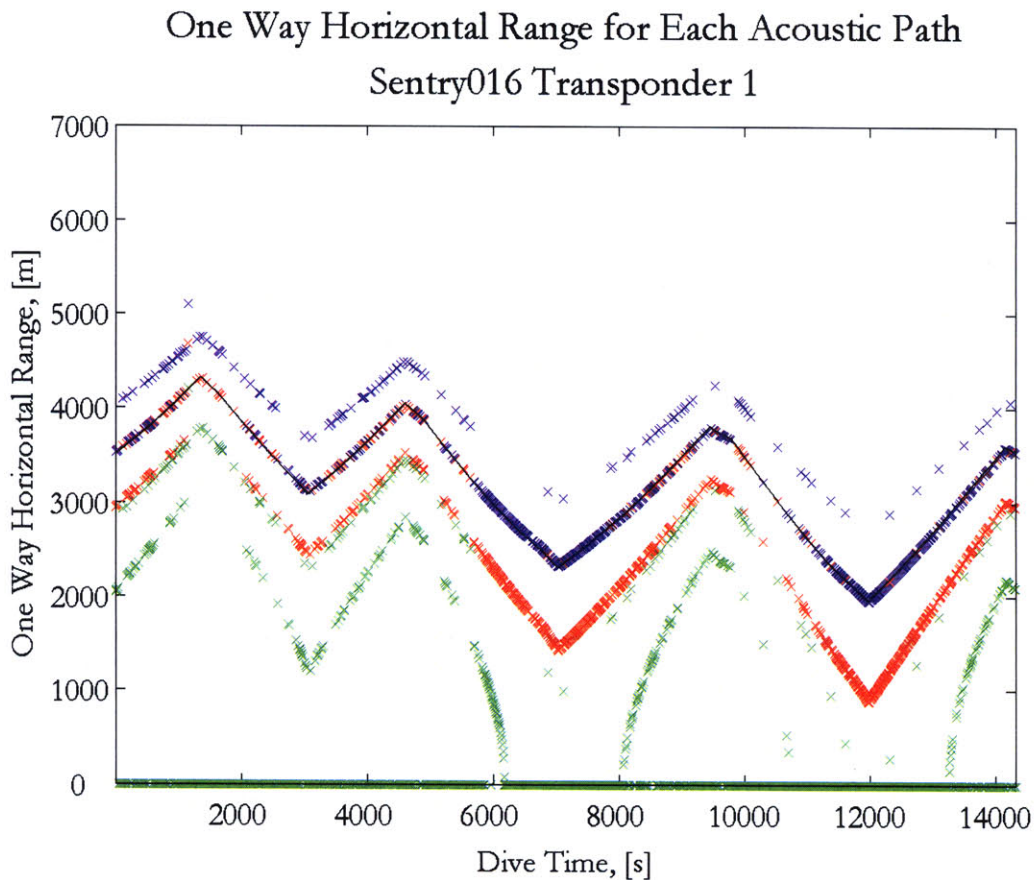
Figure 7-53: Sentry016 Transponder 1 horizontal ranges for possible acoustic paths.

For Transponder 1, there were significant periods without direct path acoustic returns and supplemented only intermittently with triangle path returns. From these horizontal range hypotheses, up to six pose hypotheses were created for the vehicle
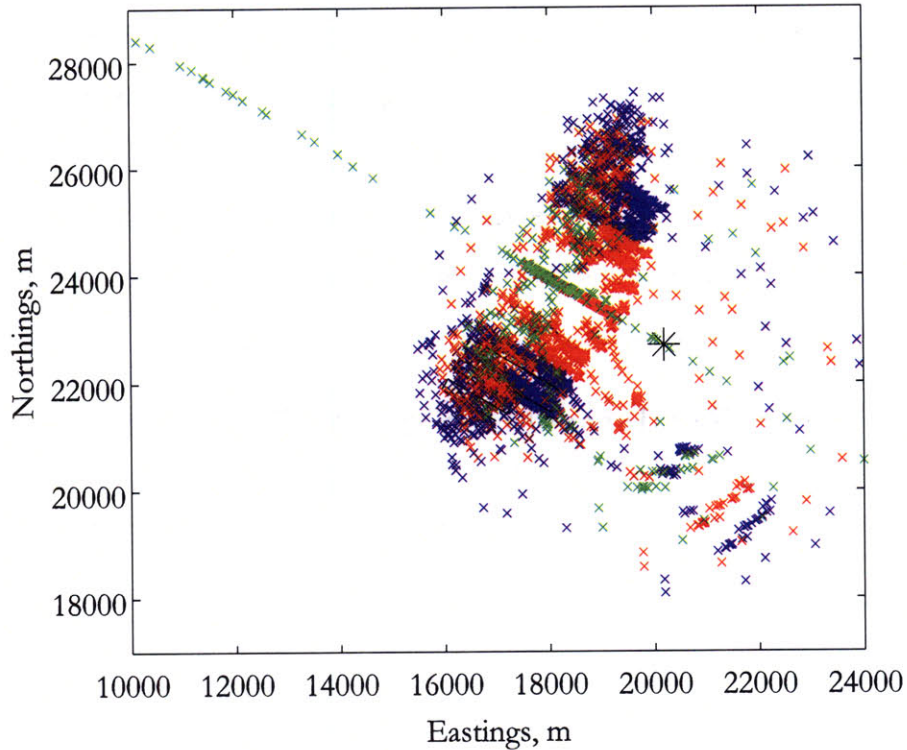
Figure 7-54: Sentry016 Transponder 1 generated pose hypotheses, plotted cumulatively over the entire course of the dive.

in each navigation cycle. Figure 7-54 shows a cumulative plot of all of the pose hypotheses created from the observed horizontal ranges over the course of the entire dive before any arbitration was conducted.

7.2.1.2 Sentry016 Transponder 1 Primary Arbitration Step

This dive was processed illustrating the PH method without the optional grid arbiter step, therefore all the pose hypotheses are input into the primary arbiter, which selects the single nearest neighbor hypothesis for every navigation cycle. Figure 7-55 depicts the acoustic range at every time frame corresponding to each chosen nearest neighbor pose hypotheses. Figure 7-56 shows the same information spatially by depicting a cumulative plot over the course of the whole dive of the nearest neighbor pose hypotheses from each navigation cycle.
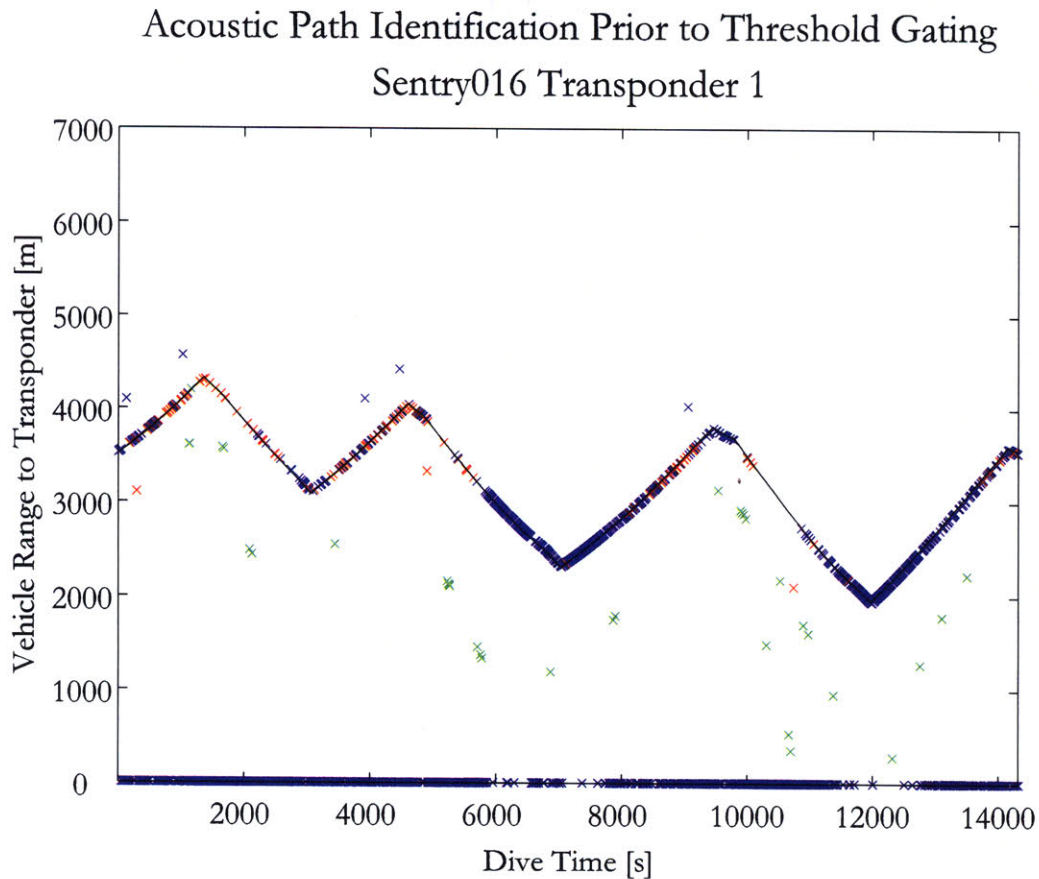
Figure 7-55: Sentry016 Transponder 1 horizontal ranges corresponding to pose hypotheses after primary arbitration.

Cumulative Location Hypotheses After Arbitration
Sentry016 Transponder 1
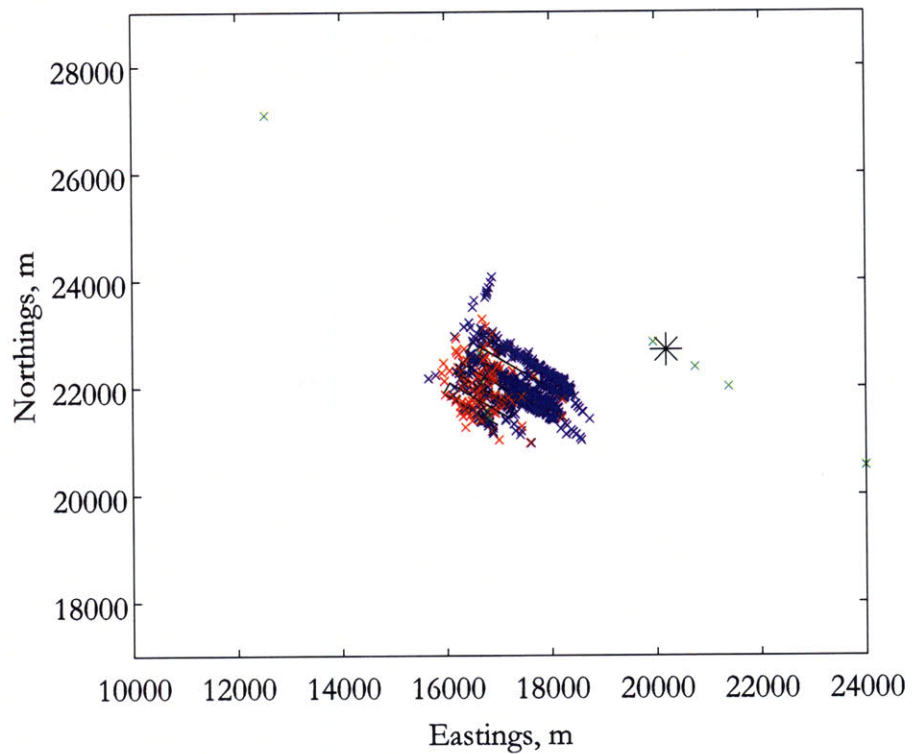
Figure 7-56: Sentry016 Transponder 1 pose hypotheses after primary arbitration, plotted cumulatively over the entire course of the dive.

7.2.1.3 Sentry016 Transponder 1 Threshold Gating Step

The pose hypothesis that is output from the primary arbiter at each navigation cycle is subject to threshold gating to ensure that it is a valid hypothesis. Figure 7-57 depicts the acoustic ranges corresponding to the pose hypotheses that survived the threshold gating process. Figure 7-58 shows the same information spatially by depicting a cumulative plot of the threshold-gated hypotheses from each navigation cycle.

Figure 7-57: Sentry016 Transponder 1 horizontal ranges corresponding to pose hypotheses after threshold gating.

Cumulative Location Hypotheses After Threshold Gating
Sentry016 Transponder 1

Figure 7-58: Sentry016 Transponder 1 pose hypotheses after threshold gating, plotted cumulatively over the entire course of the dive.

7.2.2 Sentry016 Transponder 2

The position of Transponder 2 with relation to the tracklines for Sentry016 is shown in Figure 7-59. The raw two-way travel times of the Transponder 2 returns observed by the vehicle are shown in Figure 7-60. For this transponder, there was frequent alternation between the different types of acoustic multipaths.
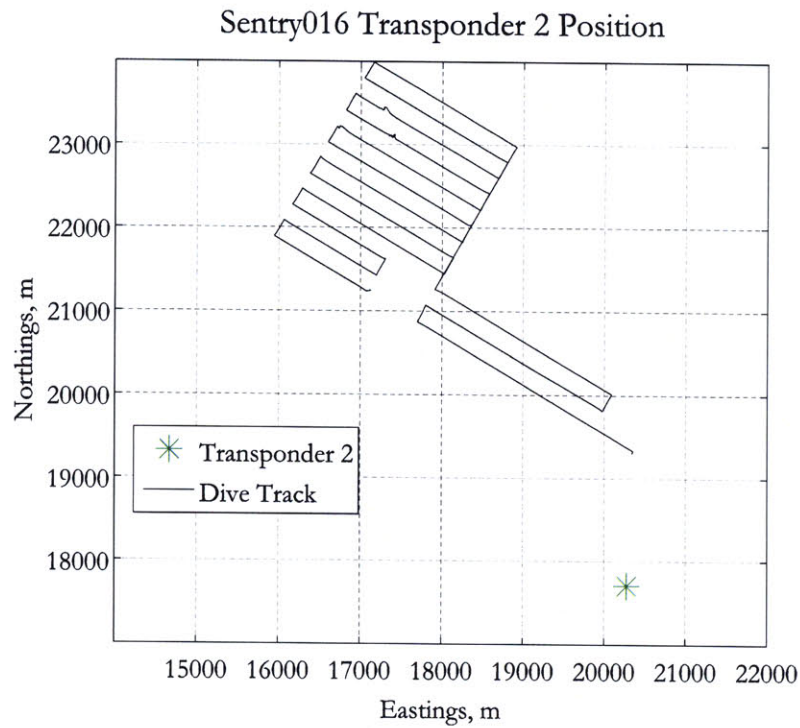
Figure 7-59: Sentry016 tracklines and Transponder 2 location.
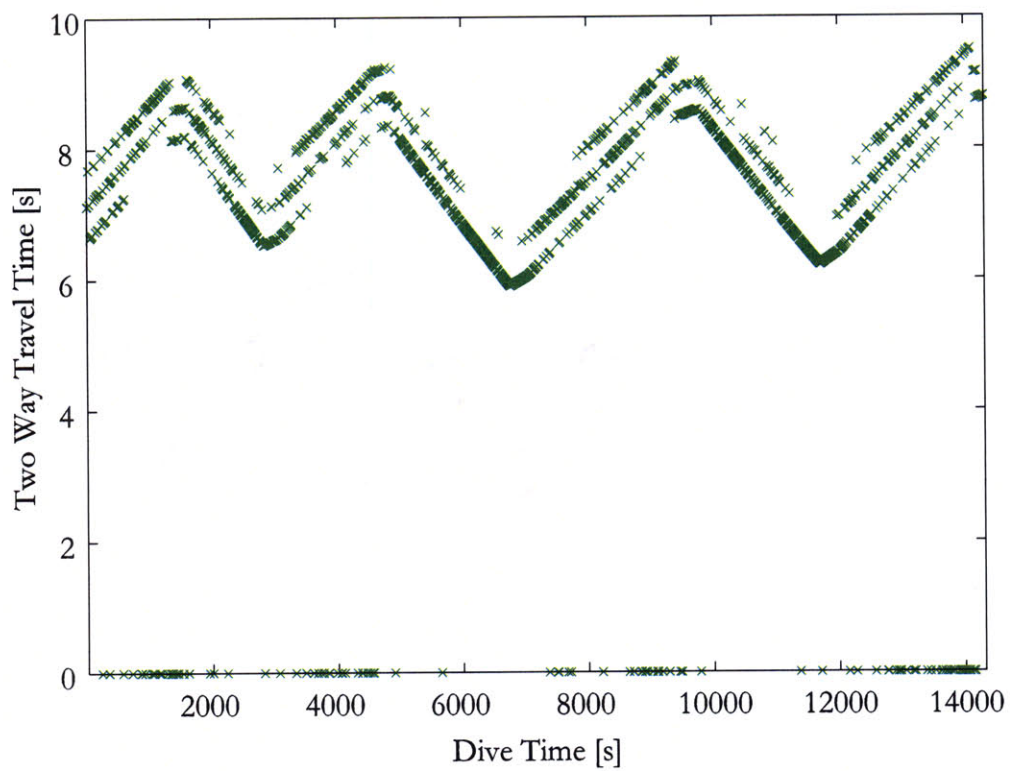
Figure 7-60: Sentry016 Transponder 2 raw two-way acoustic travel times. Note that the direct and bounce returns are close together and the direct returns are very sparse for significant stretches where one or more bounce paths were received.

7.2.2.1   Sentry016 Transponder 2 Hypothesis Generation Step

Figure 7-61 shows the raw acoustic data after it has been transformed into horizontal ranges for each of the three possible acoustic paths. For each travel time received by Sentry, the corresponding range if the signal was direct path is shown in blue, for triangle path is shown in red, and double bounce is shown in green. The black line indicates the actual distance between vehicle and transponder throughout the dive. Therefore, the ranges that fall along that line indicate which acoustic path the received acoustic signal actually followed for each navigation cycle.

Figure 7-61: Sentry016 Transponder 2 horizontal ranges for possible acoustic paths.

For Transponder 2, there was frequent alternation between the different types of acoustic multipaths. From these horizontal range hypotheses, up to six pose hypotheses were created for the vehicle in each navigation cycle. Figure 7-62 shows a

Cumulative Location Hypotheses Before Arbitration
Sentry016 Transponder 2

Figure 7-62: Sentry016 Transponder 2 generated pose hypotheses, plotted cumulatively over the entire course of the dive.

cumulative plot of all of the pose hypotheses created from the observed horizontal ranges over the course of the entire dive before any arbitration was conducted.

7.2.2.2 Sentry016 Transponder 2 Primary Arbitration Step

This dive was processed illustrating the PH method without the optional grid arbiter step, therefore all the pose hypotheses are input into the primary arbiter, which selects the single nearest neighbor hypothesis for every navigation cycle. Figure 7-63 depicts the acoustic range at every time frame corresponding to each chosen nearest neighbor pose hypotheses. Figure 7-64 shows the same information spatially by depicting a cumulative plot over the course of the whole dive of the nearest neighbor pose hypotheses from each navigation cycle.

Figure 7-63: Sentry016 Transponder 2 horizontal ranges corresponding to pose hypotheses after primary arbitration.

Cumulative Location Hypotheses After Arbitration
Sentry016 Transponder 2

Figure 7-64: Sentry016 Transponder 2 pose hypotheses after primary arbitration, plotted cumulatively over the entire course of the dive.

7.2.2.3 Sentry016 Transponder 2 Threshold Gating Step

The pose hypothesis that is output from the primary arbiter at each navigation cycle is subject to threshold gating to ensure that it is a valid hypothesis. Figure 7-65 depicts the acoustic ranges corresponding to the pose hypotheses that survived the threshold gating process. Figure 7-66 shows the same information spatially by depicting a cumulative plot of the threshold-gated hypotheses from each navigation cycle.

Figure 7-65: Sentry016 Transponder 2 horizontal ranges corresponding to pose hypotheses after threshold gating. The long gaps in the direct returns have been substantially filled with triangle and double-bounce returns.

Cumulative Location Hypotheses After Threshold Gating
Sentry016 Transponder 2

Figure 7-66: Sentry016 Transponder 2 pose hypotheses after threshold gating, plotted cumulatively over the entire course of the dive.

7.2.3 Sentry016 Transponder 3

The position of Transponder 3 with relation to the tracklines for Sentry016 is shown in Figure 7-67. The raw two-way travel times of the Transponder 3 returns observed by the vehicle are shown in Figure 7-68. There is intermittent dropout of the direct path returns with less-frequent, intermittent fill-in with triangle path returns.
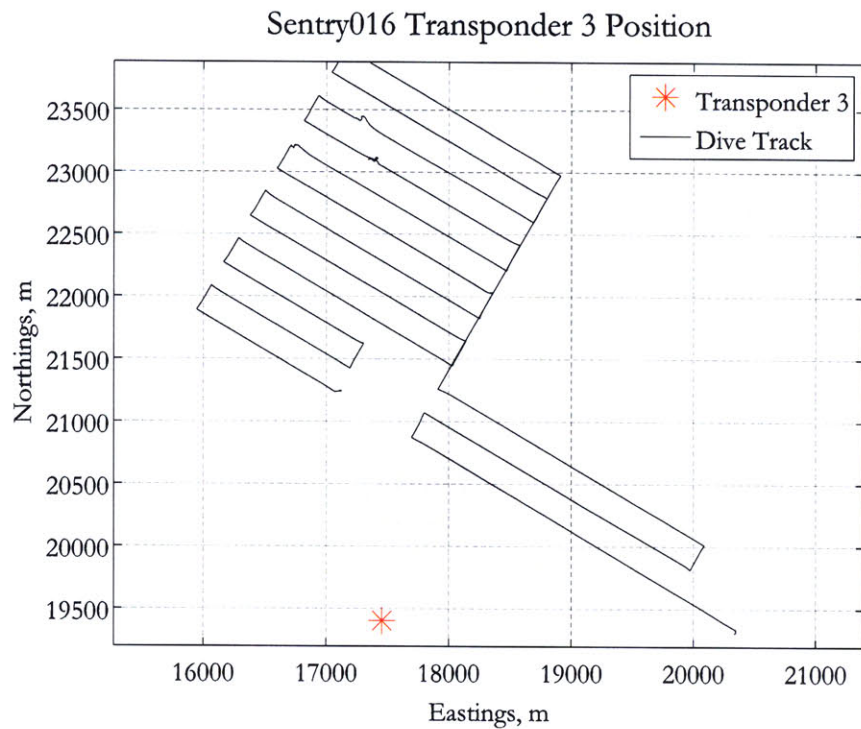
Figure 7-67: Sentry016 tracklines and Transponder 3 location.
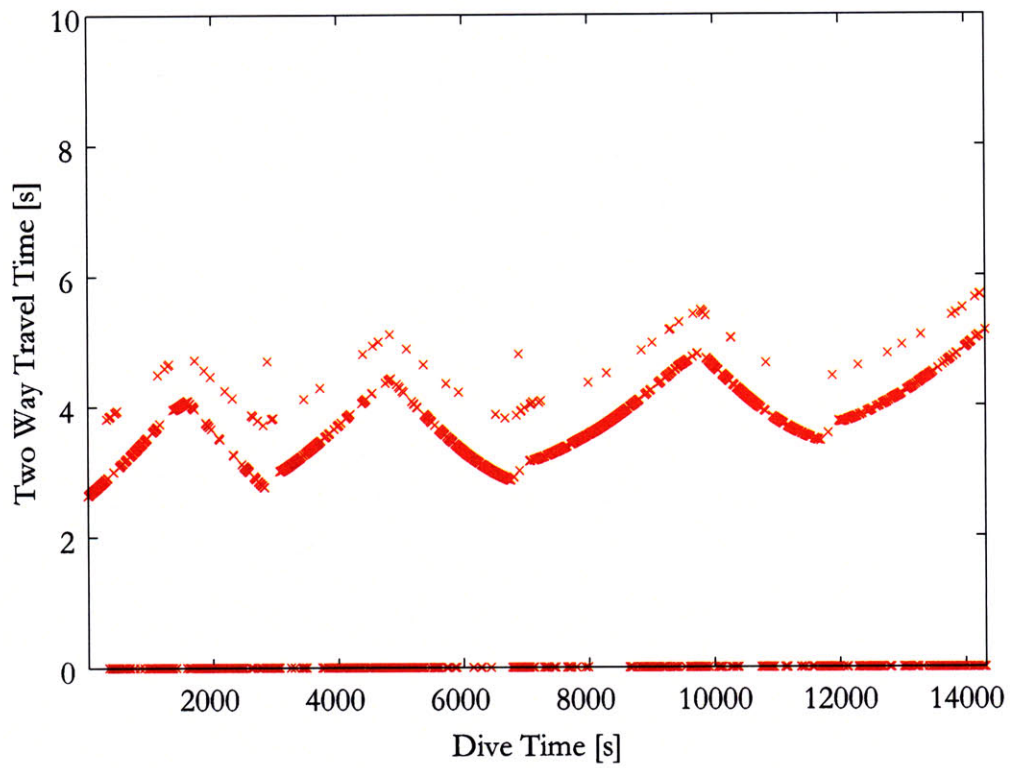
Figure 7-68: Sentry016 Transponder 3 raw two-way acoustic travel times.

7.2.3.1 Sentry016 Transponder 3 Hypothesis Generation Step

Figure 7-69 shows the raw acoustic data after it has been transformed into horizontal ranges for each of the three possible acoustic paths. For each travel time received by Sentry, the corresponding range if the signal was direct path is shown in blue, for triangle path is shown in red, and double bounce is shown in green. The black line indicates the actual distance between vehicle and transponder throughout the dive. Therefore, the ranges that fall along that line indicate which acoustic path the received acoustic signal actually followed for each navigation cycle.

One Way Horizontal Range for Each Acoustic Path
Sentry016 Transponder 3
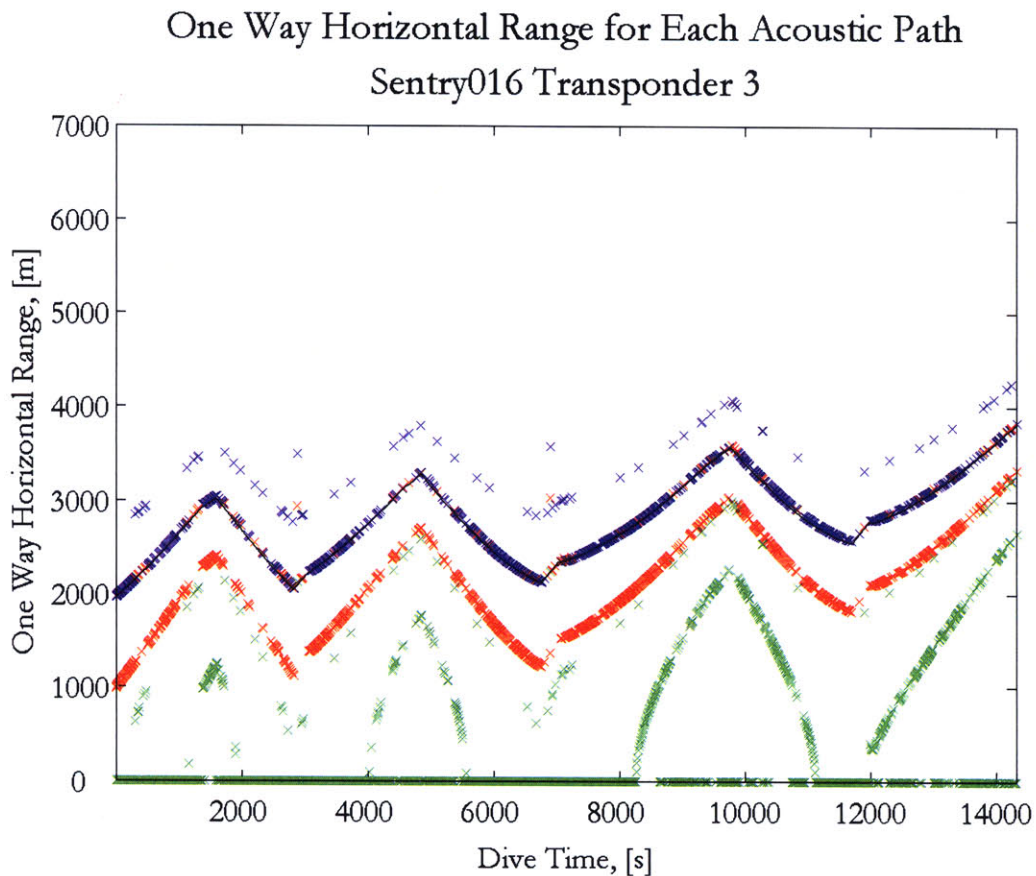
Figure 7-69: Sentry016 Transponder 3 horizontal ranges for possible acoustic paths.

For Transponder 3, there is intermittent dropout of the direct path returns with less-frequent, intermittent fill-in with triangle path returns. From these horizontal range hypotheses, up to six pose hypotheses were created for the vehicle in each

232

Cumulative Location Hypotheses Before Arbitration
Sentry016 Transponder 3
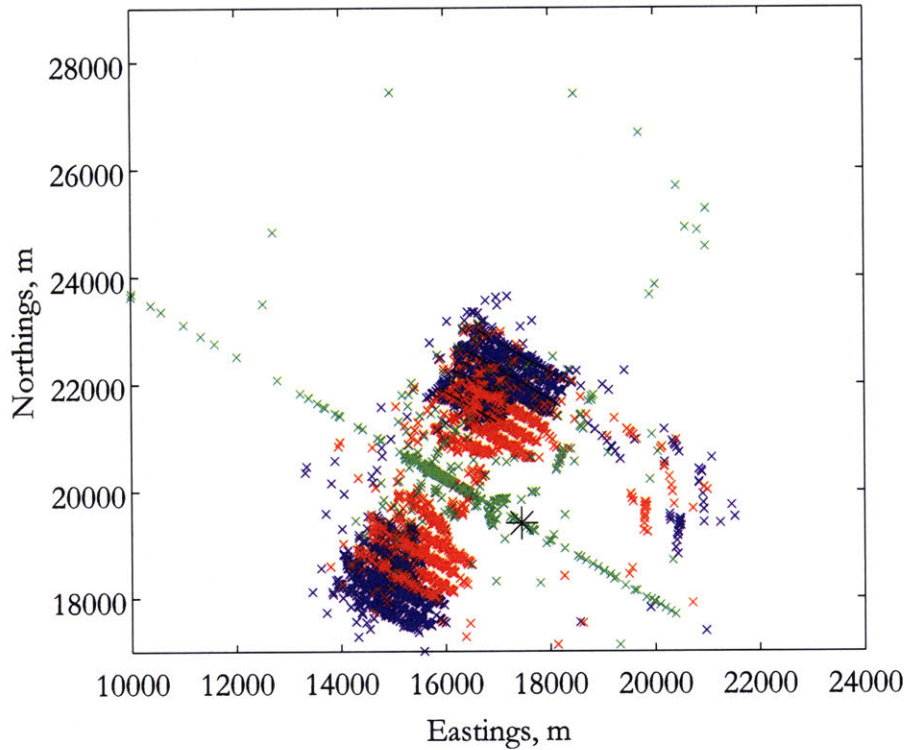
Figure 7-70: Sentry016 Transponder 3 generated pose hypotheses, plotted cumulatively over the entire course of the dive.

navigation cycle. Figure 7-70 shows a cumulative plot of all of the pose hypotheses created from the observed horizontal ranges over the course of the entire dive before any arbitration was conducted.

7.2.3.2   Sentry016 Transponder 3 Primary Arbitration Step

This dive was processed illustrating the PH method without the optional grid arbiter step, therefore all the pose hypotheses are input into the primary arbiter, which selects the single nearest neighbor hypothesis for every navigation cycle. Figure 7-71 depicts the acoustic range at every time frame corresponding to each chosen nearest neighbor pose hypotheses. Figure 7-72 shows the same information spatially by depicting a cumulative plot over the course of the whole dive of the nearest neighbor pose hypotheses from each navigation cycle.
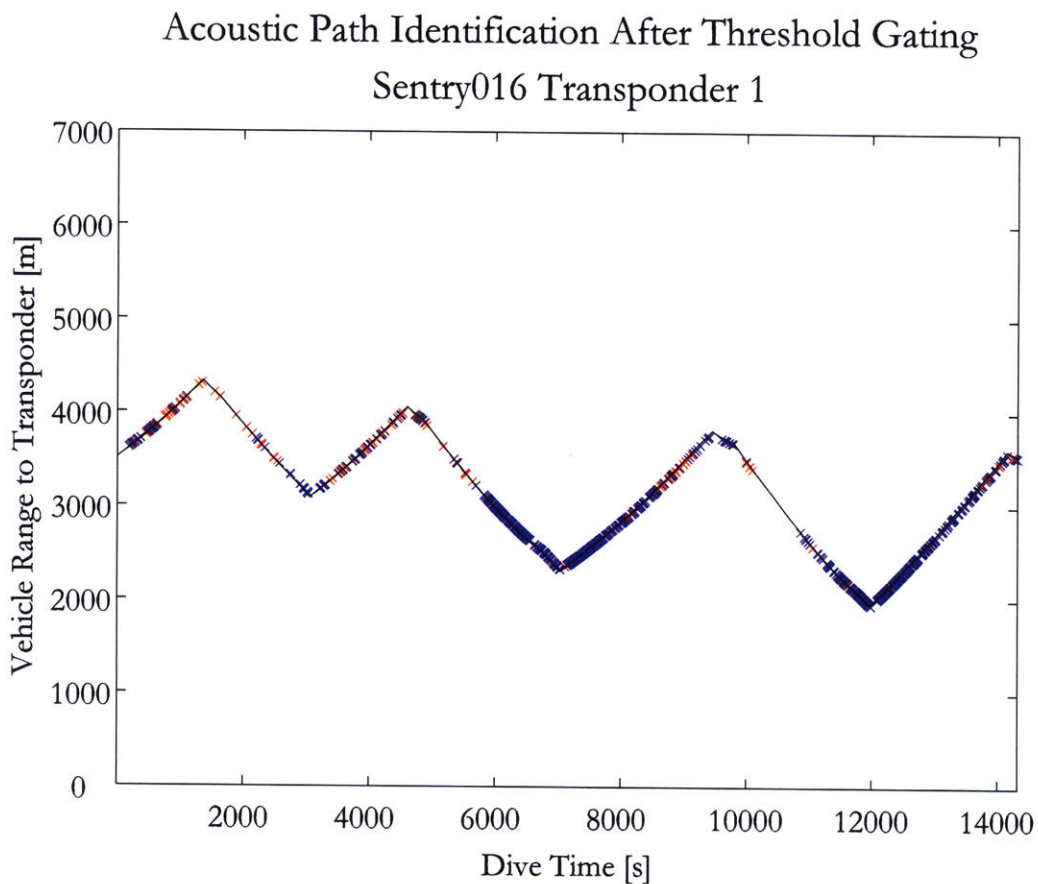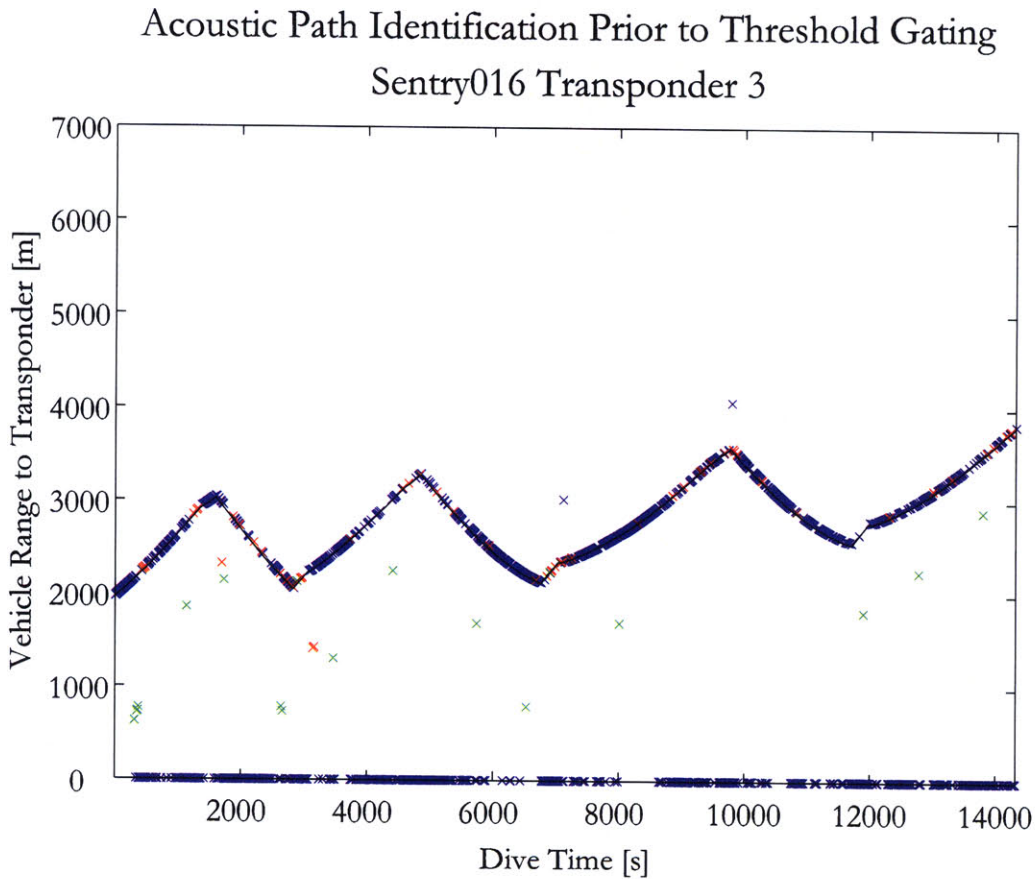

Figure 7-71: Sentry016 Transponder 3 horizontal ranges corresponding to pose hypotheses after primary arbitration.

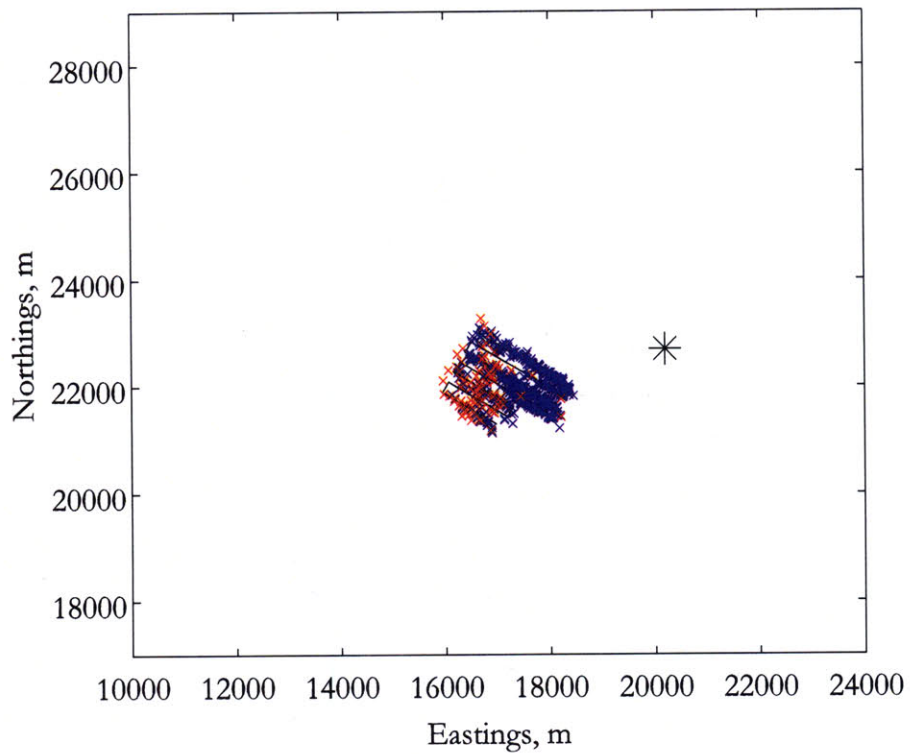Cumulative Location Hypotheses After Arbitration
Sentry016 Transponder 3

Figure 7-72: Sentry016 Transponder 3 pose hypotheses after primary arbitration, plotted cumulatively over the entire course of the dive.

7.2.3.3 Sentry016 Transponder 3 Threshold Gating Step

The pose hypothesis that is output from the primary arbiter at each navigation cycle is subject to threshold gating to ensure that it is a valid hypothesis. Figure 7-73 depicts the acoustic ranges corresponding to the pose hypotheses that survived the threshold gating process. Figure 7-74 shows the same information spatially by depicting a cumulative plot of the threshold-gated hypotheses from each navigation cycle.
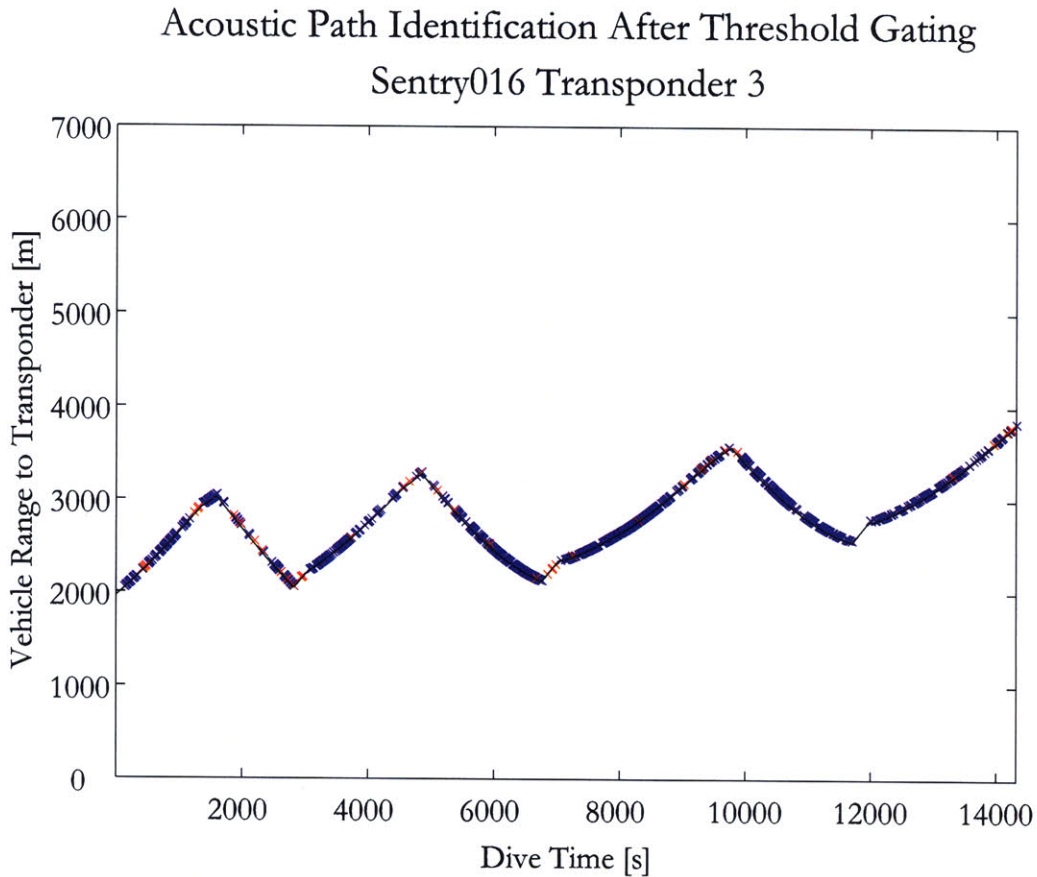
Figure 7-73: Sentry016 Transponder 3 horizontal ranges corresponding to pose hypotheses after threshold gating.

Figure 7-74: Sentry016 Transponder 3 pose hypotheses after threshold gating, plotted cumulatively over the entire course of the dive.

7.2.4 Sentry016 Transponder 4

The position of Transponder 4 with relation to the tracklines for Sentry016 is shown in Figure 7-75. The raw two-way travel times of the Transponder 4 returns observed by the vehicle are shown in Figure 7-76. Few returns were received from Transponder 4 throughout the dive.
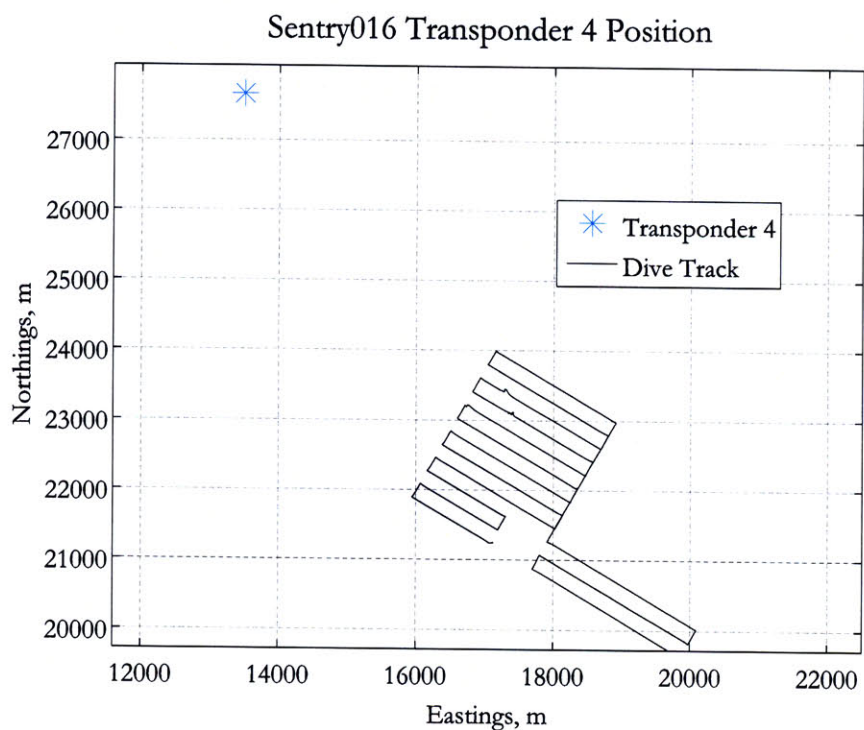
Figure 7-75: Sentry016 tracklines and Transponder 4 location.
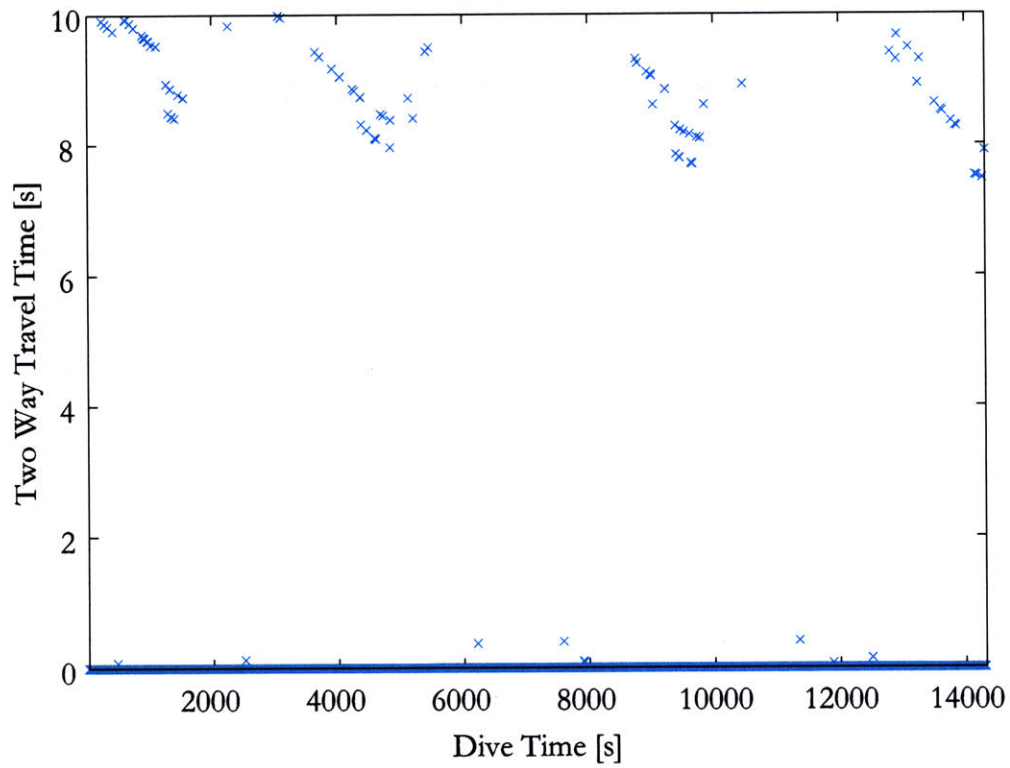
Figure 7-76: Sentry016 Transponder 4 raw two-way acoustic travel times. All returns are very sparse.

7.2.4.1 Sentry016 Transponder 4 Hypothesis Generation Step

Figure 7-77 shows the raw acoustic data after it has been transformed into horizontal ranges for each of the three possible acoustic paths. For each travel time received by Sentry, the corresponding range if the signal was direct path is shown in blue, for triangle path is shown in red, and double bounce is shown in green. The black line indicates the actual distance between vehicle and transponder throughout the dive. Therefore, the ranges that fall along that line indicate which acoustic path the received acoustic signal actually followed for each navigation cycle.
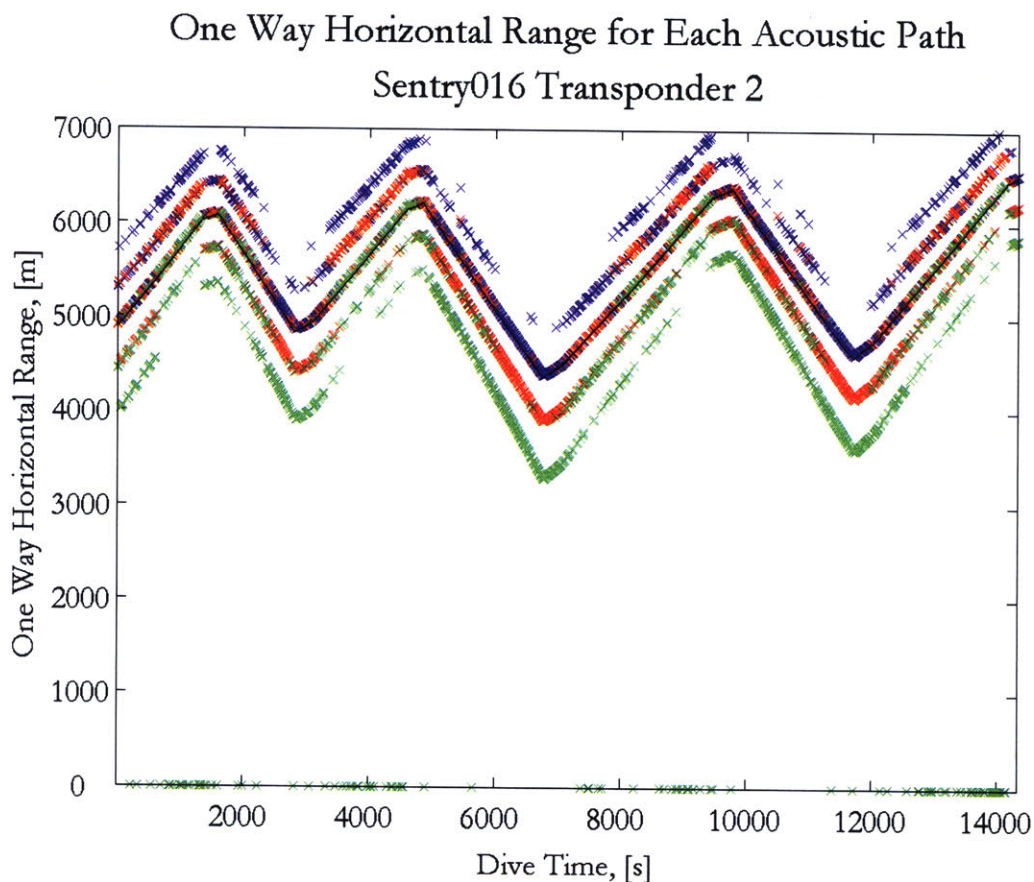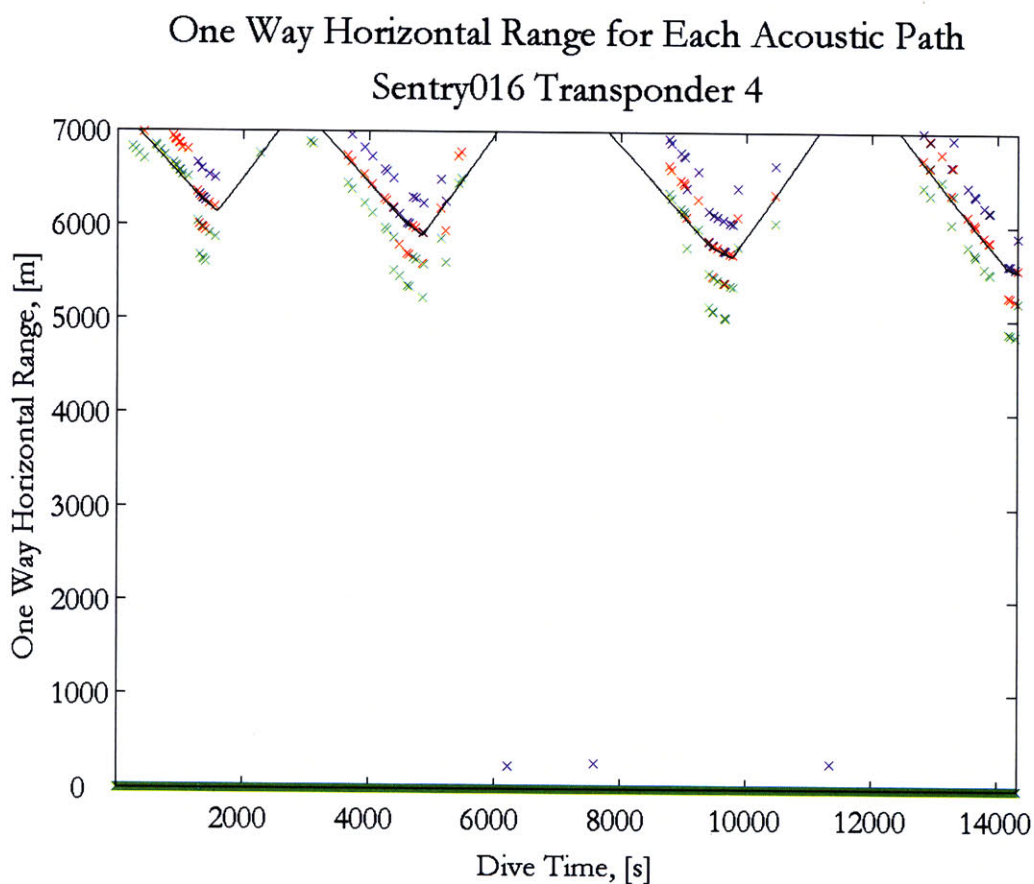

Figure 7-77: Sentry016 Transponder 4 horizontal ranges for possible acoustic paths.

For Transponder 4, there were only a small number of returns received throughout the dive. Those that were received represented all three types of acoustic multipaths. From these horizontal range hypotheses, up to six pose hypotheses were created for
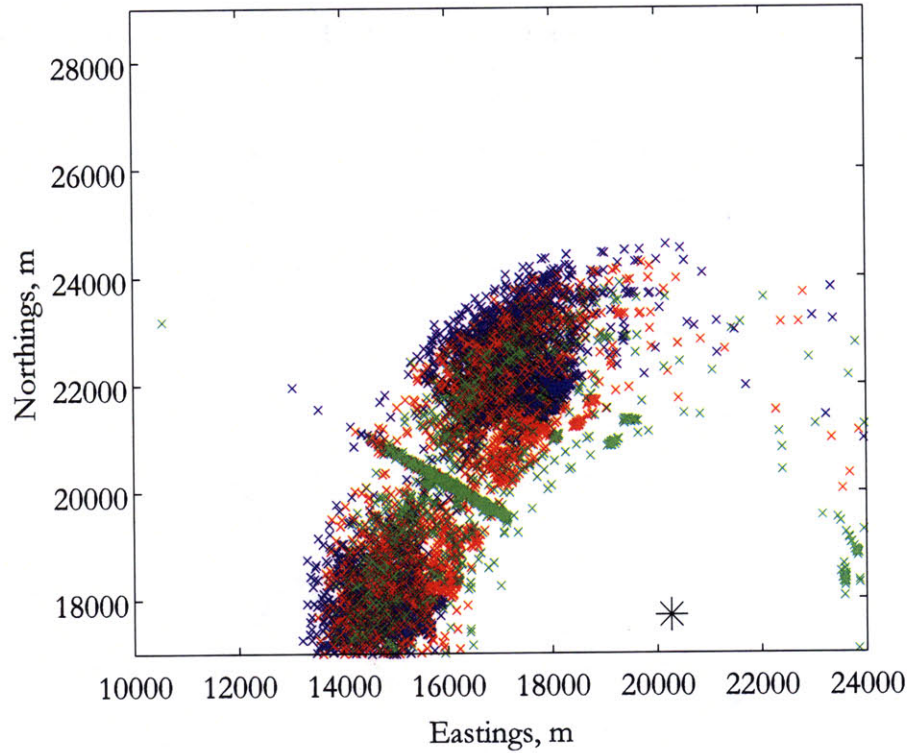
240

Cumulative Location Hypotheses Before Arbitration
Sentry016 Transponder 4
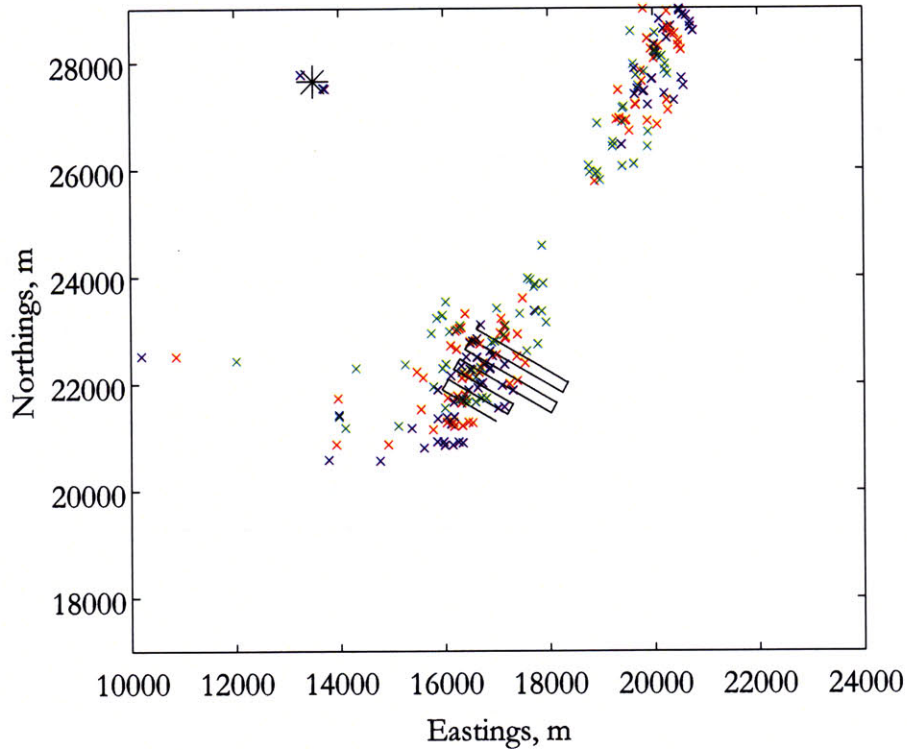
Figure 7-78: Sentry016 Transponder 4 generated pose hypotheses, plotted cumulatively over the entire course of the dive.

the vehicle in each navigation cycle. Figure 7-78 shows a cumulative plot of all of the pose hypotheses created from the observed horizontal ranges over the course of the entire dive before any arbitration was conducted.

7.2.4.2 Sentry016 Transponder 4 Primary Arbitration Step

This dive was processed illustrating the PH method without the optional grid arbiter step, therefore all the pose hypotheses are input into the primary arbiter, which selects the single nearest neighbor hypothesis for every navigation cycle. Figure 7-79 depicts the acoustic range at every time frame corresponding to each chosen nearest neighbor pose hypotheses. Figure 7-80 shows the same information spatially by depicting a cumulative plot over the course of the whole dive of the nearest neighbor pose hypotheses from each navigation cycle.
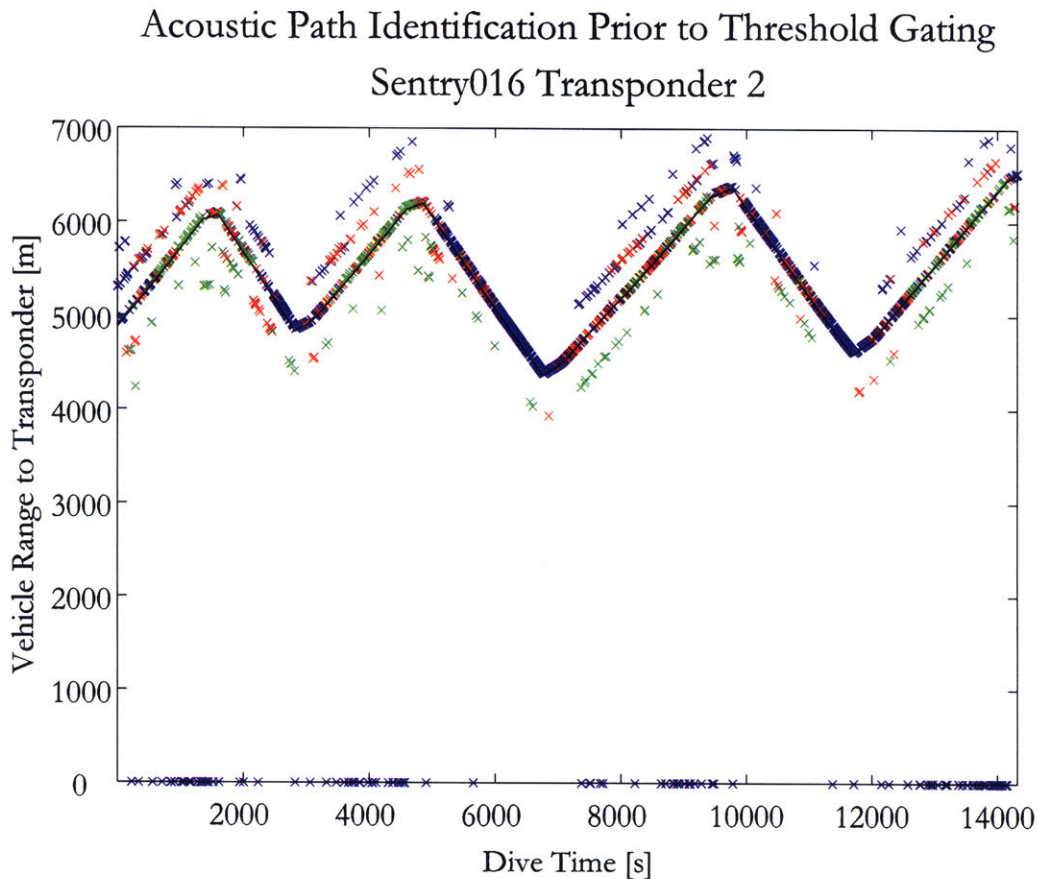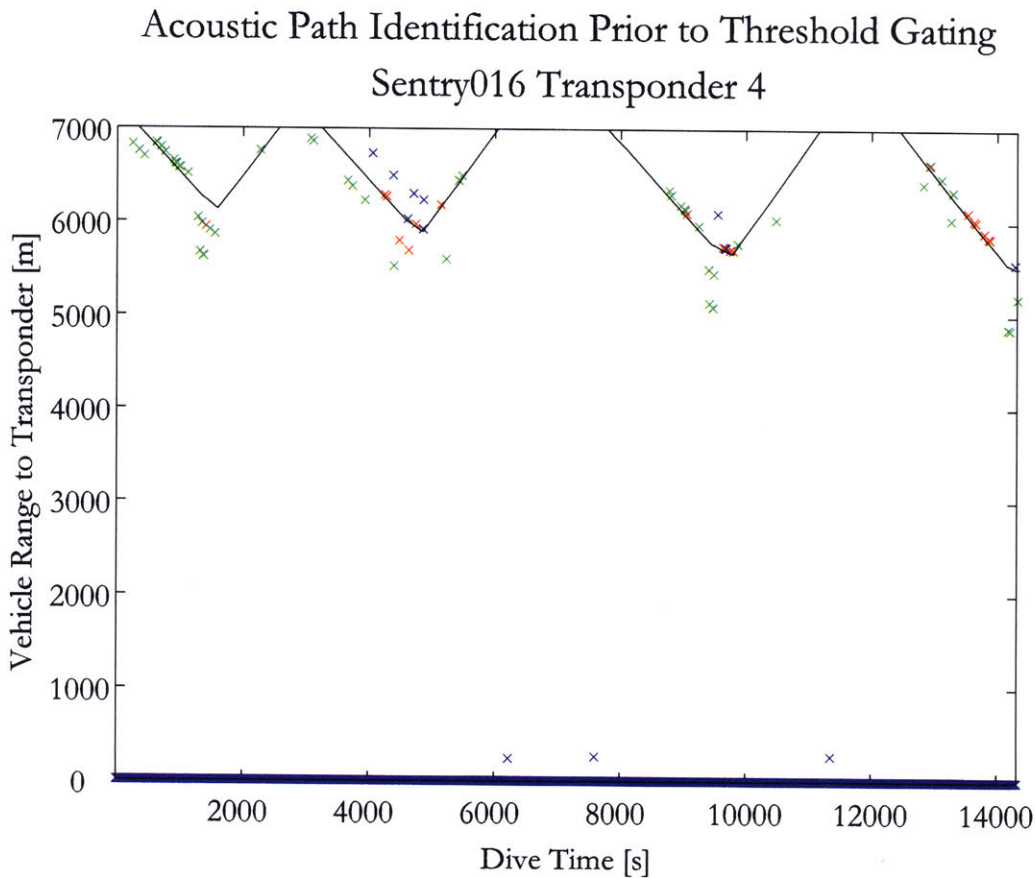

Figure 7-79: Sentry016 Transponder 4 horizontal ranges corresponding to pose hypotheses after primary arbitration.

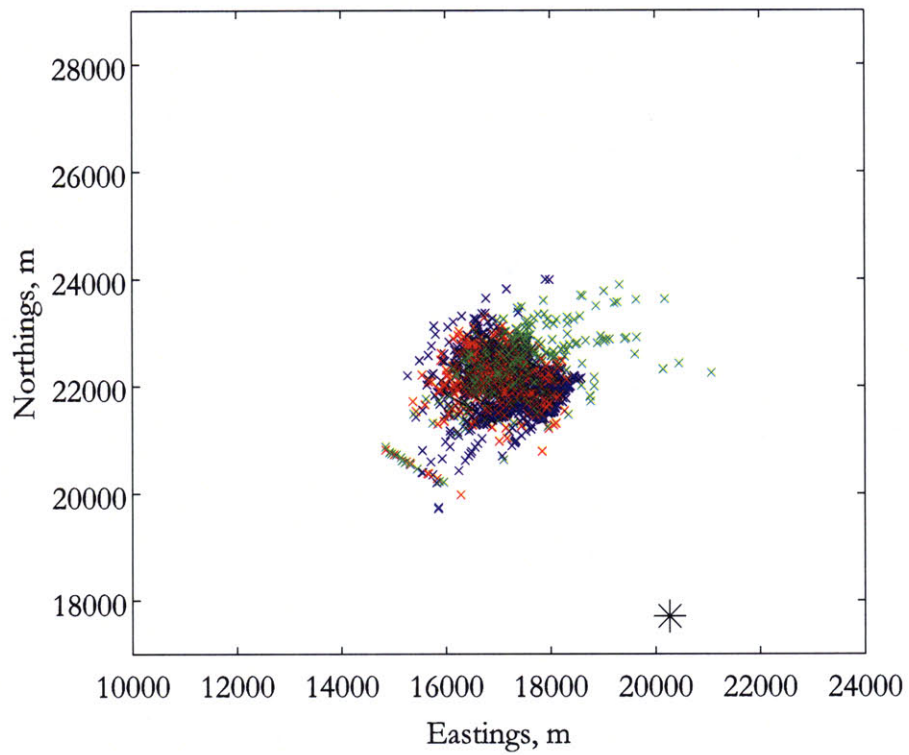Cumulative Location Hypotheses After Arbitration
Sentry016 Transponder 4
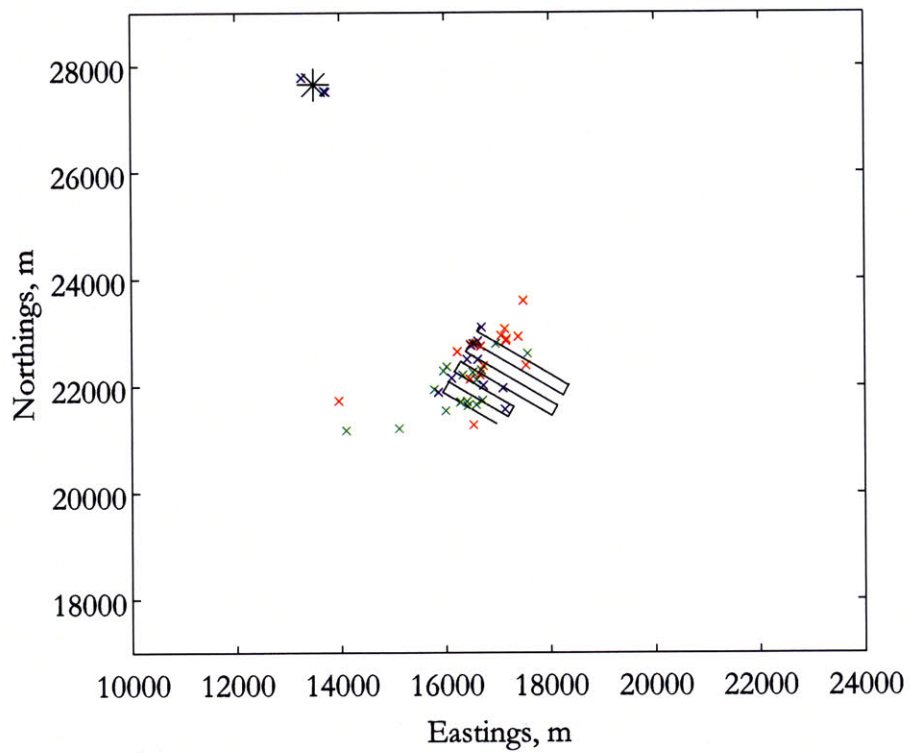
Figure 7-80: Sentry016 Transponder 4 pose hypotheses after primary arbitration, plotted cumulatively over the entire course of the dive.

7.2.4.3   Sentry016 Transponder 4 Threshold Gating Step

The pose hypothesis that is output from the primary arbiter at each navigation cycle is subject to threshold gating to ensure that it is a valid hypothesis. Figure 7-81 depicts the acoustic ranges corresponding to the pose hypotheses that survived the threshold gating process. Figure 7-82 shows the same information spatially by depicting a cumulative plot of the threshold-gated hypotheses from each navigation cycle.
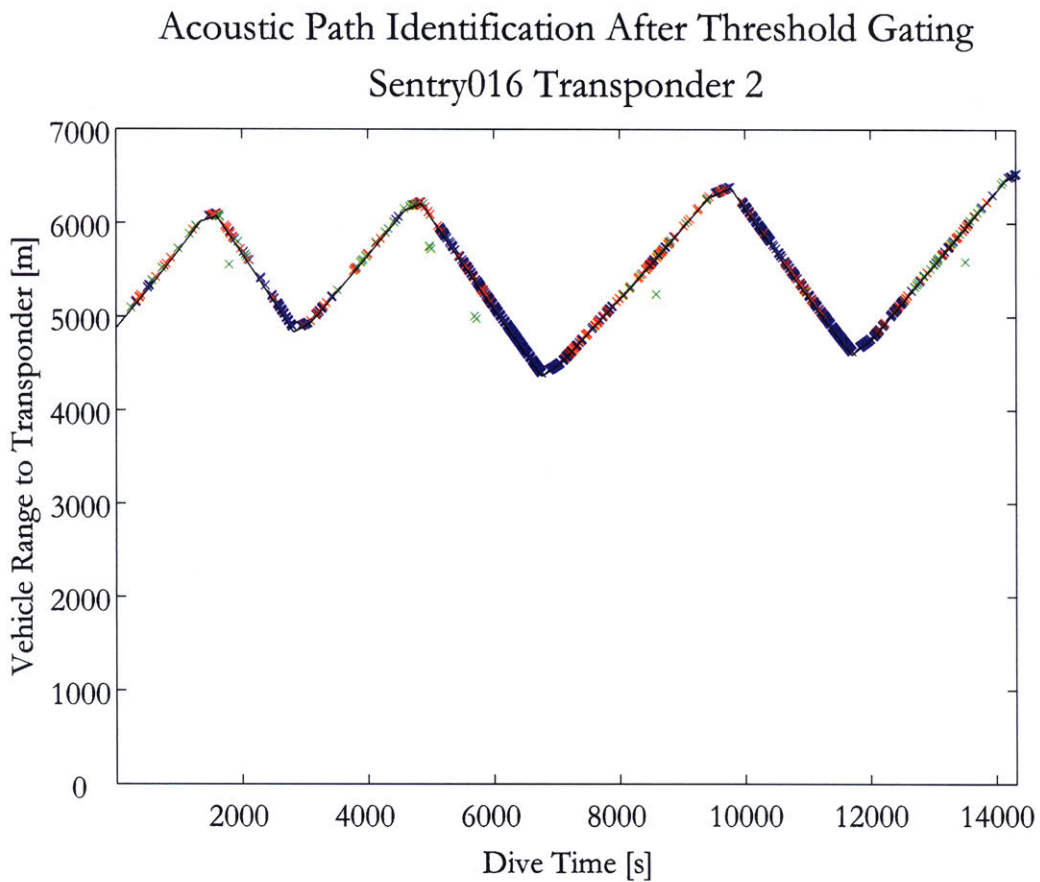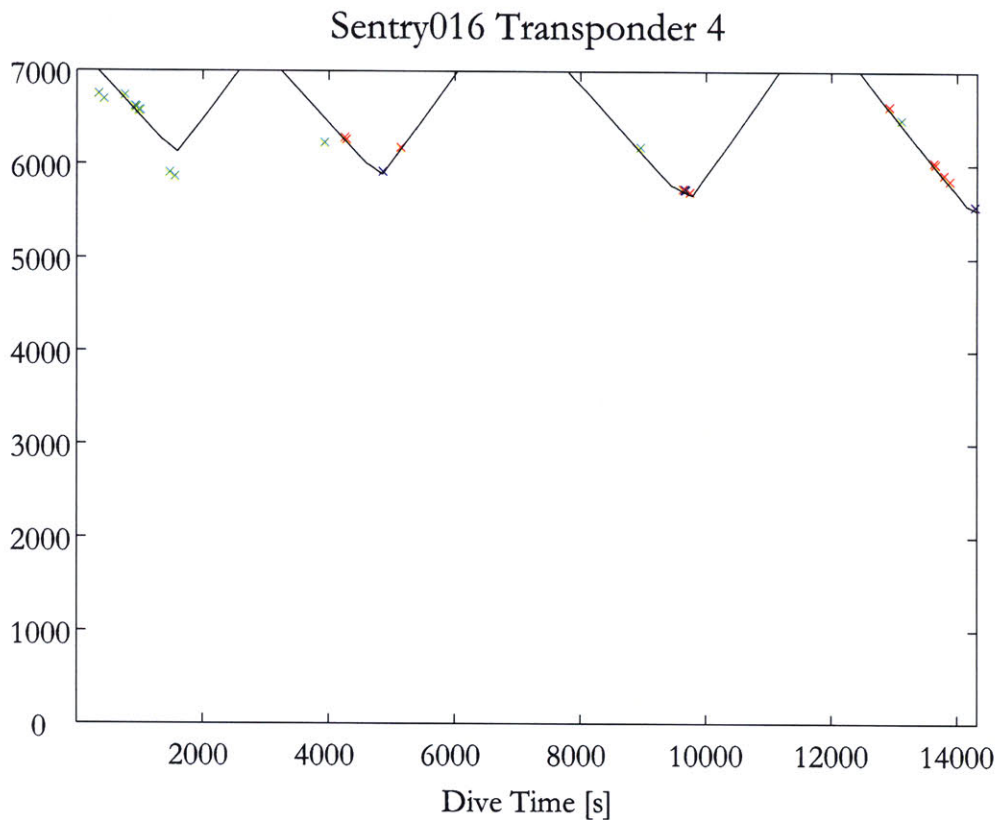

Figure 7-81: Sentry016 Transponder 4 horizontal ranges corresponding to pose hypotheses after threshold gating.

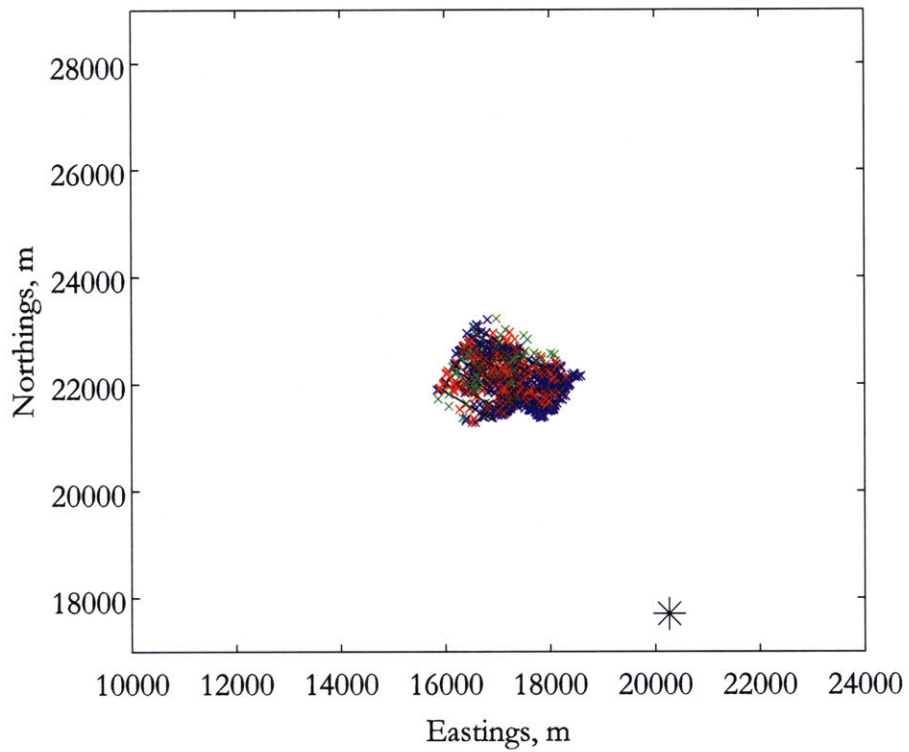Cumulative Location Hypotheses After Threshold Gating
Sentry016 Transponder 4
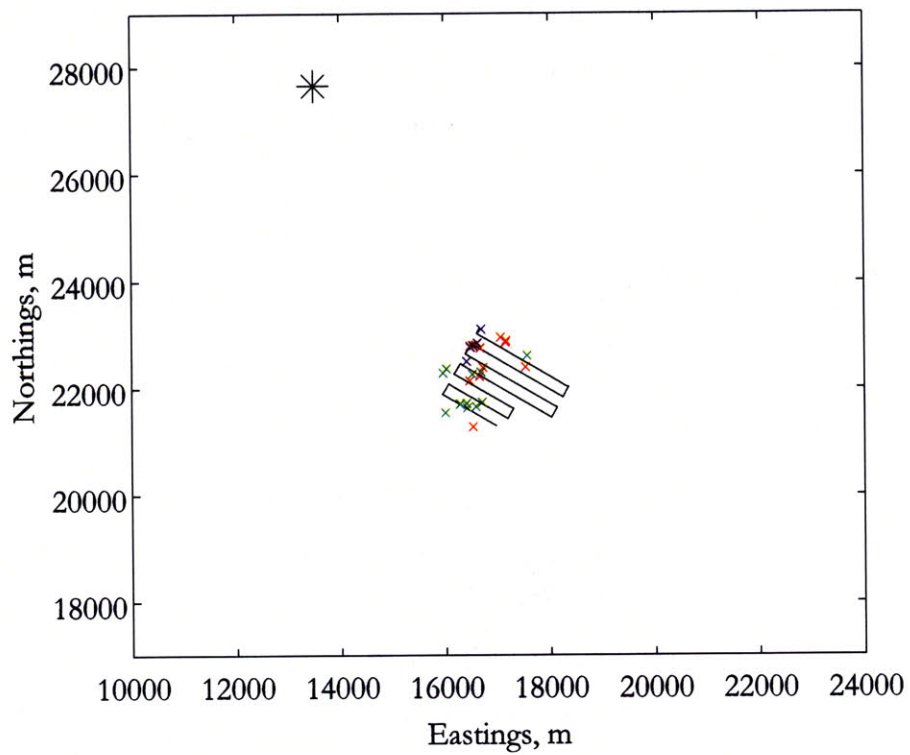
Figure 7-82: Sentry016 Transponder 4 pose hypotheses after threshold gating, plotted cumulatively over the entire course of the dive.

7.2.5 Sentry016 Update Step and Performance Metrics

In the update step, the primary navigation process combines all the acoustic path returns that were identified *in situ* through each of the single transponder parallel hypothesis filters, as shown in Figure 7-83. The returns are combined in a conventional least-squares trilateration method. For illustration purposes, the results are not filtered in any way to remove outliers. For actual navigation, an outlier rejection filter would be implemented. The blue markers indicate fixes that include only direct path returns. The red markers indicate fixes that used at least one triangle path return and any available direct path returns. The green markers indicate fixes that used at least one double bounce path return and any available direct path and triangle path returns.
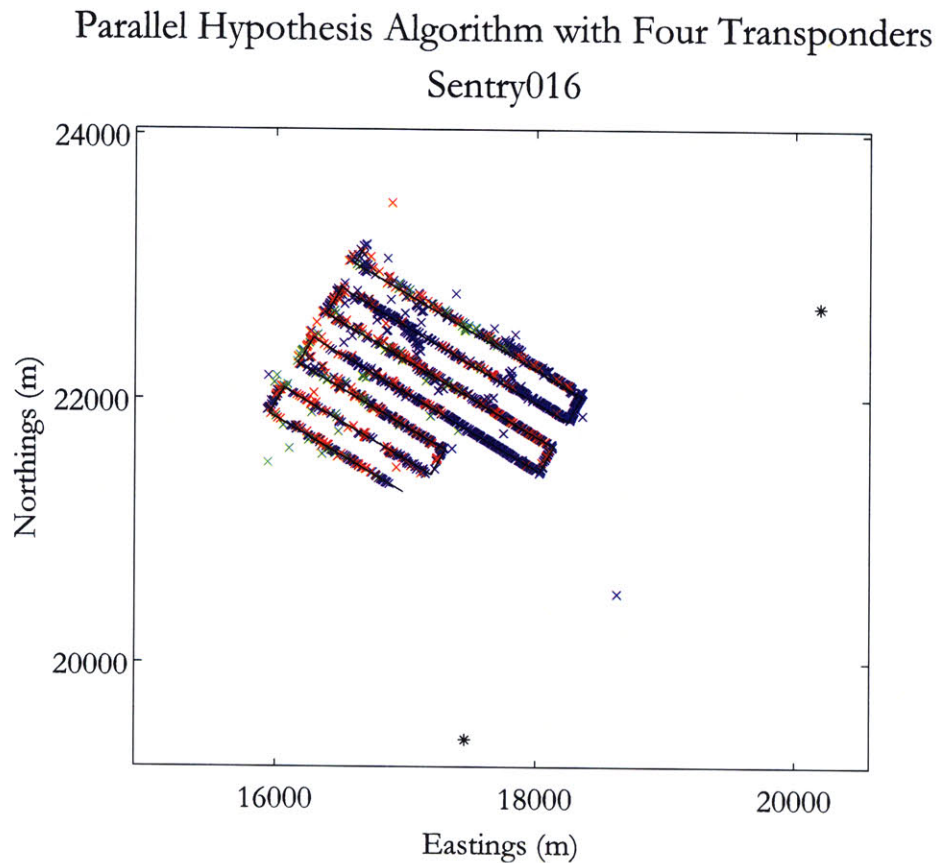
Figure 7-83: Sentry016 results of the PH navigation algorithm.

246

Table 7.6: Sentry016 performance metric comparison between the PH and LBL navigation methods using acoustic data from Transponders 1, 2, and 3.

	PH	LBL
Total number of fixes	220	132
Maximum time between fixes	1030 s	2040 s
Mean time between fixes	63.90 s	93.04 s
Median time between fixes	19.98 s	10.02 s
Minimum time between fixes	9.83 s	9.83 s

Table 7.7: Sentry016 performance metric comparison between the PH and LBL navigation methods using acoustic data from two transponder combinations from Transponders 1, 2, and 3.

	1 and 2		2 and 3		1 and 3	
	PH	LBL	PH	LBL	PH	LBL
Total number of fixes	336	204	384	332	424	270
Maximum time between fixes	940 s	2040 s	950 s	1240 s	360 s	1020 s
Mean time between fixes	420 s	690 s	366 s	420 s	333 s	520 s
Median time between fixes	10.42 s	10.02 s	10.02 s	10.02 s	10.02 s	10.02 s
Minimum time between fixes	9.83 s	9.83 s	9.83 s	9.83 s	9.83 s	9.83 s

Since the acoustic returns from Transponder 4 were so scarce, they added very little information into the navigation process. Therefore, as a metric of performance between the PH and LBL methods, total numbers of fixes generated and statistics regarding the time between three transponder fixes using Transponders 1, 2, and 3 are compared in Table 7.6. The same metrics for two transponder combinations of Transponders 1, 2 and 3 are shown in Table 7.7.

7.3 Discussion of Geometric Observability

As shown in the literature by Ross et al [75] and Gadre [26], when a vehicle is traveling on a radial trackline toward or away from a single transponder, its exact location is unobservable when using range information from only that single transponder. This is because the physical triangle necessary for successful pose localization, as discussed in Section 4.6, collapses on radial tracklines. This problem with geometric observability also affects each single transponder parallel hypothesis filter within the PH algorithm. This phenomenon is illustrated here using data from ABE163 Transponder 3. On this run, random noise was low but most channels had prolonged stretches with only bounce paths available.

Figure 7-84 shows a cumulative plot of all the location hypotheses generated based on the acoustic returns from Transponder 3 throughout the dive. As before, hypotheses based on the assumption of direct path are shown in blue, of triangle path are shown in red, and of double bounce path are shown in green. Figure 7-85 shows the hypotheses after the initial arbitration process which locates the nearest neighbor hypotheses to the estimated pose at every time.

Figure 7-86 shows the hypotheses after the threshold gating process. Figure 7-86 illustrates this issue of geometric observability that arises from the relative position of the transponder with respect to the vehicle dive track. On the tracklines where the vehicle is operating tangent or close to tangent to the transponder location, there is good observability in the hypotheses locations. However, at the northern ends of the tracklines, where the vehicle is maneuvering on a path closer to radial tracklines from the vehicle, there is a degradation in the observability of the exact position hypotheses because of the degradation, or noise, in the bearing angle information. This is consistent with existing research on the observability of AUV navigation based on returns from a single transponder.
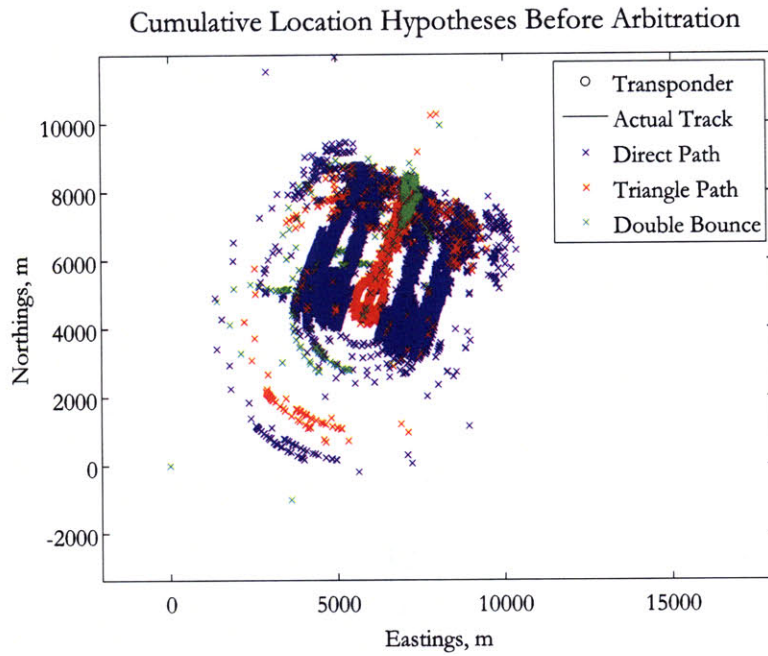
Figure 7-84: ABE163 Transponder 3 generated pose hypotheses, plotted cumulatively over the entire course of the dive.
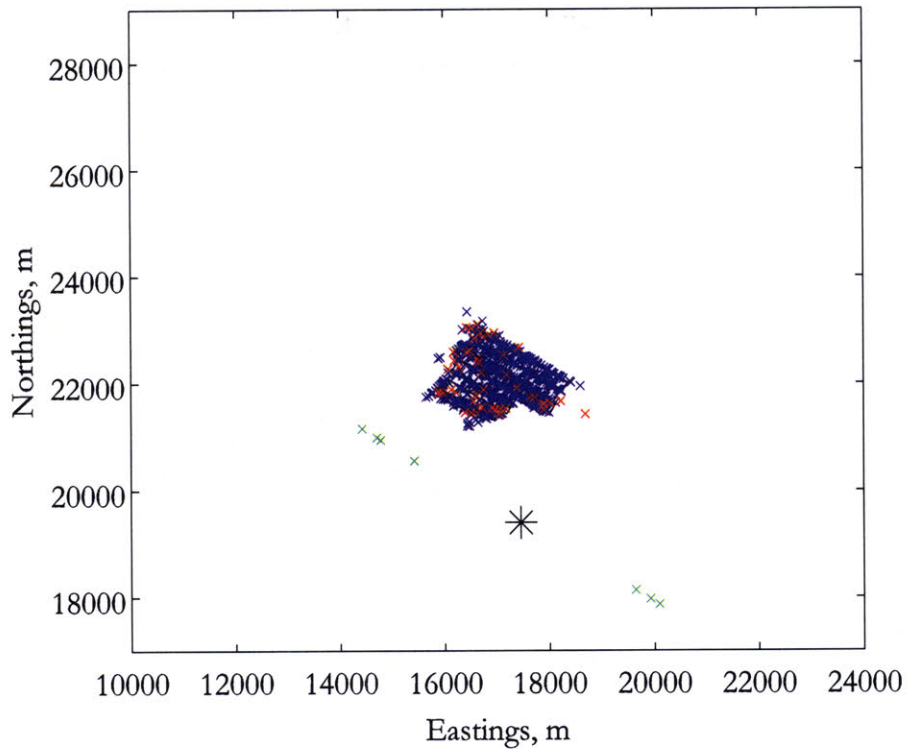

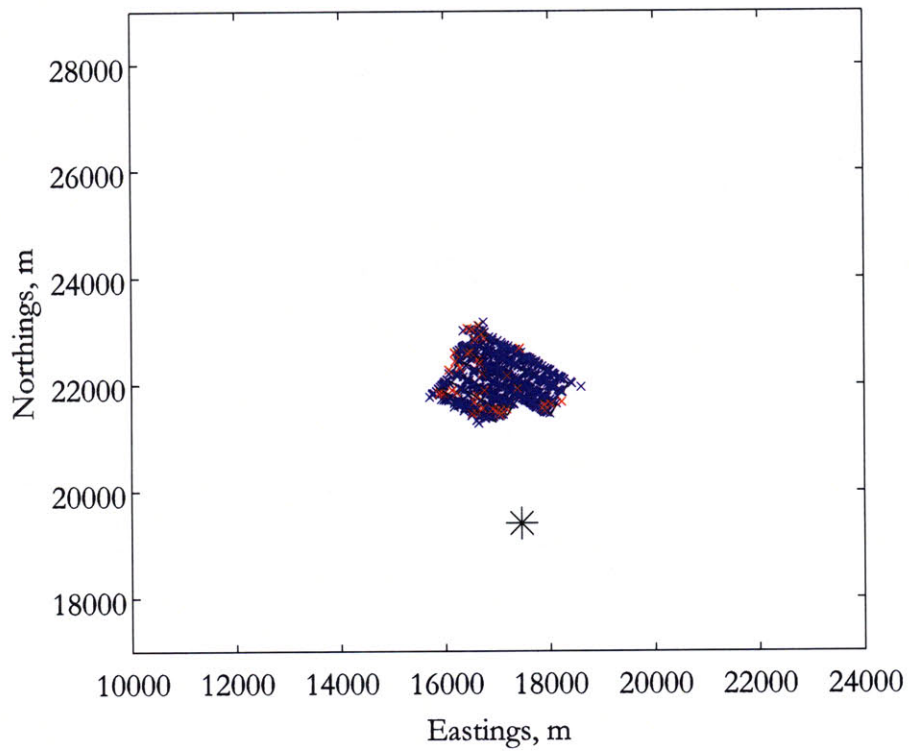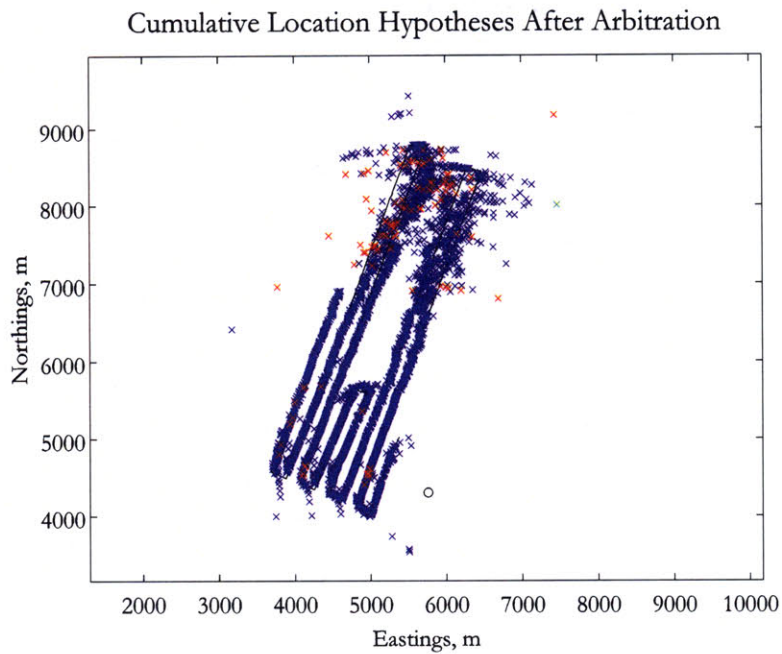Figure 7-85: ABE163 Transponder 3 pose hypotheses after primary arbitration, plotted cumulatively over the entire course of the dive.
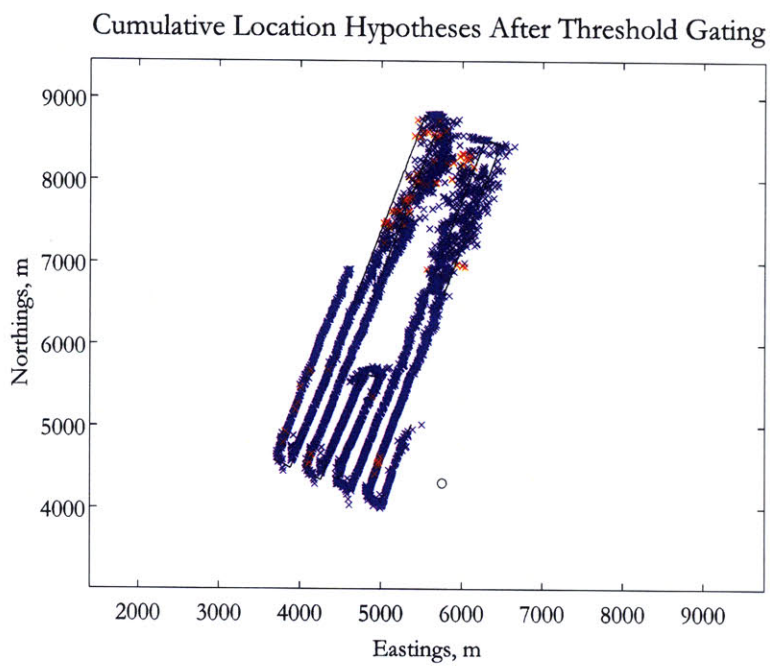
Figure 7-86: ABE163 Transponder 3 pose hypotheses after threshold gating, plotted cumulatively over the entire course of the dive.

7.4 Summary of the Proof of Concept Results

This chapter has illustrated the implementation of the PH navigation system using real-world data from both ABE and Sentry. The algorithm was illustrated both with and without the optional grid arbitration process. This proof of concept has shown that the PH method works when there are consistent returns that are either direct path, triangle path, or double bounce path from multiple transponders. It also shows that the method is effective in identifying which acoustic path the different returns have followed and incorporating that information into the real-time navigation solution. The biggest weaknesses of the PH algorithm in its current form are the potential geometric inobservability issues discussed in Section 7.3 above and the reliance on a nearest neighbor primary arbiter. Potential failures of the method could result in cluttered acoustic environments where the generated pose hypotheses are located in closer proximity to one another. Other potential failure modes could occur when large time intervals between consecutive acoustic returns of a particular type coincide with large vehicle heading changes if the course-made-good readings do not adequately capture the vehicle's motion over the time interval. It is left to future research to study the potential for failure in these or other circumstances in more detail. One distinct advantage that the PH method has over traditional LBL systems is its lack of sensitivity to baseline crossings. The only global inobservability involved in the single transponder PH building block pertains to which side of the vehicle's trackline that the transponder is located. Therefore, the navigation solution is not susceptible to failure when the vehicle crosses over a baseline between two transponders.

Chapter 8

Conclusion

8.1 Conclusions

This research presented the *parallel hypothesis* method of AUV navigation which was designed to push the existing operational envelope of LBL systems without requiring an increase in the number of deployed acoustic transponders. The PH method does this by incorporating additional information into the navigation solution that is available to the vehicle *in situ* but is not normally used in an LBL solution. Information is incorporated into the PH method in one of two ways, depending on the class of information.

Line of position information refers to any observation that provides a specific spatial relationship, such as a range or bearing, between the vehicle and an external navigation aid that is located at a particular point in space. This type of information is incorporated into the PH architecture as a multiple model filter block, producing multiple hypotheses of vehicle pose location based on the *in-situ* line-of-position measurements.

Gridded information is any physical quantity that the vehicle can measure *in situ* and compare to an *a priori* map of the distribution of that quantity in a given operating area. This type of information is incorporated into the PH architecture as

the first level of the arbiter function to reject any hypotheses that are outside the range of possibility, based on the *in-situ* measurements of this quantity.

For the proof of concept of the PH method presented in this research, one example of each type of information was used with real-world data from the ABE and Sentry vehicle operations on the Juan de Fuca Ridge. The type of line of position information used was multipath acoustic time-of-flight measurements from a single transponder. These are acoustic returns that followed multiple propagation paths through the ocean between the vehicle and the external acoustic transponder. In most existing navigation solutions, only acoustic returns following a direct path between vehicle and transponder are incorporated and any multipath returns are rejected as outliers in real-time navigation solutions. The gridded information used in this proof of concept was the comparison of observed water depth, based on *in-situ* altitude and vehicle depth measurements, to *a priori* low-resolution bathymetric maps of the operating area generated with an EM300 multibeam sonar deployed by a surface ship.

8.2 Contributions

The major contributions of this research are:

- The design of a navigation algorithm with a flexible architecture that allows the incorporation of external information as it becomes available *in situ*.

- An open-form PH algorithm architecture that allows the seamless integration of new and existing techniques by breaking the overall navigation solution down into discrete building blocks which can be individually altered or substituted.

- *In-situ* identification and incorporation of acoustic multipath time-of-flight measurements into the overall navigation solution.

- Addressing the multiscale problem of incorporating *a priori* low-resolution bathymetric data in a high-resolution navigation solution using a grid arbiter to elim-

254

inate erroneous pose hypotheses.

A brief comparison between the PH method presented in this research to some of the existing literature discussed in Chapter 2 is shown in Figure 8-1 highlighting several key characteristics.

	Passive Beacon Field: Detweiler et al., 2006	Single Beacon EKF: Vaganay et al., 2000	Under-Ice Acoustic Navigation: Deffenbaugh et al., 1993	Robust Range-Only Beacon Localization: Olson et al., 2004	Multiscale Terrain Referenced Navigation: Lucido et al., 1996	One-Way Travel Times: Eustice et al., 2006	Parallel Hypothesis Method: LaPointe, 2009
Supports unattended operations	green	green	green	green	green	red	green
Incorporates multipaths *In situ*	yellow	red	green	red	yellow	yellow	green
Works with a single transponder	red	green	yellow	red	green	yellow	yellow
Supports multi-modal distributions	green	red	green	green	yellow	red	green
Effective in deep water	green	green	yellow	green	green	green	green
Uses negative information	yellow	red	yellow	yellow	red	red	green

Figure 8-1: Comparison of the PH method to existing literature using a stop-light color scheme: Green represents compatible and been shown; yellow represents potentially compatible but has not been shown or not applicable; red represents incompatible.

The categories listed in the rows of the table refer to the following characteristics:

Supports unattended operations This category pertains to whether the navigation method is appropriate for an AUV conducting unattended operations while the host ship departs the operating area.

Incorporates multipaths *in situ* This category refers to whether the method incorporates multipath acoustic returns other than direct path during real-time navigation.

Works with a single transponder The third category refers to whether the navigation solution can work with acoustic returns from only one transponder. This is an ultimate goal of the PH method but requires an alternate primary navigation filter to function in this way.

Supports multimodal distributions The fourth category pertains to the belief representations used within the navigation method and whether multimodal distributions can be supported.

Effective in deep water This category refers to whether the method is effective for deep, open water conditions.

Uses negative information The final category highlights whether negative information can be incorporated into the navigation solution.

8.3 Future Work

Future work on the PH method could be done to incrementally improve the algorithm by improving any of the individual blocks, such as:

- Incorporating a more detailed system model in the dead reckoning prediction process.

- Increasing the level of detail in modeling the underwater acoustic environment. There are several ways this could be done ranging from simply incorporating a transmission loss element into the current model to using a more sophisticated model altogether.

- Using an improved method of acoustic ray tracing. This could be done by calculating the entering and departing angles through each constant sound velocity layer and calculating the associated incremental horizontal displacements and time steps for each layer individually.

- Including alternate acoustic eigenrays, such as bottom bounce or bottom-surface bounce, to generate more possible position hypotheses within each single transponder parallel hypothesis block.

- Incorporating more sophisticated terrain relative navigation techniques in the grid arbiter block.

- Using an alternate data association method within the primary arbiter block with better performance in cluttered environments than the current nearest neighbor technique.

- Implementing a single transponder extended Kalman filter as the primary navigation filter.

Most importantly, this novel PH method is a departure point for future research extensions which could make major contributions for vehicle navigation, especially in long-duration, long-distance, unattended deep ocean operations. Currently, the PH method would allow sparse seeding of an extensive operating area for these types of operations with pairs of transponders. In the future, after implementing a single transponder primary navigation filter, the operating area could be sparsely seeded with individual transponders. The overall robustness of the system would be increased by designing and incorporating additional PH building blocks using alternate available sources of gridded or line of position information.

Appendix A

Nomenclature

A.1 List of Acronyms

ABE Autonomous Benthic Explorer

AUV Autonomous Underwater Vehicle

BB Bottom Bounce

CMG Course Made Good

CTD Conductivity, Temperature, and Depth

DB Double Bounce

DMM Dynamic Multiple Model

DP Direct Path

DR Dead Reckoning

DSL Deep Submergence Lab

DVL Doppler Velocity Log

EKF Extended Kalman Filter

EM Expectation-Maximization

GSR Geometric Slant Range

GPB1 Generalized Pseudo-Bayesian of the First Order

GPB2 Generalized Pseudo-Bayesian of the Second Order

GPS Global Positioning System

HR Horizontal Range

ICNN Individual Compatibility Nearest Neighbor

IMM Interacting Multiple Model

IMU Inertial Measurement Unit

INS Inertial Navigation System

JCBB Joint Compatibility Branch and Bound

JPDA Joint Probabilistic Data Association

LBL Long Baseline

LOP Line of Position

MHEKF Multiple Hypothesis Extended Kalman Filter

MHL Multiple Hypothesis Localization

MHT Multiple Hypothesis Tracking

MIT Massachusetts Institute of Technology

MM Multiple Model

NDSF National Deep Submergence Facility

NN Nearest Neighbor

NSF National Science Foundation

OSR Observed Slant Range

OWTT One-Way Travel Time

PH Parallel Hypothesis

R Range

RF Radio Frequency

ROBL Range-Only Beacon Localization

ROV Remotely Operated Vehicle

SB Surface Bounce

SBB Surface-Bottom Bounce

SBL Short Baseline

SLAM Simultaneous Localization and Mapping

SLBL Synthetic Long Baseline

SMG Speed Made Good

SMM Static Multiple Model

SR Slant Range

STRONG Single Transponder Range Only Navigation

SVP Sound Velocity Profile

TERCOM Terrain Contour Matching

TMA Target Motion Analysis

TP Triangle Path

TRN Terrain Relative Navigation

TWTT Two-Way Travel Time

USBL Ultra-Short Baseline

VLBL Virtual Long Baseline

WHOI Woods Hole Oceanographic Institution

XDR Transponder

Appendix B

Modeling the Underwater Environment

A fundamental component of designing any underwater navigation system is modeling the environment in which the navigating platform is operating. Since acoustic time-of-flight measurements between the vehicle and an external acoustic transponder play an important role in the PH navigation scheme, a model of the behavior of sound in the ocean must be developed.

Modeling the acoustic multipaths between a transmitter and receiver in the ocean includes three steps. The first step is developing an accurate Sound Velocity Profile (SVP) for the operating environment based on available data. The next step is identifying the different acoustic propagation paths that are possible between a given transmitter location and receiver location. The final step is modeling the path of an acoustic ray given the local SVP to determine an accurate relationship between time-of-flight acoustic measurements and the range between the transmitter and receiver of that acoustic signal for each possible acoustic path.

B.1 Environmental Modeling Assumptions

Some of the specific assumptions used in this research include:

Range-independence The horizontal gradients in the speed of sound underwater are ignored and sound velocity is spatially considered to be a function only of depth;

Temporal stability of the sound velocity profile The sound velocity profile is considered constant throughout the duration of a dive, and for the Sentry operations on the Axial Seamount, the sound velocity profile was assumed to be constant throughout all three dives;

Smooth ocean surface The effects of surface roughness are ignored and the ocean surface is considered to be a smooth, reflective surface;

Rough ocean bottom The effects of surface roughness are assumed to be significant and the ocean bottom is not considered to be a smooth, reflective surface;

Parallel layer earth The curvature of the earth is ignored in these calculations due to the limited operating range of the vehicles relative to the earth's radius, so the water column is modeled as a vertical stack of parallel flat layers.

B.2 Sound Velocity Profile

The velocity of sound in the ocean varies throughout the water column as the physical properties of the ambient seawater vary. Although horizontal gradients of sound velocity do exist, for the purpose of this research, sound velocity is considered to vary only vertically and is, therefore, a function of depth. Before the behavior of a particular sound ray can be modeled, the vertical SVP in an operating area must be determined.

B.2.1 Sound Velocity Measurements

In order to calculate the SVP, measurements of the pressure, temperature and salinity are taken at the operation location prior to the dive operations. A ship-board Conductivity, Temperature, and Depth (CTD) Sensor is used to measure the vertical profile of these physical properties of seawater. For a single CTD cast, measurements are taken both on descent and on ascent.

B.2.1.1 Conductivity

The salinity of seawater is calculated from the conductivity using the Practical Salinity Scale of 1978 [62, 24, 70]. This scale uses the fact that all samples of water that share the same conductivity must share the same salinity, regardless of water composition. Using this scale, salinity, S, in parts per thousand is defined as

$$S = \sum_{i=0}^{5} a_i R_t^{i/2} + \Delta S \tag{B.1}$$

where

$$\Delta S = \frac{(T - 15)}{(1 + k(T - 15))} \sum_{i=0}^{5} b_i R_t^{i/2} \tag{B.2}$$

$$a_0 = 0.0080 \qquad\qquad b_0 = 0.0005$$

$$a_1 = -0.1692 \qquad\qquad b_1 = -0.0056$$

$$a_2 = 25.3851 \qquad\qquad b_2 = -0.0066$$

$$a_3 = 14.0941 \qquad\qquad b_3 = -0.0375$$

$$a_4 = -7.0261 \qquad\qquad b_4 = 0.0636$$

$$a_5 = 2.7081 \qquad\qquad b_5 = -0.0144$$

$$\Sigma a_i = 35.0000 \qquad\qquad \Sigma b_i = 0.0000$$

$$k = 0.0162 \qquad \text{and}$$

$$R_t = \frac{C(S,T,0)}{C(35,T,0)}$$

where conductivity is $C(S,T,P)$ at salinity, S, in parts per thousand or ‰, temperature, T, in degrees Celsius, and gauge pressure, P, in decibars. R_t is the conductivity ratio of a given sample of seawater to standard seawater with salinity of 35.000 ‰, with both at ambient temperature, T, and atmospheric pressure, $P = 0$. A CTD sensor measures the conductivity ratio, R_t, *in situ* using a conductance cell and then calculates a value for salinity using (B.1) above. See, for example, Millero and Sohn's *Chemical Oceanography* for details on conductance cell configurations [62].

Basic conductance cells measure the conductance of a specific geometry of water using a cell constant equivalent to the ratio of the cell's length to its cross-sectional area. The hydrostatic loading on an *in-situ* conductivity sensor affects the geometric properties of a conductance cell. Therefore, compressibility compensation equations are used to negate the effect of this hydrostatic loading. In general, these equations are automatically implemented in the software associated with a given conductivity sensor. See Sea-Bird Electronics, Inc. Application Note No. 10 for the specific

266

compensation equations for its instruments which are used on ABE, Sentry and many standard ship-deployed CTD packages [39].

B.2.1.2 Temperature

The temperature sensor in a CTD package is a thermistor, which is a temperature sensitive resistor. The relationship between temperature and resistance is derived by inverting the Steinhardt-Hart equation [80] to get:

$$T = \frac{1}{A + B\ln(R) + C\ln^3(R)} - 273.15 \qquad (B.3)$$

where R is the resistance in Ohms and T is the temperature in degrees Celsius.

Sea-Bird Electronics, Inc. CTD sensors use optimized Wien bridge oscillator circuits to determine the thermistor resistance from the frequency output of the oscillator. The resulting relationship between T and the sensor output frequency, f, in Hz is as follows:

$$T = \frac{1}{g + h\ln\frac{f_0}{f} + i\ln^2\frac{f_0}{f} + j\ln^3\frac{f_0}{f}} - 273.15 \qquad (B.4)$$

where calibration constants g, h, i, and j and arbitrary scaling term f_0 are all determined during the calibration of an individual sensor. Modern calibrations are done with respect to ITS-90 temperatures [38].

B.2.1.3 Depth

The CTD sensor measures hydrostatic pressure and from that measurement, depth is calculated. Depth sensors either perform the calculations *in situ* and output depth values, or they output pressure measurements and then depth is calculated off-line. Since gauge pressure is required to calculate the sound velocity, the latter set-up is generally used. Gauge pressure is the difference between the measured absolute pressure and the atmospheric pressure at the surface. Therefore, the depth sensor is

tared at the surface prior to deployment [76].

The development of the ocean depth equation of pressure-to-depth conversion is presented following Fofonoff and Millard (1983) [24]:

Hydrostatic pressure in the ocean increases with depth and is equal to the static weight per unit area of the seawater above any given depth, [67] as given by

$$P(z) = \rho g z \qquad \text{(B.5)}$$

where

P = Gauge hydrostatic pressure,

ρ = Seawater density,

g = Gravitational acceleration, and

z = Depth.

The hydrostatic equation (B.5) is differentiated to get

$$\frac{dP}{dZ} = \rho g, \qquad \text{(B.6)}$$

and rearranged as

$$v \, dP = g \, dz, \qquad \text{(B.7)}$$

where

$$v = \frac{1}{\rho} = \text{Specific volume of seawater.}$$

(B.7) is integrated as

$$\int_0^p v \, dP = \int_0^z g \, dz. \qquad \text{(B.8)}$$

268

The left-hand side of (B.8) is broken down into two parts as

$$\int_0^p v \, dP = \int_0^p v(35, 0, p) \, dP + \Delta D, \qquad (B.9)$$

where $v(35, 0, p)$ is the specific volume of seawater calculated at 35‰ salinity and $0 \deg C$ temperature and ΔD is a geopotential anomaly.

Although $\int_0^p v(35, 0, p) \, dP$ can be calculated exactly, it is a cumbersome and computationally intense process. Therefore, Saunders and Fofonoff fit a fourth order polynomial to a range of discrete data points from 0 to 12,000 decibar using least squares. The resulting error is on the order of $O(10^{-4})$ for full ocean depth [24]. The resulting approximation is

$$\int_0^p v(35, 0, p) \, dP \simeq \sum_{i=1}^4 C_i \, p^i \qquad (B.10)$$

where

$$C_1 = +9.72659$$
$$C_2 = -2.2512 \times 10^{-5}$$
$$C_3 = +2.279 \times 10^{-10}, \text{ and}$$
$$C_4 = -1.82 \times 10^{-15}.$$

The geopotential anomaly ΔD is calculated as

$$\Delta D = \int_0^p \delta \, dp,$$

where δ is the specific volume anomaly, $\delta = V(S, T, p) - V(35, 0, p)$. The standard equation for converting pressure to ocean depth assumes salinity of 35‰ and temperature of $0 \deg C$. Under this assumption, the geopotential anomaly is zero [76].

The right-hand side of (B.8) is $\int_0^z g \, dz$, which is just the area under the curve of $g(z)$ throughout the water column. This is equivalent to taking the product of the average value of gravity throughout the water column, $\bar{g}$, and the depth of the water column, z.

$$\int_0^z g \, dz = \bar{g} * z. \tag{B.11}$$

The average value of the gravitational acceleration can be calculated as

$$\bar{g} = g_0 + \frac{1}{2}\gamma z \tag{B.12}$$

where g_0 is the gravity at the surface and γ is the mean vertical gradient of gravity in the water column in units of $\frac{\frac{m}{s^2}}{m}$. However, since the goal of this process is to find depth as a function of pressure, the linear pressure term, p, replaces depth, z, in the calculation and becomes

$$\bar{g}\prime = g_0 + \frac{1}{2}\gamma\prime p \tag{B.13}$$

where $\gamma\prime$ is the mean pressure gradient of gravity in the water column, given as the constant value $2.184 \times 10^{-6} \frac{\frac{m}{s^2}}{decibar}$. The error introduced by this substitution is on the order of $O(10^{-6})$ at full ocean depth. Gravity at the surface, g_0, in $\frac{m}{s^2}$ is a function of latitude, ϕ, in degrees and is given by

$$g(\phi) = 9.780318 * (1.0 + 5.2788 \times 10^{-3} \sin^2 \phi + 2,36 \times 10^{-5} \sin^4 \phi). \tag{B.14}$$

The resulting depth, z, as a function of observed pressure, p, is

$$z(p) = \frac{\sum_{i=1}^4 C_i \, p^i}{g(\phi) + \frac{1}{2}\gamma\prime p}. \tag{B.15}$$

B.2.2 Sound Velocity Calculations

Salinity, temperature and pressure all affect the velocity of sound in seawater. In general, at shallow depths, salinity and temperature tend to dominate the calculation,

while in the deeper layers of the ocean, the significant hydrostatic pressure becomes more dominant.

Many different equations have been developed to model the exact dependance of sound velocity in water on salinity, temperature, and pressure. The sound velocity in seawater is calculated in this research using the equation developed by V. A. Del Grosso for the Naval Research Laboratory [17]. The equation calculates the speed of sound, C_{STP}, as a function of T, in degrees Celsius using the ITS-68 temperature scale, S, the salinity in parts per thousand using the PSS-78 scale, and P, the pressure in kilograms per square centimeter gauge.

$$C_{STP} = C_{000} + \Delta C_T + \Delta C_S + \Delta C_P + \Delta C_{STP}, \qquad \text{(B.16)}$$

where

$$C_{000} = + 1402.392,$$

$$\Delta C_T = + 0.501109398873 \times 10^1 \, T$$

$$- 0.550946843172 \times 10^{-1} \, T^2$$

$$+ 0.221535969240 \times 10^{-3} \, T^3,$$

$$\Delta C_S = + 0.132952290781 \times 10^1 \, S$$

$$+ 0.128955756844 \times 10^{-3} \, S^2,$$

$$\Delta C_P = + 0.156059257041 \times 10^0 \, P$$

$$+ 0.244998688441 \times 10^{-4} \, P^2$$

$$- 0.883392332513 \times 10^{-8} \, P^3, \ \text{and}$$

$$\Delta C_{STP} = - 0.127562783426 \times 10^{-1} \, TS$$

$$+ 0.635191613389 \times 10^{-2} \, TP$$

$$+ 0.265484716608 \times 10^{-7} \, T^2 P^2$$

$$- 0.159349479045 \times 10^{-5} \, TP^3$$

$$+ 0.522116437235 \times 10^{-9} \, TP^3$$

$$- 0.438031096213 \times 10^{-6} \, T^3 P$$

$$- 0.161674495909 \times 10^{-8} \, S^2 P^2$$

$$+ 0.968403156410 \times 10^{-5} \, TS^2 P$$

$$- 0.340597039004 \times 10^{-3} \, TSP.$$

Sound velocity calculated by (B.16) has a standard deviation of $0.05 \, m/sec$. For typical sound velocities in seawater of approximately $1500 \, m/sec$, this corresponds to a standard deviation on the order $O(10^{-5} \, m/sec)$. The temperature input into (B.16) requires use of the International Temperature Scale of 1968 (ITS-68) instead

of the current ITS-90 scale that is the output of modern temperature sensors. The two scales are linearly related through the following conversion formula [40].

$$T_{68} = 1.00024 * T_{90} \tag{B.17}$$

B.2.3   Sound Velocity Profile Synthesis

Once the discrete sound velocities have been calculated based on the CTD sampling rate, the overall SVP is synthesized. A single CTD cast includes data from both the descent and ascent of the cast that are not always monotonous in their directional movement. Therefore, the resulting aggregated data set includes discrete points with nonuniform vertical spatial distribution. To obtain an overall SVP, the water column is broken down into one meter thick vertical layers. All of the discrete sound velocity data points falling within a given layer are averaged to obtain a single sound velocity data point, c_i, for each layer of water.

$$c_i = \sum_{d=i-1} i c_d \tag{B.18}$$

where c_d is the calculated sound velocity at depth d in meters.

For example, see the sound velocity profiles calculated for the dive ABE157 in Figure B-1. The original sound velocity profiles are shown calculated at every depth where CTD data was taken, as well as the discretized versions where sound velocity is calculated as a constant value for every one meter layer of water.

There are two classes of methods for synthesizing the SVP from the vector of discrete data points, c. Either segmented constant gradient techniques or a family of techniques of curvilinear or continuous gradients may be used. The segmented constant gradient method connects the discrete data points with straight-line segments. The potential disadvantage of this method is that the discontinuities created in the first derivative of this type of piecewise linear SVP can not be handled math-
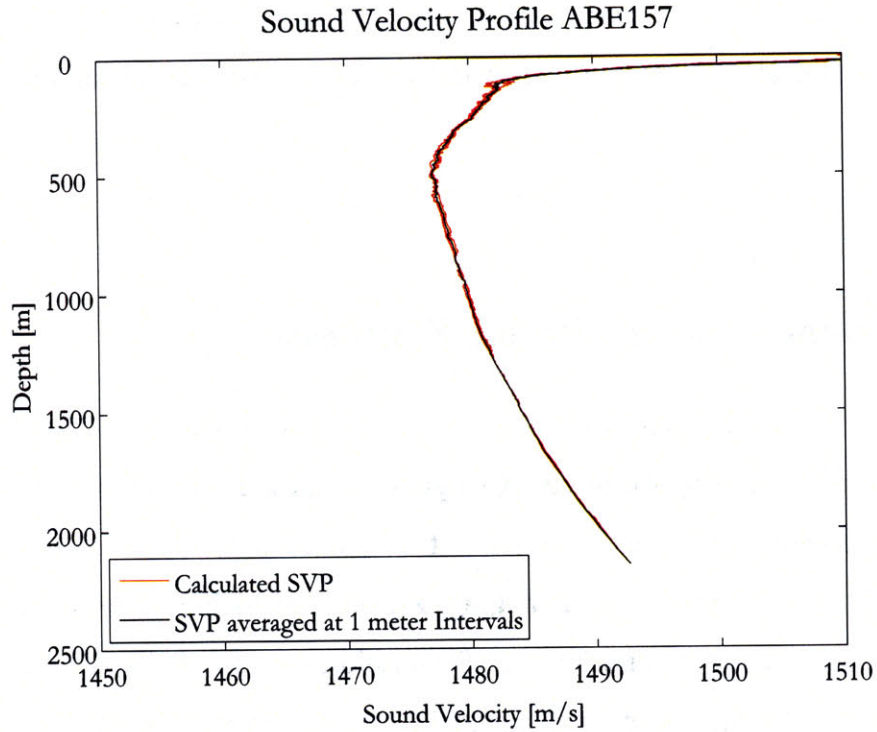
Figure B-1: ABE157 sound velocity profile.

ematically by certain ray tracing techniques. Curvilinear or continuous gradients are created by fitting higher order functions through the discrete data points. Methods have been developed using quadratic equations, cubic splines, conic sections with hyperbolic cosines, and exponential forms. These methods all attempt to overcome the discontinuity problem at the expense of added computational complexity. See Etter's discussion in *Underwater Acoustic Modeling* for more detail on these methods. [20]. The ray tracing techniques used in this research are not affected by the first derivative discontinuities, so the SVP is synthesized using segmented constant gradients.

Bibliography

[1] P. Baccou and B. Jouvencel. Homing and navigation using one transponder for AUV, postprocessing comparison results with long base-line navigation. In *Proceedings of the IEEE Conference on Robotics and Automation*, volume 4, pages 4004–4009, Washington, DC, May 2002.

[2] P. Baccou and B. Jouvencel. Simulation results, post-processing experimentations and comparison results for navigation, homing and multiple vehicle operations with a new positioning method using one transponder. In *Proceedings of the IEEE/FSJ International Conference on Intelligent Robots and Systems*, volume 1, pages 811–817, Las Vegas, NV, October 2003.

[3] T. Bailey and H. Durrant-Whyte. Simultaneous localization and mapping (SLAM): Part II. *IEEE Robotics and Automation Magazine*, 13(3):108–117, September 2006.

[4] Y. Bar-Shalom, editor. *Multitarget-Multisensor Tracking*. Artech House, 1990.

[5] Y. Bar-Shalom and T. Fortmann. *Tracking and Data Association*. Mathematics in Science and Engineering. Academic Press, 1988.

[6] Y. Bar-Shalom, X. Rong Li, and T. Kirubarajan. *Estimation with Applications to Tracking and Navigation*. John Wiley & Sons, Inc., New York, 2001.

[7] B.S. Bingham. *Precision autonomous underwater navigation*. PhD thesis, Massachusetts Institute of Technology, Cambridge, MA, May 2003.

[8] B.S. Bingham and W. Seering. Hypothesis grids: Improving long baseline navigation for autonomous underwater vehicles. *IEEE Journal of Oceanic Engineering*, 31(1):209–218, 2006.

[9] N. Bowditch. *The American Practical Navigator*. National Imagery and Mapping Agency, Bethesda, MD, 2002 bicentennial edition, 2002. Pub. No. 9.

[10] M. Caccia, G. Veruggio, G. Casalino, S. Alloisio, C. Grosso, and R. Cristi. Sonar-based bottom estimation in UUVs adopting a multi-hypothesis extended Kalman filters. In *Proceedings of the Eighth International Conference on Advanced Robotics*, pages 745–750, Monterey, CA, July 1997.

[11] S.C. Chapra. *Applied Numerical Methods with MATLAB for Engineers and Scientists.* McGraw Hill Higher Education, Boston, MA, 2005.

[12] J.H. Clark, J. Gardner, M. Torresan, and L. Mayer. The limits of spatial resolution achievable using a 30khz multibeam sonar: Model predictions and field results. In *Proceedings of MTS/IEEE OCEANS '98*, volume 3, pages 1823–1827, Nice, France, September 1998.

[13] M. Deffenbaugh. A matched field processing approach to long range acoustic navigation. MS Thesis, Massachusetts Institute of Technology, February 1994.

[14] M. Deffenbaugh, J.G. Bellingham, and H. Schmidt. The relationship between spherical and hyperbolic positioning. In *Proceedings of MTS/IEEE OCEANS '96*, volume 2, pages 590–595, Fort Lauderdale, FL, September 1996.

[15] M. Deffenbaugh, H. Schmidt, and J.G. Bellingham. Acoustic navigation for Arctic under-ice AUV missions. In *Proceedings of MTS/IEEE OCEANS '93*, volume 1, pages I204–I209, Victoria, BC, Canada, October 1993.

[16] M. Deffenbaugh, H. Schmidt, and J.G. Bellingham. Acoustic positioning in a fading multipath environment. In *Proceedings of MTS/IEEE OCEANS '96*, volume 2, pages 596–600, Fort Lauderdale, FL, September 1996.

[17] V.A. DelGrosso. New equation for the speed of sound in natural waters (with comparison to other equations). *Journal of the Acoustical Society of America,* 56(4):1084–1091, October 1974.

[18] C. Detweiler, J. Leonard, D. Rus, and S. Teller. Passive mobile robot localization within a fixed beacon field. In *Proceedings of the Seventh International Workshop on the Algorithmic Foundation of Robotics,* New York, NY, July 2006.

[19] H. Durrant-Whyte and T. Bailey. Simultaneous localization and mapping: Part Israel. *IEEE Robotics and Automation Magazine,* 13(2):99–110, June 2006.

[20] P.C. Etter. *Underwater Acoustic Modeling: Principles, Techniques, and Applications.* Elsevier Applied Science, 1991.

[21] R.M. Eustice, L.L. Whitcomb, H. Singh, and M. Grund. Recent advances in synchronous-clock one-way-travel-time acoustic navigation. In *Proceedings of MTS/IEEE OCEANS '06*, Boston, MA, September 2006.

[22] R.M. Eustice, L.L. Whitcomb, H. Singh, and M. Grund. Experimental results in synchronous-clock one-way-travel-time acoustic navigation for autonomous underwater vehicles. In *Proceedings of the 2007 IEEE International Conference on Robotics and Automation,* pages 4257–4264, Rome, Italy, April 2007.

[23] J.A. Farrell. *Aided Navigation: GPS with High Rate Sensors*. McGraw Hill, 2008.

[24] N.P. Fofonoff and R.C. Millard Jr. *Algorithms for computation of fundamental properties of seawater*. UNESCO, UNESCO/SCOR/ICES/IAPSO joint panel on oceanographic tables and standards and SCOR working group 51 edition, 1983.

[25] A. S. Gadre and D. J. Stilwell. Underwater navigation in the presence of unknown currents based on range measurements from a single location. In *Proceedings of the 2005 American Control Conference*, volume 1, pages 656–661, Portland, OR, June 2005.

[26] A.S. Gadre. *Observability analysis in navigation systems with an underwater vehicle application*. PhD thesis, Virginia Polytechnic Institute and State University, January 2007.

[27] A.S. Gadre and D.J. Stilwell. Toward underwater navigation based on range measurements from a single location. In *Proceedings of the 2004 IEEE International Conference on Robotics and Automation*, volume 5, pages 4472–4477, New Orleans, LA, April 2004.

[28] J. Gardner and L. Mayer. Cruise report: RV Ocean Alert Cruise A2-98-SC: Mapping the southern California continental margin. Open-File Report 98-475, U.S. Department of the Interior and U.S. Geological Survey, 1998.

[29] A. Gelb, editor. *Applied Optimal Estimation*. MIT Press, Cambridge, MA, 1974.

[30] J.P. Golden. Terrain contour matching (TERCOM): A cruise missile guidance aid. *SPIE*, 238:10–18, 1980.

[31] Y. Guo, W. Wei, and A. Xue. Bearings-only multiple maneuvering target tracking using sensor-array based on MHEKF, PDA/JPDA. In *Proceedings of the 5th World Congress on Intelligent Control and Automation*, pages 3088–3092, Hangzhou, P.R. China, June 2004.

[32] J.C. Hartsfield Jr. Single transponder range only navigation geometry (STRONG) applied to REMUS autonomous underwater vehicles. MS thesis, Massachusetts Institute of Technology and Woods Hole Oceanographic Institution, September 2005.

[33] T. Hester and P. Stone. Negative information and line observations for Monte Carlo localization. In *Proceedings of the IEEE International Conference on Robotics and Automation*, pages 2764–2769, Pasadena, CA, May 2008.

[34] J. Hoffman, M. Spranger, D. Gohring, and M. Jungel. Making use of what you don't see: Negative information in Markov localization. In *Proceedings of the 2005 IEEE/RSJ International Conference on Intelligent Robots and Systems*, pages 2947–2952, Edmonton, AB, Canada, August 2005.

[35] J. Hoffmann, M. Spranger, D. Gohring, M. Jungel, and H.-D. Burkhard. Further studies on the use of negative information in mobile robot localization. In *Proceedings 2006 IEEE International Conference on Robotics and Automation*, pages 62–67, Orlando, FL, May 2006.

[36] M.M. Hunt, W.M. Marquet, D.A. Moller, K.R. Peal, W.K. Smith, and R.C. Spindel. An acoustic navigation system. Technical Report WHOI-74-6, Woods Hole Oceanographic Institution, December 1974.

[37] Paroscientific Inc. Paroscientific Inc Digiquartz pressure instrumentation. Technical report, Paroscientific Inc.

[38] Sea-Bird Electronics Inc. Premium CTD temperature sensor SBE3plus. Specification sheet, Sea-Bird Electronics, Inc., Bellevue, WA, January 2007.

[39] Sea-Bird Electronics Inc. Compressibility compensation of Sea-Bird conductivity sensors. Application Note 10, Sea-Bird Electronics, Inc., Bellevue, WA, March 2008.

[40] Sea-Bird Electronics Inc. ITS-90 temperature scale. Application Note 42, Sea-Bird Electronics, Inc., Bellevue, WA, March 2008.

[41] M. Jakuba, C. Roman, H. Singh, C. Murphy, C. Kunz, C. Willis, and T. Sato. Long-baseline acoustic navigation for under-ice Autonomous Underwater Vehicle operations. *Journal of Field Robotics*, 25(11-12):861–879, 2008.

[42] J. Jouffroy and J. Reger. An algebraic perspective to single-transponder navigation. In *Proceedings of the 2006 IEEE International Conference on Control Applications*, pages 1789–1794, Munich, Germany, October 2006.

[43] G. Kantor and S. Singh. Preliminary results in range-only localization and mapping. In *Proceedings of the IEEE Conference on Robotics and Automation*, volume 2, pages 1818–1823, May 2002.

[44] I. Kazantsev, H. Haflidason, and A. Steinsland. Calibration of the Simrad EM300 and EM1002 multibeam echo sounders in the Langryggene calibration areas.

[45] J. Kinsey, R. Eustice, and L. Whitcomb. A survey of underwater vehicle navigation: Recent advances and challenges. In *Proceedings of the 2006 IFAC Conference of Manoeuvring and Control of Marine Craft*, Lisbon, Portugal, September 2006.

[46] W. Kirkwood, D.W Caress, H. Thomas, R. McEwen, F. Shane, R. Henthorn, and P. McGill. Results from MBARI's integrated mapping system. In *Proceedings of MTS/IEEE OCEANS '05*, volume 1, pages 563–570, Washington, DC, September 2005.

[47] Kongsberg-Simrad. Simrad EM 300 multibeam echo sounder. Product specification sheet, Kongsberg-Simrad.

[48] M. Kurosu and Y. Ookawa. Effects of negative information on acquiring procedural knowledge. In *Proceedings of the 2002 International Conference on Computers in Education*, volume 2, pages 1371–1372, Auckland, New Zealand, December 2002.

[49] D. Kurth, G. Kantor, and S. Singh. Experimental results in range-only localization with radio. In *Proceedings of the IEEE/RJS International Conference on Intelligent Robots and Systems*, volume 1, pages 974–979, Las Vegas, October 2003.

[50] L. Lapierre. *Mobile Robotics – Towards New Applications*, chapter Underwater Robots Part II: Existing Solutions and Open Issues, pages 362–398. Advanced Robotic Systems, 2006.

[51] C.E.G. LaPointe. Virtual long baseline (VLBL) autonomous underwater vehicle navigation using a single transponder. MS and Eng thesis, Massachusetts Institute of Technology, Cambridge, MA, June 2006.

[52] M.B. Larsen. Synthetic long baseline navigation of underwater vehicles. In *Proceedings of MTS/IEEE OCEANS '00*, volume 3, pages 2043–2050, Providence, RI, September 2000.

[53] J.J. Leonard, A.A. Bennett, C.M. Smith, and H.J.S. Feder. Autonomous underwater vehicle navigation. MIT Marine Robotics Laboratory Technical Memorandum 98-1, Massachusetts Institute of Technology, 1998.

[54] J.J. Leonard and H.F. Durrant-Whyte. Simultaneous map building and localization for an autonomous mobile robots. In *Proceedings of the IEEE/RSJ International Workshop on Intelligent Robots and Systems*, volume 3, pages 1442–1447, Osaka, Japan, November 1991.

[55] K. Llewellyn. Corrections for beam pattern residuals in backscatter imagery from the Kongsberg-Simrad EM300 multibeam echosounder. MEng thesis, The University of New Brunswick, January 2006.

[56] D. Loebis, R. Sutton, and J. Chudley. Review of multisensor data fusion techniques and their application to autonomous underwater vehicle navigation. *Journal of Marine Engineering and Technology*, (A1):3–14, 2002.

[57] L. Lucido, J. Opderbecke, V. Rigaud, R. Deriche, and Z. Zhang. An integrated multiscale approach for terrain referenced underwater navigation. In *Proceedings of the International Conference on Image Processing*, volume 2, pages 633–636, Lausanne, Switzerland, September 1996.

[58] L. Lucido, J. Opderbecke, V. Rigaud, R. Deriche, and Z. Zhang. A multiscale approach for terrain referenced underwater navigation. In *Proceedings of the IEEE-SP International Symposium on Time-Frequency and Time-Scale Analysis*, pages 393–396, Paris, France, June 1996.

[59] L. Lucido, J. Opderbecke, V. Rigaud, R. Deriche, and Z. Zhang. A terrain referenced underwater positioning using sonar bathymetric profiles and multiscale analysis. In *Proceedings of MTS/IEEE OCEANS '96*, volume 1, pages 417–421, Fort Lauderdale, FL, September 1996.

[60] L. Lucido, B. Pesquet-Popescu, J. Opderbecke, V. Rigaud, R. Deriche, Z. Zhang, P. Costa, and P. Larzabal. Segmentation of bathymetric profiles and terrain matching for underwater vehicle navigation. *International Journal of Systems Science*, 29(10):1157–1176, 1998.

[61] D.K. Meduna, S.M. Rock, and R. McEwen. Low-cost terrain relative navigation for long-range AUVs. In *Proceedings of MTS/IEEE OCEANS '08*, Quebec City, Canada, September 2008.

[62] F. Millero and M. Sohn. *Chemical Oceanography*. CRC Press, 1992.

[63] P.H. Milne. *Underwater Acoustic Positioning Systems*. Gulf Publishing Company, Houston, TX, 1983.

[64] C. Moler. *Numerical Computing with MATLAB*. Society for Industrial and Applied Mathematics, 2004.

[65] J.M.M. Montiel and L. Montano. Efficient validation of matching hypotheses using Mahalanobis distance. *Engineering Applications of Artificial Intelligence*, 11:439–448, 1998.

[66] J. Neira and J.D. Tardos. Data association in stochastic mapping using the joint compatibility test. *IEEE Transactions on Robotics and Automation*, 17(6):890–897, December 2001.

[67] J. Newman. *Marine Hydrodynamics*. MIT Press, Cambridge, MA, 1977.

[68] P. Newman and J.J. Leonard. Pure range-only sub-sea SLAM. In *Proceedings of the IEEE International Conference on Robotics and Automation*, volume 2, pages 1921–1926, Taipei, Taiwan, September 2003.

[69] E. Olson, J.J. Leonard, and S. Teller. Robust range-only beacon localization. In *Proceedings of AUV2004: IEEE Workshop on Multiple AUV Operations*, Sebasco, ME, June 2004.

[70] R. Perkin and E. Lewis. The Practical Salinity Scale 1978: Fitting the data. *IEEE Journal of Oceanic Engineering*, 5(1):9–16, January 1980.

[71] RD Instruments, San Diego, CA, USA. *ADCP coordinate transformation: Formulas and calculations*, July 1998.

[72] RD Instruments, San Diego, CA. *Navigator ADCP/DVL users guide*, September 2001.

[73] G. Recktenwald. *Numerical Methods with MATLAB*. Prentice Hall, Upper Saddle River, NJ, 2000.

[74] D. Ribas, P. Ridao, J.D. Tardos, and J. Neira. Underwater SLAM in man-made structured environments. *Journal of Field Robotics*, 25:898–921, 2008.

[75] A. Ross and J. Jouffroy. Remarks on the observability of single beacon underwater navigation. In *Proceedings of the 14th International Symposium on Unmanned Untethered Submersible Technology*, Durham, NH, August 2005.

[76] T. Schaad. Digiquartz depth sensor ocean-depth conversion. Application Note G8033, Paroscientific, Inc., Redmond, WA, 2003.

[77] A.P. Scherbatyuk. The AUV positioning using ranges from one transponder LBL. In *Proceedings of MTS/IEE OCEANS '95*, volume 3, pages 1620–1623, San Diego, CA, October 1995.

[78] J.M. Smith. *Mathematical Modeling and Digital Simulation for Engineers and Scientists*. John Wiley & Sons, Inc., 1987.

[79] T.L. Song. Observability of target tracking with range-only measurements. *IEEE Journal of Oceanic Engineering*, 24(3):383–387, July 1999.

[80] J. Steinhart and S. Hart. Calibration curves for thermistors. *Deep Sea Research*, 15(5):497–503, October 1968.

[81] W. K. Stewart, D. Chu, S. Malik, S. Lerner, and H. Singh. Quantitative seafloor characterization using a bathymetric sidescan sonar. *IEEE Journal of Oceanic Engineering*, 19(4):599–610, 1994.

[82] S. Thrun, W. Burgard, and D. Fox. A probabilistic approach to concurrent mapping and localization for mobile robots. *Machine Learning*, 31(1-3):29–53, 1998.

[83] S. Thrun, W. Burgard, and D. Fox. A real-time algorithm for mobile robot mapping with applications to multi-robot and 3D mappings. In *Proceedings of the International Conference on Robotics and Automation*, volume 1, pages 321–328, San Francisco, CA, April 2000.

[84] S. Thrun, W. Burgard, and D. Fox. *Probabilistic robotics*. MIT Press, Cambridge, MA, 2006.

[85] K. Tischler and H.S. Vogt. A sensor data fusion approach for the integration of negative information. In *Proceedings of the 10th International Conference on Information Fusion*, Quebec City, QC, Canada, July 2007.

[86] J. Vaganay, P. Baccou, and B. Jouvencel. Homing by acoustic ranging to a single beacon. In *Proceedings of MTS/IEEE OCEANS 2000*, volume 2, pages 1457–1462, Providence, RI, September 2000.

[87] J. Vaganay, J.J. Leonard, and J.G. Bellingham. Outlier rejection for autonomous acoustic navigation. In *Proceedings of the IEEE International Conference on Robotics and Automation*, volume 3, pages 2174–2181, Trondheim, Norway, April 1996.

[88] L.L. Whitcomb, D.R. Yoerger, and H. Singh. Advances in Doppler-based navigation of underwater robotic vehicles. In *Proceedings of the International Conference on Robotics and Automation*, volume 1, pages 399–406, Detroit, MI, May 1999.

[89] L.L. Whitcomb, D.R. Yoerger, and H. Singh. Combined Doppler/LBL based navigation of underwater vehicles. In *Proceedings of the 11th International Symposium on Unmanned Untethered Submersible Technology*, Durham, New Hampshire, May 1999.

[90] L.L. Whitcomb, D.R. Yoerger, H. Singh, and J. Howland. Advances in underwater robot vehicles for deep ocean exploration: Navigation, control and survey operations. In *Proceedings of the Ninth International Symposium of Robotics Research*, pages 346–353, Snowbird, UT, USA, October 1999.

[91] WHOI. New robot sub surveys the deep off the Pacific northwest. Online, August 8, 2008. News Release.

[92] W.S. Wijesoma, L.D.L. Perera, and M.D. Adams. Toward multidimensional assignment data association in robot localization and mapping. *IEEE Transactions on Robotics*, 22(2):350–365, April 2006.

[93] J. Wilbur, J. Hyland, G. Dobeck, and C. Sermarini. A multi-hypothesis filter for passive tracking of surface and sub-surface target localization. In *Proceedings of MTS/IEEE OCEANS '06*, Boston, MA, September 2006.

[94] S.B. Williams, P. Newman, J. Rosenblatt, G. Dissanayake, and H. Durrant-Whyte. Autonomous underwater navigation and control. *Robotica*, 19(5):481–496, September 2001.

[95] B.D. Wright. Negative information. *Rasch Measurement Transactions*, 10(2):504, 1996.

[96] D.R. Yoerger. Robotic undersea technology. *Oceanus*, 34(1):32–37, 1991.

[97] D.R. Yoerger and A.M. Bradley. Autonomous underwater vehicles for seafloor observatories: Challenges and opportunities. In *Proceedings of the 3rd International Workshop on Scientific Use of Submarine Cables and Related Technologies*, page 151, Tokyo, Japan, June 2003.

[98] D.R. Yoerger, A.M. Bradley, P. Bachmayer, R. Catanach, A. Duester, S. Liberatore, H. Singh, and B. Walden. Near-bottom magnetic surveys of the Coaxial Ridge Segment using the Autonomous Benthic Explorer survey vehicles. *RIDGE Events*, pages 5–9, 1996.

[99] D.R. Yoerger, A.M. Bradley, M.H. Cormier, W.B.F. Ryan, and B.B. Walden. High resolution mapping of a fast spreading mid-ocean ridge with the Autonomous Benthic Explorer. In *Proceedings of the 11th International Symposium on Unmanned Untethered Submersible Technology*, Durham, NH, August 1999.

[100] D.R. Yoerger, A.M. Bradley, H. Singh, B.B. Walden, M.H. Cormier, and W.B.F. Ryan. Multisensor mapping of the deep seafloor with the Autonomous Benthic Explorer. In *Proceedings of the 2000 International Symposium on Underwater Technology*, pages 248–253, Tokyo, Japan, May 2000.

[101] D.R. Yoerger, A.M. Bradley, and B.B. Walden. The Autonomous Benthic Explorer (ABE): An AUV optimized for deep seafloor studies. In *Proceedings of the 7th International Symposium on Unmanned Untethered Submersible Technology*, pages 60–70, Durham, New Hampshire, September 1991.

[102] D.R. Yoerger, A.M. Bradley, and B.B. Walden. Dynamic testing of the Autonomous Benthic Explorer. In *Proceedings of the 8th International Symposium on Unmanned Untethered Submersible Technology*, Durham, New Hampshire, September 1993.

[103] D.R. Yoerger, A.M. Bradley, and B.B. Walden. An AB(L)E Bodied vehicle proves its worth. *Oceanus*, 39(1):20–21, 1996.

[104] D.R. Yoerger, A.M. Bradley, and B.B. Walden. Scientific survey with the Autonomous Benthic Explorer. In *Proceedings of the 10th International Symposium on Unmanned Untethered Submersible Technology*, pages 41–49, Durham, New Hampshire, September 1997.

[105] D.R. Yoerger, A.M. Bradley, B.B. Walden, M.H. Cormier, and W.B.F. Ryan. Fine-scale seafloor survey in rugged deep-ocean terrain with an autonomous robot. In *Proceedings of the IEEE International Conference on Robotics and Automation*, volume 2, pages 1787–1792, San Francisco, CA, April 2000.

[106] D.R. Yoerger, A.M. Bradley, B.B. Walden, H. Singh, and R. Bachmayer. Surveying a subsea lava flow using the Autonomous Benthic Explorer (ABE). *International Journal of Systems Science*, 29(10):1031–1044, October 1998.

[107] D.R. Yoerger, A. Duester, A. Billings, and D. Glickson. Visions05 summary of ABE operations. Cruise report, Woods Hole Oceanographic Institution, October 2005.

[108] D.R. Yoerger, M.V. Jakuba, A.M. Bradley, and B.S. Bingham. Techniques for deep sea near bottom survey using an Autonomous Underwater Vehicle. *The International Journal of Robotics Research*, 26(1):41–54, January 2007.

[109] D.R. Yoerger, D.S. Kelley, and J.R. Delaney. Fine-scale three-dimensional mapping of a deep-sea hydrothermal vent site using the Jason ROV systems. *The International Journal of Robotics Research*, 19(11):1000–1014, November 2000.

[110] D.R. Yoerger, J. Kinsey, A. Duester, A. Billings, and D. Gomez-Ibanez. Voyage TN221 Sentry operations report. Cruise report, Woods Hole Oceanographic Institution, August 2008.

[111] S. Zhang, L. Xie, and M. Adams. An efficient data association approach to simultaneous localization and map building. *The International Journal of Robotics Research*, 24(1):49–60, 2005.